Doctoral Dissertation
Doctoral Program in Physics (31.th cycle)

ZnO nanowires for memristive devices with enhanced functionalities

Gianluca Milano

* * * * * *

Supervisor
Prof. Carlo Ricciardi

Doctoral Examination Committee:
Prof. Enrique Miranda, Referee, Universitat Autònoma de Barcelona (UAB), Spain.
Dr. Salvatore Iannotta, Referee, CNR-IMEM, Parma, Italy.
Dr. Roberto Verucchi, CNR-IMEM, Trento, Italy.
Prof. Fabrizio Giorgis, DISAT, Politecnico di Torino, Italy.
Prof. Fabrizio Bonani, DET, Politecnico di Torino, Italy.

Politecnico di Torino
February 28, 2019

This thesis is licensed under a Creative Commons License, Attribution - Noncommercial-NoDerivative Works 4.0 International: see www.creativecommons.org. The text may be reproduced for non-commercial purposes, provided that credit is given to the original author.

I hereby declare that, the contents and organisation of this dissertation constitute my own original work and does not compromise in any way the rights of third parties, including those relating to the security of personal data.

. . . .

Gianluca Milano

Turin, February 28, 2019

Summary

The emulation of human brain functionalities represents one of the main challenges in information technology, being a key element for the development of artificial intelligence and intelligent systems. For this purpose, scientists are exploring new bio-inspired computing paradigms beyond the conventional von-Neumann architecture. However, new computing paradigms require the development of new hardware components able to perform brain-inspired data processing. One of the most promising electronic devices able to fulfill this purpose is the *memristor*. The working principle of this two-terminal device is based on the change of the internal resistance state depending on the history of the applied voltage and current. In these terms, memristors are resistor with memory. Conventional memristors are realized by sandwiching an active material in between two metal electrodes in a metal-insulator-metal (MIM) structure, where the insulator is usually a metal-oxide thin film. Despite the growing interest in memristors not only for neuromorphic computing but also for storage and logic applications, a detailed understanding of the physical processes of resistive switching responsible for the memristive behaviour still represents a challenge for the scientific community.

In this work, memristive devices based on crystalline ZnO nanowires (NWs) are proposed as suitable model systems for the investigation of the physical mechanism of switching at the nanoscale. Indeed, besides exhibiting all-in-one memristive functionalities such as multistate non-volatile memory, selector capabilites and neuromorphic functionalities, NW-based devices are shown to be good platforms for a direct investigation of resistive switching due to the high localization of the switching events. After an introduction concerning the background of memristors and resistive switching devices, methods and technologies exploited during this work are summarized. Then, results of the growth process of ZnO NWs by means of Chemical Vapor Deposition (CVD) are reported, together with a detailed characterization of the chemical and structural properties of as grown nanostructures. The dissertation continues with an analysis of the corrosion and dissolution process that occurs in ZnO NWs and a method for tuning ZnO wettability by means of electron beam irradiation is proposed and analyzed. Resistive switching mechanism in ZnO NW arrays is then investigated, revealing that in this case the switching behaviour is strongly related to the peculiar device morphology. However, the main

part of the work was devoted to the investigation of electronic and ionic transport mechanisms in single isolated nanostructures. By considering single NW devices, temperature-dependent electrical characteristics and field-effect measurements allowed the investigation of the electronic conduction mechanism while memristive devices were realized by coupling ionics and electronics. The single NW model system with multiple functionalities was then employed for investigating the effect of moisture on memristive behaviour. Finally, conclusions and perspectives of NW-based memristors are discussed.

Acknowledgements

I would like to express my deep gratitude to my supervisor Prof. Carlo Ricciardi for the encouragement and useful critics during this work. I am extremely thankful and indebted for the valuable guidance given to me during all the PhD project. I would like to acknowledge also Prof. Fabrizio C. Pirri and Dr. Luca Boarino for their support during the work.

I would like to express my deep gratitude also to Prof. Rainer Waser and his group for hosting me during the researh period at the RWTH Aachen University (Germany). A special thank to Dr. Ilia Valov for sharing with me his expertise during the fruitful discussions, for the guidance and for the enthusiastic encouragement on the work.

I would like to acknowledge all the people I worked with at Politecnico di Torino and Istituto Italiano di Tecnologia (IIT), in particular Samuele Porro, Katarzyna Bejtka and Denis Perrone. Thank you very much for your collaboration and support during all my PhD work.

I would like express my deep gratitude to all the people from Istituto Nazionale di Ricerca Metrologica (INRiM) and Trustech. I am particular grateful to Luca D'Ortenzi for the support and for sharing with me his expertise.

A special thank also to Michael Luebben, Dagmar Roedingen, Thomas Poessinger, Zheng Ma and all the other colleagues from Aachen and Juelich for all the support during my research period abroad. It was a pleasure to work with all of you.

I would like to acknowledge all my collegues and people who shared with me the PhD experience: Daniele Conti, Vittorio Fra, Cecilia Giovinazzo, Roberta Calmo, and Davide Scaiola. Thank you also to Md Younus Ali and Monica Beccaria.

Special thanks to my family and friends for the support and inspiration they have been giving me for all my life. And last, but not least, thanks to Giulia for the support during all these years and for having stayed by my side in everyday adventures.

To all people and dreams that are source of inspiration.

Contents

List of Tables xiv

List of Figures xv

1 Introduction 1
- 1.1 Background . . . 1
- 1.2 Memristor: the missing circuit element . . . 2
  - 1.2.1 Memristor and resistive switching devices . . . 3
- 1.3 Resistive switching . . . 4
  - 1.3.1 Electrochemical metallization memory effect (ECM) . . . 5
  - 1.3.2 Valence change memory effect (VCM) . . . 6
- 1.4 Memristor functionalities and applications . . . 8
  - 1.4.1 Memory devices . . . 8
  - 1.4.2 Neuromorphic computing . . . 8
- 1.5 Memristor based on nanostructures . . . 9
  - 1.5.1 Single nanowires . . . 11
  - 1.5.2 Nanowire arrays . . . 11
  - 1.5.3 Nanowire networks . . . 12
  - 1.5.4 Perspectives of NW-based memristors . . . 12
- 1.6 ZnO nanostructures . . . 13
- 1.7 Dissertation outlook . . . 15

2 Methods and technologies 19
- 2.1 Chemical Vapor Deposition (CVD) . . . 19
- 2.2 Material characterization techniques . . . 22
- 2.3 Device fabrication . . . 23
- 2.4 Electrical characterizations . . . 25

3 ZnO nanowires growth and characterization 27
- 3.1 ZnO NWs growth . . . 27
  - 3.1.1 Growth mechanism . . . 27
  - 3.1.2 The role of the substrate . . . 29

3.1.3 NW dimensions and density 31
3.2 ZnO NWs Characterization 33
3.2.1 Chemical properties 33
3.2.2 Structural properties 37

4 Tuning ZnO NW corrosion and dissolution 41
4.1 Introduction 41
4.2 Dissolution of ZnO NWs in H_2O 42
4.3 Modification of wettability properties by electron beam irradiation . 44
4.4 Mechanism of e-beam induced modification of surface properties . . 46

5 Resistive switching in ZnO NW arrays 53
5.1 Introduction 53
5.2 Analysis of the device structure 54
5.3 Resistive switching characteristics 57
5.4 Resistive switching mechanism 60

6 Electronic conduction mechanism in single ZnO NWs 65
6.1 Introduction 65
6.2 Single NW device 65
6.3 Surface effects 66
6.4 I-V-T measurements 67
6.5 Field-effect measurements 70

7 Single ZnO NW memristors 75
7.1 Introduction 75
7.2 Single NW memristor devices 76
7.3 Pristine state 76
7.4 Electroforming process 78
7.5 Physical mechanism of switching 81
7.6 Multilevel non-volatile memory 84
7.7 Threshold switching and selector capability 85
7.8 Artificial synapse 88
7.9 Electrochemical properties of electrodes 92

8 Effect of moisture on ZnO NW memristive devices 95
8.1 Introduction 95
8.2 Effect of moisture on ZnO electronic conduction mechanism 95
8.3 Effect of moisture on electroforming 98
8.4 Effect of moisture on resistive switching 99
8.5 The role of moisture 101

9 Conclusions and Perspectives 103

Bibliography 107

A Additional data on the tuning of ZnO NW surface wetting properties 127
A.1 Selectivity of the e-beam induced modification of surface wetting properties 127
A.2 Effect of plasma treatment 128
A.3 Analysis of e-beam induced chemical changes by means of Raman mapping 129

B Additional electrical characterization of ZnO NW arrays and polycrystalline base layer 131
B.1 Electroforming process in ZnO NW arrays 131
B.2 Resistive switching and compliance current 132
B.3 Resistive switching and voltage polarity 133
B.4 Resistive switching and base layer thickness 134
B.5 Effect of the metal electrodes 135

C Junction properties of ZnO NWs with asymmetric electrodes: a case study 137
C.1 Theoretical background 137
C.1.1 Forward I-V-T method 138
C.1.2 Cheung and Cheung method 138
C.1.3 Norde method 139
C.1.4 Richardson method 139
C.2 Schottky barrier properties 139
C.2.1 Ideality factor and Schottky barrier height 140
C.3 Series Resistance 143

List of Tables

3.1 ZnO NW density as a function of the O_2 precursor gas flux with constant Ar flux (300 sccm). 33
5.1 Peak position and stadard deviation of first order Raman peaks of ZnO NW arrays and base. 57
5.2 XRD peak position (2θ) extrapolated from peak fitting with Voigt functions. 57
6.1 Comparison of activation energies and fitting parameters obtained from data fitting with the double activation energies model described by eq. 6.1 with literature. Values of ρ_1 and ρ_2 from ref. [204] are subjected to an uncertainty of 2% and 3%, respectively. 69

List of Figures

1.1 Classification of resistive switching phenomena. The weight of the reported phenomena depends on the number of publications, development and potential of the mechanism. Reprinted from [12]. . . . 5
1.2 Schematic representation of the working principles of an ECM cell composed of a solid electrolyte (active material) sandwiched in between an electrochemically active (Ag) and an electrochemically inert (Pt) electrode. Reprinted from [14]. 7
1.3 Schematic representation of the NW-based device configurations. a) Conventional MIM structure where the thin film active material is sandwiched in between two metallic contacts, b) single NW-based planar device where a single NW is contacted by metallic electrodes on an insulating substrate, c) NW array-based device where aligned NWs are sandwiched in between two metallic contacts and d) NW network-based planar device where disordered NWs dispersed on an insulating substrate are contacted by metal electrodes. Adapted from [29]. 10
1.4 Stick and ball representation of a) wurtzite crystal structure of ZnO and b) wurtzite unit cell. Grey and yellow balls represent Zn and O atoms, respectively. Reprinted from [118]. 14
1.5 A collection of ZnO nanostructures. Reprinted from [117]. 15
2.1 Experimental setup for the synthesis of ZnO nanostructures by Chemical Vapor Deposition (CVD). 20
2.2 Schematization of the CVD process for the growth of ZnO nanowires consisting on a heating step, a CVD growth step and a cooling step. (1) During heating, the Zn starts to evaporate from the Zn source and to deposit on the target substrate. (2) When the oxygen gas is inserted, ZnO nucleation and growth of islands occur with (3) consequent growth of nanostructures during the CVD step. 21

2.3 Fabrication of single NW devices with symmetric contacts by means of EBL. a) SEM image of the pre-patterned substrate with mechanically deposited ZnO NWs; b) optical image after the EBL process where geometries for contacting single NWs are defined on the PMMA resist; c) optical and d) SEM image of devices after metal deposition and lift-off in acetone. All scale bars are 25 μm. 24
3.1 Morphology of as grown ZnO NWs on Pt substrate. a) Tilted and b) cross-sectional SEM image of vertically aligned and hexagonal shaped ZnO NWs. The inset shows a detail of the NW tip. The CVD process was performed by flushing 200 sccm of O_2 and 300 sccm of Ar. 28
3.2 Schematization of the ZnO NWs growth process by means of CVD, composed of ZnO nucleation on a Pt substrate and subsequent growth of NWs along the preferential *c*-axis direction. 29
3.3 Comparison of the ZnO NWs grown on a a) pre-seeded and b) bare Pt substrate. The CVD process was performed by flushing 150 sccm of O_2 and 300 sccm of Ar. 29
3.4 Selectivity of the growth process. a) ZnO NWs grow only where the Pt thin film was deposited (right side) while other ZnO nanostructures are present on the bare Si substrate. Cross section images of ZnO nanostructures growth on b) bare and c) Pt-coated Si wafer. The CVD process was performed by flushing 150 scmm of O_2 and 300 sccm of Ar. 30
3.5 As grown ZnO NW dimensions as a function of the O_2 precursor gas flux with constant Ar flux (300 sccm). Box plot of a) length, b) diameter, c) aspect ratio and d) base thickness measured by means of cross-sectional SEM images. For each O_2 flux, distributions are obtained by measuring at least 200 NWs in two different samples grown in two distinct CVD processes. Midlines represent the median value, boxes the 25th and 75th percentiles, whiskers the 10th and 90th percentiles and open boxes the mean values. All the CVD processes were performed at 650°C for 20 min by keeping constant all the growth parameters, except for the O_2 flux. 32
3.6 EDX spectra of as grown ZnO NWs. Elemental composition of the specimen calculated from EDX analysis is reported as inset table. Adapted from [162]. 34
3.7 XPS survey spectra of as grown ZnO NWs. Elemental composition of the specimen calculated from XPS analysis is reported as inset table. Adapted from [162]. 35

3.8 High resolution XPS spectra of ZnO NW surface and after 10 min of sputtering (bulk). Measurements were performed on as grown ZnO NW arrays. Panels a),c),e) and g) reported C, O 1s, Zn $p_{3/2}$ and Zn $p_{1/2}$ peaks on the surface while panels b),d),f) and h) reported the same peaks after 10 min of sputtering. Raw data are open circles while red lines are cumulative fit peaks. Adapted from [162]. 36
3.9 XRD pattern of as grown ZnO NWs. ZnO peaks in correspondance of dashed lines are labelled according to JCPDS data no. 89-0511. Adapted from [162]. 37
3.10 TEM analysis of ZnO NWs. a) TEM image of the ZnO NW surface after ∼1 year of ambient exposure (adapted from [162]) and b) high resolution TEM image of the ZnO NW structure. 38
3.11 Raman spectra of ZnO NWs dispersed on a Pt substrate. Red line is the cumulative fit peak, blue lines represent interpolation of single components while black squares are raw data. First order peaks are labelled in bold. 39
4.1 Dissolution of ZnO NWs dispersed on a SiO_2 substrate. a) As deposited NWs and NWs after b) 30 min, c) 60 min and d) 120 min of interaction with deionized water. Adapted from [162]. 42
4.2 TEM and SEM investigation of the anysotropic dissolution of ZnO NWs in water. a) Bright-field TEM image, b) STEM image, c) SEM image and d) high-resolution TEM detail of the surface of a ZnO NW after being immersed in deionized water for 60 min. Adapted from [162]. 44
4.3 Effect of e-beam irradiation on ZnO NW degradation as a consequence of interaction with water. SEM image of the same electron beam treated ZnO NW a) before and b) after being immersed in deionized water for 60 min. c) SEM image of an untreated NW after water interaction (control sample). Adapted from [162]. 45
4.4 Schematization of the reversible tuning of ZnO surface wetting properties by means of e-beam irradiation and O_2 plasma treatment. Adapted from [162]. 47
4.5 Investigation of e-beam modification of surface wetting properties by Raman spectroscopy. Raman spectra acquired on the same area of ZnO NW arrays before e-beam irradiation (black line), after e-beam irradiation (red line) and after oxygen plasma treatment (blue line); a) ZnO region, b) carbon region and c) CH bands region; Spectra are the result of at least three average acquisitions in different regions of the sample and are normalized on the E_2^{high} peak after background subtraction. Adapted from [162]. 48

4.6 Investigaton of e-beam modification of surface wetting properties by FT-IR spectroscopy. FT-IR spectra of as grown ZnO NWs (black), after the e-beam treatment (red) and after oxygen plasma treatment (blue) are compared. Raw data are continous lines while cumulative fit of the peaks performed with Lorentzian/Gaussian peak functions are represent by dashed lines. Adapted from [162]. 49
4.7 Effect of e-beam irradiation on ZnO NW degradation as a consequence of interaction with PMMA. SEM image of the same electron beam treated ZnO NW a) before and b) after PMMA interaction. c) SEM image of an untreated NW after PMMA interaction (control sample). Adapted from [162]. 51
5.1 Investigation of Pt top electrode morphology. a) FESEM image acquired with backscattered electrons of a cross-section of the ZnO NW arrays covered by the sputtered Pt top electrode and b) EDX elemental map; c) Pt, d) Zn and e) O EDX maps. Adapted from [194]. 54
5.2 Removal of ZnO NWs. Cross-section FESEM image a) before and b) after mechanical removal of NWs by sonication. Top views are presented as insets. Adapted from [194]. 55
5.3 Investigation of ZnO NW arrays chemical composition by XPS depth profile. Pt, Si and Ta signals arise from the underlying substrate. Adapted from [194]. 56
5.4 Comparison of ZnO NW arrays and base layer structural properties. Raman spectra of a) ZnO NW array and b) ZnO base layer. Red line represent the cumulative fit peak, blue line the single peak components interpolated by Lorentzian function while black points are raw data. XRD patterns (intensity in log scale) of c) ZnO NW array and d) ZnO base layer. Adapted from [194]. 56
5.5 Resistive switching properties of ZnO NW arrays and ZnO base layer. *I*-*V* characteristics of a) ZnO NWs array and b) base layer. Insets show a schematization of the considered device structure during measurements. Endurance properties of c) ZnO NW arrays and d) base layer, respectively. Adapted from [194]. 58
5.6 Resistive switching parameters of ZnO NW arrays and ZnO base layer. V_{SET} and V_{RESET} as a function of cycles for a) ZnO NW arrays and b) base layer. I_{RESET} as a function of cycle for c) ZnO NW arrays and d) base layer. Adapted from [194]. 59
5.7 Retention test performed on the ZnO polycrystalline base layer. Measurements were performed at room temperature, by applying a stress voltage of 0.1 V for 5 ms every 10 s. Adapted from [194]. . . 60
5.8 Full logaritmic plot of I-V characteristics (positive polarity) of a) ZnO NW arrays and b) ZnO base layer. Fit of LRS and HRS are reported in red and blue, respectively. Adapted from [194]. 61

5.9 Resistive switching mechanism in the polycrystalline ZnO base layer. a) Schematic representation of the resistive switching mechanism based on the formation/rupture of oxygen vacancies-assisted filament along highly oriented grain boundaries. b) Bright field TEM cross section of the ZnO base sandwiched in between a top electrode (TE) and a bottom electrode (BE). Arrows indicate the grain boundaries (GBs). c) HRTEM image of a GB with corresponding FFT patterns acquired on adjacent crystalline grains. Adapted from [194]. 62
6.1 Single ZnO NW device. a) Schematic representation with electrical connections and b) SEM image of a single ZnO NW contacted with Pt electrodes. 66
6.2 Effect of surface states on electrical characteristics of single ZnO NWs. a) *I-V* characterization of a single ZnO NW at 300 K in vacuum before and after annealing treatments. Inset shows a detail of the I-V characteristic pre 1^{st} annealing. b) I-V characterization of a previously annealed NW by progressively increasing the pressure. The insets show the resistivity dependence on pressure and a schematic representation of the NW modelled as a semiconductor core surrounded by an insulating shell layer due to the presence of adsorbed species. 67
6.3 Electrical conductivity of a single ZnO NW as a function of temperature in vacuum conditions. a) Arrhenius plot of the conductivity as a function of temperature and b) schematic representation of the band structure of the ZnO NW (band structure is schematized according to Chiu et al. [133]) 69
6.4 Field-effect in single ZnO NW. a) I_{DS} vs V_{DS} curves acquired with different gate voltage bias and b) I_{DS} vs V_{GS} curves for different drain-source bias. Measurements were performed in vacuum at room temperature. 70
6.5 Temperature-dependent field-effect in single ZnO NW. a) Transconductance characteristics as a function of temperature (measurements were acquired by increasing temperature with a step of about 10 K, from 81.6 K up to 350 K). Arrhenius plot of b) charge density and c) field effect mobility as a function of the reciprocal temperature. d) Field-effect mobility as a function of charge density, where the color scale represents the temperature. 73
7.1 Single ZnO NW memristor device. a) SEM image (in false colors) of a single ZnO nanowire (orange) contacted by means of asymmetric Ag (blue) and Pt (yellow) contacts and b) schematic representation of the device with electrical connections. Adapted from [218]. 76

7.2 Pristine state of ZnO NW memristors. Pristine state comparison of single ZnO NWs contacted by Pt symmetric and Pt-Ag asymmetric electrodes. Insets reported the equivalent circuits of the device. Adapted from [218]. 77

7.3 Electroforming of ZnO NW memristors. a) Forming curve of an Ag/ZnO NW/Pt device characterized by a (1.) diode-like behaviour, (2.) a saturation regime and (3.) a sharp current transition (electroforming). Current compliance (10 μA) was used for avoiding full breakdown of the device. b) Forming voltage dependence on the electrode spacing for different voltage sweep rates. In all measurements, forming was induced by applying a positive voltage bias to the electrochemically active Ag electrode. Adapted from [218]. . . . 79

7.4 Effect of the metal electrode and the substrate during the electroforming process. a) Tentative electroforming of ZnO NWs contacted by symmetric Pt electrodes. b) Tentative electroforming of an Ag-Pt asymmetric device without the presence of the NW in order to investigate the role of the SiO_2 substrate. Insets show the SEM images in flase colors of the devices, where the Pt electrodes are colored in yellow while Ag electrodes in blue. Adapted from [218]. 80

7.5 Breakdown of ZnO NWs due to Joule overheating. a) Electrical characterisitic of an hard breakdown of a ZnO NW contacted by means of Pt electrodes. After the current saturation regime (current self-limitation), the device exhibited an increase of current due to the breakdown current of the inversely polarized junction. An abrupt decrease of current occurs in correspondence of about $\sim 25\,\mu$A due to hard break down of the device. b) SEM image of a NW memristor after breakdown. Adapted from [218]. 81

7.6 Cyclic voltammetry and SEM analyses of resistive switching mechanism. a) CV measurements performed on a single NW memristive device before the forming process, exhibiting a peak attributable to the Ag oxidation process. b) Morphological analysis of the device after resistive switching by means of SEM. The SEM image is in false colors, where the Pt and Ag electrodes are colored in yellow and blue, respectively, while the ZnO NW is in orange. Adapted from [218]. 82

7.7 TEM and EDX analyses of resistive switching mechanism. a) TEM analysis of a NW cross section obtained by cutting the NW in the electrode spacing after resistive switching and compositional EDX maps of b) Zn and c) Ag. d) Ag nanocluster size distribution acquired from TEM analyses. e) HRTEM with corresponding FFT patterns of the ZnO NW/Ag nanocluster interface, revealing their crystal structure. f) HRTEM with corresponding FFT pattern of the NW core after resistive switching, revealing no traces of Ag atoms in the bulk structure. Yellow arrows indicate the crystallographic orientations. Adapted from [218]. 83
7.8 Transconducatance characteristic of the Ag/ZnO NW/Pt device in NW-FET configuration after the formation of the Ag conductive path (in LRS). During voltage sweep of the gate bias, the drain-source voltage (V_{DS}) was fixed at 0.1 V. Adapted from [218]. 84
7.9 Multilevel memory capability of a single ZnO NW memristor. a) *I*-*V* curves of the NW-based device stimulated by DC voltage sweeps by externally imposing different values of CC. Bipolar resistive switching behaviour was observed, with the LRS that depends on the applied CC. b) HRS and LRS of the device (read at 0.4 V) as a function of the imposed CC exhibiting multilevel capability. Box plots are obtained from 15 consecutive cycles for each CC value on the same NW device. Midlines represent the median value, boxes the 25^{th} and 75^{th} percentiles while whiskers the 10^{th} and 90^{th} percentiles. c) Endurance and d) retention properties of the device. Adapted from [218]. 85
7.10 Non-volatile and volatile switching. a) Long write pulses (880 ms, 6 V) resulted in non-volatile resistive switching behaviour where a RESET pulse (180 ms, -1.5 V) was necessary for erasing the ON state. A reading voltage of 0.5 V was applied for reading the device resistance state. b) Volatile resistive switching behaviour was observed after short programming pulses (10 ms, 5 V). The device spontaneously relaxed back to the ground (HRS) state (current relaxation was measured at a reading voltage of 0.4 V). The inset shows a detail of the current relaxation process with discrete conductance steps. Adapted from [218]. 86

7.11 Threshold switching and selector capabilities of single ZnO NW memristors. a) Threshold switching behaviour of the device observed by applying short programming pulses (10 ms, 8 V). After 1 s from the programming pulse, a reading pulse (10 ms, 0.4 V) revealed that the device has spontaneously relaxed back to the ground state. b) Endurance of the NW memristor operating as a selector device. Blue data are sampled during the programming pulse while red data are sampled during the read pulse. The applied pulse shape is schematized as inset. b) Current response of the device during programming pulses with different amplitudes and d) current response of the device during reading pulses (0.4 V, after 1 s from the programming pulse) as a function of the programming pulse amplitude. The time length of both programming and reading pulses were 10 ms. Box plots were realized by considering 100 consecutive threshold switching cycles. Midlines represent median values, box the 25^{th} and 75^{th} percentiles while whiskers the 10^{th} and 90^{th} percentiles. Adapted from [218]. . . 87
7.12 Single ZnO NW memristor response to train of voltage pulses. a) Higher panel shows the input pulse stimuli composed of 50 voltage pulses with length of 22 ms, spaced by 22 ms and with voltage amplitude ranging from 1.2 V up to 4 V. The lower panel shows the current response of the device to the different pulse trains. While for low voltages (< 2.4 V) no switching events were observed, jumps of current were observed after a certain amout of pulses (i.e. incubation time) by increasing the voltage amplitude. For amplitudes ≥ 3.2 V, the device jumped in the ON state during the first pulse. b) Device current response (lower panel) to voltage pulse stimuli (higher panel) characterized by a pulse length of 220 ms, spaced by 220 ms and with voltage amplitude of 1, 1.5 and 2 V. Adapted from [218]. 89

7.13 Neuromorphic functionalities of the single NW memristor. a) Gradual increase of conductivity under low voltage pulse stimulus (3 V, 100 ms). The device spontaneously relaxed back to the ground state after the voltage stimulus, as observed by applying a subsequent reading voltage of 0.4 V. A detail of the conductance relaxation process interpolated with an exponential decay function is presented as inset. b) Experimental demonstration of PPF by applying a train of short voltage pulses (2 ms pulses, 2 ms of waiting time, 2.5 V). c) Conductance change (Δw) as a function of the pulse number, measured for different waiting times in between pulses. d) Dependence of the device response on the voltage pulse frequency. Low frequency pulses (2 ms, 4 V, 10 Hz) are not sufficient for inducing PPF (1.); PPF is observed by increasing the pulse frequency (250 Hz, 50 pulses) while the device relaxed back to the ground state when frequency is again lowered to 10 Hz. Adapted from [218]. 91

7.14 Similarities between a) Ca^{2+} dynamics in biological synapses and b) Ag^{+} dynamics in single NW memristors. The field-assisted migration of Ag^{+} ions in artificial synapses can be exploited for the emulation of the Ca^{2+} influx process of biological synapses, while Ca^{2+} extrusion process can be imitated by the spontaneous physico-chemical dissolution of the Ag conductive path. Adapted from [218]. 92

7.15 Resistive switching of ZnO NWs asymmetrically contacted by means of Cu and Pt electrodes. a) Electroforming of the device exhibiting a single diode-like characteristic (1.), a saturation current regime (2.) and a current jump due to the formation of a conductive path in between electrodes (3.). b) SEM image (in false colors) of the Cu (orange)/ZnO NW (yellow)/ Pt (blue) device after resistive switching, evidencing Cu nanoclusters on the ZnO NW surface. c) Bipolar resistive switching of the device after electroforming. A detail of the negative branch of the voltage sweep is shown as inset. Adapted from [219]. 94

8.1 Analysis of the adsorption of water vapour molecules on ZnO. a) SIMS depth profile of a single crystal ZnO after exposure to deuterium atmosphere and b) multilayer structure of chemisorbed and physisorbed water on the crystalline ZnO surface. 96

8.2 Effect of moisture on single NW resistance. a) NW resistance as a function of RH acquired in Pt/ZnO NW/Pt devices. Resistance were extrapolated from *I-V* measurements at a reading voltage of 0.4 V. Measurements were performed at various RH content in an N_2 (dry) environment. Black and blue points were obtained by measuring the NW resistance after an annealing at 200°C and without annealing (after ambient exposure), respectively. b) Schematization of upward band bending at the ZnO NW surface as a consequence of OH adsorbed species. The NW can be modelled as a semiconductor core characterized by an effective radius r_{eff} surrounded by a depleted shell layer. 97
8.3 Effect of RH on electroforming of Ag/ZnO NW/Pt memristive devices. a) Electroforming process of a NW device with electrode spacing of 376 nm. Electroforming occurred only when RH was increased to 71 %. b) Electroforming of three different devices with electrode spacing of about 150 nm in different RH conditions. c) Forming voltage of single NW devices as a function of electrode spacing for 2 different RH conditions (constant sweep rate of 0.7 V/s). 98
8.4 Effect of moisture on resistive switching. a) I-V cycles and b)endurance properties of a single NW in air (RH ∼30%). c) I-V cycles and d) endurance properties of the same device in dry air (N_2 environment). Resistance values during endurance tests were extrapolated at a reading voltage of 0.4 V. 100
8.5 Direct observation of the effect of moisture on resistive switching. Initially, the device was cycled in air and exhibited resistive switching characteristics (resistance values were extrapolated at a reading voltage of 1 V). In correspondance of cycle 25, the vacuum pump was started and the chamber was evacuated. The device performances were observed to degrade as the RH content was progressively diminished. The whole I-V characteristic of significant cycles are shown (cycle 1,30 and 40). 101
A.1 Selectivity of the modification of surface wetting properties by e-beam irradiation. SEM image of ZnO NWs dispersed on a SiO_2 substrate after 60 min of interaction with water. The area surrounded by the red rectangle was previously e-beam treated. Adapted from [162]. 128
A.2 SEM image of a ZnO NW that was e-beam treated, then treated with an oxygen plasma and subsequently exposed to deionized water for 60 min. Only some residues of ZnO can be observed as a consequence of an almost complete dissolution. Adapted from [162]. 129

A.3 Selectivity of the modification of surface wetting properties by e-beam irradiation investigated by Raman spectroscopy. SEM image of vertically aligned ZnO NWs where electron beam irradiation was performed (red square) and investigated by means of Raman mapping (blue rectangle). Raman map of b) peak intensity and c) peak area of the G band (1600 cm^{-1}); d) M-C stretching band intensity (520 cm^{-1}); e) intensity ratio map of peaks located at 2925 cm^{-1} and 2890 cm^{-1} (CH region); f) LO band over E_2^{high} peak intensity ratio map. Adapted from [162]. 130
B.1 Electroforming of ZnO NW arrays with Pt electrodes. a) First electroforming cycle and b) the following RESET process. c) Stabilization cycles are necessary before that the device exhibited stable characteristics. d) Bipolar resistive switching characteristic after stabilization. Adapted from [194]. 132
B.2 Resistive switching behaviour of ZnO NW arrays for low applied CC. a) I-V characteristic obtained by imposing a CC of 3 mA and b) endurance properties of the device under these conditions (resistance read at 0.1 V). Adapted from [194]. 133
B.3 Resistive switching and voltage polarity. Bipolar resistive switching of a) ZnO NW arrays and b) ZnO base layer with SET process induced with negative polarity applied to the top electrode. Adapted from [194]. 133
B.4 Resistive switching in a polycrystalline base layer with thickness of ~320 nm and contacted by means of Pt electrodes. a) SEM image of the polycrystalline base layer. b) *I-V* characteristic showing bipolar resistive switching. c) Endurance properties (resistance read at 0.1 V) and d) V_{SET} and V_{RESET} as a function of cycles. Adapted from [194]. 134
B.5 Bipolar resistive switching of the ZnO base layer with Cu and Pt electrodes. A SET process in these devices can be induced both in a) positive and b) negative polarities applied to the electrochemically active Cu electrodes. In this cofiguration, devices exhibited high resistance variability over cycling with low endurance, as reported in the insets. Adapted from [194] 135
C.1 Device structure and electrical characterization of Cu/ZnO NW/Pt devices. a) SEM image of the device and b) I-V-T measurements performed in vacuum by biasing the Cu electrode and keeping the Pt electrode at ground. The *lnI-V* plot is presented as inset. Adapted from [219] 140

C.2 Junction parameters as a function of temperature. Temperature dependence of a) ideality factor and b) Schottky barrier height calculted with different methods. Black points were obtained from the forward I-V-T method, blue points from the Cheung and Cheng method while green points from the Norde method. All data were estrapolated by considering I-V-T data presented in Figure C.1. Adapted from [219]. 141
C.3 Apparent barrier height estrapolated with different methods vs $q/2k_bT$. Black points were obtained from the forward I-V-T method, blue points from the Cheung and Cheng method while green points from the Norde method. Two straight lines (in red) are used to interpolate the whole range of data, according to the existance of two Gaussian distribution of barrier heights (G_1 and G_2). Adapted from [219]. . . 142
C.4 Richardson plots. a) Ordinary richardson plot of $ln(I_0/T^2)$ vs q/k_bT and b) modified Richardson plot of $ln(I_0/T^2)-q^2\sigma_s^2/2k_b^2T^2$ vs q/k_bT. Deviation from linearity was observed in the ordinary Richardson plot. According to the existance of two Gaussian distribution of barrier heights (G_1 and G_2), two different values of standard deviations were considered in the modified Richardson plot. σ_{s1} was used in region G_1 (full squares) while σ_{s2} was used in region G_2 (open squares) Red lines represent linear interpolation of data. Adapted from [219]. 143
C.5 Temperature dependence of R_s. Black and blue points were obtained from the Cheung and Cheng method while green points from the Norde method. The Arrhenius plot of data is presented as inset, where the whole set of data were interpolated according to a thermally activated mechanism of electronic conduction. Adapted from [219]. 144

Chapter 1

Introduction

1.1 Background

Artificial intelligence (AI) is becoming one of the main challenges for scientists, promising to be disruptive in a wide range of fields such as information and communication technology, Internet of Thinkgs (IoT), connected networks and autonomous systems. In this context, machine learning and big data are nowadays reshaping other fields of science, industry and the entire society. Despite artificial machines are able to compute and store a huge amount of data in a short amount of time, our brain consumes order of magnitude less power than a supercomputer and is able to execute more complex tasks. Even if a deep comprehension of the human brain behaviour still represent a challenge, the emulation of human brain functionalities and effectiveness seems to be the key element for improving the AI performances. Conventional computing machines are based on the Von Neumann architecture, designed by John von Neumann in the half of the 20th century. This architecture is characterized by the presence of two distinct units for computation and memory and, for this reason, is subjected to the so called "von Neumann bottleneck" that is related to the limited data transfer in between the two units. Note that the distinction in between computation and memory units is not present in the brain where all functions are performed by neural networks composed of highly interconnected neurons that process and transmit information through electro-chemical signalling. The connection in between neurons is provided by means of synapses that regulate the signal transmission. Taking inspiration from nature, brain ispired networks enabling computing and memory in the same physical location (processing-in-memory) are one of the most promising candidates for overcoming the von Neumann architecture. Interestingly, the development of this research field is necessarily related to different branches of science, such as computer science, biology, psychology, material science and physics. The interdisciplinarity of this research topic is an exciting challenge for the entire scientific community.

In order to be effective, artificial neural networks require new nanoelectronic devices able to implement neuromorphic type of data processing. As discussed in this dissertation, *memristors* acting as resitive switching devices represent not only a promising candidate for storage applications but can also be exploited for the emulation of synaptic plasticity, the milestone process for learning and memory in neuromorphic systems. However, a deep comprehension of physical phenomena underlying the mechanism of switching, that is a fundamental prerequisite for understanding and dominating the device functionalities, still represents a challenge for the entire scientific community. Another challenge is represented by the device miniaturization, a crucial aspect for realizing compact and portable devices with high computing and storage power. In this scenario, memristors based on nanostructures such as nanowires (NWs) synthetized with a bottom-up approach represent not only an optimal platform and model system for investigating the physical mechanism of switching at the nanoscale, but also one of the most promising candidate for ultimate device scaling.

1.2 Memristor: the missing circuit element

Memristor (that is a contraction for *memory* and *resistor*) was postulated as the forth fundamental circuit element in 1971 by Prof. Leon Chua by means of symmetrical reasoning [1]. These reasonings arise from the relationship in between the fundamental circuit variables that are charge q, current i, flux linkage φ and voltage v. The definition of charge and flux linkage give rise to the relationships:

$$q = \int i dt \tag{1.1}$$

$$\varphi = \int v dt \tag{1.2}$$

while other relationships result in the axiomatic definition of resistor R, capacitor C and inductor L:

$$dv = R di \tag{1.3}$$

$$dq = C dv \tag{1.4}$$

$$d\varphi = L di \tag{1.5}$$

In this framework, only the relationship between charge and flux linkage was missing. In his works, L. Chua demostrated that this constitutive relationship is underlying the basis of the forth passive circuit element that he called memristor, through the equations:

$$\varphi = f(q(t)) \tag{1.6}$$

$$d\varphi = M(q))dq \tag{1.7}$$

where $M(q)$ represent the memresistance. In a more convenient form, the constitutive equation of the memristor can be rewritten in terms of current and voltage:

$$v(t) = M(q(t))i(t) \tag{1.8}$$

In a later work by Chua and Kang [2], the concept of memristor was generalized in a the broader concept of *memristive systems*, where other dependencies of memresistance different from the charge were enclosed in the state variable $x(t)$. Memristive systems can be thus described by a set of equation (in terms of voltage and current):

$$\begin{cases} v(t) = M(q, x(t))i(t) \\ \frac{dx(t)}{dt} = g(x, i) \end{cases} \tag{1.9}$$

The internal state variable $x(t)$ depends on the physical properties underlying devices, whose dynamical aspects are described by the function $g(x, i)$. To summarize, the memristor is a two terminal and non-linear circuit element that acts as a resistor in which the internal resistance state is defined by the history of the applied current and voltage. In these terms, this circuit element is a resistor with memory and its electrical fingerprint is an hysteretic loop in the first and third quadrant of the I-V plane that is pinched in the origin, whose amplitude depends on the frequency. In this framework, it is important to underline that memristor represents nowadays a widely confused concept and the ideal memristor theorized in 1971 was shown to be physically unfeasible, as discussed in the work by Vongehr et al. [3] and further clarified in a later work by Abraham et al. [4]. Despite this, the concepts of memristor and memristive system are related to resistive switching devices, as discussed in the following.

1.2.1 Memristor and resistive switching devices

The first experimental demonstration of a memristive device was reported only in 2008 by the research group guided by Stanley Williams at HP labs [5]. In their work, authors reported a two terminal device that exhibited the previously described features of a memristive system. The physical mechanism underlying memristive behaviour was proposed to be based on resistive switching phenomena, in which atomic rearrangement driven by the applied electric field is responsible for the modulation of the internal resistance state of the device. It is necessary to underline that, even if the concept of resistive switching was already discussed and widely investigated in previous works (as for example reviewed by Waser et al. [6] in 2007), the work of the HP group represented a milestone, attracting a large audience of scientist and boosting the attention on resistive switching phenomena. Even if the ideal memristor is far from being realized in practice, in a later work Chua clarified that all non-volatile resistive switching devices are memristors, unregarding both the physical mechanism of switching and the materials involved [7]. For

these reasons, in this dissertation it is referred to resistive switching devices and memristors indistinctly. In the following, a brief discussion and analysis of the physical mechanisms responsible for resitive switching are presented.

1.3 Resistive switching

Resistive switching devices are usually two terminal devices based on a capacitor-like structure, in which an insulating material is sandwiched in between two electrodes in a metal-insulator-metal (MIM) stack [6, 8–11]. Despite the simple structure, a wide range of physical mechanisms have been reported to be responsible for resistive switching phenomena. The underlying working principle depends not only on the choice of the insulating and electrode materials but also on the device structure, the interface properties and the operational conditions. Since all these aspects influence the device performances, it is clear that a deep understanding of the physical mechanism of switching is the key element for the development of reliable memristive devices. According to Prof. Rainer Waser [12], resistive switching phenomena can be classified accordingly to the operating principle that can be based on magnetic effects, on electrostatic effects or on the recombination of the atomic configuration. The classification of resistive switching mechanisms proposed by R. Waser is schematized in Figure 1.1. Even if a wide variety of resistive memories has been proposed by exploiting magnetic and electrostatic effects, the most relevant group of phenomena underlying resistive switching is based on the atomic configuration as the state variable of the system. This group of memories can be further divided in subgroups that are redox-based resistance random access memories (ReRAM), phase-change memories (PCM), organic molecules and nanomechanical switches. Even if PCM memories where the change of the internal resistance of the device is linked to the modification of the material phase in between amorphous and crystalline result to be promising, most of the attention of the scientific community is given to ReRAM systems. In these devices, the resistive switching mechanism is driven by electrochemical reactions and nanoionic transport processes [13]. Depending on the ionic species involved in the physical mechanism, ReRAMs can be further classified in electrochemical metallization memories (ECM) where the mobile species are cations, valence change memories (VCM) that are anion-based and thermochemical memories (TCM) where both cations and anions are involved [13]. ECM and VCM cells give rise to bipolar resistive switching where different voltage polarities applied to the device have to be considered during device operations. Instead, TCM cells are unipolar since switching events are not related to the applied voltage polarity. In this framework, it is clear that a detailed understanding of the working principles of resistive switching requires a combination of physical, chemical and engineering approaches. From the physical point of view, the main challenge is understanding both electronic and ionic transport phenomena

related to the properties of the involved materials. Instead, a chemical approach is fundamental for understanding electrochemical reactions while device engineering is essential for the fabrication of reliable devices to be implemented in electronic circuits. In the following, working principles of ECM and VCM, that represent the switching mechanisms discussed in this dissertation, are briefly analysed.

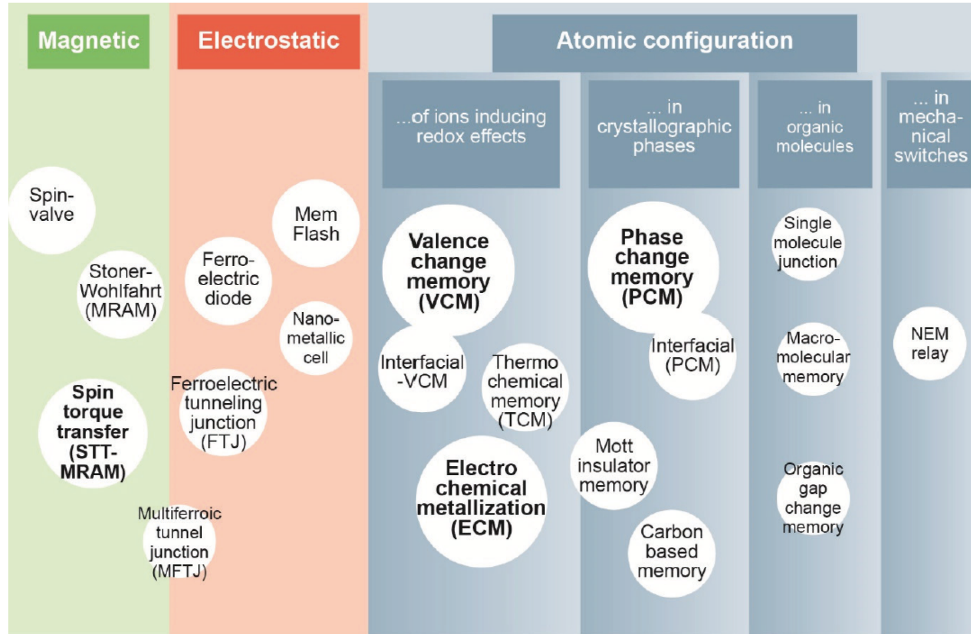

Figure 1.1: Classification of resistive switching phenomena. The weight of the reported phenomena depends on the number of publications, development and potential of the mechanism. Reprinted from [12].

1.3.1 Electrochemical metallization memory effect (ECM)

The electrochemical metallization cells, also named programmable metallization cells (PMC) or conductive bridging random access memories (CBRAM), are two terminal devices based on a MIM structure composed of a solid electrolyte acting as ionic conductor sandwiched in between an electrochemically active electrode and an inert counter electrode [14]. The working principles of these cells can be explained by referring to the schematization reported in Figure 1.2. In the pristine state (A), the ECM cell is highly insulating and the device resistance is determined by the electronic conduction properties of the solid electrolyte material and by the metal-insulator interfaces. When a sufficient positive voltage is applied to the electrochemical active electrode (for example Ag), anodic dissolution of the metal M occurs according to the reaction:

$$M \rightarrow M^{n+} + ne^- \tag{1.10}$$

and metal ions start to migrate in the solid electrolyte towards the counter electrode, under the action of the applied electric field (B). Subsequently, reduction of metal ions occurs according to the reaction:

$$M^{n+} + ne^{-} \rightarrow M \tag{1.11}$$

resulting in the formation of a conductive filament of metal atoms in between the two electrodes (C). As a consequence, the electronic current flowing into the device increases abruptly when the two electrodes are completely bridged by a metallic filament. This is the so-called *forming process* where the device is turned to a lower resistace state, since the metallic filament that is formed acts as a short-circuit (D). Note that, when the metallic path is formed, a current compliance is usually externally imposed to the device in order to prevent the device breakdown due to Joule overheating. Afterwards, the conductive filament can be destroyed by applying a negative voltage that results in the migration of metal ions in the opposite direction, restoring the high resistance state of the device (E). After the forming process that is responsible for the initial assessment of the conductive filament, bipolar resistive switching arises from the reversible formation and rupture of the metallic filament during SET and RESET processes, respectively. The switching properties and kinetics of these cells are determined by the electrochemical properties of the electrodes as well as by the metal ions mobility through the solid electrolyte matrix [15]. Due to their high affinity to dissolution, Ag and Cu are the most widely exploited metals for realizing electrochemical active electrodes.

1.3.2 Valence change memory effect (VCM)

The valence change memory effect is based on electrochemical processes involving both redox reactions and transport of ions in metal oxides, similarly to ECM cells. However, in these cells where usually both electrodes are electrochemically inerts, the switching mechanism is not based on the migration of foreign ions in the metal-oxide matrix but on the migration of oxygen-related defects. The name of this effect is associated to the change in the average valence state of the involved atoms. In this case, redox processes are based on the oxidation/reduction of the metal oxide through the oxygen exchange reaction (using the Kröger-Vink notation)[10]:

$$O_O \rightleftharpoons \frac{1}{2}O_2(g) + V_O^{\bullet\bullet} + 2e' \tag{1.12}$$

where O_O are oxygen ions of the metal-oxide lattice sites and $V_O^{\bullet\bullet}$ are oxygen vacancies. When an electric field is applied to the cell, anodic oxidation of the metal-oxide occurs resulting in an excorporation of oxygen with the creation of oxygen vacancies. Thus, during the *forming process*, the drift of oxygen ions results in the creation of a sub-stoichiometric metal-oxide region characterized by a higher electronic conductivity that propagates towards the counter electrode, driven by the applied electric

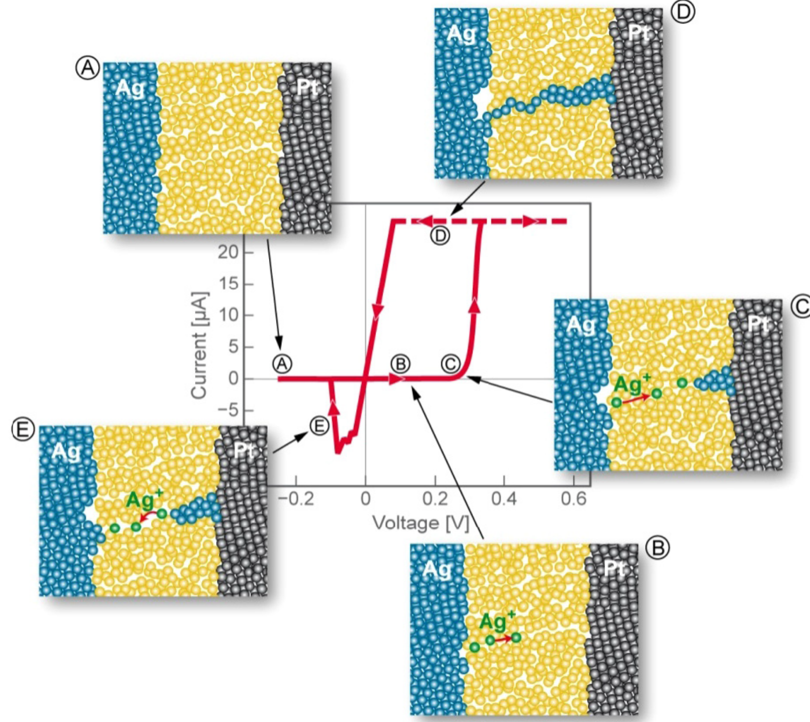

Figure 1.2: Schematic representation of the working principles of an ECM cell composed of a solid electrolyte (active material) sandwiched in between an electrochemically active (Ag) and an electrochemically inert (Pt) electrode. Reprinted from [14].

field. As a consequence, the device is turned to a lower resistance state. The formation/retraction of this substoichiometric region is responsible of SET and RESET processes underlying bipolar resistive switching. In other terms, this mechanism can be explained by the formation/rupture of conductive paths composed of oxygen vacancies, even if it is important to underline that these species cannot be considered as chemical species. In VCM cells, it is necessary to distinghish in between a filamentary type of switching, where the mechanism is based on formation/rupture of localized sub-stoichiometric nanosized conductive paths in the active material, and the more delocalized interfacial switching, where the whole electrode area is involved in the switching events [10]. Despite the switching mechanism in VCM cells is widely attributed to the migration of oxygen anions with consequent redistribution of oxygen vacancies in the metal-oxide matrix, it was proved that also metal cations can participate in the switching process, evidencing an unavoidable interconnection in between ECM and VCM effects [16].

1.4 Memristor functionalities and applications

Memristors and resistive switching technologies promise to be disruptive not only for the realization of next-generation nonvolatile memory chips but also for neuromorphic computing [17–25]. Depending on the final application, memristors characterized by different electrical/physical features and functionalities have been engineered. The aim of this section is to provide a brief summary of the key features required for the various applications of memristive devices.

1.4.1 Memory devices

As non-volatile memories, memristors are promising because of high density of integration, high operational speed and low-cost production [9]. Usually, resistive switching devices for memory applications are characterized by two non-volatile resistance states (0 and 1). The storage capacity can be further improved by multistate capability that enables multi-bit operations. In order to be compatible with low-power electronics, devices require low operational voltages and currents combined with fast write/erase/read operations. In addition, a *resistance ratio* (also called ON/OFF ratio) > 10 is required for providing reliable read-out operations [10]. For memory applications, key aspects are *endurance* (the minimum number of program/erase cycles that a single cell is able to withstand) and *retention* (the ability of retaining the stored information, i.e. the resistance state, over an extended period of time). For the storage of a large amount of data, the integration of resistive switching devices in large arrays can be achieved by exploiting a crossbar array architecture. In this configuration, selector devices are usually required to prevent sneak currents that can lead to read errors, write disturbs and large power consumption [26]. As an alternative to diodes and field-effect transistors, selector devices can be realized by exploiting threshold resistive switching with volatile resistance states [27]. The requirements for the realization of selector devices based on threshold switching are a high nonlinearity combined with fast switching speed (the selector response must be faster than the memory element), low voltage operations and low variability over cycling (high endurance).

1.4.2 Neuromorphic computing

The ability of reproducing human brain functionalities requires new computing paradigms based on neuromorphic data processing. This type of computing is based on learning processes typical of neural networks. Biological neural networks are characterized by the presence of an high number of highly interconnected neurons. The connection in between these entities is provided by the so-called synapses that propagate and regulate the transmission of signals over the network. The key element for the learning process of the network is represented by synaptic

plasticity, that is the ability to modify the synaptic strength as a consequence of pre-synaptic and post-synaptic stimuli (action potentials) [28]. By exploiting similar electrochemical fundamentals as biological synapses, memristors can be exploited as artificial synapses [17]. Indeed, in a similar way to biological synapses, the internal resistance state of the memristor (synaptic weight) can be modulated by applying electrical stimuli to the device terminals. In this context, a realistic mimicking of biological synapses requires multilevel resistance switching capability in order to obtain a large number of resistance states that emulates the synaptic strength. Moreover, the volatility of resistance states can be exploited for the imitation of the forgetting process. While long retention is desired for the emulation of long-term synaptic plasticity (LTP), spontaneous relaxation to the device ground state of resistance is needed for the emulation of short-term synaptic plasticity (STP) [22]. It is thus clear that the key element of neuromorphic computing with memristors is to understand and control resistive switching dynamics.

1.5 Memristor based on nanostructures

Reference paper:

[29] *Milano, Gianluca, et al. "Recent developments and perspectives for memristive devices based on metal oxide nanowires." Advanced Electronic Materials, Accepted Manuscript.*

Two terminal memristive devices are conventionally realized by means of a capacitor-like MIM structure in which an insulating thin-film material is sandwiched in between two metal electrodes. For this purpose, resistive switching properties of a wide range of amorphous and polycrystalline metal-oxide thin films such as TiO_2[5], Ta_2O_5 [30], HfO_2 [31], SiO_2 [32] ZrO_2 [33], CuO [34], ZnO [35], Fe_2O_3 [36] and perovskite oxides [37] have been investigated by exploiting various metal electrodes and configurations. Despite the great efforts, a deep understanding of the mechanism of switching driven by the co-action of physical, electrochemical and thermochemical processes that occur in the bulk structure and/or at interfaces still represent a challenge. In addition, the investigation of the physical mechanism of switching is further complicated by the atomic scale nature of the switching events that are related to spatial inhomogeneous phenomena [38, 39]. In this framework, quasi one dimensional nanostructures such as metal-oxide nanowires represent an optimal platform for investigating resistive switching mechanism at the nanoscale, providing not only high localization with consequent direct observation of the switching events but also the possibility of investigating the role of surroundings on the switching mechanism because of the high exposed surface. The high surface-to-volume ratio of NWs can also be exploited to realize a new class of memristive devices where the switching properties can be modulated by surface

treatments/functionalizations or by applying light stimuli [40–46]. In addition, NWs represent a promising candidate for device miniaturization since they can be synthetized with a bottom-up approach through self-assembling. In this case, the NW dimensions can be controlled directly during the growth process at the atomic scale, overcoming the scaling issues of the conventional top-down lithography [47, 48]. For all these reasons, NWs have attracted great attention since the first experimental demostration of resistive switching in a single nanowire by Kim et al. [49] in 2008. Resistive switching has been investigated not only in electrically contacted single isolated NWs but also in NW arrays where highly ordered and aligned NWs are sandwiched in between two metal electrodes in a stacked structure and in NW networks where highly disordered NWs dispersed on a substrate are contacted in a planar structure. The different NW-based device configurations are schematized and compared to the conventional MIM structure based on thin films in Figure 1.3. In the following, the state of art of NW-based memristors is briefly reviewed.

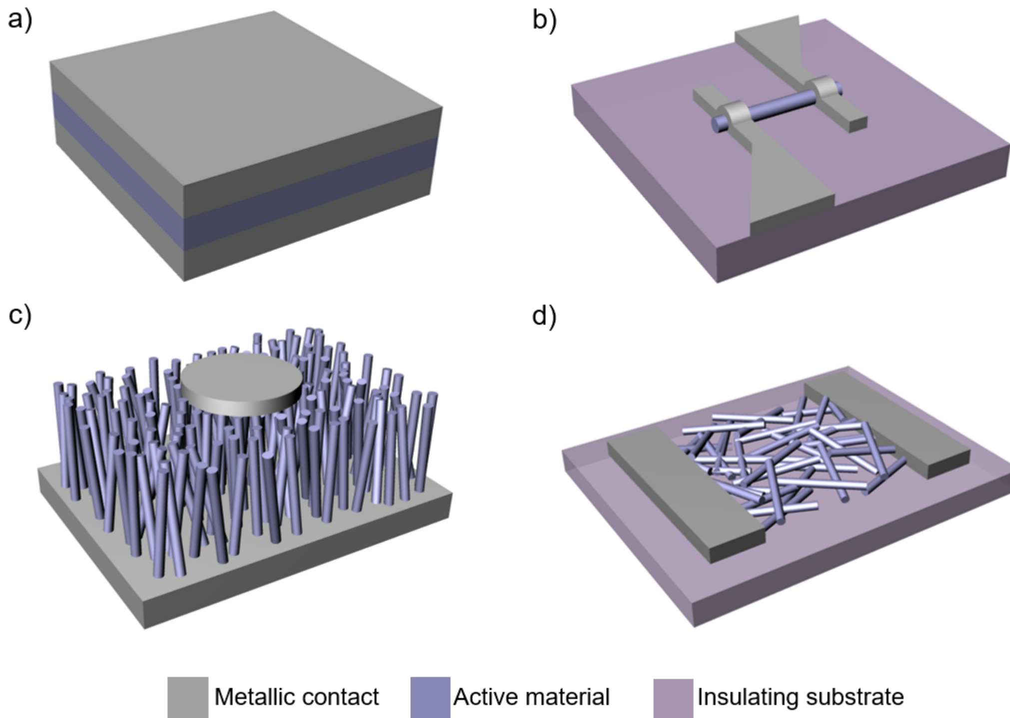

Figure 1.3: Schematic representation of the NW-based device configurations. a) Conventional MIM structure where the thin film active material is sandwiched in between two metallic contacts, b) single NW-based planar device where a single NW is contacted by metallic electrodes on an insulating substrate, c) NW array-based device where aligned NWs are sandwiched in between two metallic contacts and d) NW network-based planar device where disordered NWs dispersed on an insulating substrate are contacted by metal electrodes. Adapted from [29].

1.5.1 Single nanowires

Single isolated NWs represent an ideal platform for investigating resistive switching, providing localization of the switching events in the nanosized NW section. In order to realize two-terminal single NW memristors, NWs are usually dispersed on an insulating substrate and then metallic contacts are realized by lithographic techniques such as electron beam lithography (EBL) or optical lithography, with subsequent metal deposition. Another approach is the direct realization of metallic contacts by means of electron beam induced deposition (EBID) that does not require any lithographic step. Differently from conventional thin film-based devices where the switching mechanism is buried in a stacked structure, single NW devices characterized by a planar structure allow a deep investigation of the switching phenomena. Indeed, as reported by Nagashima et al. [50], these devices allow (i) atmosphere controlled measurement useful to investigate the conduction mechanism and for studying redox reactions, (ii) field-effect measurements in NW field-effect transistor (NW-FET) configuration for understanding the carrier type of the conductive path and (iii) multiprobe measurements for spatial analysis of the switching events. Different physical mechanisms of switching were observed in a wide range of single isolated metal-oxide NWs such as NiO [49], ZnO [42, 44, 51–61], TiO_2 [62–64], CuO [65, 66], VO_2 [67] and WO_3 [68]. By comparing the memristive behaviour reported in these works, it is possible to observe that the switching mechanism depends not only on the NW material and defectivity but also on the NW microstructure (single crystalline or polycrystalline), the metal/NW interface and the metal electrode material. Furthermore, resistive switching phenomena were observed also in heterostructured NWs, such as core-shell [50, 69–78] and multisegmented [79–81] NWs. By considering core-shell nanostructures, the shell layer acts usually as the active material while the inner core can be either insulating (acting merely as a support) or metallic (acting as an electrode). Thus, the switching mechanism can be located both along the axial or longitudinal direction of the wire, depending on the device configuration and on the choice of materials. Instead, the switching mechanism in multisegmented NWs is mainly dominated by interfaces that are present in the heterostructure. It should be noticed that the physical mechanism of switching in single NWs is far from being dominated and NW-based devices usually suffer from low endurance and retention, high SET and RESET voltages and/or limitated functionalities compared to conventional memristors based on thin-films.

1.5.2 Nanowire arrays

A simple approach for the realization of NW-based devices consists of considering NW arrays. Indeed, arrays of oriented NWs can be directly grown by means of several techniques such as chemical vapor deposition (CVD), pulsed laser deposition (PLD), electrochemical anodization and hydrothermal techniques directly

on a metallic substrate that can be exploited as bottom electrode. The memristive device is then simply realized by depositing a top electrode on the NW array, avoiding complex lithographic processes needed to contact single isolated nanostructures. Using this approach, resistive switching was reported in a broad variety of NW and nanorod (NR) arrays such as NiO [49, 82–84], TiO_2 [85–90], GeO_2 [91], WO_3 [92] and ZnO [41, 93–104]. In all these cases, each memristive cell consists of hundreds of vertically aligned nanowires connected in parallel in between the two electrodes. As discussed in this dissertation, the switching mechanism in NW array-based devices can strongly differ from the case of sigle isolated NWs as a consequence of the different device structure.

1.5.3 Nanowire networks

Randomly distributed NW networks represent an attractive solution for the realization of resistive switching devices, reducing the device fabrication complexity and allowing new computing paradigms. For understanding resistive switching in NW networks it is necessary to consider junctions in between NWs. Cagli et al. [105] demostrated that a cross-point junction in between two NWs can give rise to resistive switching phenomena. This concept can be extended to NW networks, where the global behaviour is determined by the randomly distributed cross-point junction dynamics that regulate the network connectivity and conductivity. By exploiting this paradigm, resistive switching properties have been observed in metallic NWs sheathed by an oxide or polymeric shell structure [106–110]. In this scenario, it is important to notice that complex networks represent promising candidates for hardware realization of biologically inspired Touring's unorganized machines where the collective behaviour arises from single processing units [111].

1.5.4 Perspectives of NW-based memristors

Resistive switching devices based on self-assembled nanostructures represent a fascinating alternative to conventional thin-film devices not only for device miniaturization but also for investigating the physical mechanism of switching at the nanoscale, as previously discussed. Usually, resistive switching devices are realized by employing amorphous materials. In this case the disordered matter and the deviation of its properties with time is considered as an internal source of stochastic variability, hampering a detailed understanding of the relationship in between ionic/electronic processes and device functionalities. In these terms, low-dimensional single crystal NWs can be exploited as model systems to provide new insights on the physical mechanism of switching, as presented in this thesis. Moreover, as a consequence of the high surface-to-volume ratio, the possibility of modulating resistive switching properties by applying external stimuli (such as light stimuly, mechanical stimuly, environment) makes these devices particularly promising for

the realization of a new class of devices called memsensors. Despite the numerous applications of NWs in nanoelectronics, the most important challege is represented by the development of a NW-based architecture to overcome technological difficulties due to the integration of NWs in nanoelectronic devices, since this requires manipulation and assembling of these nanostructures at the nanoscale. However, several techniques such as magnetic field [105] and AC electric field [112] alignement, dielectrophoresis [113] and Langmuir-Blodgett technique [114] have been developed for these purposes. From the physical point of view, the main challenge is still represented by a deep comprehension of the physical/electrochemical phenomena underlying resistive switching. In this context, as discussed in this dissertation, single crystalline NWs can serve as model systems for gaining new insights on the resistive switching phenomena, avoiding the sources of stochastic variability that are present in amorphous thin film materials and providing new insights on the role of surfaces and interfaces.

1.6 ZnO nanostructures

In this PhD project, zinc oxide (ZnO) nanostructures were employed for the realization of memristive devices. The choice of ZnO as metal-oxide is related to the fact that this II-VI semiconductor compound represents one of the most widely studied nanostructures material as a consequence of the relative easiness of synthesis of a wide range of nanostructures and the outstanding properties such as the wide and direct bandgap (3.37 eV), large exciton energy (60 meV), large piezoelectric constant and strong luminescence [115, 116]. Even if ZnO can crystallize in three different forms, the hexagonal wurtzite is by far the most common structure since it is stable in ambient conditions, oppositely to the zinc blende and rocksalt counterparts. The ZnO wurtzite crystal structure (w-ZnO) is defined by alternating planes of tetrahedrally coordinated Zn^{2+} and O^{2-} ions that are stacked along the c-axis direction, giving rise to the crystal structure schematized in Figure 1.4 [117, 118]. The non-central symmmetry arising from non-tetrahedral coordination results in the piezoelectric and pyroelectric properties of w-ZnO. Indeed, the wurtzite structure is characterized by polar surfaces that give rise to a dipole moment and spontaneous polarization along the c-axis direction [119].

One of the most important aspect of this material is that it can be synthetized in a pletora of self-assembled nanostructures such as nanowires, nanorods, nanotubes, nanobelts, nano-tetrapods, nanorings, nanohelixes, nanosprings, nanobows, nanocombs and nanocages by controlling the growth kinetics [115, 117, 120]. A collection of synthesized ZnO nanostructures is presented in Figure 1.5. Furthermore, these nanostructures can be grown on a wide range of substrates or independently, by means of vapor or solution phase syntheses [118, 121]. *Vapor phase synthesis*

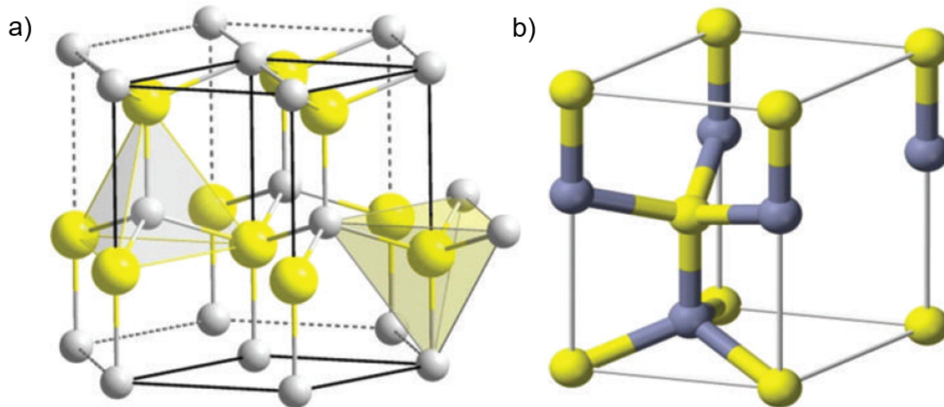

Figure 1.4: Stick and ball representation of a) wurtzite crystal structure of ZnO and b) wurtzite unit cell. Grey and yellow balls represent Zn and O atoms, respectively. Reprinted from [118].

refers to growth processes in which a precursor material is evaporated and transported thanks to a carrier gas towards a target substrate, where chemical species condensate and nucleate facilitated by the presence of a catalyst or a seed layer [122–130]. The precursor materials can be either metallic Zn or ZnO. When metallic Zn is used as precursor, ZnO is formed by inserting oxygen as gas precursor during the growth process [127]. Instead, when ZnO is used as precursor, carbon species like graphite are usually mixed to the precursor powder in order to decrease the process temperature [122, 128]. The vapor phase synthesis is usually performed in a temperature range of 500°C-1500°C [118]. Instead, *solution phase synthesis* is generally performed at lower temperatures (usually < 200°C), resulting in a low-cost production process, easy of handling and allowing a larger choice of target substrates [118]. In this case, the growth process is generally performed in an aqueous solution (hydrothermal growth) which comprises a precursor metal salt [119]. Among ZnO nanostructures, ZnO NWs have been proposed as building blocks for the realization of a wide range of nanoelectronic devices because of their peculiar electronic, mechanical, photonic and plasmonic properties [131–134]. Taking into advantage of these characteristics, ZnO NWs have been exploited for a broad variety of applications such as sensors [135, 136], photodetectors [137], field effect transitors [138] and biomedical devices [139]. In addition, ZnO NWs have been extensively exploited for the realization of resistive switching devices both in form of single NWs and NW arrays (refer to section 1.5).

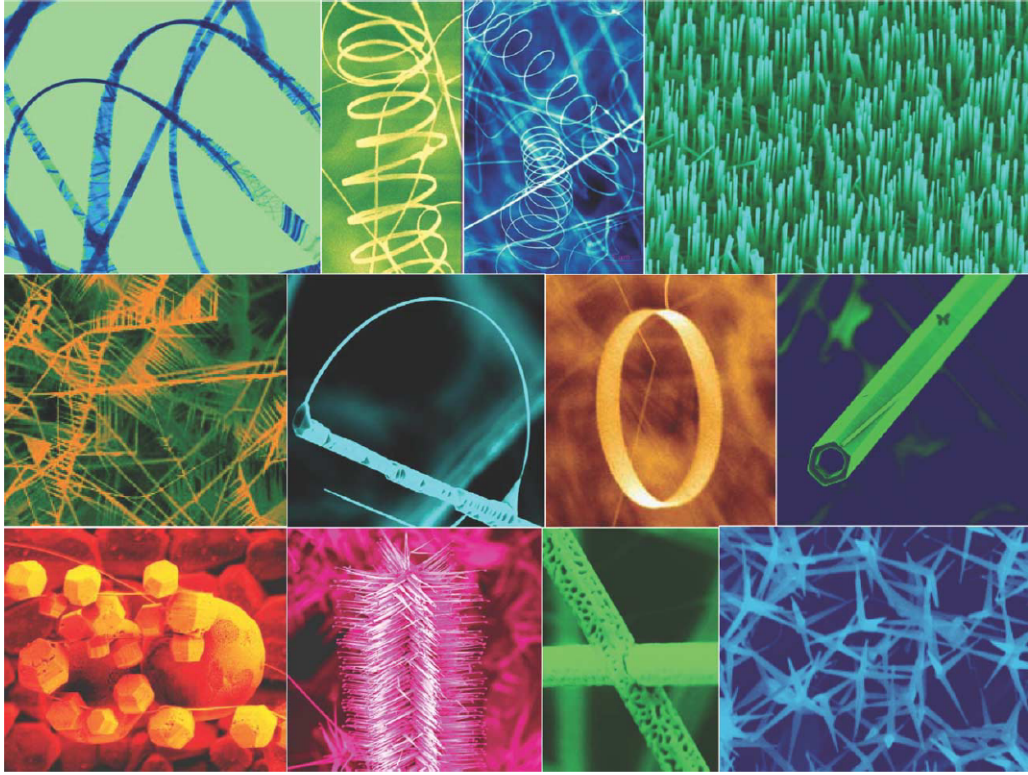

Figure 1.5: A collection of ZnO nanostructures. Reprinted from [117].

1.7 Dissertation outlook

In the following, a brief outlook of the dissertation is provided with a brief overview of the main contents of each chapter.

Chapter 1. The first introductive chapter is devoted to present the background of the main topics of this work. Initially, the theoretical concept of memristor as well as the main features of resistive switching devices are introduced. A classification of resistive switching devices depending on the involved physical mechanism is described. In addition, main features and applications of memristors are discussed. Then, the state-of-the-art of memristive devices realized with nanowires in different device configurations is provided. The chapter ends with an overview of ZnO nanostructures.

Chapter 2. The second chapter provides a general overview of methods and technologies exploited for the realization of the PhD project. This includes a description of the experimental setup and processes for NW synthesis as well as material characterization techniques, fabrication steps for the realization of devices and setups adopted for electrical characterizations.

Chapter 3. In this chapter, the synthesis and characterization of ZnO NWs is discussed. In particular, the growth mechanism is analyzed and the effect of different growth conditions on the NW morphology is shown. The characterization of as grown ZnO nanostructures allowed to investigate their chemical and structural properties.

Chapter 4. Here, the dissolution and corrosion process of ZnO nanowires is investigated and a method for tuning the wetting properties of these nanostructures based on electron beam irradiation is proposed. The mechanism of e-beam induced change of surface wetting properties is discussed by investigating surface modifications by means of spectroscopic techniques.

Chapter 5. In this chapter, new insights on resistive switching mechanism of ZnO NW arrays are provided. After an anlysis of the device structure, electrical characteristics of these devices are reported and analysed. In the end, the physical mechanism of switching is discussed on the base of the electrical behaviour and the peculiar structural properties of the nanostructures.

Chapter 6. This chapter presented an analysis of the electronic conduction mechanism in single ZnO NWs. As preliminar characterization, the effect of surface states on electronic properties of the NWs is discussed. Then, the electronic conduction mechanism is investigated by analyzing temperature-dependent electrical characteristics and field-effect measurements.

Chapter 7. This chapter presents the realization of NW memristors based on single ZnO NWs. Initially, the pristine state and the electroforming process of these devices are analyzed. The physical mechanism of switching was investigated by means of a combined approach that involved electrical, chemical and structural characterizations. The single NW memristor was observed to exhibit most of the memristive functionalities such as multistate non-volatile memory, threshold switching with selector capability and neuromorphic functionalities. In particular, these devices were observed to be able to emulate features of synaptic plasticity and the analogies in between artificial and biological synapses are described. At the end, electrochemical properties of metal electrodes and their influence on the memristive behaviour are discussed.

Chapter 8. Here, the effect of moisture on the memristive behaviour of ZnO NWs is discussed on the base of atmosphere controlled measurements. At the beginning, the influence of moisture on the NW electronic transport properties is analysed. Then, the effects of moisture on electroforming and resistive switching behaviour are investigated and discussed.

Chapter 9. In the end, this chapter provides a summary of the main results presented in this dissertation together with future perspectives.

Chapter 2

Methods and technologies

The interdisciplinarity of the memristor research field requires competences ranging from physics to material science, electronic and engineering. The aim of this chapter is to provide the details of all methods and technologies exploited during the realization of the PhD project, from the synthesis and processing of nanostructures to material characterization techniques, memristive device engineering and electrical characterizations.

2.1 Chemical Vapor Deposition (CVD)

ZnO NWs were synthetized by means of Chemical Vapor Deposition (CVD) technique that exploits the deposition of materials from a vapor phase through chemical reactions. The activation of chemical reactions is supplied by thermal energy (high temperatures) or, as alternatives, plasma or light. Depending on the energy source, it is possible to refer to thermal CVD, plasma enhanced CVD (PECVD) and photon-assisted CVD (PCVD). Moreover, thermal CVD can be further classified in atmospheric pressure CVD (APCVD) or low pressure CVD (LPCVD), depending on the process pressure. Despite the large variety of CVD techniques, all of them follow the same principles as described in details in the Pierson work [140]. In the first stage, a vapor phase of precursor elements is transported towards a target substrate and, when these molecules reach the substrate surface, are physisorbed. Subsequently, the adsorbed molecules can diffuse on the substrate untill nucleation sites are reached. After nucleation, growth of islands occurs while volatile surface reaction products are desorbed. It is important to notice that the growth process is affected by several parameters such as the source species, their transport towards the target substrate (that depends on the type and on the flux amount of carrier gas), the geometry of the system, the type of substrate (morphology, presence of a catalyst or a seed layer) and the temperature that regulates the thermodynamics and the kinetics of the process [141, 142]. An optimization of the

combination of all these parameters is the key element for the controlled growth of the desired nanostructures. In the following, the experimental setup and the LPCVD process employed for the synthesis of ZnO nanostructures are described.

Experimental setup

The LPCVD process was performed in an horizontal tubular furnace. The apparatus, schematized in Figure 2.1, is composed of a quartz tube that can be heated up by means of the surrounding heating components while two gas lines allow the insertion of carrier and precursor gases. The regulation of gas fluxes into the chamber is provided by means of flowmeters, allowing the control of the total gas flux as well as the ratio in between different gas species. As a target substrate, a Pt thin film was realized by sputtering on a Si or SiO_2/Si commercial wafer. The adhesion of the Pt thin film on the underlying substrate was increased by inserting a sputtered Ta adhesion layer prior to Pt deposition. As discussed in the following sections (section 3.1.2), the growth process was performed both on bare and seeded Pt substrates. For the realization of a ZnO seed layer, a solution of zinc acetate dihydrate (22 mg) and ethanol (10 ml) was prepared. Then, the solution was dropped on the clean target substrate and uniformely distributed by spin coating. After spinning, the substrate was dipped in ethanol and the first seed layer is thus prepared. Five layers were realized by repeating this procedure and then the substrate was placed in the tubular oven and annealed for 20 min at 350°C. When the substrate was cooled down, other five layers were realized and then annealed again, realizing a total of 10 coating layers. By following this procedure, a uniform seed layer was prepared. Independently from the presence of a seed layer or not, the target substrate was then inserted in the quartz tube on an alumina boat, surrounded by a Zn foil (purity 99.99%) that acts as the Zn source. Note that an accurate cleaning of the quartz tube from Zn and ZnO residues evaporated

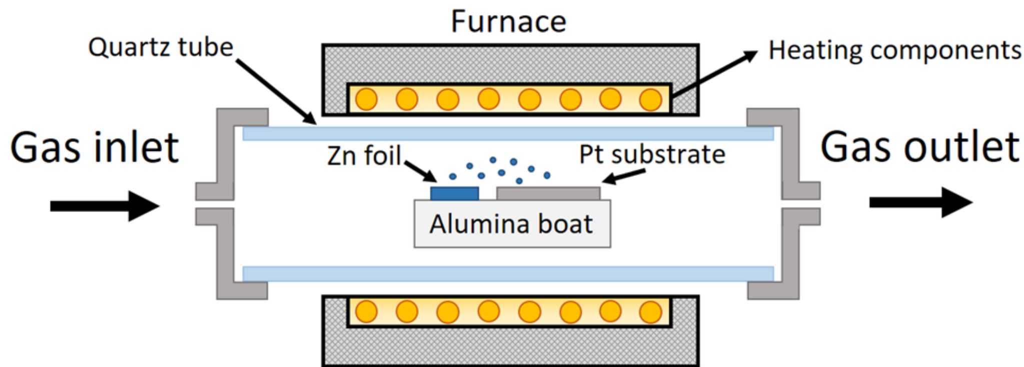

Figure 2.1: Experimental setup for the synthesis of ZnO nanostructures by Chemical Vapor Deposition (CVD).

on the inner surface during previous growth processes is fundamental in order to obtain reproducible growth conditions. For this reason, the tube was cleaned with a solution of HCl after each growth process.

LPCVD process

The LPCVD process started with the initial evacuation of the vacuum chamber (down to $\sim 10^{-2}$ Torr) to remove all contaminations. Then, the substrate and the Zn source were heated up with a ramp rate of 8.6 °C/min with a constant flow of 60 sccm of Ar. When the temperature reached 300 °C, the flux of the Ar carrier gas was increased to the desired value needed for the CVD process (typically in the range of 250-400 sccm). During this first step, the Zn source melts (Zn melting point is about 420 °C in ambient conditions) and, when the vapor tension of the liquid Zn is high enough, starts to partially evaporate and to be transported to the target substrate helped by the carrier gas. When the temperature of 650 °C was reached, a flux of O_2 precursor gas (in the range of 50-200 sccm) was inserted into the chamber. Thus, ZnO starts to nucleate with consequent growth of islands on the Pt substrate. During the CVD step, the temperature was fixed at 650 °C for 20 min while the pressure was measured to be in the range of 1-1.6 Torr, depending on the amount of gas fluxes. At this stage, the growth of nanostructures occurred. At the end, the O_2 flux was removed and the chamber was cooled down to room temperature in an Ar environment.

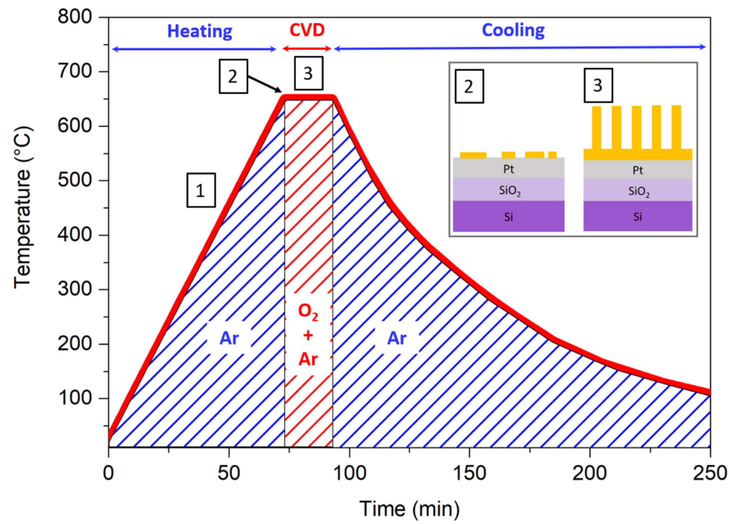

Figure 2.2: Schematization of the CVD process for the growth of ZnO nanowires consisting on a heating step, a CVD growth step and a cooling step. (1) During heating, the Zn starts to evaporate from the Zn source and to deposit on the target substrate. (2) When the oxygen gas is inserted, ZnO nucleation and growth of islands occur with (3) consequent growth of nanostructures during the CVD step.

2.2 Material characterization techniques

The development of reliable memristive devices is closely related to a deep understanding of the interrelationship between the induced switching events and the local changes in the material properties. Indeed, as reported in the review of Yang and Huang [39], this represents a key aspect for further technological innovation, optimization and design of memristive devices. In this framework, material characterization tools are fundamental not only for investigating the switching mechanism but also for the optimization of the involved materials synthesis.

In this work, the morphology of as grown nanostructures was assessed by means of field-emission scanning electron microscopy (FE-SEM, Zeiss Merlin) equipped with a Oxford X-act that mounts a SSD detector for Energy dispersive X-ray spectroscopy (EDX) in order to perform elemental analyses. EDX elemental mapping was performed by using an electron beam accelerated at 20 kV as excitation source. The chemical composition of nanostructures was investigated with X-ray photoelectron spectroscopy (XPS) by using a PHI 5000 VersaProbe (Physical Electronics) system. A monochromatic Al Kα radiation with energy of 1486.6 eV was used as the X-ray source while an Ar ion gun was exploited for XPS depth profile measurements, by progressively etching the material surface. The C peak position (284.8 eV) was used as the internal standard energy in all measurements. High resolution XPS peaks were interpolated by means of Gaussian-Lorentz functions after Shirley's background subtraction. Structural properties were analyzed with X-ray diffraction (XRD) using a Panalytical X'Pert Pro Diffractometer in Bragg-Brentano θ-2θ configuration with a Cu Kα as radiation source ($\lambda = 1.54059$ Å) and by means of Raman spectroscopy with a Renishaw inVia Reflex micro-Raman spectrophotometer equipped with a cooled charge-coupled device camera (excitation laser wavelengths of 514 nm). Raman spectroscopy and mapping for investigating modifications after electron beam irradiation were performed by using a confocal Thermo Fischer Scientific DXR Raman microscope system with a 100x microscope objective, an excitation laser wavelength of 532 nm with a full range grating (acquisition range of 50-3500 cm^{-1}) that possesses spectral resolution of 5 cm^{-1}. All Raman measurements were performed with an unpolarized light source in backscattering geometry. FT-IR measurements were performed with a iN10 Thermo Fisher Scientific microscope with a liquid nitrogen cooled MCT detector in reflectance mode, with a spot size of $100 \times 100\,\mu$m. Transmission electron microscopy (TEM) was performed by means of a FEI Tecnai F20ST with a field emission gun (FEG) operating at 200 kV. The preparation of cross section specimen for TEM analysis was realized by using a focus ion beam (FIB) system (Zeiss Dual Beam Auriga) operating at 30 kV. In order to achieve the final thickness and minimize the damage of the sample, a final cleaning step was performed by using a FIB voltage of 2 kV. Instead, the TEM investigation of single nanowires was performed by simply transferring the ZnO NWs from the growth substrate onto the TEM grid by

using a mounted hair. The switching mechanism in single NWs was investigated by means of a FEI Titan G2 60-200 ChemiSTEM microscope operating at 200 kV with a spherical aberration corrector for the probe forming system. Super-X energy-dispersive X-ray spectroscopy (EDX) was used to perform elemental analyses and for high angle annular dark-field (HAADF) imaging. In this case, the cross section sample preparation was performed with a FEI dual-beam FIB Helios Nanolab 460F1 workstation. Initially, a carbon layer was electron beam deposited to protect the area of interest. Further protection of the specimen was provided by an additional Pt layer deposited through Ga ion beam. The TEM sample was then prepared by using a "lift-out" technique. At the end, an additional step of polishing was performed to eliminate contaminations and to reduce surface roughness with a Fischione's Model 1040 NanoMill system.

2.3 Device fabrication

The fabrication of memristive devices requires different processing techniques depending not only on the device design but also on the involved materials. In the following, the main aspects involved in the realization of devices based on NW arrays and on single isolated NWs are discussed.

ZnO NW array devices

Devices based on NW arrays represent the simplest configuration for the realization of resistive switching cells based on ZnO NWs, as previously discussed in section 1.5.2. Indeed, since ZnO NW arrays can be directly grown on a Pt substrate, the MIM structure can be simply realized by evaporation of a metal contact on the top of the NW array. Thus, in this configuration, the Pt substrate can be exploited both as the growth substrate and as the bottom electrode while the top electrode metal is realized by DC sputtering (in case of Pt). Note that the bottom electrode was accessed by etching part of the NW array with a HCl solution. The top electrode geometry composed of circular pads with diameter of 1 or 2 mm was defined by using a shadow mask. In order to improve the contact quality, the electrical connections to the top electrode were realized by means of tungsten cylinders.

Single ZnO NW devices

The realization of single NW devices requires a more complex procedure that combines optical lithography and electron beam lithography (EBL). At the beginning, a SiO_2 (450 nm)/Si (p-type, B doped) substrate was patterned by optical lithography to realize a customized millimiter-sized Ti/Au probe circuit. Then, NWs were mechanically transferred from the growth substrate to a selected area of

the probe circuit by using a mounted hair or a Cu wire with the help of an optical microscope. Proper markers were used as references for the NW positioning. After that, electron beam lithography (Quanta 3D Microscope) was exploited to define contact geometries for connecting isolated NWs to the probe circuit. Poly(methyl methacrylate) (PMMA) was used as the e-beam resist during the lithographic processes. For this purpose, PMMA with a thickness of $\sim$300 nm was deposited on the sample by means of spin coating prior to electron-beam irradiation. EBL was followed by metal deposition (80 nm) by sputtering (Kurt J. Lesker, PVD 75) and lift-off technique in acetone. The contact quality and reliability was ensured by an oxygen plasma treatment using 40 W of power for 30 s (Bdiscom plasma matrix) before metal deposition. Images of the fabrication steps required for contacting single NWs are reported in Figure 2.3.

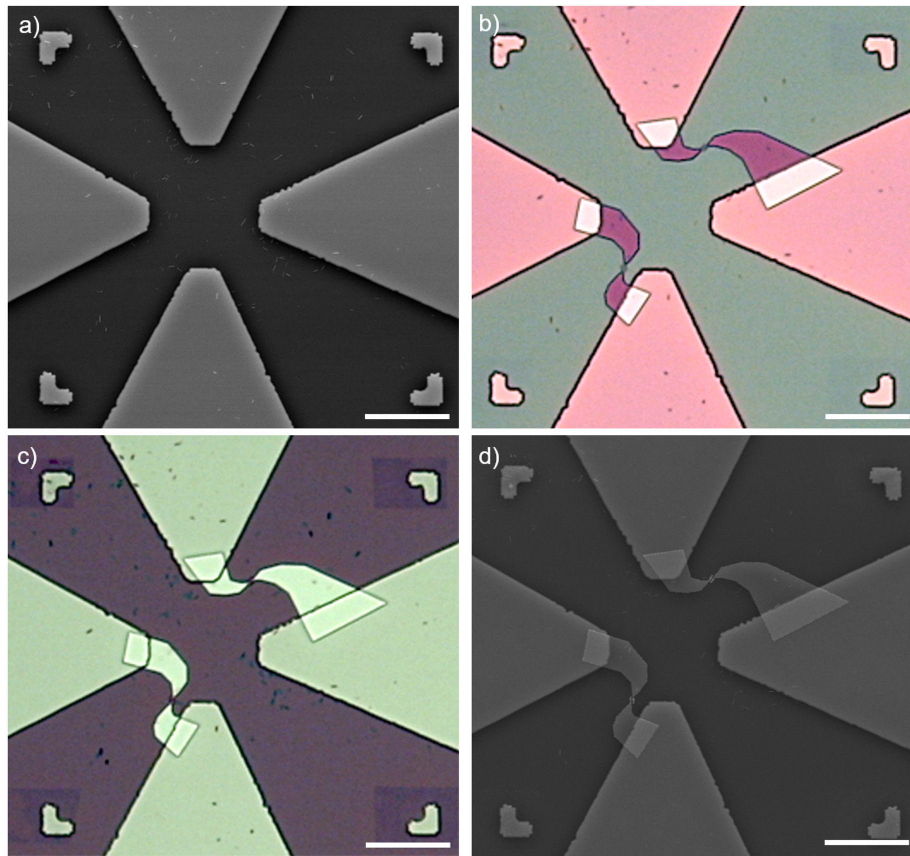

Figure 2.3: Fabrication of single NW devices with symmetric contacts by means of EBL. a) SEM image of the pre-patterned substrate with mechanically deposited ZnO NWs; b) optical image after the EBL process where geometries for contacting single NWs are defined on the PMMA resist; c) optical and d) SEM image of devices after metal deposition and lift-off in acetone. All scale bars are 25 μm.

Note that two different EBL processes were necessary to define single ZnO NW devices contacted with asymmetric metallic contacts. The morphology of the devices was assessed by means of scanning electron microscopy (SEM; FEI Inspect F). The engineering of single ZnO NW based devices requires a deep understanding of the interaction between ZnO NWs and all the chemicals used during the fabrication process in order to prevent ZnO NW degradation and corrosion. For this reason, water-based solvents were avoided during all the fabrication steps for preventing damaging of the ZnO NW surface. All these aspects were analyzed, as discussed in details in chapter 4.

2.4 Electrical characterizations

Electrical characterizations of NW arrays were performed in air at room temperature by using a Keithley 4200 semiconductor parameter analyzer coupled with a probe station equipped with micromanipulators and tungsten probes. Instead, electrical responses of single NWs were probed in various configurations and by using different characterization tools, as described in the following. Temperature dependent electrical measurements were performed in a modified cryostat (Janis ST-100H) [143], by inserting the sample on a cold finger into a vacuum chamber equipped with turbomolecular and rotative pumps. A Lake-Shore 331 temperature controller coupled with a heater and a liquid-nitrogen transfer line allowed sample characterization in a wide range of temperatures (from about 81 K up to 480 K). A platinum resistor (Pt-100) embedded in the cold finger ensured accurate measurement of the sample temperature. In this configuration, electrical measurements were performed by means of a Keithley 6430 Sub-Femtoamp SourceMeter with remote preamplifier while a Keithley 2410 was exploited for applying a gate bias in NW field effect transistor configuration (the gate leakage current was measured to be negligible during all measurements). All the instruments connected to the cryostat were controlled by using a Labview routine. Pristine state characterization as well as CV measurements of memristive devices were performed by using a Keithley 6430 sub-femtometer sourcemeter with remote preamplifier, DC characterization and long pulse measurements were performed by means of a Keithley 2636A or Keithely 2634B in customized probe stations while short pulse measurements were performed by using the Keithley 4200 semiconductor parameter analyzer coupled with Pulse Measuring Units (PMUs) and a Semiprobe probe station. Electrical measurements in a controlled atmosphere were performed in an appropriate chamber coupled with a Keithley 2636B and a Keithley 6430 sub-femtometer sourcemeter with remote preamplifier. Before measurements, the chamber was filled with the desired gas composition after evacuation (down to $\sim 10^{-5}$ mbar) through a turbomolecular pump. The humidity controlled measurements were performed in dry air, by flushing N_2 in a cascade of gas wash bottles filled with deionized

water. The relative humidity was measured with a humidity sensor inserted into the chamber. During all electrical characterizations of stacked devices (NW array devices), the bottom electrode was grounded while a voltage bias was applied to the top electrode.

Chapter 3

ZnO nanowires growth and characterization

In this chapter, the development and optimization of a growth process for the bottom-up synthesis of ZnO nanowires is discussed. The growth process represents a fundamental step for the realization of resistive switching devices since it affects the chemical and structural properties of the nanostructures. For these reasons, a detailed characterization of as grown nanostructures is essential not only for investigating and optimizing the growth process but also for understanding the resistive switching mechanism discussed in the following chapters.

3.1 ZnO NWs growth

3.1.1 Growth mechanism

There is a wide literature concerning the growth of ZnO nanostructures and nanowires by means of CVD, reporting not only a wide range of process parameters and setup configurations but also different growth mechanisms such as Vapor-Liquid-Solid (VLS) and Vapor-Solid (VS) [123–125, 127–129, 141, 142, 144–159]. In case of VLS process, the formation of a small liquid metal clusters acting as catalysts on the growing substrate is required for incorporation of precursor atoms and subsequent growth of nanostructures by precipitation. Instead, the VS process does not require any catalyst since nanostructures crystallize directly on the growing substrate [146]. In this scenario, there is not an optimal recipe for the growth of these nanostructures since the synthesis process has to be optimized depending on the desired material quality and/or final application. For the realization of ZnO NW-based resistive switching devices, the growth of nanostructures on a metallic substrate with a VS mechanism is desired. Indeed, in this case the growing substrate can be directly exploited as metallic electrode for electrical characterization, avoiding any metal catalyst contamination of the nanostructure and ensuring the

absence of a metal cluster on the NW tip that can complicate the device designing and electrical characterization (note that a metal cluster on the NW tip is always present in case of VLS growth). In view of these observations, ZnO NWs were grown by self-seeding VS mechanism on a Pt substrate. The experimental setup as well as the CVD process are described in details in Section 2.1. The typical morphology of as grown ZnO NWs assessed by means of SEM is presented in Figure 3.1, revealing uniform growth of vertically aligned and hexagonal shaped NWs. In addition, the growth was observed to be uniform over a large area ($\sim 2 \times 2$ cm). As can be observed from the inset of Figure 3.1 a, the high-resolution SEM images ensured the absence of metallic particles on the NW tip, confirming a VS type of growth mechanism. Moreover, cross-sectional SEM images (as reported in Figure 3.1 b) revealed the presence of a ZnO layer in between the Pt growth substrate and the NWs. During this thesis, this layer was called *base*. The growth can be explained accordingly to the self-seeding VS mechanism proposed by Jeong et al. [153]. In the first growth stage, ZnO seeds start to form on the Pt substrate when oxygen is inserted into the chamber. It is important to notice that the nucleation of ZnO seeds is facilitated in correspondence of substrate defects [158]. Then, epitaxial growth of ZnO NWs occurs starting from the ZnO seeds while additional seeds are formed near the exhisting ones. This lead to the formation of a ZnO continous layer (base layer) underneath NWs. Thus, the growth of vertically aligned NWs results from self-organization of ZnO atoms along the *c*-axis preferential direction starting from a self-formed ZnO seed layer, as schematized in Figure 3.2.

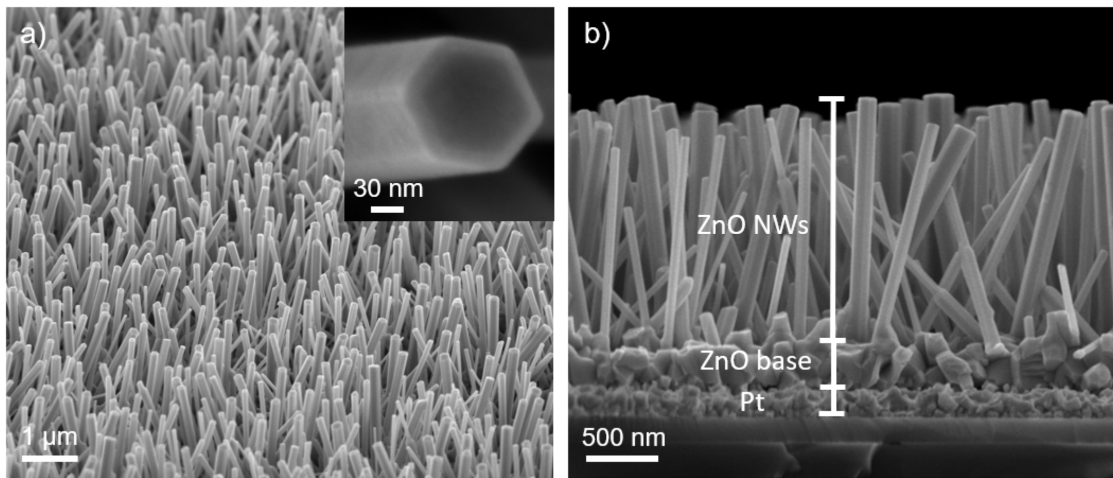

Figure 3.1: Morphology of as grown ZnO NWs on Pt substrate. a) Tilted and b) cross-sectional SEM image of vertically aligned and hexagonal shaped ZnO NWs. The inset shows a detail of the NW tip. The CVD process was performed by flushing 200 sccm of O_2 and 300 sccm of Ar.

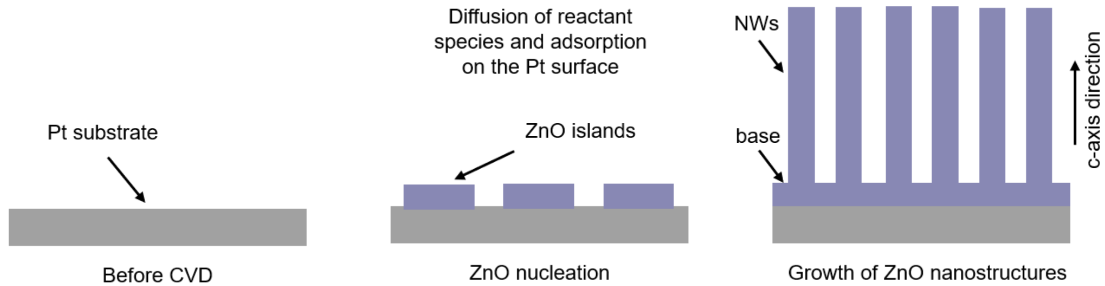

Figure 3.2: Schematization of the ZnO NWs growth process by means of CVD, composed of ZnO nucleation on a Pt substrate and subsequent growth of NWs along the preferential *c*-axis direction.

3.1.2 The role of the substrate

The self-seeding approach previously described can overcome all the issues related to the pre-deposition of a seed layer. However, the defect-driven nucleation responsible for self-seeding is strongly influenced by the properties of the growth substrate. Our observations revealed that a Pt thin film realized by sputtering is an optimal substrate for self-seeding and nucleation of ZnO nanostructures. In order to investigate this aspect, a CVD process was performed by inserting into the growth chamber a pre-seeded and a bare Pt substrate (details of methods of the seeding process can be found in Section 2.1). As can be observed from figure 3.3, similar ZnO NW morphologies were obtained in both cases.

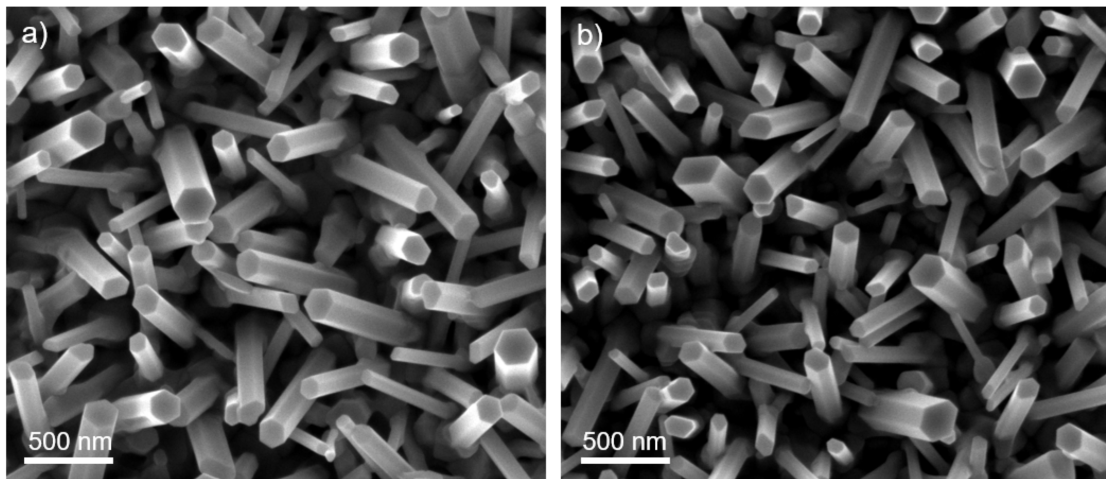

Figure 3.3: Comparison of the ZnO NWs grown on a a) pre-seeded and b) bare Pt substrate. The CVD process was performed by flushing 150 sccm of O_2 and 300 sccm of Ar.

The Pt substrate can be thus considered a catalyst layer for self-seeding of ZnO NWs [124]. In other words, by exploiting a Pt substrate the seeding procedure can be avoided. Recently, also other metals such as Ti, Mo and W were reported to be suitable substrates for initiating the ZnO NW growth [160]. An interesting aspect is that, by using the above described seed-free CVD process, it is possible to obtain a selective growth of ZnO NWs by pre-patterning the deposition of the Pt thin film. Indeed, as can be observed from Figure 3.4, ZnO NWs are selectively grown only where the Pt buffer layer was present and not on the bare Si substrate where nucleation is suppressed and deposition of other ZnO nanostructures such as nanobelts and sponge-like structures occurs. Following these results, all the growth processes on Pt substrates were performed by avoiding any pre-deposition of seed layers.

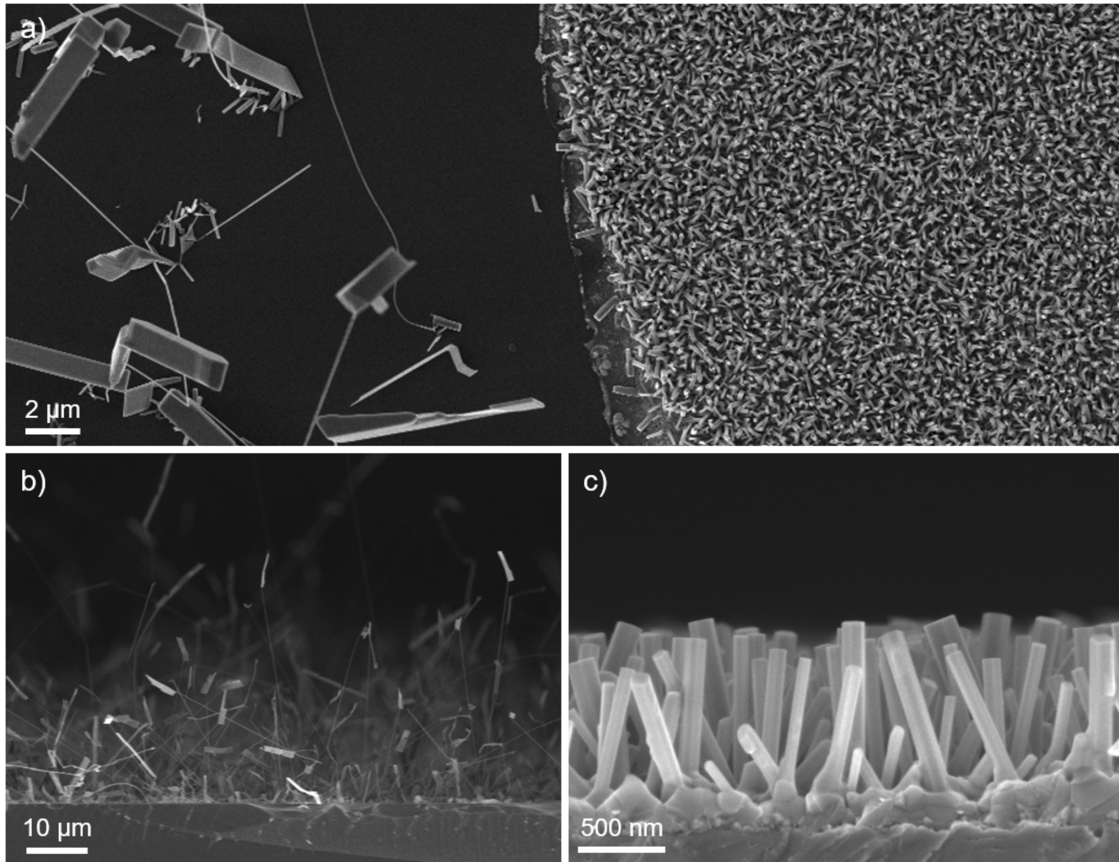

Figure 3.4: Selectivity of the growth process. a) ZnO NWs grow only where the Pt thin film was deposited (right side) while other ZnO nanostructures are present on the bare Si substrate. Cross section images of ZnO nanostructures growth on b) bare and c) Pt-coated Si wafer. The CVD process was performed by flushing 150 scmm of O_2 and 300 sccm of Ar.

Moreover, it is important to notice that the high temperature process (650°C) did not affect the continuity of the Pt substrate that did not exhibit evident dewetting and cracking due to the thermal conductivity mismatch between Pt and the underlying SiO_2/Si substrate. Note that the stability of the Pt layer was enhanced by the insertion of a Ta adhesion layer (20 nm). As discussed by Tiggelaar et al. [161], Pt/Ta films remain stable at 650 °C for even long exposure time, without revealing changes in the film resistivity. It is important to notice that the continuity of Pt after the growth process ensured good electrical conductivity of the bottom electrode during electrical measurements in NW array configuration.

3.1.3 NW dimensions and density

The control of the nanostructure dimensions during the growth process is the fundamental aspect of the bottom-up synthesis approach through self-assembling. At this scope, the nanowire dimensions can be tuned by varying the set of growth parameters. In order to evaluate the effect of the precursor gas flux, different CVD processes were performed by changing the amount of O_2 flux in the range 50-200 sccm by keeping all the other parameters fixed (T =650 °C, t = 20 min, 300 sccm of Ar). In all cases, an almost uniform growth of ZnO NWs on the whole Pt substrate was obtained. The NW length and diameter distributions as well as the base layer thicknesses were evaluated by measuring dimensions in cross-sectional SEM images acquired in different areas of the samples (see for example Figure 3.1) while the NW density was evaluated by top-view SEM images (see for example Figure 3.3). All measurements were performed on two different samples realized by two distinct CVD growth processes with same O_2 flux and parameters, in order to take into account of the process-to-process variability. A statistical analysis of the NW dimensions obtained by using different growth conditions is presented in Figure 3.5. As can be observed from Figure 3.5 a, by varying the O_2 flux it is possible to obtain NWs with average length from 980 nm by fluxing 150 scmm of O_2 up to 1.7 μm with 200 scmm of O_2. Counter-intuitively, the increase of the precursor gas from 50 to 150 sccm resulted in a decreasing of the NW length. Note that, in this case an increasing of O_2 flux resulted also in an increasing of the total flux, since the Ar flux was fixed during all processes. This aspect can explain the decrease of length by increasing the precursor gas, since the change of the total flux can be responsible of strongly different thermodynamical conditions. Instead, the change in the gas flux during CVD seems not to strongly affect the NW diameter that resulted almost constant at about 80 nm, as reported in Figure 3.5 b. Since the diameter remained almost constant, the aspect ratio followed the same trend of the NWs lenght, as can be observed in Figure 3.5 c. Aspect ratio from ∼ 12 up to ∼ 22 can be obtained by fluxing 150 and 200 sccm of O_2, respectively. Interestingly, the base thickness follows the same trend as the NW length, as shown in Figure 3.5 d. This reveals that the growth of the NW in length occurs in parallel to an increase

of the base layer thickness. In addition, it should be noted that the NW density is not strongly affected by the O_2 flux, as reported in Table 3.1.

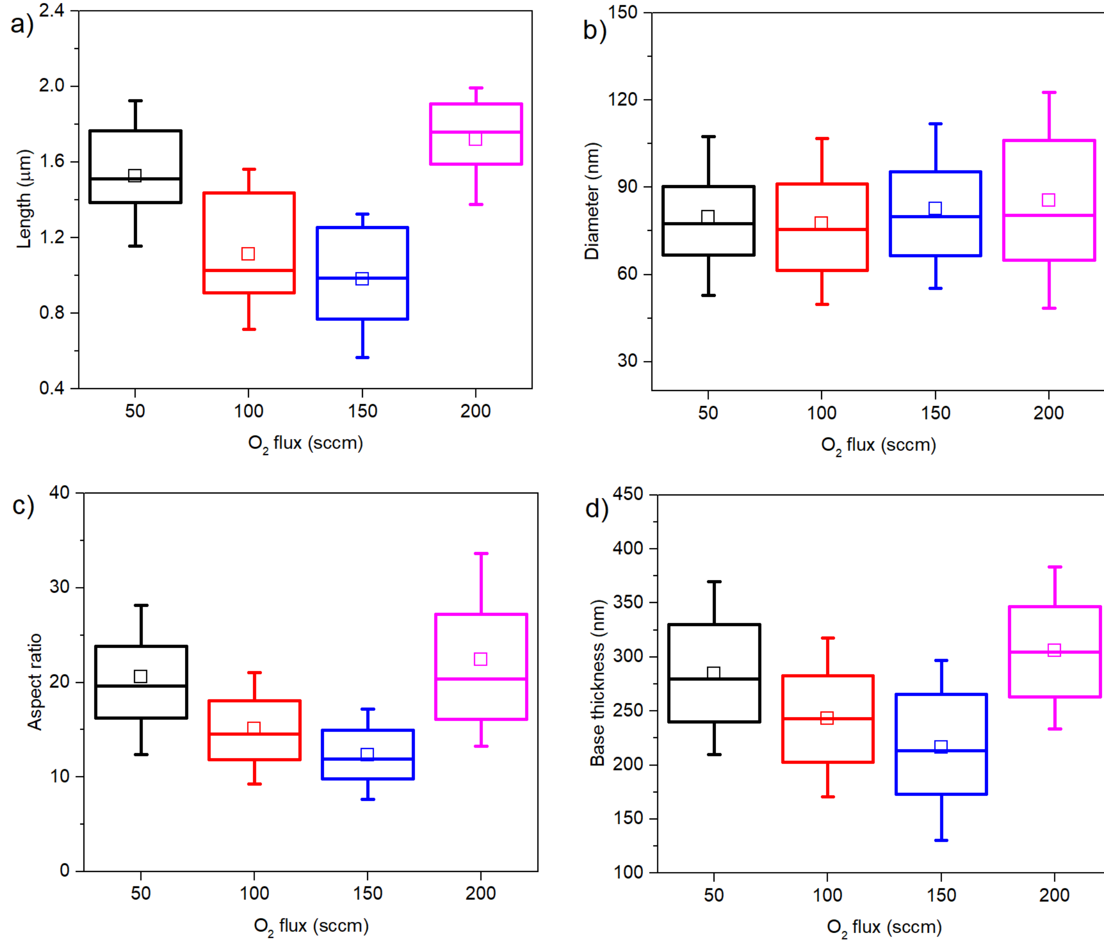

Figure 3.5: As grown ZnO NW dimensions as a function of the O_2 precursor gas flux with constant Ar flux (300 sccm). Box plot of a) length, b) diameter, c) aspect ratio and d) base thickness measured by means of cross-sectional SEM images. For each O_2 flux, distributions are obtained by measuring at least 200 NWs in two different samples grown in two distinct CVD processes. Midlines represent the median value, boxes the 25th and 75th percentiles, whiskers the 10th and 90th percentiles and open boxes the mean values. All the CVD processes were performed at 650°C for 20 min by keeping constant all the growth parameters, except for the O_2 flux.

Table 3.1: ZnO NW density as a function of the O_2 precursor gas flux with constant Ar flux (300 sccm).

O_2 flux ($sccm$)	**NW density** (μm^{-1})
50	14.3
100	12.1
150	13.7
200	12.7

3.2 ZnO NWs Characterization

Chemical and structural properties of ZnO NWs were assessed by means of different techniques such as EDX, XPS, XRD, TEM and Raman spectroscopy. In this way, it was possible to obtain a general overview of the material properties of ZnO nanostructures used for the realization of resistive switching devices. Since comparable chemical and structural properties were observed in case of NWs grown with different precursor fluxes, this section reports the analysis on ZnO nanostructures grown with an O_2 and Ar flux of 200 and 300 sccm, respectively. Details of methods for material characterization are reported in section 2.2.

3.2.1 Chemical properties

The investigation of chemical properties was assessed by means of EDX and XPS analyses on as grown ZnO NW arrays.

EDX analysis

Results of EDX analysis are reported in Figure 3.6 and confirmed the presence of Zn and O species. Table in the inset reports the atomic percentage of elements calculated from the EDX spectra. The presence of Si and Pt peaks is attributable to the underlying substrate. In addition, the C peak can be ascribed to the presence of carbon species due to sample exposure to the environment. This aspect will be further discussed in chapter 4, where a discussion concerning the chemical compounds present on the NW surface due to atmospheric exposure is provided. Even if EDX can provide only a qualitative description of the chemical composition because of this technique is not suitable for investigating the presence of traces of elements (especially light elements on the surface), this analysis excludes the presence of strong contaminations in as grown nanostructures.

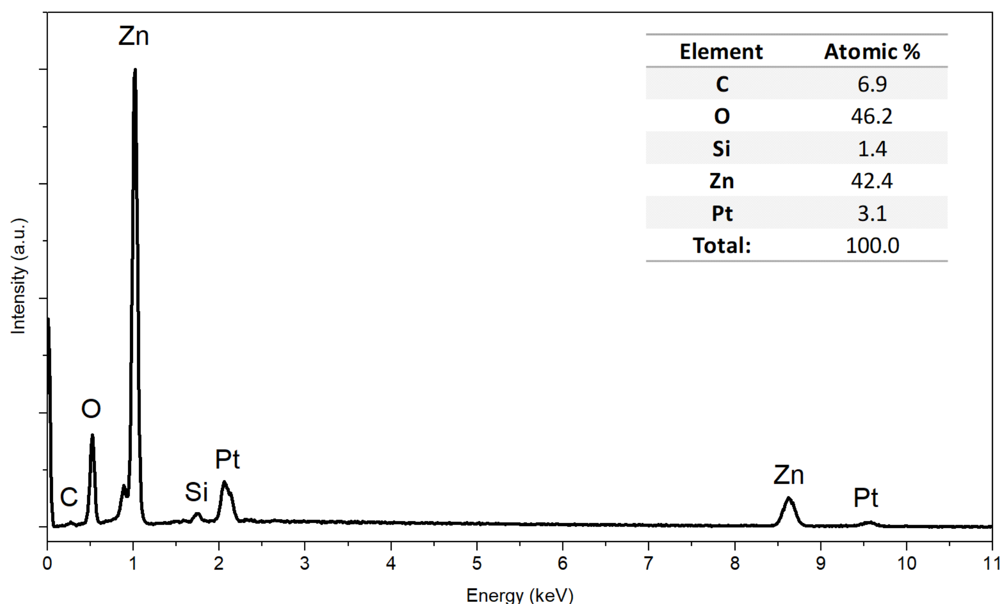

Figure 3.6: EDX spectra of as grown ZnO NWs. Elemental composition of the specimen calculated from EDX analysis is reported as inset table. Adapted from [162].

XPS analysis

High chemical purity of the nanostructures was confirmed also by XPS measurements presented in Figure 3.7 that revealed the presence of only Zn and O and confirmed the presence of carbon contaminations on the surface. Table in the inset reports the atomic percentage of elements calculated from the XPS spectra. In order to gain more insights about the NW surface defectivity, high resolution XPS measurements were performed. In particular, XPS measurements on the ZnO surface and after 10 min of Ar^+ sputtering (bulk) were compared. Results are reported in Figure 3.8. It can be observed that the carbon contaminations due to environmental exposure are present only on the ZnO NW surface since the C peak disappears after sputtering (see Figure 3.8 a and b). By considering the ZnO surface, the C peak is resulting from three components: 285.0 eV (C_a), 286.7 eV (C_b) and 289.0 eV (C_c) that are associated to C-H bonds, C-O bonds and carbonate groups, respectively. By considering the O 1s high resolution spectra of the surface and bulk in Figure 3.8 c and d, respectively, it can be observed that three components can be identified. The dominant component located at 530.3 eV for the surface and 530.5 eV for the bulk (O_a) can be assigned to the Zn-O bond in wurtzite crystal structure [163]. Instead, the component located at 531.6 eV for the surface and 531.7 eV for the bulk (O_b) is attributable to oxygen ions in oxygen-deficint

regions [153]. The third component located at 532.2 eV and 532.6 eV for surface and bulk, respectively, can be assigned to hydroxyl groups [164]. The XPS high-resolution spectra of Zn $2p_{3/2}$ revealed the presence of asymmetric peaks arising from two components (Figure 3.8 e and f). The most intense component located at 1021.6 eV and 1021.8 eV for surface and bulk, respectively, can be attributed to the Zn-O bond while the less intense component located at 1022.6 eV and 1023.0 eV for surface and bulk, respectively, is attributable to the hydrated layer on the surface [165]. For the same reason, two components can be identified also in case of the Zn $p_{1/2}$ peaks, as presented in Figure 3.8 g and h. In this case, the main components are located at 1044.7 eV and 1044.9 eV while the less intense components are located at 1045.9 eV and 1046.3 eV for surface and bulk, respectively. Interestingly, the XPS analyses revealed that the ZnO surface is more defective compared to the bulk structure, with a higher amount of oxygen vacancies and hydroxyl groups, as testified by the higher O_c and O_d components as well as the higher Zn_b and Zn_d peak shoulders.

Element	Atomic %
C1s	42.4
O1s	36.9
Zn2p3	20.7
Total:	100.00

Figure 3.7: XPS survey spectra of as grown ZnO NWs. Elemental composition of the specimen calculated from XPS analysis is reported as inset table. Adapted from [162].

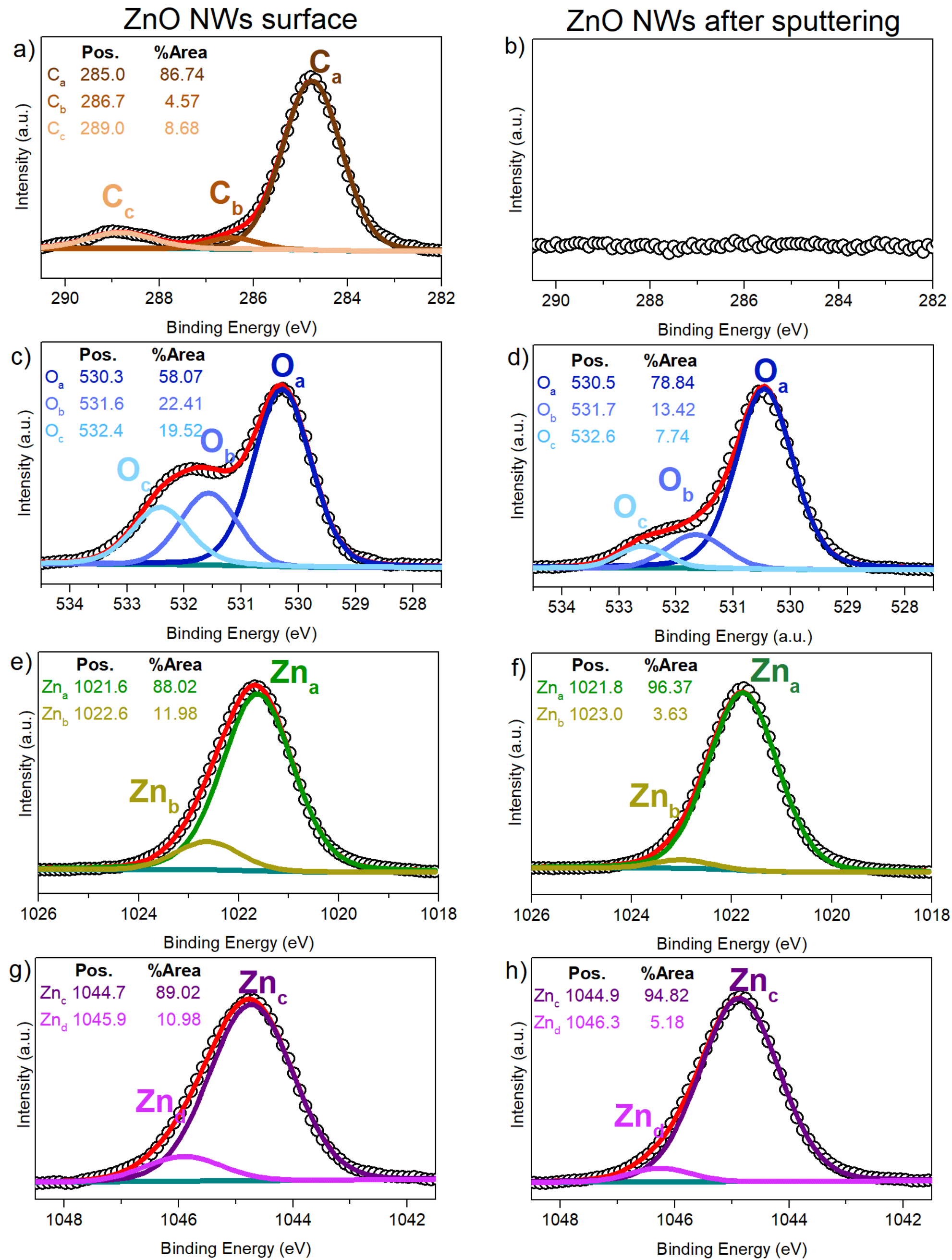

Figure 3.8: High resolution XPS spectra of ZnO NW surface and after 10 min of sputtering (bulk). Measurements were performed on as grown ZnO NW arrays. Panels a),c),e) and g) reported C, O 1s, Zn $p_{3/2}$ and Zn $p_{1/2}$ peaks on the surface while panels b),d),f) and h) reported the same peaks after 10 min of sputtering. Raw data are open circles while red lines are cumulative fit peaks. Adapted from [162].

3.2.2 Structural properties

The investigation of structural properties was assessed by means of XRD analysis of as grown ZnO NW arrays, TEM analyses on single NWs and Raman spectroscopy on NWs mechanically dispersed on a supporting Pt substrate.

XRD analysis

The XRD pattern presented in Figure 3.9 well matches with the wurtzite crystal structure of ZnO (JCPDS data no. 89-0511). Moreover, additional peaks attributable to the Pt and Si underlying substrate can be identified in the diffraction pattern. The most prominent ZnO peak is located at $2\theta = 34.53°$ and is due to the diffraction of (002) planes of *w*-ZnO. The narrow width of this peak revealed high crystal quality. In addition, peaks located at $2\theta = 36.37°$ and $2\theta = 63.06°$ can be attributed to the diffraction of (101) and (103) planes. By comparing the relative intensities of XRD peaks from ZnO NWs with ZnO powder (JCPDS data no. 89-0511), it can be noticed that NWs are highly oriented along the *c*-axis direction.

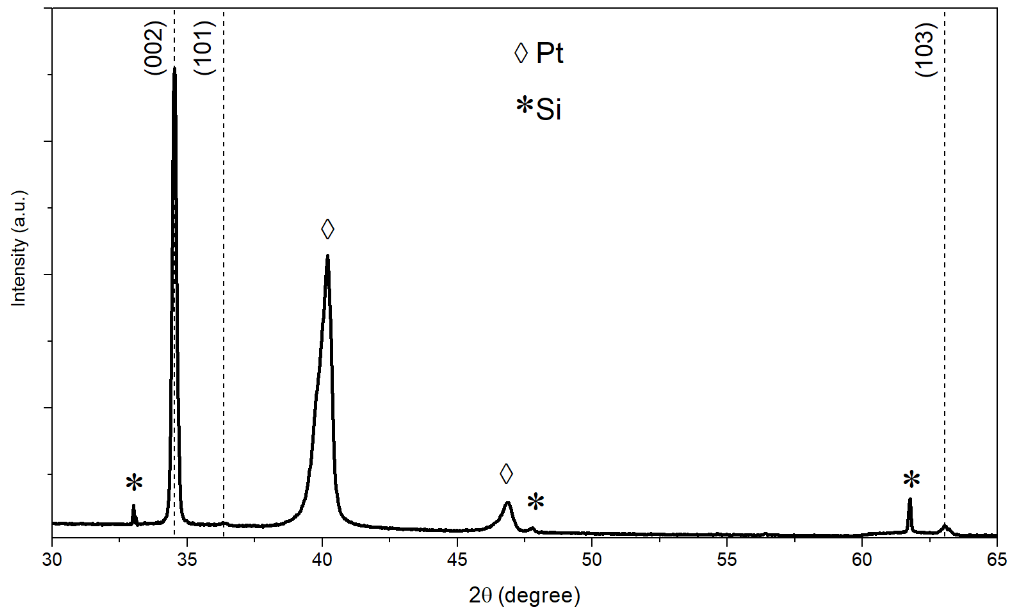

Figure 3.9: XRD pattern of as grown ZnO NWs. ZnO peaks in correspondance of dashed lines are labelled according to JCPDS data no. 89-0511. Adapted from [162].

TEM analysis

The fine structure of the nanostructures can be investigated by means of TEM measurements that revealed that each NW is a single crystal with perfect crystal lattice structure, as presented in Figure 3.10. A detail of the ZnO NW surface after about 1 year of exposure to ambient environement (Figure 3.10 a) evidenced a clean surface without the presence of surface amorphous layers such as zinc carbonates. By considering the high resolution TEM image in Figure 3.10 b, the distance between planes calculated by fast Fourier transform (FFT) pattern resulted to be 2.60 Å, in good agreement with interplane distance expected in between (002) planes of *w*-ZnO.

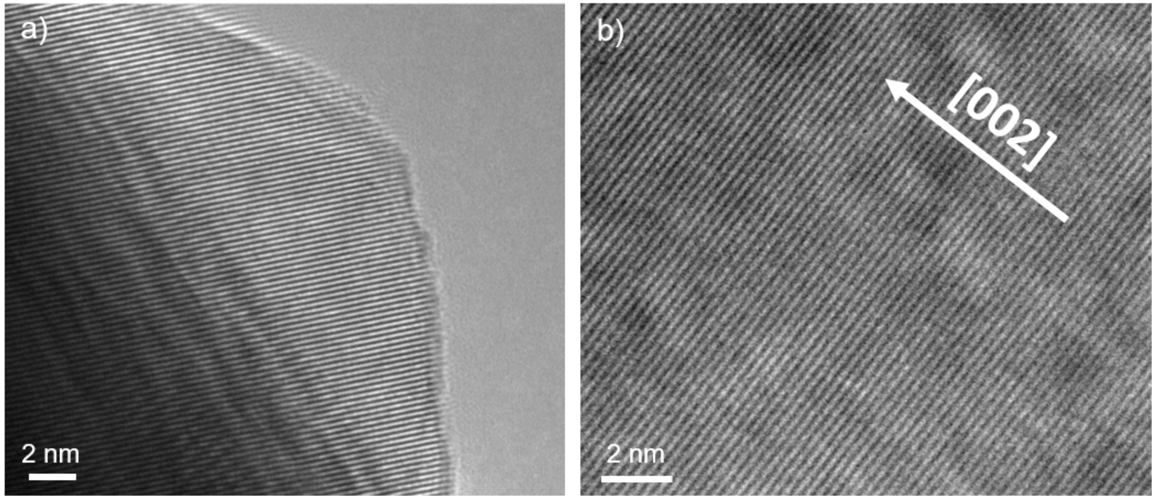

Figure 3.10: TEM analysis of ZnO NWs. a) TEM image of the ZnO NW surface after ∼1 year of ambient exposure (adapted from [162]) and b) high resolution TEM image of the ZnO NW structure.

Raman analysis

The crystal structure was assessed also by means of Raman spectroscopy performed on ZnO NWs that were mechanically dispersed on a Pt bare substrate. Typical Raman spectrum, interpolated by means of Lorentzian peak functions, is presented in Figure 3.11 and reveals the typical features of *w*-ZnO [166, 167]. The *w*-ZnO belongs to the space group C_{6v}^4 and, according to this group theory, the irreducible representation of phonon vibrations in this crystal structure can be described as (considering only optical modes) [168]:

$$\Gamma_{opt} = \mathrm{A}_1 + 2\mathrm{B}_1 + \mathrm{E}_1 + 2\mathrm{E}_2 \tag{3.1}$$

In the wurtzite structure, *a* and *b* axes are symmetrically equivalents, differently from the *c*-axis. As a consequence, optical phonon can be splitted in one mode

with atomic displacement along the *c*-axis (A-symmetry) and a degenerate pair of modes with atomic displacement along *a* and *b* axes (E-symmetry). By considering first order Raman peaks, the E_2^{high} peak located at $(438.04 \pm 0.04)\,\mathrm{cm}^{-1}$ dominates the spectrum. This peak results from the non-polar modes involving the motions of the oxygen sublattice perpendicularly to the *c*-axis. The narrow E_2^{high} peak with FWHM of $(8.7 \pm 0.2)\,\mathrm{cm}^{-1}$ revealed high crystal quality [168], in accordance to XRD and TEM analyses previously discussed. In addition, the polar A_1 and E_1 modes involving mainly the oxygen vibration give rise to four peaks, as a consequence of the splitting into LO and TO components. The A_1(LO) and E_1(LO) modes can be associated with peaks located at $(380.6 \pm 0.3)\,\mathrm{cm}^{-1}$ and $\sim 410\,\mathrm{cm}^{-1}$. Instead, as a consequence of the close wavenumber, A_1(LO) and E_1(LO) modes give rise to a unique LO band that is located at $(580.6 \pm 0.7)\,\mathrm{cm}^{-1}$. By considering second order peaks, the low frequencies ($< 540\,\mathrm{cm}^{-1}$) are dominated by acoustic overtones, high frequencies ($> 820\,\mathrm{cm}^{-1}$) are dominated by optical overtones while combinations of acoustic and optical phonons are present in the intermediate range [166]. In addition, peaks attributable to B_1 silent modes can be identified as a consequence of the breakdown of the translational symmetry in the crystal structure that has to be attributed to the presence of impurities and defects [169].

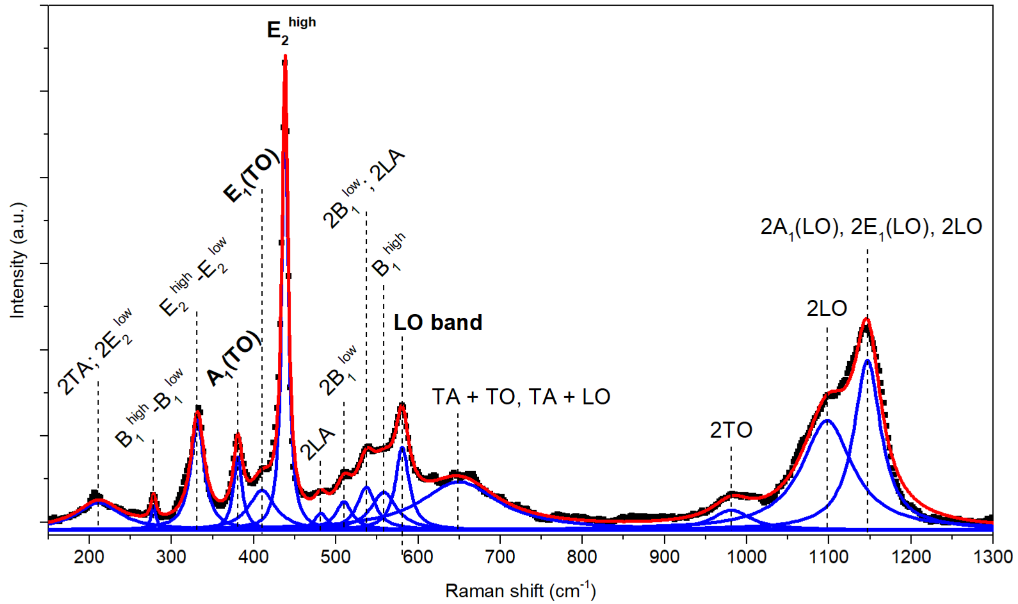

Figure 3.11: Raman spectra of ZnO NWs dispersed on a Pt substrate. Red line is the cumulative fit peak, blue lines represent interpolation of single components while black squares are raw data. First order peaks are labelled in bold.

Chapter 4

Tuning ZnO NW corrosion and dissolution

Reference paper:

[162] *Milano, Gianluca, et al. "Tuning ZnO Nanowire Dissolution by Electron Beam Modification of Surface Wetting Properties." The Journal of Physical Chemistry C 122.14 (2018): 8011-8021*

4.1 Introduction

Chemical stability and solubility of ZnO NWs can strongly impact not only chemical and biological applications but also electronic device reliability. Despite these nanostructures are usually considered chemically stable, corrosion and degradation of ZnO was observed as a consequence of long exposure to ambient moisture or after interaction with water [170–174]. As reported by Cimatu et al. [172], the interaction of ZnO with water molecules is responsible for the formation of zinc hydroxide, that can further react with CO_2 to form zinc carbonates on the NW surface. The presence of a zinc carbonate layer on the surface can strongly affect both optical and electrical properties of the nanostructures. In addition, the degradation and dissolution process, observed also in biofluids as reported by Zhou et al. [170], represents an important aspect for ZnO NWs biocompatibility and biodegradability. For this reason, if the dissolution rate can be controlled, ZnO nanostructures result to be promising for the realization of "deliver and dissolve" platforms for drug targeting and cancer imaging [139]. Thus, understanding and controlling dissolution of ZnO nanostructures is fundamental for a wide range of applications. In this section, the degradation mechanism of ZnO NWs in water is analyzed and a reversible approach based on electron-beam irradiation for tuning the surface wetting properties is discussed. In addition, it was shown that the e-beam treatment of the NW surfaces can influence the ZnO-PMMA interaction with

consequent degradation of ZnO. All these aspects are fundamental for the development of a corrosion-free fabrication process of reliable electronic devices based on ZnO nanostructures.

4.2 Dissolution of ZnO NWs in H_2O

As synthetized ZnO NWs resulted to be stable under prolonged exposure to normal environment conditions and did not evidenced the formation of a zinc carbonate layer on the surface, as previously discussed in section 3.2.2. In order to investigate the dissolution process in water, ZnO NWs were mechanically dispersed on a SiO_2 supporting substrate and then immersed in deionized water (pH in the range 6.7-6.9, conductivity of $\sim 150\,\mu\mathrm{S\,cm^{-1}}$). The degradation of ZnO NWs in water as a function of exposure time was analysed by SEM and results are reported in Figure 4.1. After 30 min of interaction with water, the surface of ZnO NWs

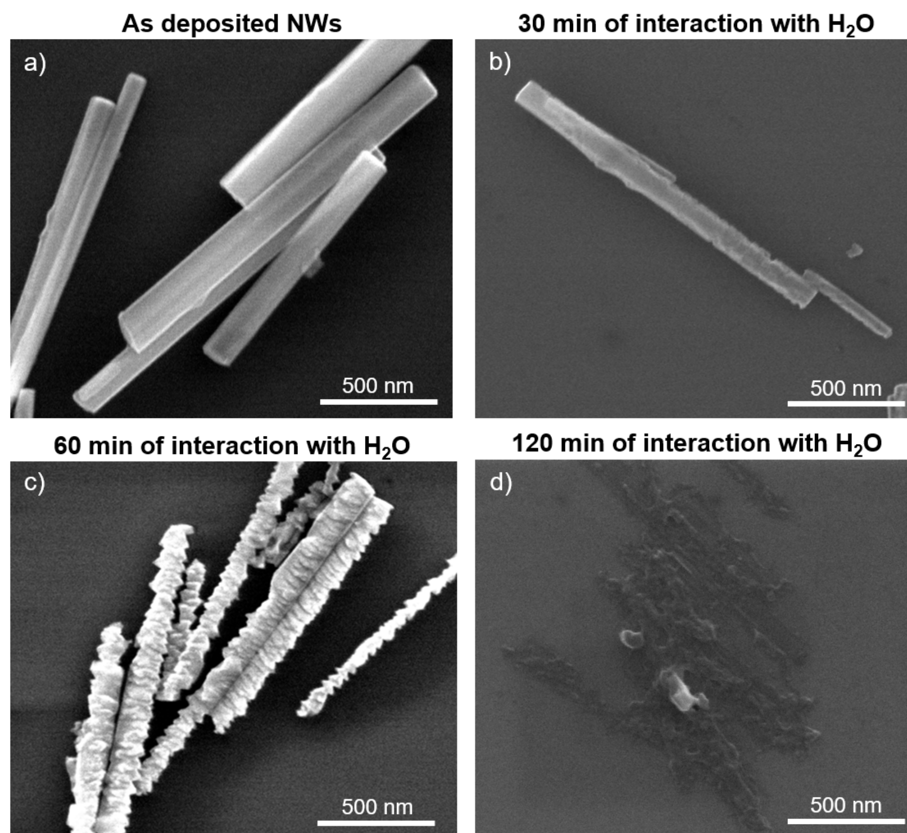

Figure 4.1: Dissolution of ZnO NWs dispersed on a SiO_2 substrate. a) As deposited NWs and NWs after b) 30 min, c) 60 min and d) 120 min of interaction with deionized water. Adapted from [162].

resulted to be slightly corroded (Figure 4.1 b) if compared to as deposited NWs (Figure 4.1 a). The corrosion becomes more evident after 60 min of interaction, with NWs that presented wrinkled and irregular surfaces as can be observed in Figure 4.1 c. Instead, an almost complete dissolution was observed after 120 min of interaction, after which only some residues of ZnO NWs were left on the underlying substrate (Figure 4.1 d). A more detailed characterization of the NW dissolution process was performed by means of TEM analyses. As can be observed from Figure 4.2 a and b, the dissolution process is not isotropic. Similarly, anisotropic dissolution was previously observed also by Qi et al. [175] in case of ZnO NW interaction with an HCl solution. Interestingly, after water interaction the length of the NW was not strongly affected by corrosion untill the complete NW dissolution, while a strong reduction in diameter with mass loss was observed. Results in Figure 4.2 a and b suggest that the (002) polar surfaces are less prone to be corroded respect to the non-polar surfaces. This can be clearly observed also in the SEM image of Figure 4.2 c, where it is possible to observe a smooth (002) surface (the top of the NW) while lateral non-polar surfaces are corrugated with sharp edges. Note that the lateral (100) surfaces were smooth walls prior to water interaction. A more detailed analysis of the lateral surface corrosion can be performed by means of high-resolution TEM, as presented in Figure 4.2 d where a detail of a lateral sharp edge is reported. As previously discussed in section 3.2.2, the NW presented high crystal quality characterized by an interplane spacing of 0.52 nm along the c-axis direction. The analysis of the edge reveled the presence of an angle of $\sim 62°$ respect to the [002] crystallographic direction. According to JCPDS data no. 89-0511, the formed angle is compatible with the presence of the (101) crystallographic orientation (note that the angle in between (101) and (002) planes is expected to be 61.6° from JPDS data). Thus, it can be concluded that the lateral (100) surfaces are more prone to be damaged compared to (101) and (002) surfaces. Moreover, a clean surface was observed after water interaction, excluding the creation of any amorphous layer such as zinc carbonates. Dissolution of ZnO in water can be explained by the chemical dissociation [176, 177]:

$$\mathrm{ZnO(s)} + \mathrm{H_2O} \rightarrow \mathrm{Zn^{2+}} + 2\mathrm{OH^-} \tag{4.1}$$

Note that dissolution is strongly influenced by surface wetting properties of the nanostructures that are related to the surface defectivity [178, 179]. Indeed, the existance of defects on the surface as previously discussed in section 3.2.1, can promote the corrosion and dissolution of ZnO since defects can act as active sites for dissociation and adsorption of H_2O. Double charged oxygen vacancies ($V_O^{\bullet\bullet}$) can be considered as active sites for water chemisorption through the reaction:

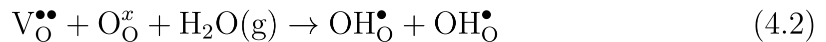

$$\mathrm{V_O^{\bullet\bullet}} + \mathrm{O_O^{x}} + \mathrm{H_2O(g)} \rightarrow \mathrm{OH_O^{\bullet}} + \mathrm{OH_O^{\bullet}} \tag{4.2}$$

where the Kröger-Vink notion is used. In addition, the hydroxyl groups that are already present on the ZnO NW surface as a consequence of ambient exposure (see

XPS measurements reported in section 3.2.1) can increase the hydrophilicity and wettability [179], facilitating water interaction with the ZnO surface.

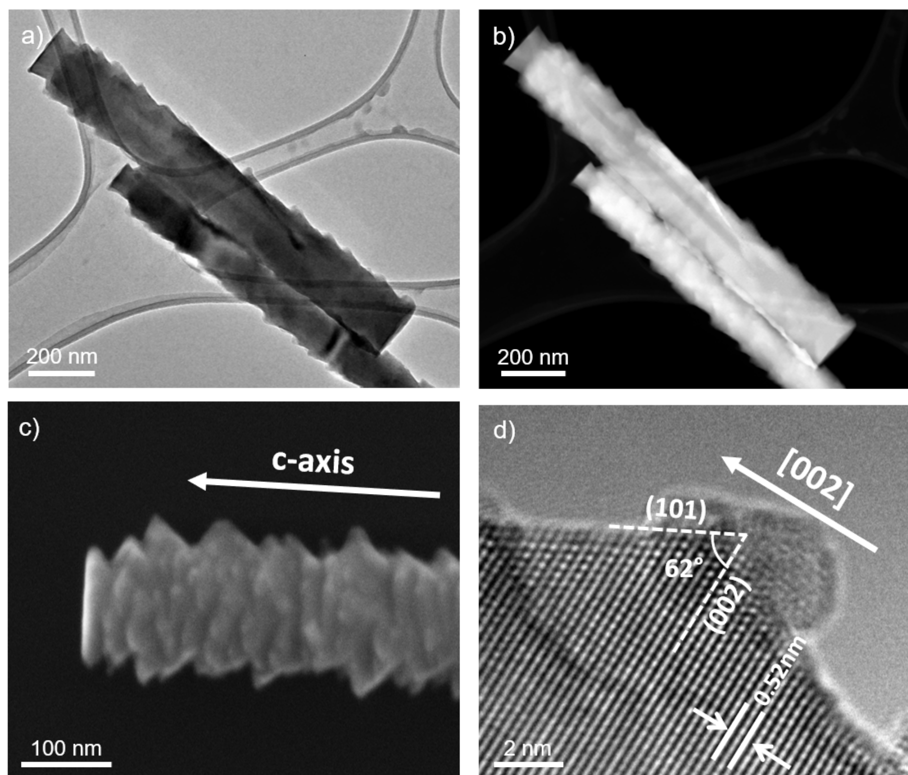

Figure 4.2: TEM and SEM investigation of the anysotropic dissolution of ZnO NWs in water. a) Bright-field TEM image, b) STEM image, c) SEM image and d) high-resolution TEM detail of the surface of a ZnO NW after being immersed in deionized water for 60 min. Adapted from [162].

4.3 Modification of wettability properties by electron beam irradiation

The surface wetting properties of the nanostructures can be modified by means of electron beam irradiation. In this fashion, it is possible to prevent corrosion and degradation of ZnO NWs in water. The effect of electron beam irradiation was evaluated by the following experiment. Single ZnO NWs dispersed on a SiO_2 substrate were selected and then irradiated in vacuum conditions ($\sim 10^{-5}$ mbar) by means of an e-beam gun in a SEM chamber. Electron irradiation was performed by scanning the beam over the surface to reduce heating of the sample [180], accelerating electrons at 30 kV. Exposure time and magnification were set to 120 s and

120000 ×, respectively, while the beam current was measured to be 116 pA. These experimental conditions resulted in an electron dose of $Q = 0.26\,\mathrm{C\,cm^{-2}}$. After e-beam irradiation, the sample was immersed in deionized water for 60 min together with an unirradiated control sample. Thanks to proper reference markers, the morphology of the same NW was investigated before and after water interaction. Note that it was not possible to investigate NW morphology of the same unirradiated NW before water interaction, since SEM investigation necessarily requires e-beam irradiation of the sample. As can be observed from Figure 4.3, the morphology of the irradiated NWs was not affected by water interaction. Instead, as expected, the unirradiated control sample exhibited ZnO NW corrosion (in analogy to results reported in Figure 4.1). As a consequence, electron beam irradiation can be exploited to selectively tune the wetting properties of selected ZnO NWs (details of the selectivity of e-beam irradiation can be found in Appendix A.1).

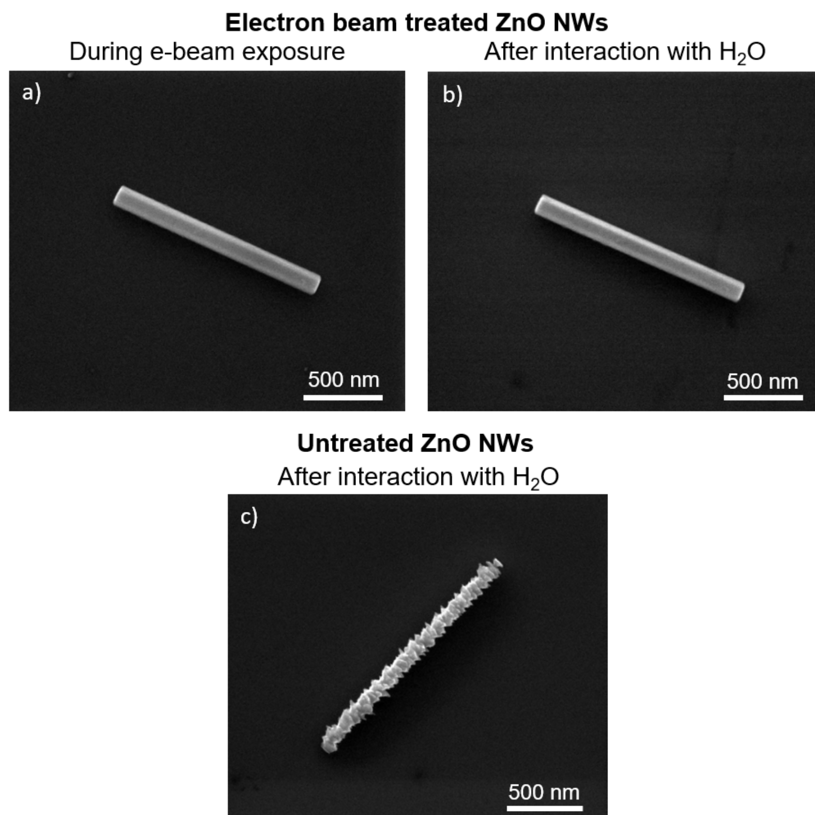

Figure 4.3: Effect of e-beam irradiation on ZnO NW degradation as a consequence of interaction with water. SEM image of the same electron beam treated ZnO NW a) before and b) after being immersed in deionized water for 60 min. c) SEM image of an untreated NW after water interaction (control sample). Adapted from [162].

4.4 Mechanism of e-beam induced modification of surface properties

Electron beam irradiation of solid surfaces can induce several effects such as defect generation, electrical charging effects and chemical modifications that can change the surface energy and wettability [181–183]. In our case, the electron-induced generation of defects can be excluded since the energy required for atomic displacement in wurtzite ZnO is one order of magnitude higher than the energy of 30 kV used in our experiments [184]. This can be further confirmed by TEM investigations that, even if performed with electrons accelerated at higher energy (200 kV), did not show any generation of defects (refer to section 3.2.2). While for low electron irradiation doses charging effects control the change in wettability of surfaces, chemical changes are responsible for the modification of surface energy in case of high electron doses ($Q > 1.5\,\mu C\,cm^{-2}$) [181]. Since high electron doses are implied in our experiments ($Q = 0.26\,C\,cm^{-2}$), the modifications of the NW wettability have to be attributed to e-beam induced chemical reactions on the ZnO surface. XPS and EDX measurements discussed in section 3.2.1 and 4.2 evidenced the presence of organic species on the surface ascribable to atmospheric exposure. When these organic compounds, that are mainly composed of hydrocarbons, are exposed to e-beam irradiation, sequences of radical reactions involving decomposition and reorganization of hydrocarbon chains occur. The main reactions can be summarized in the following [185]:

$$-\,CH_3 \xrightarrow{e^-} -CH_2^\bullet + H^\bullet \tag{4.3}$$

$$-\,CH_2 \xrightarrow{e^-} -CH^\bullet + H^\bullet \tag{4.4}$$

$$-\,CH_2 - CH_3 \xrightarrow{e^-} -CH_2^\bullet + CH_3^\bullet \tag{4.5}$$

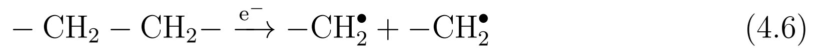

$$-\,CH_2 - CH_2- \xrightarrow{e^-} -CH_2^\bullet + -CH_2^\bullet \tag{4.6}$$

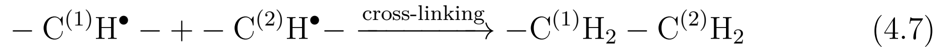

$$-\,C^{(1)}H^\bullet - + -\,C^{(2)}H^\bullet - \xrightarrow{\text{cross-linking}} -C^{(1)}H_2 - C^{(2)}H_2 \tag{4.7}$$

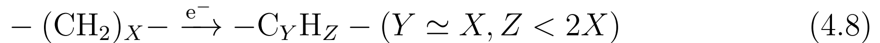

$$-\,(CH_2)_X- \xrightarrow{e^-} -C_YH_Z - (Y \simeq X, Z < 2X) \tag{4.8}$$

Electron beam irradiation is responsible for the scission of C-H and C-C bonds (reactions 4.3, 4.4, 4.5, 4.6) with consequent reorganization of organic chains (reaction 4.7). Instead, reaction 4.8 refers to the formation of a carbonaceous material as a consequence of the favourable loss of H atoms respect to C atoms during irradiation, with formation of H_2 and CH_4 volatile species. It cannot be excluded that also hydrocarbons coming from residual gases in the vacuum chamber can participate in the above mentioned radical reactions, as previously discussed in the works of Botman et al. [186] and Djenizian et al. [187]. Since the formed radicals are highly reactive species, these species can be bounded to the ZnO NW surface creating

an electron-deposited CH-rich layer. This layer is characterized by hydrophobic and oleophilic properties, resulting in a modification of the surface wettability as a consequence of e-beam irradiation [183, 188]. In other terms, e-beam irradiation can be exploited to induce hydrocarbon reactions on the ZnO NW surface that are responsible for the change in the surface wettability from hydrophilic to hydrophobic. The created CH-rich layer on the surface can be thus considered a protective layer that decreases the chemical etching rate, as previously discussed by Sabayev et al. [189] for an e-beam treated Ga-doped ZnO film interacting with oxalic acid ($C_2H_2O_4$) and sodium hydroxide (NaOH) etchants. Note that the process of modification of the surface wettability is reversible, since the CH-deposited layer can be removed by an oxygen plasma treatment. Indeed, it was observed that the initial hydrophilic conditions can be restored by means of oxygen plasma (40 W, 60 s). After this treatment, degradation of ZnO NWs in water was observed again (see Appendix A.2). The schematization of the afore described reversible tuning of ZnO surface wetting properties is presented in Figure 4.4

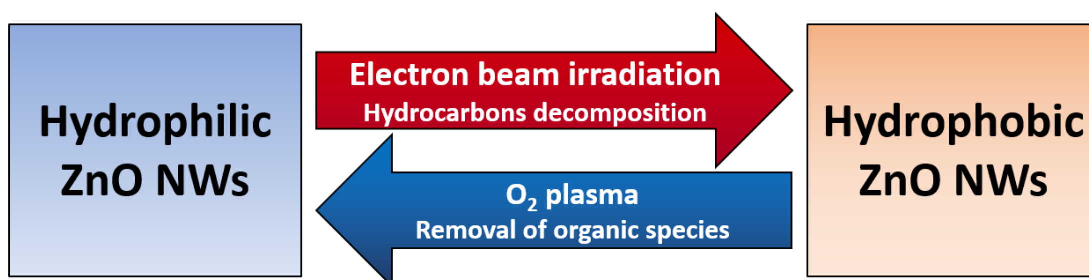

Figure 4.4: Schematization of the reversible tuning of ZnO surface wetting properties by means of e-beam irradiation and O_2 plasma treatment. Adapted from [162].

The mechanism of e-beam induced modifications of surface properties was investigated in details by means of Raman and FT-IR spectroscopy. For this purpose, a selected area of 5.4×10^4 μm^2 of ZnO NW arrays was e-beam irradiated (dose of $Q = 0.066\,C\,cm^{-2}$) and then treated by oxygen plasma (40 W, 60 s). At each step, surface modifications were investigated by means of Raman and FT-IR analyses. Results of Raman spectroscopy can be found in Figure 4.5. As reported in Figure 4.5 a, typical features of wurtzite ZnO can be observed (for a detailed discussion of Raman features of ZnO NWs refer to section 3.2.2). By considering the spectral range 1200-1800 cm^{-1}, features of carbonaceous materials characterized by the presence of the G band at $\sim$1600 cm^{-1} due to C-C sp^2 bonds and the D band arising from defects at $\sim$1350 cm^{-1} can be identified (Figure 4.5 b). The presence of these bands in untreated ZnO NWs is due to organic species as a consequence of ambient exposure. Moreover, bands attributable to the symmetric and asymmetric stretching of CH_2 and CH_3 groups can be observed in the 2800-3000 cm^{-1} range

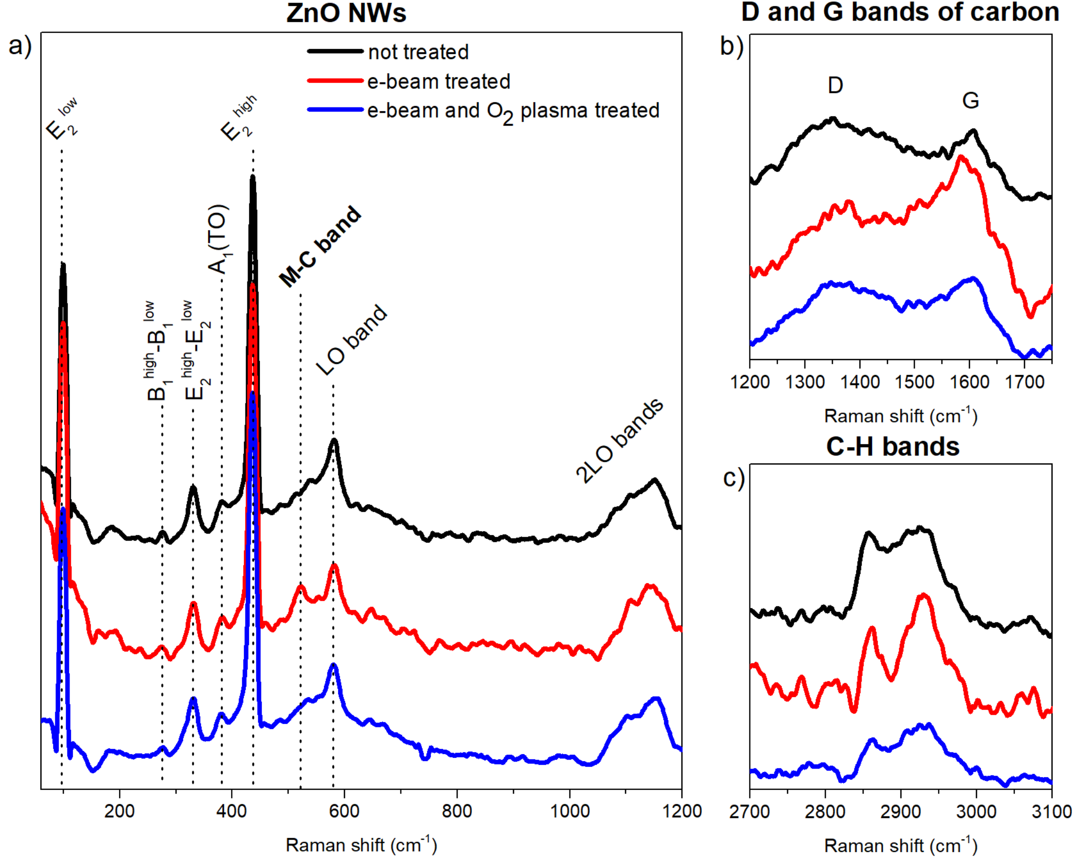

Figure 4.5: Investigation of e-beam modification of surface wetting properties by Raman spectroscopy. Raman spectra acquired on the same area of ZnO NW arrays before e-beam irradiation (black line), after e-beam irradiation (red line) and after oxygen plasma treatment (blue line); a) ZnO region, b) carbon region and c) CH bands region; Spectra are the result of at least three average acquisitions in different regions of the sample and are normalized on the E_2^{high} peak after background subtraction. Adapted from [162].

[190] (Figure 4.5 c). After e-beam irradiation, changes in the Raman spectrum can be observed. By considering the carbon region, the increasing of the I_G/I_D ratio can be ascribed to an e-beam induced carbonization process of organic species on the surface according to reaction 4.8. Indeed, the increase of the G band is a result of the increase of the C-C sp^2 content in carbonized products [191]. In addition, changes were observed also in the C-H_x stretching region. After irradiation, this band was characterized by two more resolved peaks with reduced bandwidth located at about 2860 and 2925 cm^{-1}, suggesting a more ordered chemical structure. In addition, after the e-beam treatment a band located at $\sim 520\,cm^{-1}$ appeared

and can be tentatively assigned to metal-carbon (M-C) stretching (this band is expected in the range 420-775 cm^{-1} for metal-alkyl and metal-alkenyl stretching [192]). These observations suggest that the e-beam energy can induce the bonding of C atoms on Zn atoms of the NW surface. Moreover, the initial conditions were restored after the oxygen plasma treatment. More in details, the initial I_G/I_D ratio was restored, the CH_x stretching bands were not anymore well resolved and the M-C band disappeared. The chemical changes on the surface were investigated also by Raman mapping confirming that the modifications are not puntual but occurred all over the irradiated area (details in Appendix A.3). FT-IR measurements confirmed chemical modification of organic species on the surface after e-beam irradiation, as reported in Figure 4.6. By considering FT-IR spectra before treatments, symmetric and asymmetric CH_2 stretching modes are responsible for peaks located at 2853 an 2961 cm^{-1}, respectively. Instead, bands at 2872 and 2961 cm^{-1} can be attributed to symmetric and asymmetric CH_3 stretching modes, respectively. As a consequence of the reduction of C-H_x bonds due to e-beam irradiation (reactions 4.3, 4.4, 4.5, 4.6), the intensity of the C-H_x stretching modes decreased after e-beam treatment. More interestingly, a slight shift in the peak position towards higher wavenumbers of the most intense bands was observed. This evidence supports the previously

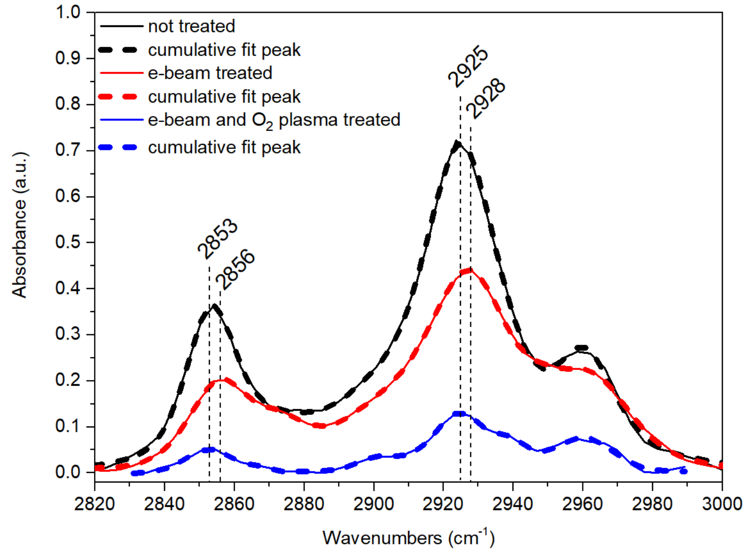

Figure 4.6: Investigaton of e-beam modification of surface wetting properties by FT-IR spectroscopy. FT-IR spectra of as grown ZnO NWs (black), after the e-beam treatment (red) and after oxygen plasma treatment (blue) are compared. Raw data are continous lines while cumulative fit of the peaks performed with Lorentzian/Gaussian peak functions are represent by dashed lines. Adapted from [162].

discussed hyphotesis of C atoms bonding on the NW surface, since this shift is expected when C atoms are bounded to electronegative substituents. Note that this shift was not clearly observed in the Raman spectra since vibrational modes of dipolar bonds are characterized by low Raman activity [193]. In addition, the intensity of C-H_x stretching bands was further reduced by the oxygen plasma treatment that is responsible for a global reduction of the amount of organic species, while the position of the main bands was observed to be shifted back to the initial values.

The creation of an organic layer on the surface of the nanostructures by e-beam irradiation can influence the interaction of ZnO NWs with organic compounds. For this reason, the interaction of e-beam irradiated NWs with an organic polymer, poly-methyl methacrylate(PMMA), was investigated through the following experiment. PMMA diluted in anisole was deposited on SiO_2 substrate with dispersed ZnO NWs through spin-coating and then baked at 165°C for 5 min in order to eliminate solvents. Then, PMMA was removed by acetone and the ZnO NW morphology was examinated. The same procedure was applied to an unirradiated control sample. Results, presented in Figure 4.7, revealed that degradation occurred only in e-beam irradiated NWs. Indeed, in this case organic molecules of PMMA can easily react and be bounded to the organic CH layer on the surface, leading to a corrosion process probably when organic chains are dissolved in acetone during the polymer removal. It is important to notice that the previously discussed observations are fundamental for the development of a reliable device fabrication process involving ZnO NWs, especially during EBL where PMMA is commonly used as the e-beam resist polymer. In light of these observations, water-free solvents were used during all the fabrication steps, taking care of reducing as much as possible the NW exposure to e-beam prior to the unavoidable interaction of ZnO with PMMA during lithography.

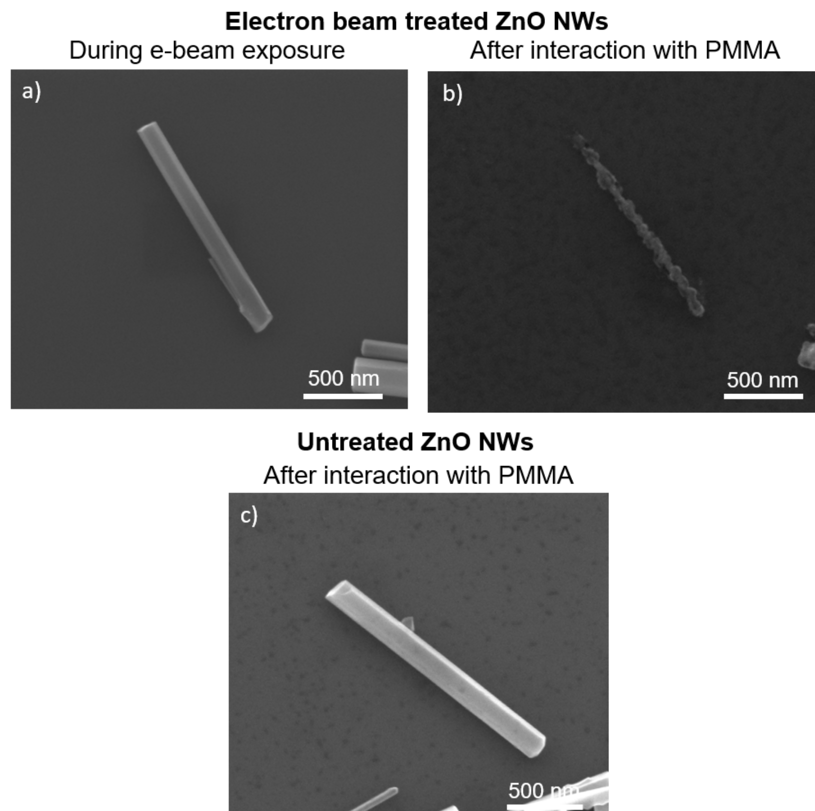

Figure 4.7: Effect of e-beam irradiation on ZnO NW degradation as a consequence of interaction with PMMA. SEM image of the same electron beam treated ZnO NW a) before and b) after PMMA interaction. c) SEM image of an untreated NW after PMMA interaction (control sample). Adapted from [162].

Chapter 5

Resistive switching in ZnO NW arrays

Reference paper:

[194] *Milano, Gianluca, et al. "Unravelling Resistive Switching Mechanism in ZnO NW Arrays: The Role of the Polycrystalline Base Layer." The Journal of Physical Chemistry C 122.1 (2017): 866-874.*

5.1 Introduction

Resistive switching devices based on NW and NR arrays represent an easy approach for the realization of NW-based memristors, as previously discussed in section 1.5.2. By considering ZnO nanostructures, first observations of resistive switching in ZnO NR arrays were reported already in 2010 by Chang et al. [94], even before the first experimental observation of switching phenomena in single isolated ZnO NWs. In this case, bipolar resistive switching characteristics were observed in ZnO NW arrays synthetized with an hydrothermal growth on a ITO substrate and contacted by a Pt top electrode. In particular, the *I*-*V* hysteretic loop was characterized by low SET and RESET voltages ($< 1\,V$), despite the average length of the NWs was about $2.9\,\mu m$. Compared to thin film devices where the active material thickness is usually few tens of nm, these NW array devices exhibitedy similar operating voltages but much higher electrode spacing. This means that lower electric fields seem to be required for inducing resistive switching in NW arrays. Even if the lower electric field required for switching can be explained in terms of higher mobility of oxygen ions species on the NW surface rather than in the bulk structure of a stacked thin film device, a detailed investigation of the physical mechanism of switching was missing. In this chapter, a novel understanding of the switching mechanism in ZnO NW arrays is discussed. In particular, it is proposed

that the ZnO thin film layer (here called *base*), that is unavoidably present in between the bottom electrode and the NWs as a consequence of the growth process, can affect and even dominate resistive switching. Thus, the switching mechanism in ZnO NW arrays can differ from the case of single isolated NWs because of the peculiar device structure.

5.2 Analysis of the device structure

The MIM device structure based on ZnO NW arrays was realized by sputtering a Pt top electrode on as grown ZnO NW arrays and by exploiting the growth Pt substrate as bottom electrode. In this configuration, the morphology of the sputtered top electrode is crucial for understanding the location of electronic and ionic transport mechanisms underlying the switching events. For these reasons, cross-sectional analyses of the Pt/ZnO NW array/Pt devices by means of SEM and EDX were performed. Results are reported in Figure 5.1. As revealed by using SEM backscattered electrons (Figure 5.1 a), Pt can be deposited not only on the NW tip but also along the lateral surfaces during the sputtering process of the top electrode, coating ZnO NWs down to the base layer. This aspect was further

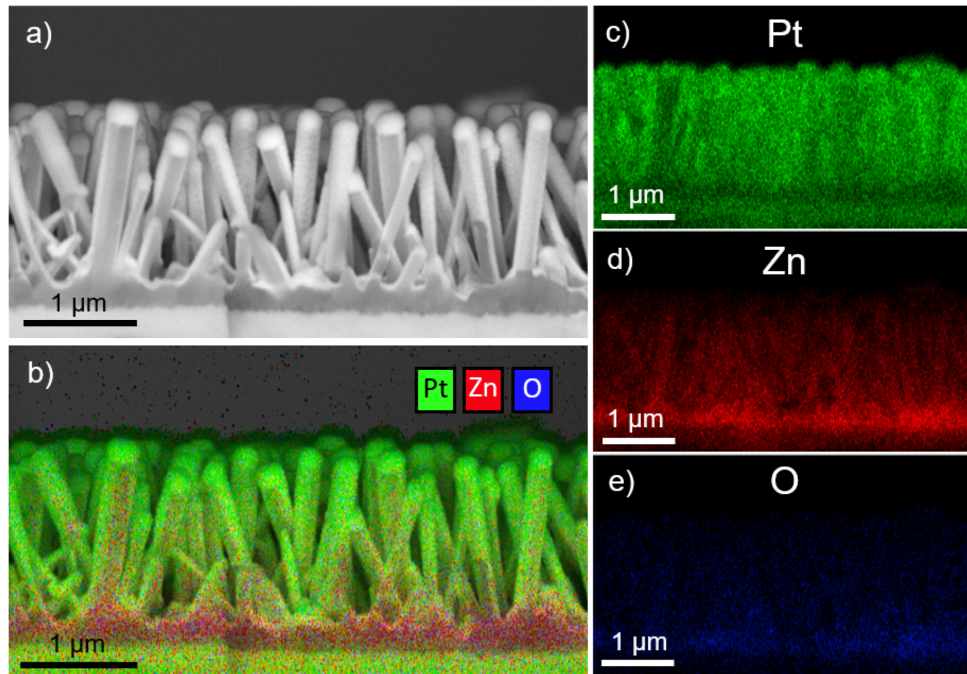

Figure 5.1: Investigation of Pt top electrode morphology. a) FESEM image acquired with backscattered electrons of a cross-section of the ZnO NW arrays covered by the sputtered Pt top electrode and b) EDX elemental map; c) Pt, d) Zn and e) O EDX maps. Adapted from [194].

confirmed by means of EDX analyses that revealed the presence of Pt along ZnO NWs down to the base layer, as reported in Figure 5.1 b-e. Thus, it is necessary to take into account not only the ZnO NWs but also the ZnO base layer during the investigation of the physical mechanism of switching. In order to investigate the influence of the base layer on resistive switching behaviour of ZnO NW arrays, NWs were mechanically removed by means of sonication in ethanol for 60 min (135 W, 59 kHz). As can be observed from Figure 5.2, under these conditions the sonication process allows an entire and uniform removal of NWs, leaving a continous polycrystalline base layer. This layer is characterized by grain size ranging from ~100 nm up to ~ 250 nm, as revealed by SEM analyses (Figure 5.2 b).

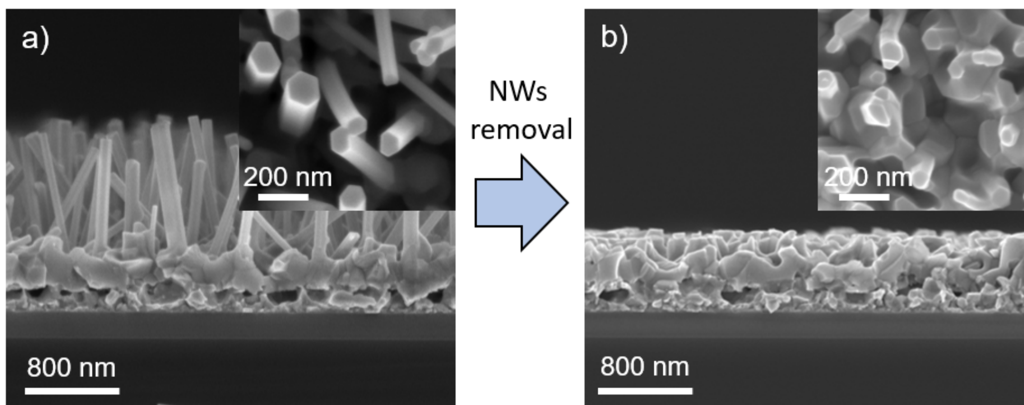

Figure 5.2: Removal of ZnO NWs. Cross-section FESEM image a) before and b) after mechanical removal of NWs by sonication. Top views are presented as insets. Adapted from [194].

Chemical and structural properties of the ZnO base layer were assessed and compared to the NW array properties. Chemical compositions of the ZnO NW array and the base layer were investigated by means of XPS depth profile, that revealed an atomic concentration ratio of approximately 1:1 for Zn and O along the entire ZnO structure, including the base layer (Figure 5.3). Therefore, no substantial differences in stoichiometry can be found in NWs and base layer. Structural properties were investigated by means of Raman spectroscopy and XRD. Raman spectra of ZnO NW arrays and base presented in Figure 5.4 a and b, respectively, revealed typical feature of *w*-ZnO in both cases (refer to section 3.2.2 for a detailed discussion about Raman features of *w*-ZnO). Interestingly, ZnO NW array and the bare ZnO base layer exhibited no significant differences in the Raman spectra in terms of peak position, peak width and relative intensities. For the benefit of the reader, positions of first order Raman peaks extrapolated from data interpolation with Lorentzian peaks are reported in Table 5.1. Instead, typical XRD diffractograms of the NW array and base layer are presented in Figure 5.4 c and d, respectively, where peaks can be labelled according to the *w*-ZnO crystal structure

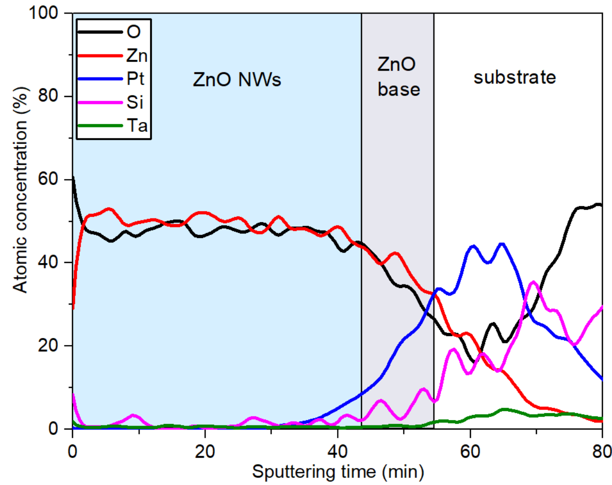

Figure 5.3: Investigation of ZnO NW arrays chemical composition by XPS depth profile. Pt, Si and Ta signals arise from the underlying substrate. Adapted from [194].

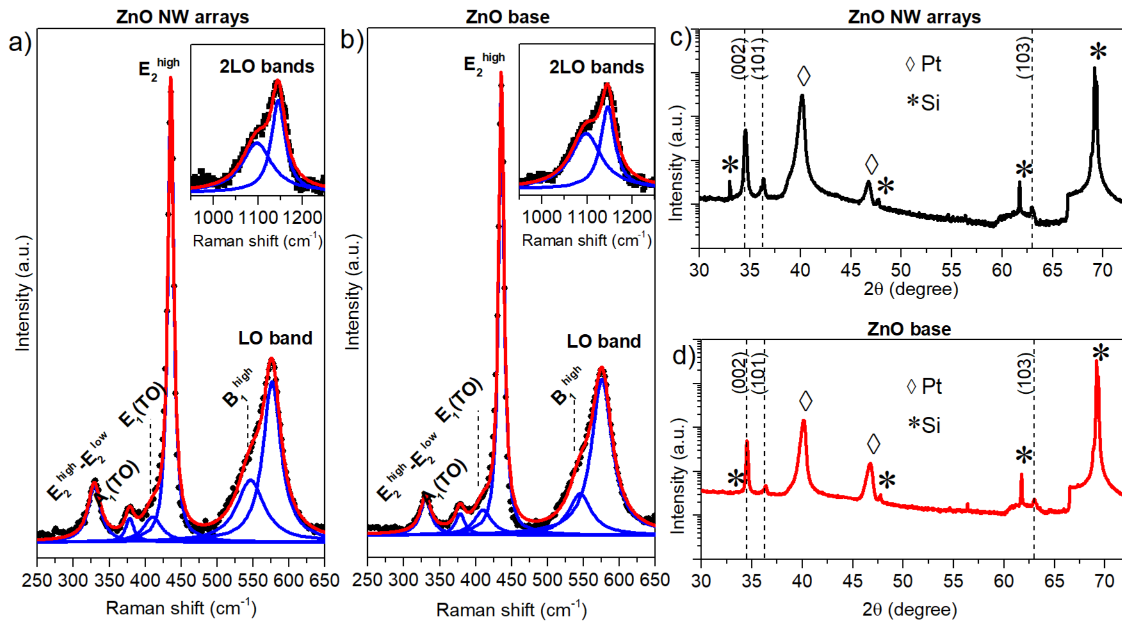

Figure 5.4: Comparison of ZnO NW arrays and base layer structural properties. Raman spectra of a) ZnO NW array and b) ZnO base layer. Red line represent the cumulative fit peak, blue line the single peak components interpolated by Lorentzian function while black points are raw data. XRD patterns (intensity in log scale) of c) ZnO NW array and d) ZnO base layer. Adapted from [194].

(refer to section 3.2.2 for a detailed discussion about XRD features of *w*-ZnO). Peak positions extrapolated from data fitting by means of Voigt functions are reported in table 5.2. The comparison of XRD peak relative intensities with peak intensities from the ZnO powder diffraction pattern (from JPDS No. 89-0511 data) revealed that both ZnO NW arrays and base layer are highly oriented in the [002] direction. According to SEM analyses, this indicates that ZnO NWs grow as a prolongation of base grains. In addition, no significant peak shifts can be observed by comparing XRD patterns from the NW array and the bare base layer. Thus, it can be concluded that ZnO NWs and the ZnO base layer are characterized by similar chemical and structural properties.

Table 5.1: Peak position and stadard deviation of first order Raman peaks of ZnO NW arrays and base.

	A_1(TO) (cm^{-1})	E_1(TO) (cm^{-1})	E_2^{high} (cm^{-1})	LO band (cm^{-1})
NW array	(378.3 ± 1.4)	410 (fixed)	(435.52 ± 0.06)	(576.3 ± 0.5)
base layer	(378.2 ± 1.7)	410 (fixed)	(435.59 ± 0.06)	(575.6 ± 0.6)

Table 5.2: XRD peak position (2θ) extrapolated from peak fitting with Voigt functions.

	(100)	(002)	(101)	(102)	(110)	(103)
NW array	/	34.54°	36.32°	/	/	62.98°
base layer	/	34.52°	36.34°	/	/	63.07°

5.3 Resistive switching characteristics

In order to understand the role of the polycrystalline base layer, Pt/ZnO/Pt devices were realized by considering both as grown ZnO NW arrays and the bare base as switching layers. In this fashion, it was possible to evaluate and compare resistive switching characteristics of the two structures. As reported in Figure 5.5 a and b, both structures exhibited bipolar resistive switching characteristics. By applying a positive voltage sweep to the top electrode, a SET process can be identified in correspondence of V_{SET} where an abrupt increase of current can be observed. Here, the device turns from HRS to LRS. In both cases, a CC of 11 mA was externally imposed for preventing an irreversible breakdown of the device due to

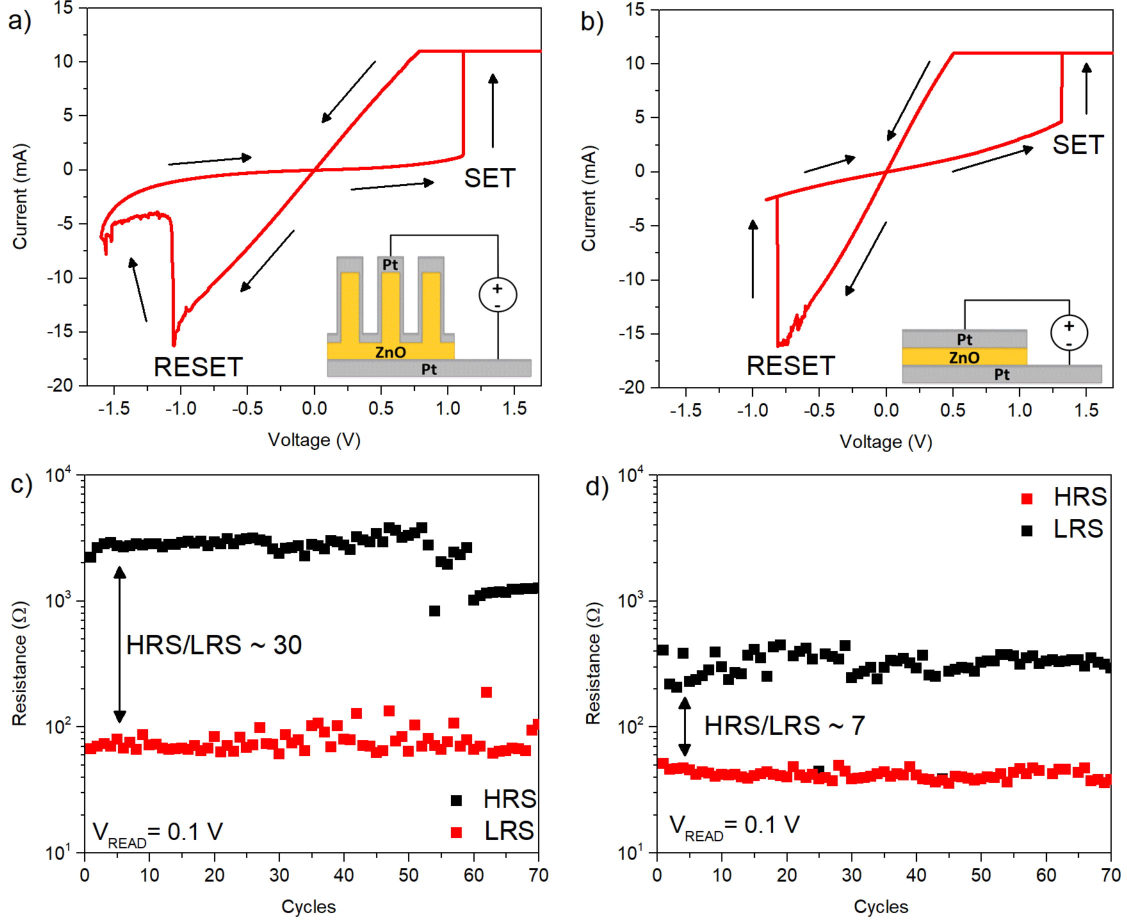

Figure 5.5: Resistive switching properties of ZnO NW arrays and ZnO base layer. *I*-*V* characteristics of a) ZnO NWs array and b) base layer. Insets show a schematization of the considered device structure during measurements. Endurance properties of c) ZnO NW arrays and d) base layer, respectively. Adapted from [194].

Joule overheating. Then, when a negative voltage sweep is applied, the device turns from LRS to HRS in correspondence of V_{RESET} (RESET process). Note that, a forming process consisting of several voltage sweeps was necessary before observing repeatable bipolar resistive switching characteristics (details of the electroforming process in appendix B.1). Also, it is important to notice that the value of imposed CC strongly influences the the resistance states as well as the device stability, as discussed in appendix B.2. Both devices exhibited good stability for 70 cycles, as can be observed from endurance measurements presented in Figure 5.5 c and d. It is important to notice that the NW removal resulted in a lower HRS/LRS window, that was decreased from ~ 30 in NW arrays to ~ 7 in the base layer. This behaviour can be mainly attributed to different values of HRS, since similar values of LRS were observed in both devices. V_{SET}, V_{RESET} and I_{RESET} as a function of cycles

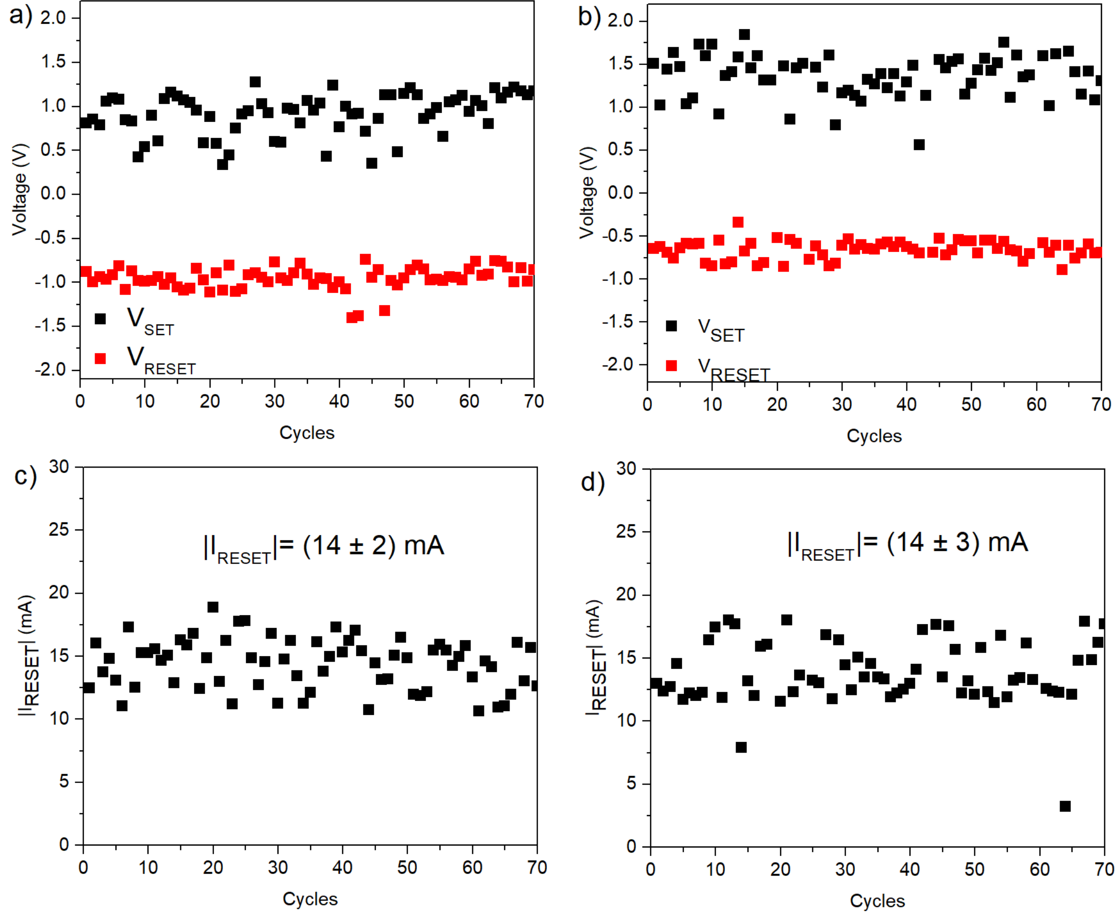

Figure 5.6: Resistive switching parameters of ZnO NW arrays and ZnO base layer. V_{SET} and V_{RESET} as a function of cycles for a) ZnO NW arrays and b) base layer. I_{RESET} as a function of cycle for c) ZnO NW arrays and d) base layer. Adapted from [194].

are reported in Figure 5.6. As can be observed from Figure 5.6 a and b, both SET and RESET voltages exhibited small fluctuations around the mean values. Mean values of SET voltages were calculated as (0.9 ± 0.2) V and (1.4 ± 0.3) V for ZnO NWs and base, respectively. Instead, mean values of RESET voltages for ZnO NWs and base were (-1.0 ± 0.1) V and (-0.7 ± 0.1) V, respectively. Interestingly, similar RESET currents of ~ 14 mA were observed in both devices. It is important to notice that resistance states are non-volatile at room temperature. Indeed, retention test performed on a ZnO base layer showed resistance state stability for at least 10^4 s at room temperature, as reported in Figure 5.7.

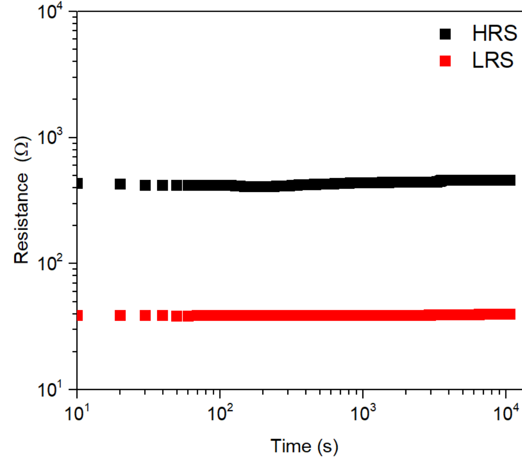

Figure 5.7: Retention test performed on the ZnO polycrystalline base layer. Measurements were performed at room temperature, by applying a stress voltage of 0.1 V for 5 ms every 10 s. Adapted from [194].

5.4 Resistive switching mechanism

In view of the previously discussed results, it is clear that the base layer cannot be disregarded for explaining the resistive switching mechanism of ZnO NW arrays. More in details, since the top electrode can penetrate down to the base layer even in presence of NWs and the base layer alone exhibits resistive switching, it can be concluded that the physical mechanism of swithing in ZnO NW arrays is located in the base layer. Electrical measurements corroborated this hyphotesis, since similar electronic conduction mechanisms were observed in both NW arrays and base layer devices. This aspect can be clearly visualized by considering full logaritmic plots of the I-V curves of ZnO NW arrays and base layer, as reported in Figure 5.8 a and b , respectively. In both cases, an ohmic conduction mechanism was obseved in LRS ($I \sim V$) while the HRS was characterized by an ohmic behaviour in the low voltage regime and a trap-controlled space charge limited conduction (SCLC) mechanism ($I \sim V^{\alpha}, \alpha > 1$) for higher voltages. Moreover, despite the relevant morphological differences in between the devices, comparable operating voltages and currents were observed in ZnO NW array and base layer devices, as previously discussed. All these observations suggest that in both devices the switching mechanism is located in the base layer and is dominated by the formation/rupture of a metallic-like filament. In these terms, the reduction of the HRS/LRS ratio after the removal of NWs can be explained as follows. Both devices exhibited similar LRS values since in both cases the ON state is attributable to the creation of a confined conduction path through the ZnO base layer. An important aspect is that in both devices a similar amount of power was necessary for destroying the filament, since comparable RESET currents were observed. In a filament-based scenario, this suggests that similar

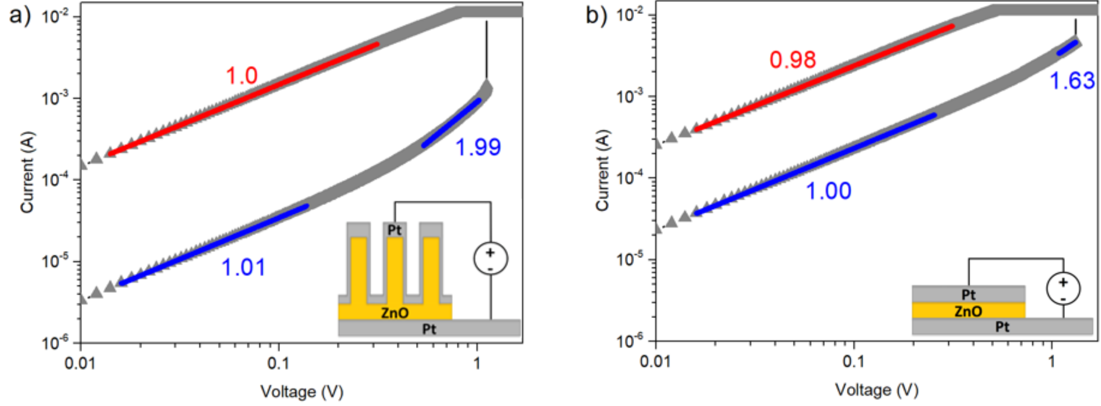

Figure 5.8: Full logaritmic plot of I-V characteristics (positive polarity) of a) ZnO NW arrays and b) ZnO base layer. Fit of LRS and HRS are reported in red and blue, respectively. Adapted from [194].

amount of filaments or filaments characterized by similar sizes are present in devices [195]. Instead, the value of HRS decreased after NW removal as a consequence of a more delocalized electronic conduction mechanism over the whole electrode due to the rupture of the localized conductive paths. Thus a higher resistance in HRS is expected in presence of NWs. For all these reasons, the resistive switching mechanism has to be investigated by considering the columnar-grained structure of the base layer, even in presence of NWs. In polycrystalline materials, grain boundaries (GBs) are well known to be electrically more conductive regions, while grain centers are less conductive and generally not involved in resistice switching, as discussed by Muenstermann et al. [196] in $SrTiO_3$ and Moriyama et al. [197] in NiO films. This behaviour can be attributed to the higher concentration of defects at GBs that locally affect both electronic and ionic conductivity properties of the material. During the electroforming process, positively charged defects such as oxygen vacancies are expected to migrate under the action of the electric field and to assemble, forming a conductive filament at GBs where faster defect motion is enabled [198, 199]. For clarity, it is important to underline that oxygen vacancies are not chemical species and their migration should be attributed to the movement of negatively charged oxygen ion species towards the opposite direction. In our polycrystalline ZnO film, GBs can be considered oxygen reservoirs that promote the formation of highly localized conductive filaments. After the formation of a conductive path, by applying an opposite polarity, the RESET process can be attributed to the creation of a depleted gap Δx in the thinnest area of the conductive filament. Indeed, the high temperatures induced by Joule heating are responsible for an increase of the ionic mobility. As a consequence, in correspondence of V_{RESET}, oxygen vacancies start to migrate towards the grounded electrode inducing the rupture of the conductive path. Initialy, Pt/ZnO/Pt devices are symmetric and thus the SET

process can be induced by applying both polarities to the top electrode, depending on the initial electroforming procedure, as discussed in appendix B.3. After the initial assessment of a conductive path by electroforming, the bipolar resistive switching behaviour can be attributed to the rupture/formation of conductive filaments along grain boundaries of the base layer, as schematized in Figure 5.9 a. The previously discussed structural properties of the ZnO base layer, characterized by crystallographic preferential orientation of grains in the [002] direction, result in highly oriented grain boundaries (GBs) in the perpendicular direction respect to the metal electrodes. The high orientation of GBs can be clearly visualized by means of TEM analysis, as reported in Figure 5.9 b. A detail of the interface in between two grains, with corresponding fast Fourier transform (FFT) patterns, is reported in Figure 5.9 c. In this framework, GBs can promote the formation of highly oriented conductive paths perpendicularly to the electrodes. Under these conditions, the creation of straight rather than branched conductive paths is favorited resulting in a narrow dispersion of resistance states and low electric fields required during the forming process, as previously discussed by Chang et al.[200] by considering ZnO thin films realized by sputtering. Moreover, the high temperature growth process results in a polycrystalline base characterized by coarse grains with a reduced number of GBs, as shown in TEM analyses of Figure 5.9 b. As previously reported by Zhuge et al. [201], the limited amount of GBs can improve the resistive switching stability by reducing the randomization of the formation/rupture of the conductive filaments. In addition, it should be noticed that resistive switching

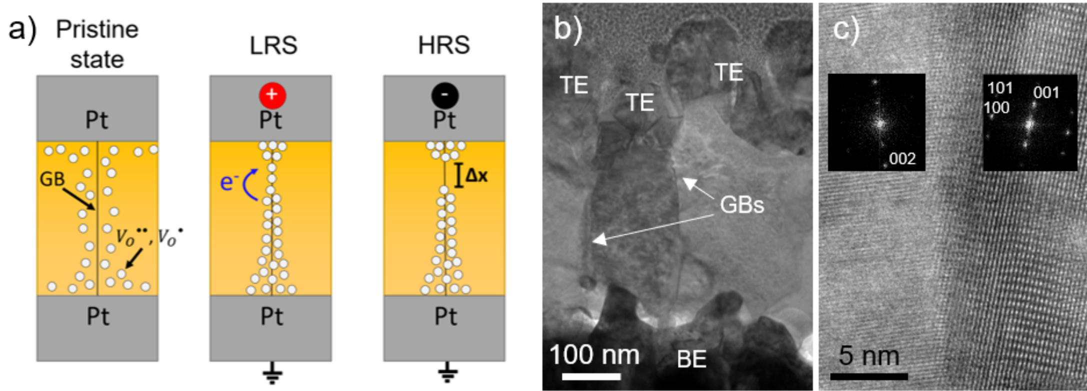

Figure 5.9: Resistive switching mechanism in the polycrystalline ZnO base layer. a) Schematic representation of the resistive switching mechanism based on the formation/rupture of oxygen vacancies-assisted filament along highly oriented grain boundaries. b) Bright field TEM cross section of the ZnO base sandwiched in between a top electrode (TE) and a bottom electrode (BE). Arrows indicate the grain boundaries (GBs). c) HRTEM image of a GB with corresponding FFT patterns acquired on adjacent crystalline grains. Adapted from [194].

was observed by considering ZnO base layers with thickness up to ∼320 nm (see appendix B.4), a considerably higher thickness compared to ZnO thin films with thickness ranging from 25 nm to 150 nm usually exploited for resistive switching, as described in the review by Laurenti et al. [35]. By comparing our results with the work of Chiu et al. [202] that investigated resistive switching in ZnO films realized by radio frequency magnetron sputtering with thickness of 25 nm and sandwiched in Pt electrodes (same configuration of our work), it is possible to observe that there are no significant differences in operating voltages despite the huge difference in film thickness (Chiu et al. [202] observed SET and RESET voltages of 1.2 V and 0.5 V in absolute values, respectively). All these observations further confirmed the importance of cristallinity and GBs orientation in facilitating resistive switching even in case of high ZnO film thicknesses. It is important to underline that the switching mechanism of ZnO NW arrays here proposed was further confirmed by analyzing electrical behaviour of single isolated NWs. Indeed, no resistive switching was observed in single isolated ZnO NWs contacted by means of Pt symmetric electrodes (see section 7.4), further corroborating that the physical mechanism of switching is located in the polycrystalline base layer of the ZnO NW arrays. Furthermore, it should be noticed that devices exhibited better performances in VCM configuration, since a probable interplay in between oxygen vacancies and metal host ions (Cu^{z+}) in ECM configuration was observed to reduce the stability of resistive switching in the ZnO base layer, as discussed in appendix B.5.

To summarize, these results clarified that resistive switching in NW arrays cannot be attributed solely to the NW properties. Strictly speaking, it was revealed that the switching mechanism in such structures is analogous to the mechansim proposed in case of polycrystalline ZnO thin films reported for example in the work by Conti et al. [203]. More importantly, these results suggested the importance of the development of an appropriate fabrication/electrode deposition technique to take into advantage of the properties of NWs in devices based on nanostructure arrays. Despite this, the most appropriate approach to investigate resistive switching in these structures is the development of single-NW memristive devices, as discussed in the following chapters.

Chapter 6

Electronic conduction mechanism in single ZnO NWs

6.1 Introduction

The realization of electronic devices based on single crystalline ZnO NWs requires a comprehension of the electronic conduction mechanism. Several charge transport mechanisms such as thermally activated conduction mechanism [133, 204, 205], fluctuation induced tunnelling conductance (FITC) [205], nearest-neighbour hopping [133, 204] and variable range hopping [206] have been proposed for explaining experimental results in different temperature ranges. The wide range of mechanisms reported in literature can be explained in terms of different material properties such as crystal quality, defectivity and amount of intrinsic doping, as a consequence of diverse growth techniques and/or growth parameters. In this chapter, electronic conduction mechanism of single crystalline ZnO NWs is investigated by means of temperature-dependent I-V measurements and transconductance measurements in NW field effect transistor (NW-FET) configuration.

6.2 Single NW device

Single NWs dispersed on an electrically insulating SiO_2 substrate were contacted by Pt electrodes through an EBL process, following the procedure described in details in section 2.3. A schematic representation and a SEM image of the single ZnO NW device can be found in Figure 6.1 a and b, respectively. Note that field effect measurements were realized by exploiting the highly doped Si back gate contact, with the SiO_2 layer acting as the gate dielectric. Instead, due to the low tendency of Pt to form oxide forms, Pt electrodes ensured reliable metal/semiconductor junctions without the presence of an interfacial oxide layer.

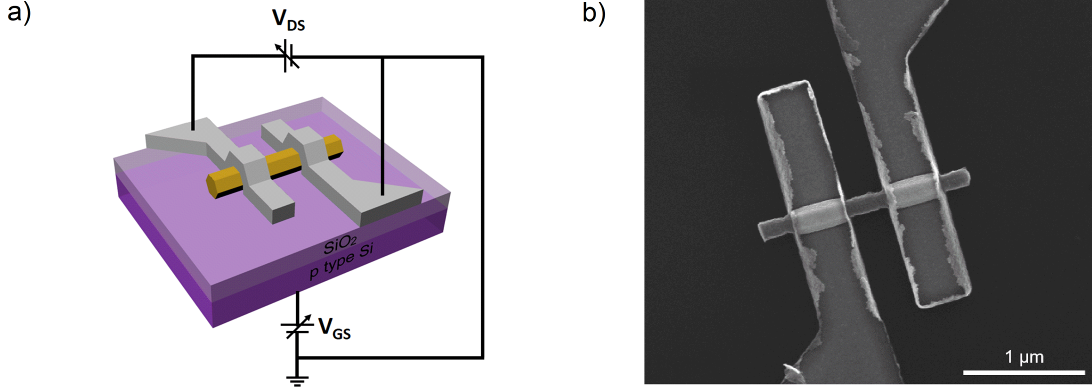

Figure 6.1: Single ZnO NW device. a) Schematic representation with electrical connections and b) SEM image of a single ZnO NW contacted with Pt electrodes.

6.3 Surface effects

The high surface-to-volume ratio strongly influences the conduction properties of nanostructures, where surface states play a crucial role in regulating the charge transport mechanism. For this reason, the electrical conductivity of NWs is strongly influenced by adsorbed species on the surface due to sample exposure to different environments as well as on the processing history. Initially, the effect of an annealing step on the electrical characteristics of a single NW was evaluated. For this purpose, I-V characteristics of the same NW were compared before and after annealing at 450 K for about 90 min. (I-V were acquired at 300 K, $\sim 4{\cdot}10^{-3}$ mbar). Results are presented in Figure 6.2 a. As can be observed, the NW was characterized by a non linear behaviour with high resistivity before annealing (before 1^{st} annealing). After annealing, the I-V characteristic exhibited a linear and symmetric behaviour, with a resistivity of about 0.004 Ω m (post 1^{st} annealing). In this case, the annealing improved the contact quality and removed adsorbed species from the NW surface. This is a fundamental step for the realization of ohmic contacts. Subsequently, the NW was exposed to atmospheric conditions and electrically measured in vacuum (Pre 2^{nd} annealing). The effect of the exposure to atmosheric conditions was to increase the resistivity as a consequence of adsorbed species on the NW surface. In this case, the observed resistivity was about 0.035 Ω m. The electrical conductivity achieved after the first annealing can be restored by removing again adsorbed species through a new annealing step (Post 2^{nd} annealing). In order to further investigate the role of adsorbed species on the surface, I-V characteristics were measured by progressively increasing the pressure inside the vacuum chamber after an annealing step (by inserting atmospheric air). Results are reported in Figure 6.2 b, where it is possible to observe that the NW resistivity increased about 3 times starting from the pressure of $3.4 \cdot 10^{-3}$ mbar up to atmospheric conditions.

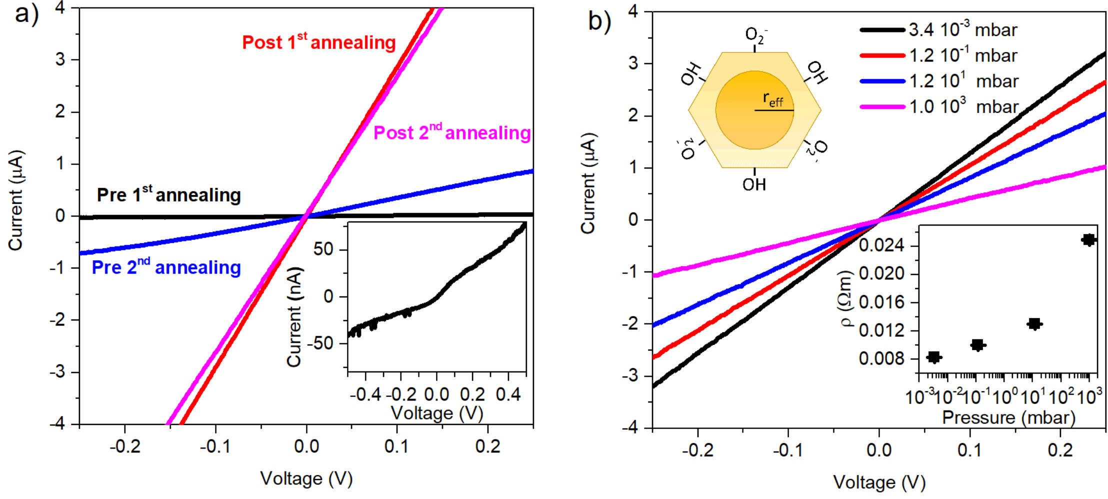

Figure 6.2: Effect of surface states on electrical characteristics of single ZnO NWs. a) *I-V* characterization of a single ZnO NW at 300 K in vacuum before and after annealing treatments. Inset shows a detail of the I-V characteristic pre 1^{st} annealing. b) I-V characterization of a previously annealed NW by progressively increasing the pressure. The insets show the resistivity dependence on pressure and a schematic representation of the NW modelled as a semiconductor core surrounded by an insulating shell layer due to the presence of adsorbed species.

These results revealed that adsorbed species on the NW surface act as charge traps that increase the overall resistivity of the NW, capturing free electrons and creating a depletion region on the surface due to upward band bending of the ZnO band structure. The upward band bending on the ZnO NW surface can be attributed to the adsorption of O_2 [207, 208] and/or OH species [45]. It is important to notice that the annealing process at 450 K removes almost all the adsorbed O species, considering that Chen et al. [208] observed a removal of most of O species on the ZnO NW surface after an annealing at only 373 K. Instead, a detailed discussion concerning the influence of moisture on the electronic properties of ZnO is presented in chapter 8.

6.4 I-V-T measurements

In order to investigate the electronic conduction mechanism, *I-V* measurements were performed in a wide range of temperature (81.7 K - 480 K) in vacuum conditions. The conductivity (σ) dependence on temperature, estrapolated from a linear fit of the *I-V* curves acquired at different temperatures, is presented as Arrhenius plot in Figure 6.3 a. Note that before measurements, an annealing step at 450 K

was performed in order to remove the influence of adsorbed species on the surface, as discussed in the previous section. At room temperature, the NW exhibited low resistivity ($3{\cdot}10^{-3}\ \Omega\,\mathrm{m}$ at 300 K), revealing a high concentration of intrinsic doping. Interestingly, two different trends of conductivity can be observed in Figure 6.3 a. For T < 350 K, an increase of conductivity was observed by increasing temperature, while for T > 400 K an opposite trend was reported. In the low temperature range (81.7 K-250 K), two different slopes can be identified in the Arrhenius plot, in accordance to the presence of two thermally activated conduction processes. According to Chiu et al. [133] and Tsai et al. [204], the conduction mechanism in natively doped ZnO NWs can be described as:

$$\sigma = \frac{1}{\rho_1} e^{-\frac{E_1}{k_b T}} + \frac{1}{\rho_2} e^{-\frac{E_2}{k_b T}} \tag{6.1}$$

where ρ_1 and ρ_2 are temperature independent parameters, E_1 and E_2 are the activation energies corresponding to the two thermally activated conduction processes and k_b is the Boltzmann constant. The presence of two thermally activated processes can result from the peculiar band structure of intrinsically doped ZnO NWs. For high doping concentration, it is well established that the interaction between randomly distributed impurity states results in the creation of an impurity energy band. In addition, the impurity band can be further splitted in two D and D^- sub-bands, under certain doping conditions. The D and D^- sub-bands can be formed by the impurity wavefunctions overlapping of ground states and negative-ion states, respectively [209, 210]. Thus, the band structure of intrinsically doped ZnO NWs can be schematized as in Figure 6.3 b with the Fermi level laying on the top of the D band, according to Chiu et al. [133]. At low temperatures (T <∼120 K), the thermal energy of electrons is not sufficient for being excited to the conduction band. However, the thermal energy is enought to excite electrons from the D band to the unoccupied states of the D^- band, giving rise to the so-called E_2 conduction channel. By increasing the temperature, the thermal energy becomes enought for promoting electrons from the D band to the conduction band and conduction occurs mainly through the E_1 conduction channel. Note that a third channel of conduction due to nearest neighbour hopping (NNH) inside the D band is here neglected since it was shown to be relevant only for temperatures below 20 K [133]. The conduction model above mentioned well interpolates experimetal data in the range (81.7 K - 250 K), as reported in Figure 6.3. From data interpolation, the activation energies E_1 and E_2 were calculated to be (35.1 ± 1.2) meV and (3.8 ± 1.4) meV, respectively. Extrapolated fitting parameters are reported in Table 6.1 and compared with literature data. As can be observed, activation energies well match with the ones obtained in previous works. By considering high temperatures, a transition from a semiconductor to a metallic behaviour can be observed. This is the result of a Mott metal-to-insulator transition (MIT) that occurs in correspondence of a critical temperature (T_c ∼365 K). Indeed, an increase of temperature results in

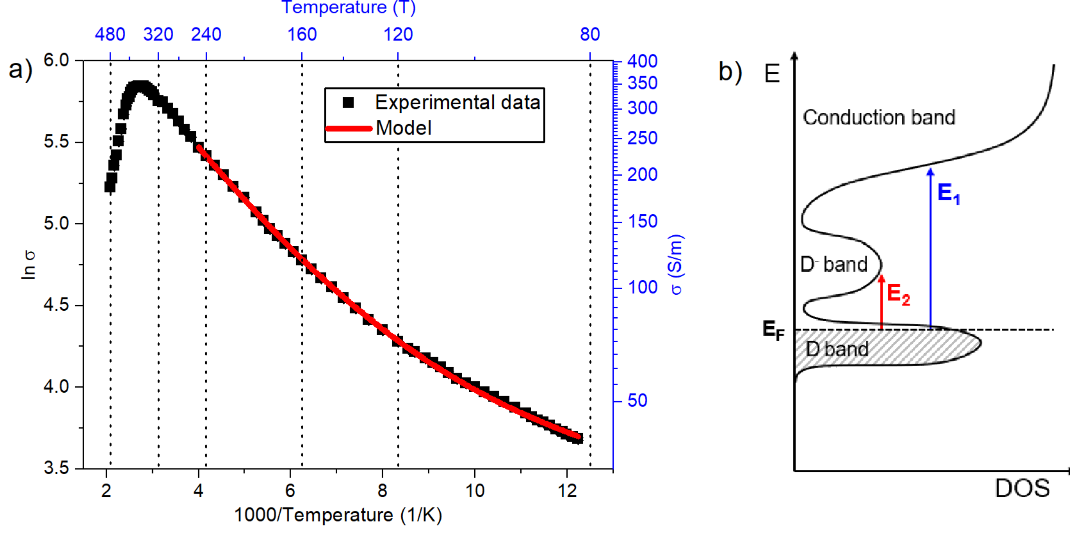

Figure 6.3: Electrical conductivity of a single ZnO NW as a function of temperature in vacuum conditions. a) Arrhenius plot of the conductivity as a function of temperature and b) schematic representation of the band structure of the ZnO NW (band structure is schematized according to Chiu et al. [133])

Table 6.1: Comparison of activation energies and fitting parameters obtained from data fitting with the double activation energies model described by eq. 6.1 with literature. Values of ρ_1 and ρ_2 from ref. [204] are subjected to an uncertainty of 2% and 3%, respectively.

Reference	NW diameter (nm)	ρ (300 K) (Ω·m)	ρ_1 (Ω·m)	E$_1$ (meV)	ρ_2 Ω·m)	E$_2$ meV
This work	146	0.0033	(0.00103±0.00002)	(35.1±1.2)	(0.017±0.004)	(3.8±1.4)
[133]Z-L011	200±11	0.00078	(0.00019±0.00001)	(44±1)	(0.0029±0.0001)	(3.7±0.1)
[133]Z-f-R	87±10	0.00078	(0.00031±0.00001)	(28±1)	(0.0059±0.0005)	(4.8±0.3)
[133]Z-k1	103±5	0.0015	(0.00051±0.00003)	(34±1)	(0.0071±0.0005)	(4.0±0.2)
[204] Z-1^a	60±3	0.00031	0.00091	(26.1±0.3)	0.0011	(2.23±0.01)
[204] Z-2	105±5	0.00037	0.00072	(22.8±0.7)	0.0013	(2.34±0.12)
[204] Z-3	95±5	0.00047	0.00031	(26.3±0.7)	0.0048	(4.47±0.19)

an increase of thermally ionized electrons and, when a critical concentration n$_c$ is reached, the transition to a metallic behaviour occurs as a consequence of Coulomb interactions [211]. The MIT transition in doped semiconductors can be explained by means of the Mott criteria [212]:

$$n_c^{1/3} a_B^* \cong 0.25 \tag{6.2}$$

where a_B^* is the effective Bohr radius that can be estimated to be $a_B^* \approx 1.9\,\mathrm{nm}$ in ZnO from the equation $a_B^* = \frac{\epsilon}{m_e^*/m_e}$, by considering an effective mass of $m_e^* =$

0.24 m_o and a dielectric constant of $\epsilon = 8.66$ for wurtzite ZnO [213]. According to eq. 6.2, the critical carrier concentration can be estimated to be $n_c \approx 2.3{\cdot}10^{18}\,\mathrm{cm}^{-3}$. Since the dielectric constant of ZnO NWs has been shown to be dependent on the NW radius due to surface weakening effects, as discussed by Yang et al. [214], this reprents only a rough estimation of the critical carrier concentration. A more accurate estimation can be performed by considering a dielectric constant of $\epsilon \approx 3.5$ estrapolated from the work of Yang et al. [214] in case of a NW with diameter comparable to our work (about 150 nm). By considering these values, the Bohr radius was calculated to be $\approx 0.8\,\mathrm{nm}$, with a corresponding critical carrier concentration of $\mathrm{n}_c \approx 3.0{\cdot}10^{19}\,\mathrm{cm}^{-3}$.

6.5 Field-effect measurements

The conduction mechanism was further investigated by means of field-effect measurements, on the same NW previously considered for *I-V-T* measurements. I_{DS} vs V_{DS} measurements as a function of a fixed gate bias (in the range +50/-50 V) are reported in Figure 6.4 a while transconductance curves (I_{DS} vs V_{GS} curves) performed by applying different V_{DS} (in the range 10-250 mV) are reported in Figure 6.4 b. All these measurements, performed in vacuum at room temperature after an annealing process at 450 K, evidenced a *n*-type field-effect behaviour characterized by an increasing of resistivity by reducing the gate bias. The *n*-type intrinsic doping of ZnO is attributable to the presence of point defects such as O vacancies

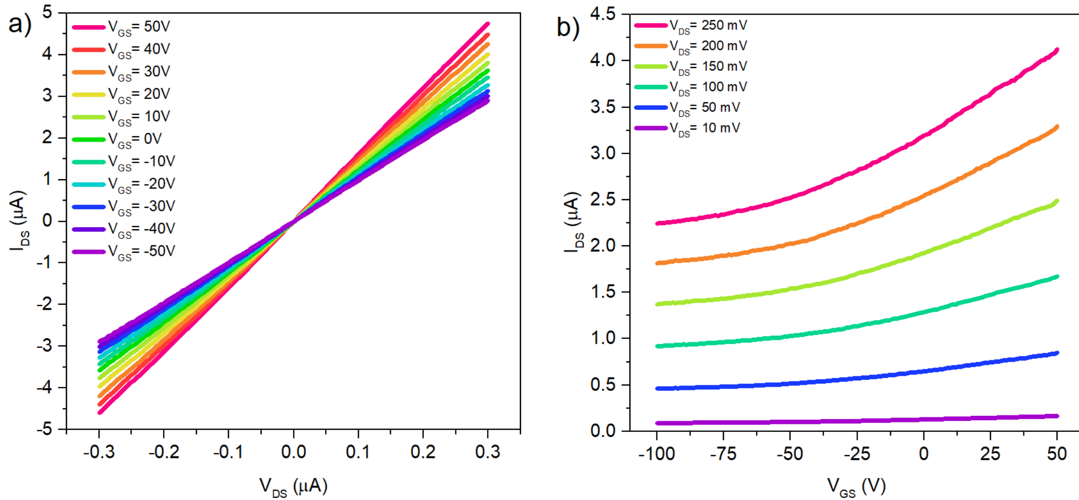

Figure 6.4: Field-effect in single ZnO NW. a) I_{DS} vs V_{DS} curves acquired with different gate voltage bias and b) I_{DS} vs V_{GS} curves for different drain-source bias. Measurements were performed in vacuum at room temperature.

and/or Zn interstitials [211, 215]. The temperature dependence of transconductance characteristics acquired with a constant V_{DS} bias of 200 mV are presented in Figure 6.5 a. Measurements were performed in vacuum in stationary conditions, by sweeping the gate bias voltage with a step of 1 V (delay time of 1 s) and by progressively increasing the temperature from 81.5 K up to 360 K. By considering the metallic NW on plate model, it is possible to estimate charge density as [216]:

$$n \approx \frac{C_{NW} V_{th}}{q \pi r^2 L} \tag{6.3}$$

and field-effect mobility as [217]:

$$\mu \approx \frac{dI_{SD}}{dV_g} \cdot \frac{L^2}{C_{NW} V_{DS}} \tag{6.4}$$

where the gate capacitance was estimated through the relation [217]:

$$C_{NW} \approx \frac{2\pi \epsilon_0 \epsilon_r L}{cos^{-1}(\frac{r+d_{ox}}{r})} \tag{6.5}$$

where ϵ_0 the vacuum permittivity, ϵ_r=3.9 the relative permittivity of the SiO_2 gate oxide, d_{ox}= 500 nm the gate oxide thickness, r=73 nm the NW radius, L=350 nm the electrode spacing and V_{th} the threshold voltage calculated by the extrapolation of the intersection between the linear regime of the transconductance curves and $I = 0$ for each temperature. Arrhenius plots of charge density and mobility are presented in Figure 6.5 b and c, respectively. By considering temperatures below 250 K, charge density exhibited an exponential dependence on the reciprocal temperature, according to the relation $n \propto e^{-E_a/(k_b T)}$. The value of activation energy E_a obtained from the best fit is (36.9 ± 1.3) meV and is in accordance to the activation energy E_1 extrapolated from the I-V-T measurements. Instead, the lower increase of carrier density observed for temperature higher than 250 K is reasonably ascribable to an almost complete ionization of the donor impurities. Note that charge densities of $\sim 6 \cdot 10^{18}$ cm^{-3} observed for temperatures just before the critical temperature are in qualitative agreement with critical carrier concentration predicted by the Mott criteria previously discussed. By considering the carrier mobility in Figure 6.5 c, two different behaviours can be observed depending on the temperature range. Starting from a value of 4.9 cm^{2}V^{-1}s^{-1} at 81.6 K, the mobility decreased by increasing temperature and reached a pleateau of about 1.7 cm^{2}V^{-1}s^{-1} in the range 200 K-250 K. Instead, an opposite trend was observed for higher temperatures where mobility was observed to increase by increasing temperature. By considering the relationship between carrier mobility and density presented in Figure 6.5 d, it is possible to observe that an increase of the carrier concentration resulted in a decreasing of carrier mobility. When the carrier concentration reached the value of about $6 \cdot 10^{18}$ cm^{-3} at about 250 K (i.e. when almost all donors are ionized) the NW

conductivity results to be mainly driven by the change in mobility that increased as a function of temperature while the carrier density remained nearly constant.

To summarize, temperature-dependent *I-V* measurements and transconductance measurements were exploited to investigate semiconductive properties of single crystalline ZnO NWs. In particular, results revealed the importance of surface effects in regulating the electronic conduction properties and the importance of sample pre-treatments. *I-V-T* measurements were in good agreements with a two thermally activated conduction process and revealed the occurrence of a metal-insulator-transition at a critical temperature of about 365 K. Moreover, field-effect measurements revealed an n-type semiconductive behaviour and carrier concentration in the order of $\sim 10^{18}$ and a carrier mobility in the range 1.7-4.9 $\mathrm{cm^2V^{-1}s^{-1}}$

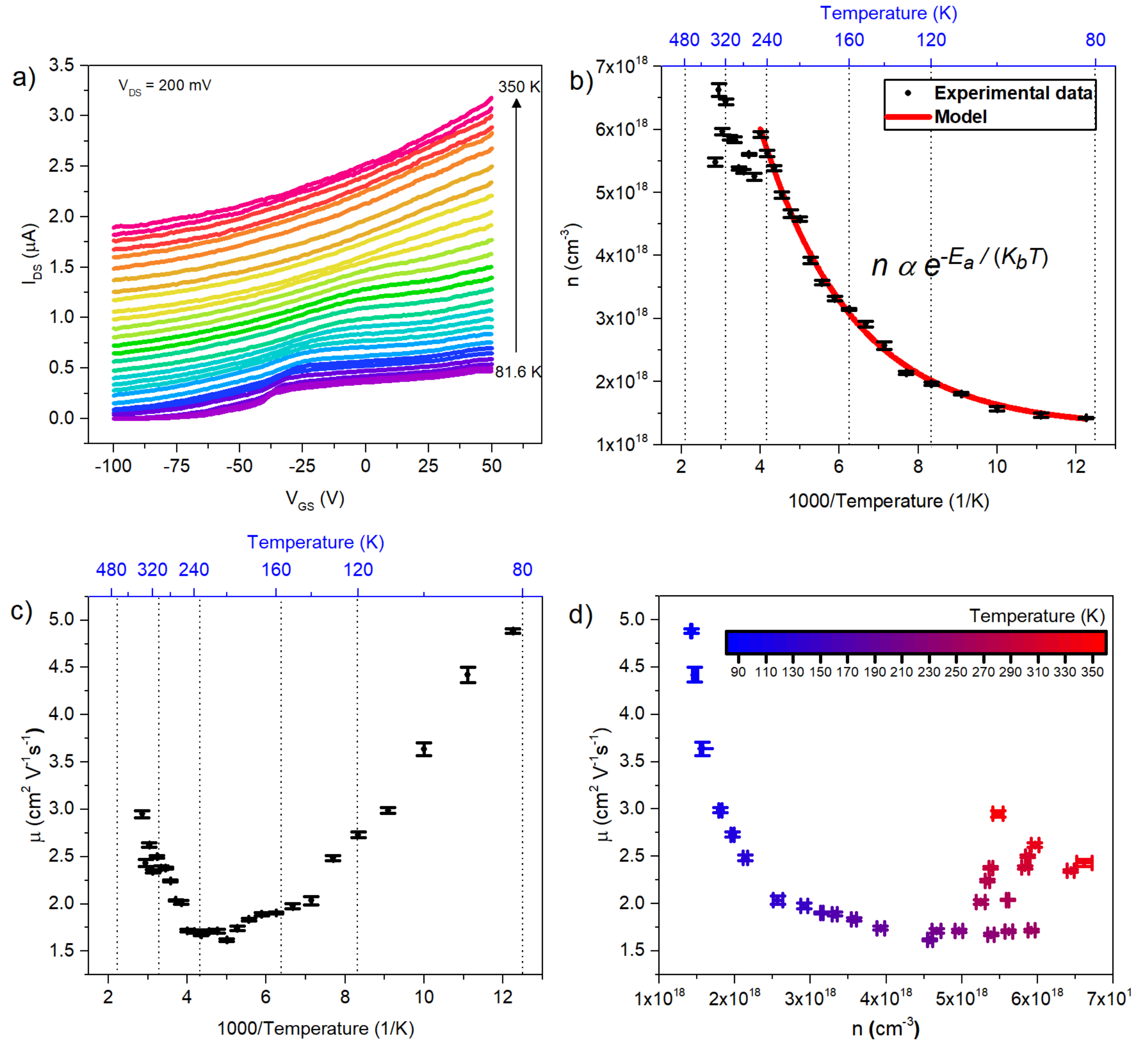

Figure 6.5: Temperature-dependent field-effect in single ZnO NW. a) Transconductance characteristics as a function of temperature (measurements were acquired by increasing temperature with a step of about 10 K, from 81.6 K up to 350 K). Arrhenius plot of b) charge density and c) field effect mobility as a function of the reciprocal temperature. d) Field-effect mobility as a function of charge density, where the color scale represents the temperature.

Chapter 7

Single ZnO NW memristors

Reference papers:

[218] *Milano, Gianluca, et al. "Self-limited single nanowire systems combining all-in-one memristive and neuromorphic functionalities." Nature communications 9.1 (2018): 5151*
[219] *Milano, Gianluca, et al. "Junction properties of single ZnO nanowires with asymmetrical Pt and Cu contacts", Submitted.*

7.1 Introduction

The development of memristive model systems is fundamental for a detailed understanding of the physical mechanism of resistive switching at the nanoscale. In this chapter, a single crystalline ZnO NW was proposed as a suitable memristive model system by coupling its electronic and ionic transport properties. In this fashion, the single NW exhibited a full range of memristive functionalities such as non-volatile bipolar memory, multilevel switching, selector capability and emulation of synaptic plasticity. The analysis of the physical mechanism of switching, investigated through combined electrical, structural and chemical characterizations, revealed that the memristive functionalities are determined by the ionic migration of Ag^+ ions on the NW surface, proving experimentally that ionic transport is suppressed in the bulk of crystalline materials and pointing out the importance of surfaces and interfaces in resistive switching devices. The importance of metal/semiconductor interfaces and electrochemical properties of the metal electrodes are discussed by analyzing the behaviour of different metal contacts, providing new insights for the development of suitable design rules for the realization of reliable resistive switching devices. Self-assembled single ZnO NW memristors can be considered not only as memristive model systems but also as suitable candidates for ultimate device miniaturization beyond the scaling limits of conventional lithography.

7.2 Single NW memristor devices

Single NW memristors were realized by means of contacting ZnO NWs dispersed on a SiO_2 substrate with two asymmetric electrodes. A detailed description of the device fabrication process is reported in section 2.3. An SEM image of a single ZnO NW memristor is reported in Figure 7.1 a, while the schematization of the device with electrical connections is reported in Figure 7.1 b. In analogy with previously discussed symmetric devices (section 6.2), the heavily doped Si back gate can be exploited for transconductance measurements in NW-FET configuration. As discussed in the following sections, the choice of asymmetric electrodes with different electrochemical properties is a fundamental aspect for the realization of an ECM cell based on a single crystalline ZnO NW. The memristive mechanism and properties were studied by considering Ag as the electrochemically active electrode, while Pt was used as inert counter electrode. In addition, the use of Cu as active electrode instead of Ag is discussed in section 7.9.

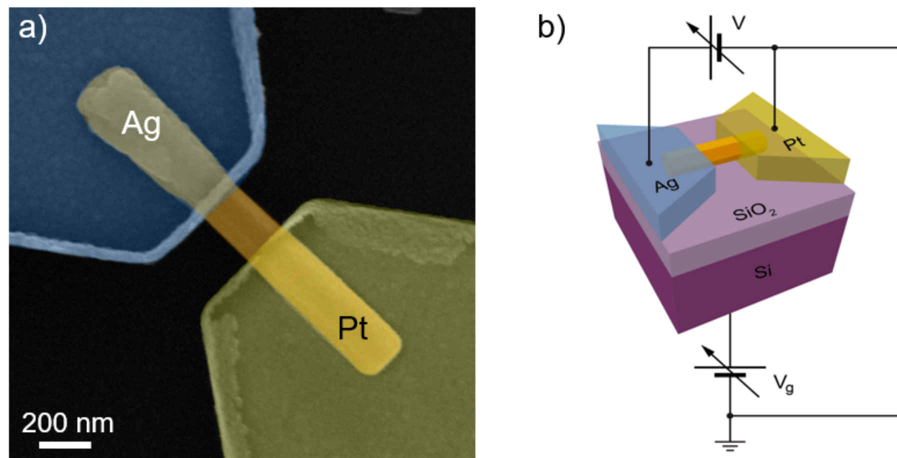

Figure 7.1: Single ZnO NW memristor device. a) SEM image (in false colors) of a single ZnO nanowire (orange) contacted by means of asymmetric Ag (blue) and Pt (yellow) contacts and b) schematic representation of the device with electrical connections. Adapted from [218].

7.3 Pristine state

An initial investigation of electrical properties of single NW memristors was performed by comparing the pristine state of asymmetric Ag/ZnO NW/Pt devices with symmetric Pt/ZnO NW/Pt devices. The *I-V* pristine state curves reported in Figure 7.2 can be modelled by means of back-to-back Schottky diodes where the

total current can be expressed by the equation [220, 221]:

$$I = \frac{2I_{S+}I_{S-}sinh(qV/2k_bT)}{I_{S-}exp(qV/2k_bT) + I_{S+}exp(-qV/2k_bT)} \tag{7.1}$$

where I_{s+} I_{s-} are the saturation currents observed for $V \rightarrow \infty$ and $V \rightarrow -\infty$, respectively. This equation assumes the ideality factor of both barriers equal to 1 and no series resistances in the circuit, differently from real experimental conditions where higher ideality factors are expected and the NW resistance in series (R_{NW}) cannot be neglected. The equivalent circuits of NW devices are presented as insets of Figure 7.2. It can be observed that symmetric and asymmetric devices resulted in symmetric and asymmetric I-V curves, respectively. This can be explained in terms of different Schottky barrier heights at metal/semiconductor interfaces. In the opposite way respect to experimental results, higher saturation currents are theoretically expected for reversely polarized Pt/ZnO junctions compared to Ag/ZnO junctions according to the thermionic emission (TE) model (theoretical background of TE model in section C.1), because of the higher Pt work function and the n-type nature of ZnO. Indeed, by considering an n-type semiconductor, the Schottky barrier height at the metal-semiconductor interface can be determined according to the Schottky-Mott rule:

$$\phi_{b,n} = \phi_M - \chi_{sc} \tag{7.2}$$

where ϕ_M is the metal work function while χ_{sc} the electron affinity of the semiconductor. Note that Pt and Ag work functions are 5.12 eV and 4.26 eV, respectively,

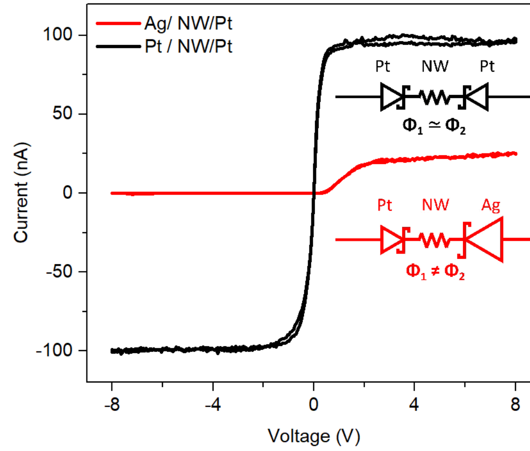

Figure 7.2: Pristine state of ZnO NW memristors. Pristine state comparison of single ZnO NWs contacted by Pt symmetric and Pt-Ag asymmetric electrodes. Insets reported the equivalent circuits of the device. Adapted from [218].

while the electron affinity of ZnO is 4.29 eV. Thus, a higher Schottky barrier resulting in lower saturation current values is expected in case of reversely polarized Pt/ZnO junctions while an almost ohmic contact is expected at Ag/ZnO interface. However, the Schottky-Mott rule for alignement of energy levels can predict the Schottky barrier height only in the ideal case, since energy barriers are strongly influenced by the interface chemistry, as discussed by Liu et al. [222]. In our case, the interface chemistry strongly influences the barreir height at the Pt/ZnO interface as a consequence of the formation of eutectics in between Pt and Zn that leads to interfacial chemical bonds, as discussed by Brillson et al. [223]. In these terms, it can be explained the higher saturation current observed in reversely polarized Pt/ZnO junctions respect to Ag/ZnO junctions. It is important to notice that in the above described back-to-back diode configuration an applied voltage across the electrodes results in an increase of the barrier height on one side by the quantity qV [224]. When low voltages are applied, Pt/ZnO Schottky barriers exhibited the characteristics of ohmic contacts because of the low energy barrier at the inteface. This explains why a linear behaviour is observed in Pt/ZnO NW/Pt devices for low applied fields, where the conduction mechanism is dominated by the NW resistance, as previously discussed in chapter 6. Instead, high applied voltages resulted in an increased barrier height on one side and, as a result, a lower amount of electrons can be injected through tunnelling effects. For this reason, high applied voltages resulted in a current saturation regime. Since Pt/ZnO junctions exhibited features of ohmic contacts for low applied voltages, a single diode-like characteristic in the low voltage range can be observed in asymmetric Ag/ZnO NW/Pt devices where the conduction is regulated by the Ag/ZnO Schottky interface.

7.4 Electroforming process

The asymmetrically contacted single ZnO NWs can be considered ECM cells, where the NW represents a single crystal electrolyte while Ag and Pt are the electrochemically active and inert electrodes, respectively. A detailed description of the ECM mechanism can be found in section 1.3.1. By applying a positive voltage to the Ag electrochemical active electrode, anodic dissolution of Ag atoms with consequent migration of Ag^+ ions under the action of the applied electric field occurs. This resulted in the formation of a conductive path along the NW (electroforming process) that turned the device in the LRS [59, 60, 225]. The formation of the conductive path can be observed in Figure 7.3 a, where a typical electroforming process of an Ag/ZnO NW/Pt device is shown. In particular, the I-V characteristic here presented can be divided in three regions: (1.) diode-like behaviour regulated by the Ag/ZnO interface, (2.) electronic current saturation regime and (3.) sharp current transition due to the formation of a conductive path. Note that a CC of 10 μA was externally imposed to the device in order to avoid an irreversible breakdown.

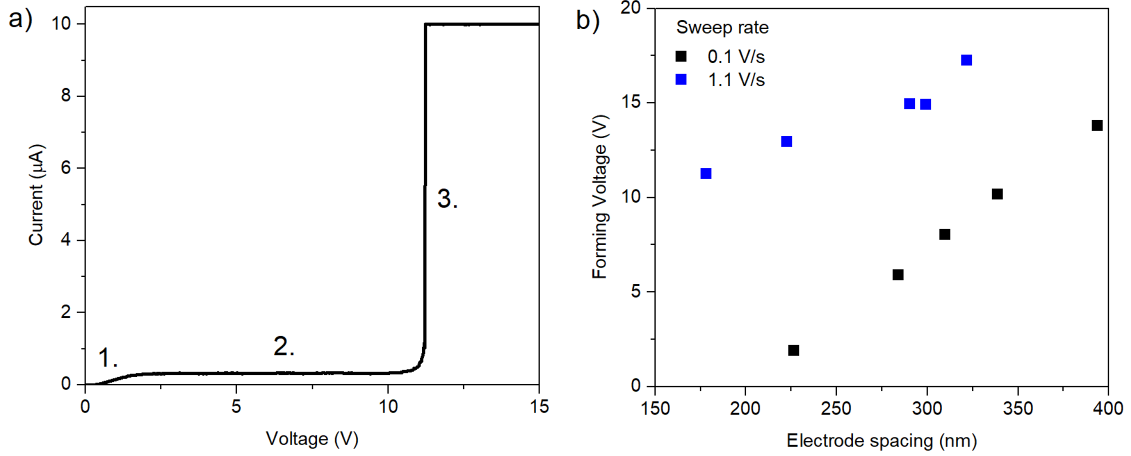

Figure 7.3: Electroforming of ZnO NW memristors. a) Forming curve of an Ag/ZnO NW/Pt device characterized by a (1.) diode-like behaviour, (2.) a saturation regime and (3.) a sharp current transition (electroforming). Current compliance (10 μA) was used for avoiding full breakdown of the device. b) Forming voltage dependence on the electrode spacing for different voltage sweep rates. In all measurements, forming was induced by applying a positive voltage bias to the electrochemically active Ag electrode. Adapted from [218].

The forming process was observed to depend both on the electrode spacing as well as on the voltage sweep rate, as presented in Figure 7.3 b. These observations revealed that this process is dependent on both electric field and time. More importantly, it is experimentally proved that electroforming process can be induced for applied voltages lower than 5 V by properly adjusting the device design and operating conditions. This is an important aspect since high forming voltages can affect reliability and the device integration in low-voltage electronics. It is necessary to point out that electroforming was not possible without using an electrochemical active electrode. Indeed, as reported in Figure 7.4 a, no current jumps attributable to electroforming and no hysteretic loops in the I-V characteristics were observed in NWs contacted by means of Pt symmetric electrodes. Moreover, the influence of the substrate during resistive switching can be safely excluded, since Ag-Pt asymmetric devices without NWs cannot be formed even for high applied voltages and slow sweep rates, as reported in Figure 7.4 b. Indeed, as observed by Yang et al. [226], the ionic migration of Ag^+ ions is suppressed on the surface of thermal SiO_2 substrates with dense structure. The resistance of the SiO_2 substrate was measured to be $> 10^{11}\Omega$. It is worth noticing that the current self-limitation regulated by the inversely polarized junction plays a crucial role during the electroforming process, preventing NW melting due to Joule overheating. Figure 7.5 a reported the electrical characteristic of an hard breakdown in a single NW contacted by Pt electrodes.

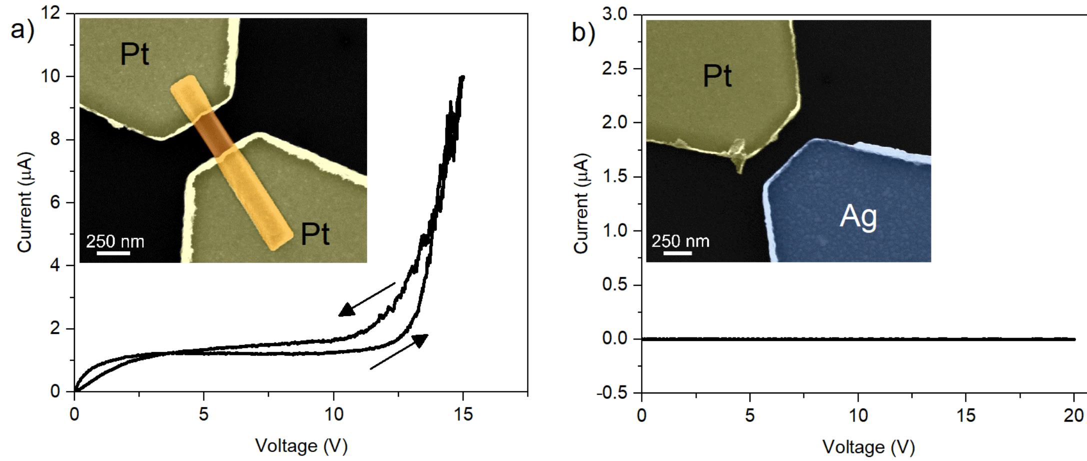

Figure 7.4: Effect of the metal electrode and the substrate during the electroforming process. a) Tentative electroforming of ZnO NWs contacted by symmetric Pt electrodes. b) Tentative electroforming of an Ag-Pt asymmetric device without the presence of the NW in order to investigate the role of the SiO_2 substrate. Insets show the SEM images in flase colors of the devices, where the Pt electrodes are colored in yellow while Ag electrodes in blue. Adapted from [218].

As can be observed, after the saturation current regime, an increase of current can be observed for $V > 15\,V$. This is due to the breakdown current of the reversibly polarized Pt/ZnO junction. Interestingly, a drop of current was observed when the critical value of $\sim 25\,\mu A$ was reached. In this case, the high current density flowing into the device caused NW melting, leading to a permanent device failure with the creation of an open circuit. A SEM image of a NW memristor after breakdown due to Joule overheating is reported in Figure 7.5 b, where it is possible to clearly observe NW melting in the electrode spacing. Note that melting was reported to be one of the main causes of failure of NW-based devices where high current densities are unavoidable as a consequence of the nanosized cross-section of the nanostructures [48, 59, 66, 73]. In this work, it is proposed that the current flowing in the NW device can be self-limited in the resistive switching operational voltage window by properly engineering the metal-semiconductor interfaces, as previously discussed in section 7.3. In this fashion, the current limitation allows not only to apply to the device the voltage required for forming without observing NW melting but also to regulate the HRS of the device. The regulation of the electronic current provides an adjustment of the ratio between ionic and electronic partial conductivities, i.e. the ionic transference number, an important parameter for electrochemical reactions and charge transport. In these terms, current self-limitation represented a key element for obtaining reliable devices with multiple functionalities.

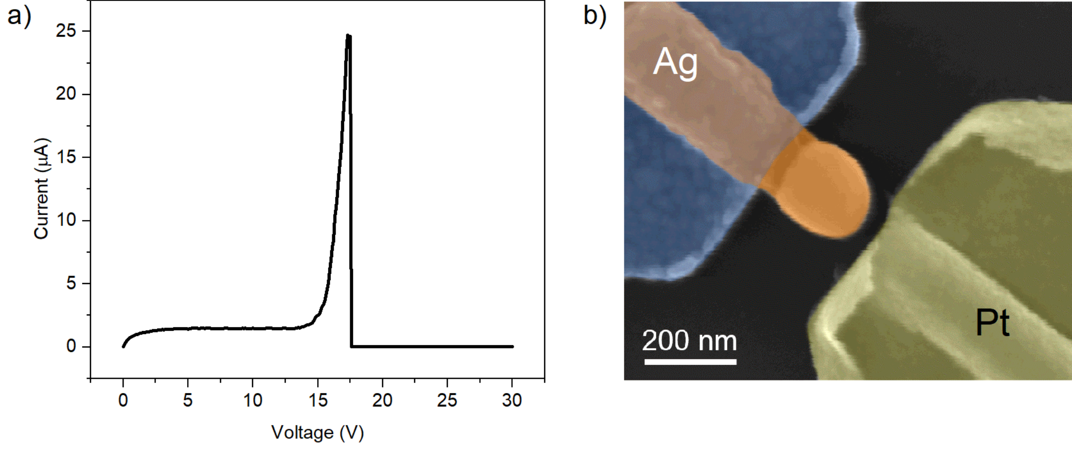

Figure 7.5: Breakdown of ZnO NWs due to Joule overheating. a) Electrical characterisitic of an hard breakdown of a ZnO NW contacted by means of Pt electrodes. After the current saturation regime (current self-limitation), the device exhibited an increase of current due to the breakdown current of the inversely polarized junction. An abrupt decrease of current occurs in correspondence of about $\sim 25\,\mu$A due to hard break down of the device. b) SEM image of a NW memristor after breakdown. Adapted from [218].

7.5 Physical mechanism of switching

The resistive switching mechanism was investigated through a combined approach which comprised electrical, structural and chemical characterization techniques. In order to investigate electrochemical properties of the single NW memristive cells, cyclic voltammetry (CV) measurements were performed prior to induce the formation of the conductive path through electroforming. Results are presented in Figure 7.6 a. At a voltage sweep rate of 1.5 mV/s, a peak can be clearly resolved at about 0.1 V. Despite the absence of a reference electrode in two-terminal memristive devices, this redox peak can be attributed to the anodic dissolution of Ag, according to the electrochemical reaction:

$$\mathrm{Ag} \rightarrow \mathrm{Ag}^{+} + \mathrm{e}^{-} \tag{7.3}$$

Despite the different device configuration and solid electrolyte materials, these measurements are in good accordance with previously reported oxidation peaks for Ag dissolution in thin films. For example, the Ag oxidation peak in Ag/Ta_2O_5/Pt thin film devices was observed at about 0.12 V [227]. These evidences demonstrate the feasibility of CV measurements on a single NW-based memristive cell where the NW acts as a solid electrolyte at the nanoscale. After switching events, direct investigation of the conductive path morphology can be performed by means of

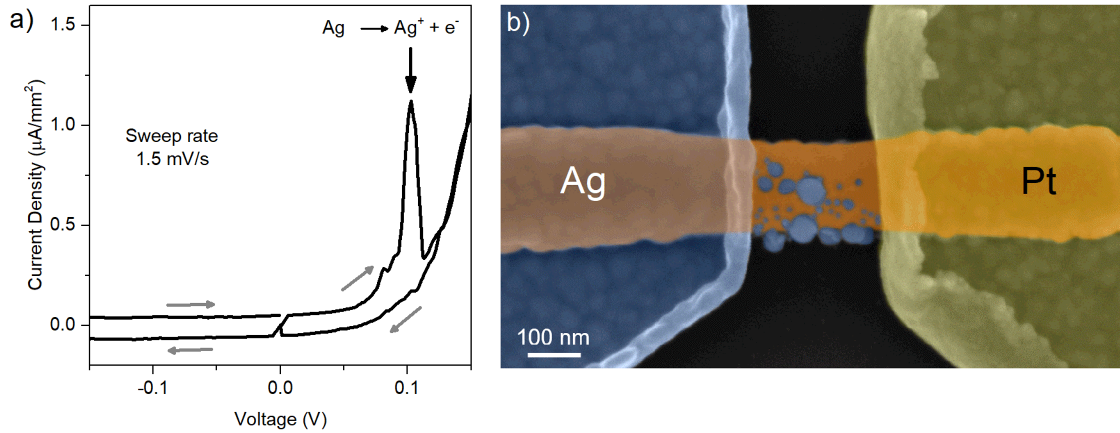

Figure 7.6: Cyclic voltammetry and SEM analyses of resistive switching mechanism. a) CV measurements performed on a single NW memristive device before the forming process, exhibiting a peak attributable to the Ag oxidation process. b) Morphological analysis of the device after resistive switching by means of SEM. The SEM image is in false colors, where the Pt and Ag electrodes are colored in yellow and blue, respectively, while the ZnO NW is in orange. Adapted from [218].

SEM. As can be observed from Figure 7.6 b, the conductive path is composed of Ag nanoclusters along the NW. A more detailed investigation of the switching mechanism was performed by means of TEM analyses on a NW cross-section in between the electrodes (perpendicularly from the filament growth direction). As reported by TEM analyses and EDX mapping in Figure 7.7 a-c, a large number of Ag nanoclusters can be observed only on the crystalline surface of the ZnO NW. This is due to the higher mobility of Ag^+ ions on the surface compared to the bulk and to the absence of spatial constrictions, evidencing a correlation in between structural properties of the solid electrolyte material and its ionic transport properties. Diameter distribution of Ag nanoclusters acquired from TEM analyses is reported in Figure 7.7 d, where the mean nanocluster size was (4.5 ± 1.4) nm. However, a larger cluster with diameter of ∼28 nm can be observed on the NW surface and is likely to play the main role for electronic conduction. HRTEM analyses across the Ag nanocluster/NW interface revealed that the Ag nanoclusters are characterized by a face-centered cubic (FCC) crystal structure while the wurtzite crystal structure of ZnO remained preserved after switching (Figure 7.7 e). Instead, HRTEM analysis performed on the NW core further excluded the presence of Ag atoms in the bulk wurtzite crystal structure of the NW, as presented in Figure 7.7 f. In these terms, a single crystalline NW can be considered an ECM model system. Differently from amorphous materials usually employed for the realization of memristive devices, in single crystalline materials it is possible to avoid stochastic variability of physico-chemical properties typical of disorder matter. The planar device

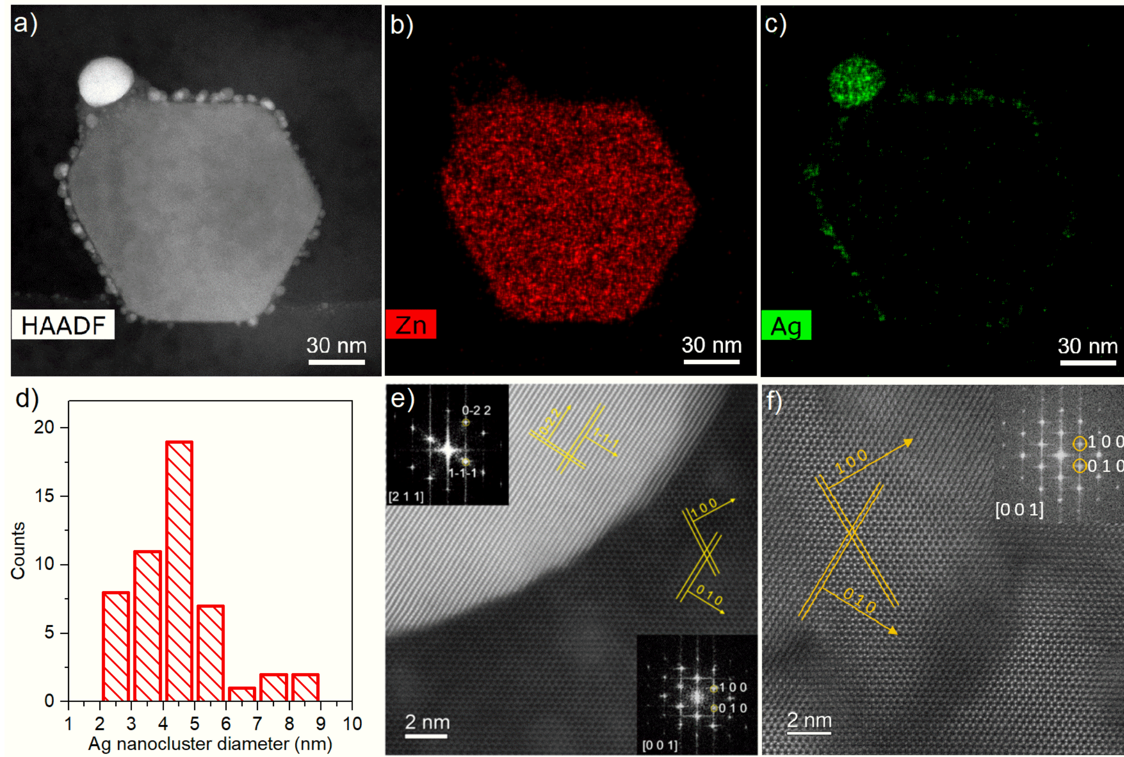

Figure 7.7: TEM and EDX analyses of resistive switching mechanism. a) TEM analysis of a NW cross section obtained by cutting the NW in the electrode spacing after resistive switching and compositional EDX maps of b) Zn and c) Ag. d) Ag nanocluster size distribution acquired from TEM analyses. e) HRTEM with corresponding FFT patterns of the ZnO NW/Ag nanocluster interface, revealing their crystal structure. f) HRTEM with corresponding FFT pattern of the NW core after resistive switching, revealing no traces of Ag atoms in the bulk structure. Yellow arrows indicate the crystallographic orientations. Adapted from [218].

structure of single NW memristors allows the evaluation of the electronic conduction mechanism through field-effect measurements. In previous section (section 6.5), field effect measurements in NW-FET configuration were performed on single ZnO NWs symmetrically contacted by Pt electrodes, revealing the n-type nature of the intrinsic ZnO doping. By considering single ZnO NW memristive devices, transconductance measurements can be performed in LRS in order to elucidate the conduction mechansism in the formed conductive path. Measurements reported in Figure 7.8 evidenced no dependence of the drain-source current on the applied gate bias voltage, revealing a metallic-like electronic conduction mechanism when the conductive Ag path across electrodes is established.

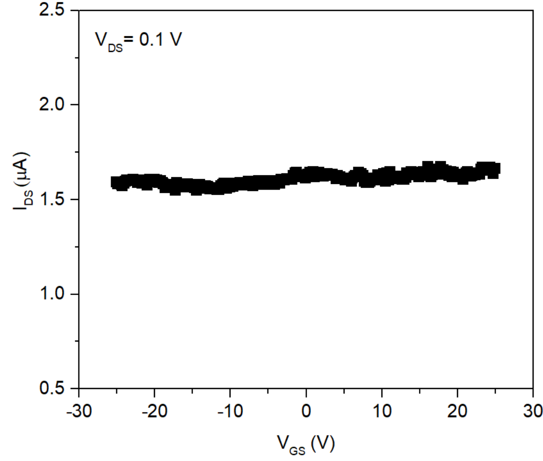

Figure 7.8: Transconducatance characteristic of the Ag/ZnO NW/Pt device in NW-FET configuration after the formation of the Ag conductive path (in LRS). During voltage sweep of the gate bias, the drain-source voltage (V_{DS}) was fixed at 0.1 V. Adapted from [218].

7.6 Multilevel non-volatile memory

After the forming process, memristive behaviour of a single ZnO NW was investigated by means of DC voltage sweeps, as presented in Figure 7.9 a. Single ZnO NW memristors exhibited bipolar resistive switching. Indeed, by applying a positive voltage sweep to the Ag electrode, a current jump corresponding to a SET process was observed, turning the device to a lower resistance state. Note that a CC current was applied to the device in order to prevent Joule overheating. Insted, a voltage sweep in the opposite direction is responsible for a RESET process where the device switches back to the HRS. In particular, it was observed that the LRS value can be controlled through the modulation of the imposed CC, as presented in Figure 7.9 b. An increasing of the CC resulted in a decrease of the LRS, revealing a reinforcement of the Ag conductive filament by increasing CC as previously discussed by La Barbera et al. [22]. In this way, the single NW memristor can be programmed as a multilevel memory through the modulation of the LRS over more than one order of magnitude, enabling multi-bit capability as well as synaptic weight storage in neural networks. Results from an endurance test performed by means of full-sweep cycles and by imposing a CC of 20 μA are presented in Figure 7.9 c, revealing high stability of the device with low dispersion of both HRS and LRS. Instead, the resistance state stability over time was evaluated through retention measurements for over 10^3s (Figure 7.9 d), revealing no degradation of both LRS and HRS.

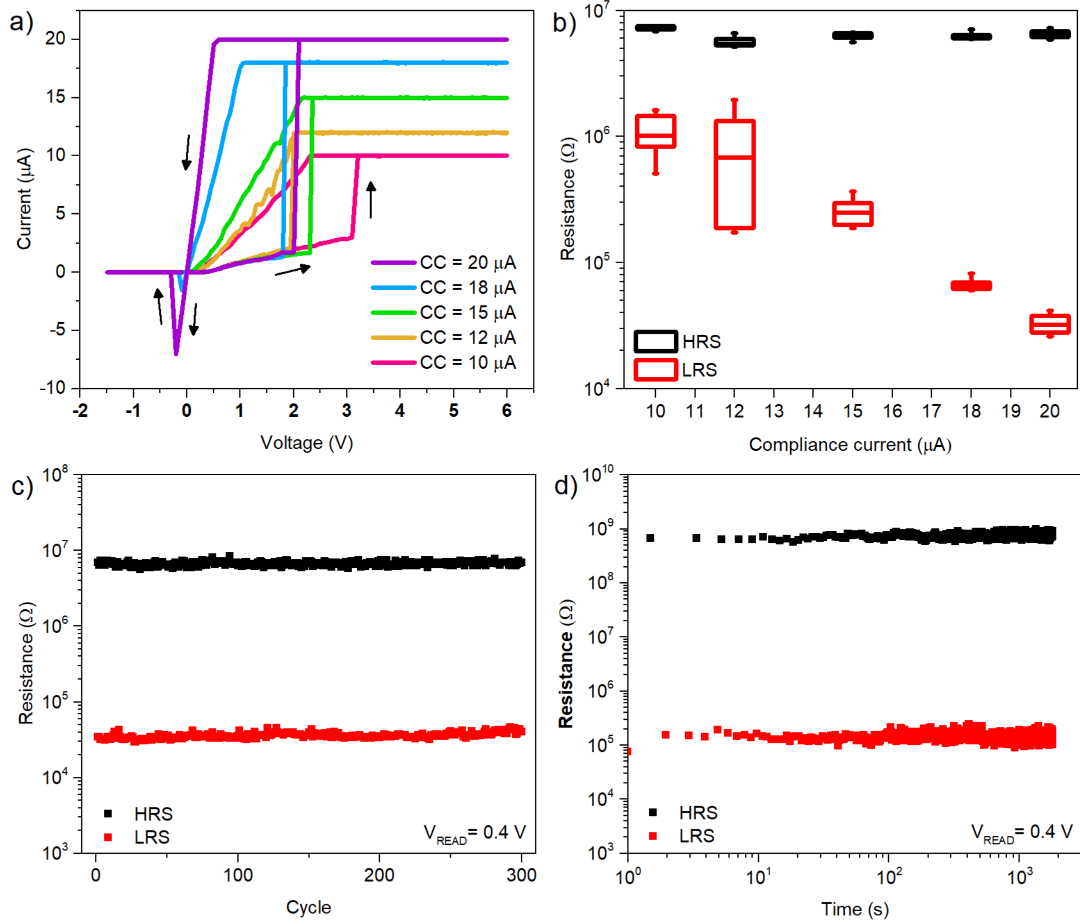

Figure 7.9: Multilevel memory capability of a single ZnO NW memristor. a) *I*-*V* curves of the NW-based device stimulated by DC voltage sweeps by externally imposing different values of CC. Bipolar resistive switching behaviour was observed, with the LRS that depends on the applied CC. b) HRS and LRS of the device (read at 0.4 V) as a function of the imposed CC exhibiting multilevel capability. Box plots are obtained from 15 consecutive cycles for each CC value on the same NW device. Midlines represent the median value, boxes the 25^{th} and 75^{th} percentiles while whiskers the 10^{th} and 90^{th} percentiles. c) Endurance and d) retention properties of the device. Adapted from [218].

7.7 Threshold switching and selector capability

Our observations revealed that, depending on the input voltage stimuli, the single NW memristor can exhibit both non-volatile and volatile resistive switching, as described in the following. By considering voltage pulses as input stimuli, long

programming pulses (800 ms, 6 V) resulted in a non-volatile bipolar resistive switching as presented in Figure 7.10 a. In this case, the ON state was preserved after the SET programming pulse and a RESET pulse (180 ms, -1.5 V) was necessary to restore the HRS of the device. Instead, short programming pulses (10 ms) resulted in volatile resistive switching behaviour, as presented in Figure 7.10 b. Here, the programming pulse induced a SET of the device while, after the pulse stimuli, the device spontanously relaxed back to the ground state (HRS) without needing a RESET process.

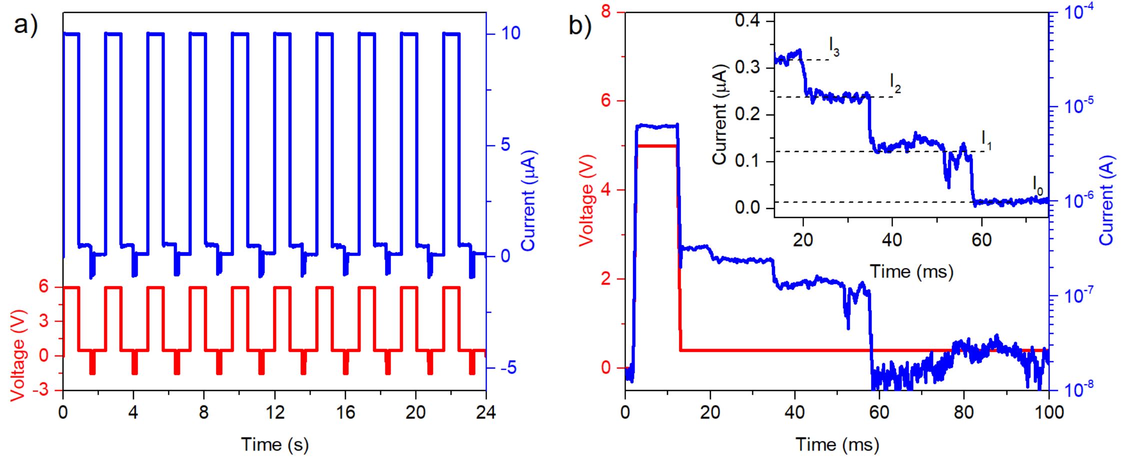

Figure 7.10: Non-volatile and volatile switching. a) Long write pulses (880 ms, 6 V) resulted in non-volatile resistive switching behaviour where a RESET pulse (180 ms, -1.5 V) was necessary for erasing the ON state. A reading voltage of 0.5 V was applied for reading the device resistance state. b) Volatile resistive switching behaviour was observed after short programming pulses (10 ms, 5 V). The device spontaneously relaxed back to the ground (HRS) state (current relaxation was measured at a reading voltage of 0.4 V). The inset shows a detail of the current relaxation process with discrete conductance steps. Adapted from [218].

The device relaxation is linked to the spontaneous dissolution of the Ag conductive path along the NW to form Ag nanoclusters. This process is driven by nanobattery effects including minimization of interfacial energy (Gibbs-Thomson effect) and electromotive forces arising from the diffusion potential [24, 27, 228, 229]. The progressive disconnection of the conductive path resulted in a stepwise relaxation of the device conductivity characterized by discrete conductance level (the detail of the conductance relaxation is presented as inset of Figure 7.10 b). Resistance values during discrete conductance levels were observed to be higher than the quantum point contact resistance, suggesting the occurrence of tunneling effects. As a consequence of the spontaneous relaxation, short programming pulses resulted in threshold switching behaviour of the device (Figure 7.11 a). In this

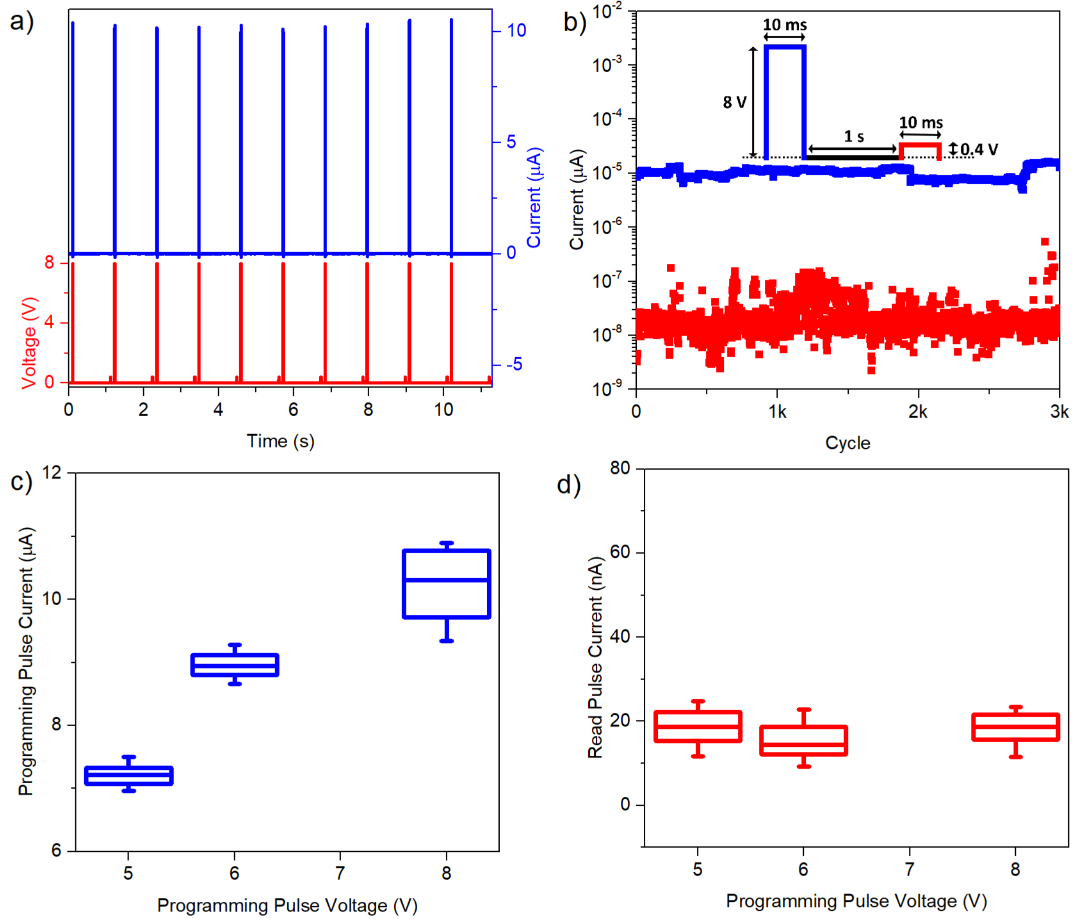

Figure 7.11: Threshold switching and selector capabilities of single ZnO NW memristors. a) Threshold switching behaviour of the device observed by applying short programming pulses (10 ms, 8 V). After 1 s from the programming pulse, a reading pulse (10 ms, 0.4 V) revealed that the device has spontaneously relaxed back to the ground state. b) Endurance of the NW memristor operating as a selector device. Blue data are sampled during the programming pulse while red data are sampled during the read pulse. The applied pulse shape is schematized as inset. b) Current response of the device during programming pulses with different amplitudes and d) current response of the device during reading pulses (0.4 V, after 1 s from the programming pulse) as a function of the programming pulse amplitude. The time length of both programming and reading pulses were 10 ms. Box plots were realized by considering 100 consecutive threshold switching cycles. Midlines represent median values, box the 25^{th} and 75^{th} percentiles while whiskers the 10^{th} and 90^{th} percentiles. Adapted from [218].

case, the device switched to the LRS during the programming pulse (10 ms, 8 V) while a following reading pulse revealed that the device spontaneously relaxed to the HRS after 1 s. Endurance test presented in Figure 7.11 b revealed high repeatability of threshold switching over cycling with high current-non linearity. These characteristics demostrate the realization of single NW selector devices. Note that the current output during the programming pulse depends on the pulse amplitude (Figure 7.11 c), while no dependence of current on the programming pulse amplitude was observed during read pulses since in all cases the device relaxed to the HRS ground state (Figure 7.11 d).

7.8 Artificial synapse

Integration of memristive devices in neuromorphic neural networks requires the implementation of train pulses as input stimuli. Our observations revealed that the device response to pulse trains depends not only on the pulse amplitude and length but also on the waiting time in between pulses (pulse frequency). The device response to an input stimuli of train of voltage pulses with legth of 22 ms and different voltage amplitudes is presented in Figure 7.12 a. As can be observed, no changes in the device conductivity were observed for low voltage pulse amplitudes (≤ 2 V). Instead, current jumps corresponding to SET processes can be observed after a certain amout of applied pulses (incubation time) by increasing the amplitude of the input stimuli. Note that an increasing of the pulse voltage amplitude resulted in a shortening of the incubation time. By further increasing the pulse amplitude (≥ 3.2 V), the device switched to the LRS directly during the first applied pulse. The voltage pulse amplitude necessary for inducing a SET as well as the incubation time can be modulated by changing the pulse length, as can be observed in Figure 7.12 b where the device was stimulated by means of 10 times longer voltage pulses (pulse length of 220 ms). In this case, while no changes in the device conductivity were observed by stimulating the device with a pulse train characterized by voltage amplitude of 1 V, resistive switching was already observed by stimulating the device at 1.5 V. Further increasing the voltage amplitude to 2 V resulted in a shortening of the incubation time, in analogy to results reported in Figure 7.12 a previously discussed. Results presented in Figure 7.12 revealed abrupt current jumps during the change of the device conductance. However, by properly adjusting the pulse parameters such as amplitude, length and time in between pulses it is possible to induce a gradual change in the device conductance. Under these conditions, the Ag^{+} dynamics on the NW crystalline surface can be exploited for the emulation of Ca^{2+} dynamics that regulate synaptic plasticity of biological synapses. It is well recognized that chemical synapses play a fundamental role in determining brain functions. Indeed, synaptic plasticity regulates processes such as memory and learning by controlling the change in the strength of synaptic connections in

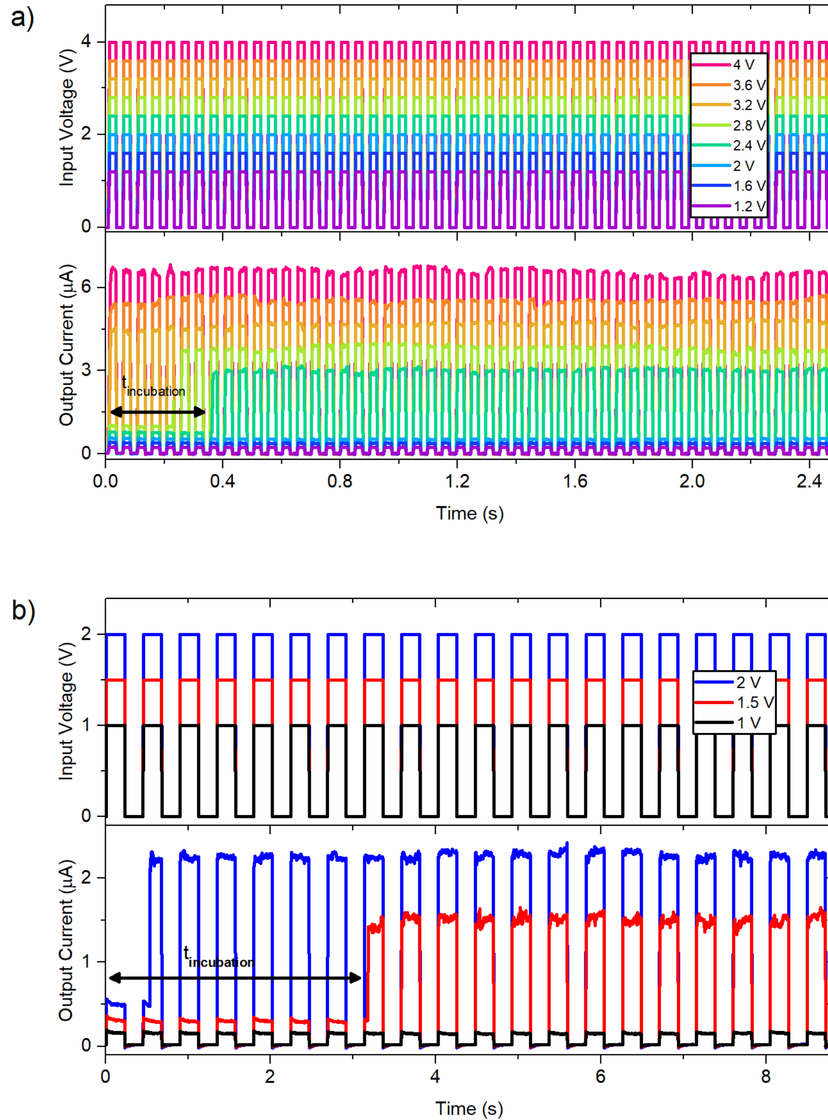

Figure 7.12: Single ZnO NW memristor response to train of voltage pulses. a) Higher panel shows the input pulse stimuli composed of 50 voltage pulses with length of 22 ms, spaced by 22 ms and with voltage amplitude ranging from 1.2 V up to 4 V. The lower panel shows the current response of the device to the different pulse trains. While for low voltages (<2.4 V) no switching events were observed, jumps of current were observed after a certain amout of pulses (i.e. incubation time) by increasing the voltage amplitude. For amplitudes ≥ 3.2 V, the device jumped in the ON state during the first pulse. b) Device current response (lower panel) to voltage pulse stimuli (higher panel) characterized by a pulse length of 220 ms, spaced by 220 ms and with voltage amplitude of 1, 1.5 and 2 V. Adapted from [218].

between pre and post neurons [28]. More in details, action potentials (electrical stimuli) that reach the pre-synaptic terminals of the synapse resulted in an opening of voltage-dependent Ca^{2+} channels (VDCCs) [230]. Then, neurotransmitters are released in the synaptic cleaf as a consequence of the influx of Ca^{2+} ions in the neuron terminal, resulting in an enhanced synaptic transmission [230]. Afterwards, the extrusion of Ca^{2+} ions out of the cell occurs through plasma membrane transport proteins such as Ca^{2+} ATPase (PMCA) and Na^{+}/Ca^{2+} exchanger (NCX) [231]. In analogy to biological synapses, a gradual increase of the NW conductivity due to the Ag^{+} dynamics regulated by electrical pulse stimuli can emulate the Ca^{2+} influx process, while Ca^{2+} extrusion can be imitated by the spontaneous dissolution of the Ag conductive path. The gradual change in conductivity in the single NW memristor can be observed in Figure 7.13 a, under device stimulation with a 100 ms pulse voltage of 3 V. The progressive rearrangement in time of the Ag adatoms on the NW surface resulted in a progressive reinforcement of the conductive path in between electrodes, resulting in a quantized change of NW conductivity that emulates Ca^{2+} influx. Note that the gradual change in conductivity here observed is a consequence of the slowdown of the Ag^{+} kinetics due to lower applied electric fields, making possible to temporally resolve multiple discrete conductance steps. Instead, it is not possible to resolve a gradual change in conductance if higher voltage amplitudes are applied because of faster kinetics determine an abrupt and immediate jump of device conductivity [232], as for example previously reported in Figure 7.10. After the voltage pulse stimulus, the device spontaneously relaxed back to the ground state as a consequence of the resistance state volatility. Note that the relaxation process can be here interpolated by means of an exponential decay, thus emulating the previously discussed Ca^{2+} extrusion process. Interestingly, the decay time constant of relaxation obtained from the best fit of data ($\sim$23 ms) is of the same order of biological synapses [28]. By exploiting these dynamics, it was possible to emulate typical features of short-term plasticity (STP) in a single NW device. Emulation of paired pulse facilitation (PPF) can be observed in Figure 7.13 b, where a train of short pulses (2 ms, 2.5 V) resulted in a gradual increase of device conductance. Since the gradual change of device conductivity is based on the interplay and competition in between filament formation and dissolution, the percentage of conductance change Δw (calculated as $\Delta w = [I(n) - I(1)]/I(1)$, where I(n) represent the current flowing into the device during the n-th pulse) can be modulated by changing the time between pulses. Indeed, as reported in Figure 7.13 c, higher waiting time in between pulses resulted in lower percentage of conductance change (weight). Thus, the frequency of voltage pulses play a key role in determining the variation of the device conductivity. Indeed, as reported in Figure 7.13 d, device stimulation by means of low frequency voltage pulses did not induce a variation of the device conductivity (1.) while PPF was observed by increasing the voltage pulse frequency (2.). Note that the device relaxed back to the ground state when subsequent low frequency pulses are applied (3.). Analogies in between

biological and NW-based artificial synapses are depicted in Figure 7.14.

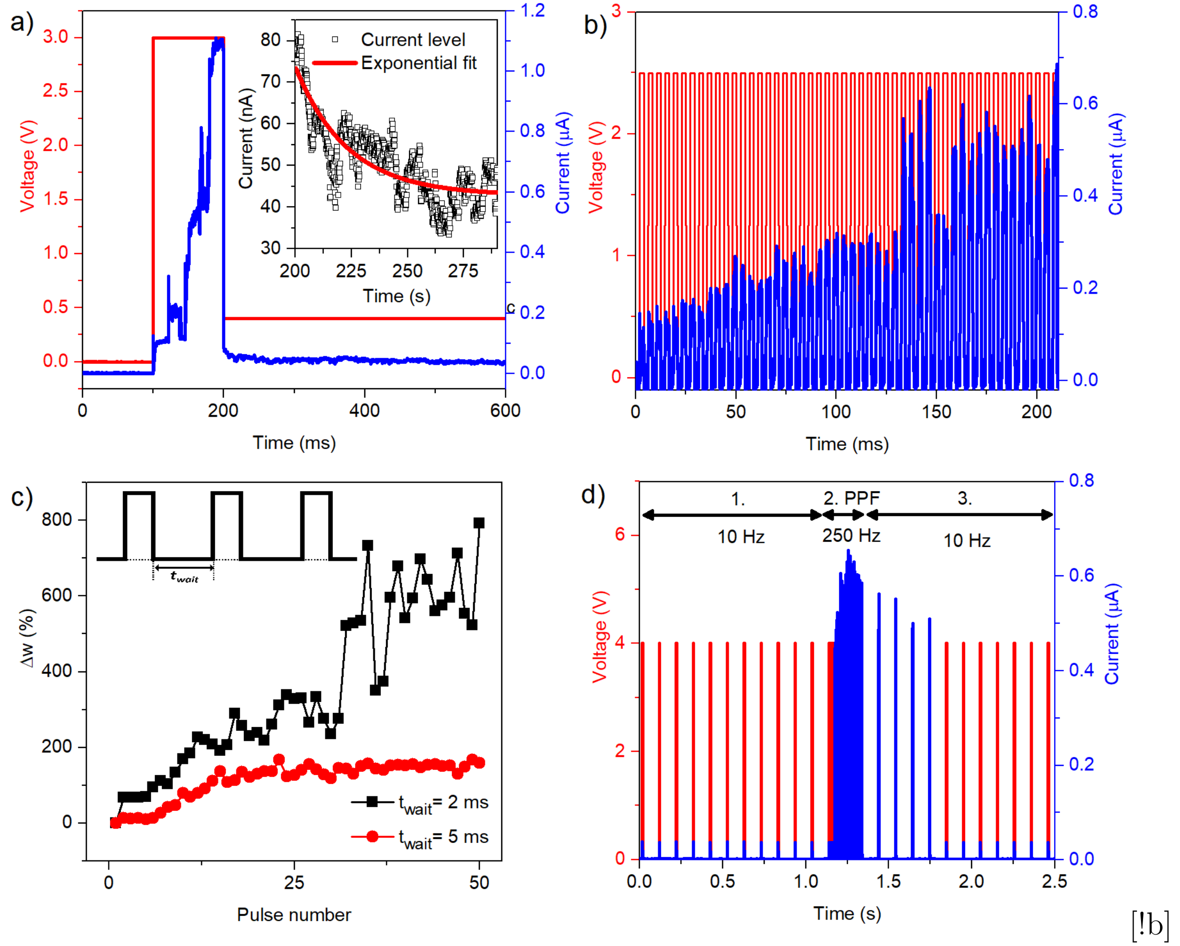

[!b]

Figure 7.13: Neuromorphic functionalities of the single NW memristor. a) Gradual increase of conductivity under low voltage pulse stimulus (3 V, 100 ms). The device spontaneously relaxed back to the ground state after the voltage stimulus, as observed by applying a subsequent reading voltage of 0.4 V. A detail of the conductance relaxation process interpolated with an exponential decay function is presented as inset. b) Experimental demonstration of PPF by applying a train of short voltage pulses (2 ms pulses, 2 ms of waiting time, 2.5 V). c) Conductance change (Δw) as a function of the pulse number, measured for different waiting times in between pulses. d) Dependence of the device response on the voltage pulse frequency. Low frequency pulses (2 ms, 4 V, 10 Hz) are not sufficient for inducing PPF (1.); PPF is observed by increasing the pulse frequency (250 Hz, 50 pulses) while the device relaxed back to the ground state when frequency is again lowered to 10 Hz. Adapted from [218].

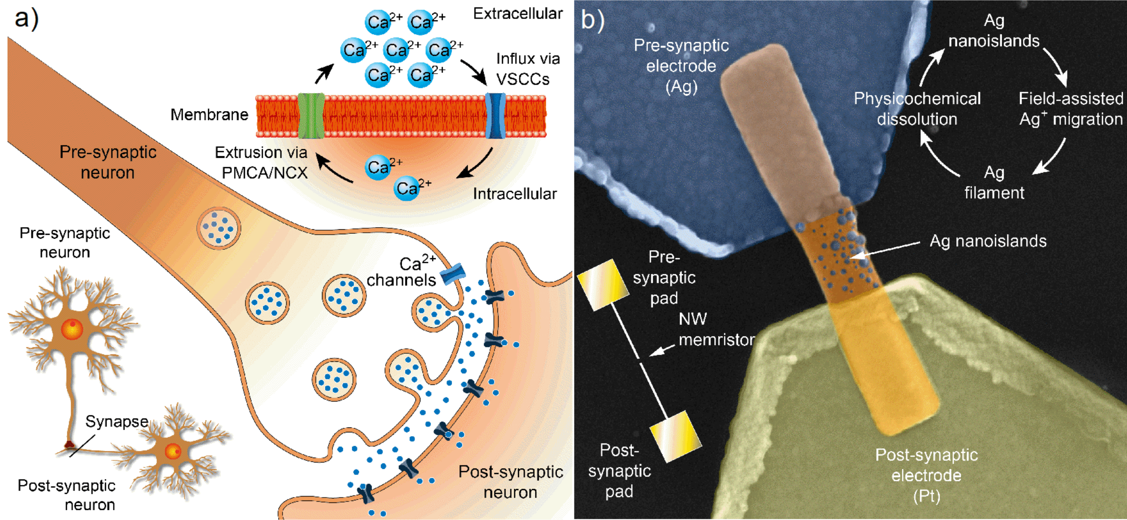

Figure 7.14: Similarities between a) Ca^{2+} dynamics in biological synapses and b) Ag^{+} dynamics in single NW memristors. The field-assisted migration of Ag^{+} ions in artificial synapses can be exploited for the emulation of the Ca^{2+} influx process of biological synapses, while Ca^{2+} extrusion process can be imitated by the spontaneous physico-chemical dissolution of the Ag conductive path. Adapted from [218].

7.9 Electrochemical properties of electrodes

As discussed in previous sections, the electrochemical properties of the metal eletrodes determine and regulate the memristive functionalities of the NW-based devices. For this reason, the choice of the metal electrodes (both active and inert electrodes) is a crucial aspect, as discussed in the following. In our work, Pt was exploited as counter electrode. First of all, this ensures no migration of metal ions from the counter electrode during electrical measurements. Indeed, as theoretically analysed by Raffone et al. [233], migration of Pt adatoms on the ZnO NW surface is suppressed in practice as a consequence of the high energy required for Pt atom extraction. In addition, the use of Pt excludes the formation of an oxide interlayer at the metal-semiconductor interface. As for example observed in case of using Ti as electrode, a TiO_2 interlayer is formed at the Ti/ZnO interface as revealed by Chiang et al. [51] by means of TEM investigations. Thus, in several works concerning single ZnO NWs [42, 51, 56, 234], the switching mechanism can be explained in terms of oxygen ions migration at the TiO_2/ZnO interface (VCM mechanism), as similarly observed by Huang et al. [79] in ZnO/TiO_2 multi-segmented NWs. This means that the switching mechanism can be located and buried at the metal/ZnO interface and not along the NW in case of formation of a metal-oxide interlayer.

In our case, the choice of Pt as counter electrode can safely exclude this scenario due to the low tendency of Pt to form oxide forms. Instead, the choice of Ag as electrochemically active electrode is driven by the lower electric field required for dissolution compared to other metals, as reported by Yang et al. [235] by investigating the dynamics of nanoscale inclusions in dielectrics. This means that Ag dissolution and migration of ions can be induced by means of lower electric fields compared to other metals, facilitating the formation of a metallic conductive path on the NW surface. As an alternative, Cu/ZnO NW/Pt devices were realized in order to investigate properties of the Cu electrochemically active electrodes. As can be observed in Figure 7.15 a, Cu/ZnO NW/Pt devices exhibited similar behaviour of Ag/ZnO NW/Pt devices during the electroforming process. For low applied voltages, a single diode-like characteristic was observed (1.). As a case study, junction parameters such as Schottky barrier height, ideality factor and series resistances were calculated through different methods from I-V-T measurements, as reported in appendix C. By increasing the applied voltage bias, current saturation regime was observed (2.) followed by a current jump due to the formation of a conductive path along the NW (3.). As reported in the SEM image of Figure 7.15 b, Cu nanoclusters were observed on the ZnO NW surface after the swithing events. This reveals that migration of Cu adatoms on the ZnO NW surface is responsible for resistive switching in these devices, in analogy with the previously analyzed mechanism in Ag/ZnO NW/Pt devices. In case of using Cu instead of Ag as the electrochemically active electrode, the anodic dissolution occurs accordingly to the electrochemical reactions:

$$\mathrm{Cu} \rightarrow \mathrm{Cu}^{+} + \mathrm{e}^{-} \tag{7.4}$$

or

$$\mathrm{Cu} \rightarrow \mathrm{Cu}^{2+} + 2\mathrm{e}^{-} \tag{7.5}$$

After migration of Cu ions with consequent formation of a conductive path through electroforming, bipolar resistive switching was observed, as reported in Figure 7.15 c. However, devices exhibited poor endurance since breakdown occurred after very few I-V cycles. Moreover, it is necessary to underline that electroforming and resistive switching cycles presented in Figure 7.15 a and c were obtained in vacuum. Indeed, no forming of Cu/ZnO NW/Pt devices were observed in air, differently from the case of Ag/ZnO NW/Pt devices. In order to understand the peculiar behaviour of Cu as active electrode, electrochemical properties of this metal have to be considered. First of all, Cu requires higher dissolution energies compared to Ag as discussed by Yang et al. [235], and thus higher electric fields are required for the formation of a conductive path. As a consequence of the higher energy required for dissolution, a smaller amount of Cu respect to Ag was observed on the ZnO NW surface after switching (for comparison, refer to Figure 7.15 b for Cu and 7.6 b for Ag). The lower amount of metal ions on the ZnO surface is responsible for

the formation of a less stable conductive path, resulting in lower endurance and stability of the device. Moreover, by considering the Ellingham diagram, it can be noted that Cu is more prone to form oxide forms rather than Ag. This can explain why in atmospheric conditions it is possible to observe stable resistive switching behaviour of Ag/ZnO NW/Pt devices while memristive behaviour is suppressed in Cu/ZnO NW/Pt devices where Cu adatoms possess high tendency to oxidize. The influence of surroundings on resistive switching mechanism underlying Ag/ZnO NW/Pt devices is discussed in details in chapter 8.

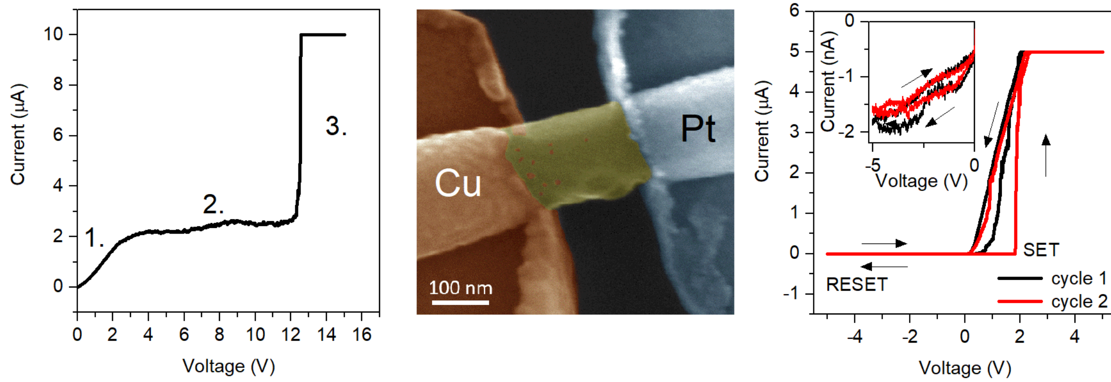

Figure 7.15: Resistive switching of ZnO NWs asymmetrically contacted by means of Cu and Pt electrodes. a) Electroforming of the device exhibiting a single diode-like characteristic (1.), a saturation current regime (2.) and a current jump due to the formation of a conductive path in between electrodes (3.). b) SEM image (in false colors) of the Cu (orange)/ZnO NW (yellow)/ Pt (blue) device after resistive switching, evidencing Cu nanoclusters on the ZnO NW surface. c) Bipolar resistive switching of the device after electroforming. A detail of the negative branch of the voltage sweep is shown as inset. Adapted from [219].

Chapter 8

Effect of moisture on ZnO NW memristive devices

8.1 Introduction

The comprehension of the environment influence on the memristive device performances is a key element for the realization of reliable resistive switching devices. In particular, moisture was reported to be one of the sources of device variability affecting not only the ionic diffusion in the metal-oxide matrix but also electrochemical reactions at metal/metal-oxide interfaces [236–239]. However, all studies concerning the influence of moisture on resistive switching mechanism were performed by considering amorphous or polycrystalline thin film memristive devices where the incorporation of water molecules is affected by the stacked device structure as well as on material density and porosity. In this chapter, the effect of moisture on the ECM physical mechanism of switching is investigated by considering the previously characterized memristor model system based on single crystalline ZnO NWs. In these devices, the investigation of the role of moisture on resistive switching performances is facilitated by the planar structure of devices that allows direct exposure of the conductive path to the surrounding environment. In particular, results showed that moisture affects both electronic and ionic transport properties of the single crystalline ZnO NWs, modulating electronic conductivity as well as switching kinetics.

8.2 Effect of moisture on ZnO electronic conduction mechanism

As previously discussed in section 6.3, adsorbed species on the NW surface can strongly influence the electronic conductivity of ZnO NWs. In this section, the influence of moisture on electronic properties of ZnO NWs is discussed in details. In

case of single crystalline ZnO NWs, H_2O can be chemically adsorbed according to the reaction 4.2 previously discussed in section 4.2, where oxygen vacancies act as active sites for dissociative water chemisorption. This leads to the creation of OH groups on the NW surface. In order to investigate in more details the adsorption of water molecules in the ZnO crystal structure, depth profile SIMS measurements were performed on a ZnO crystal (Crystek P27513) after exposure to a D_2O environment for 1 h. As reported in Figure 8.1 a, the D signal in SIMS measurements quickly decreased as a function of the sputtering time (i.e depth in the crystal), revealing that D species cannot be incorporated in the ZnO bulk structure but are likely to be adsorbed only on the crystalline surface. As a consequence, the surface adsorption of water can be schematized as depicted in Figure 8.1 b. It is important to notice that, besides the first hydroxide layer due to water chemisorption, additional layers of physisorbed water can be present.

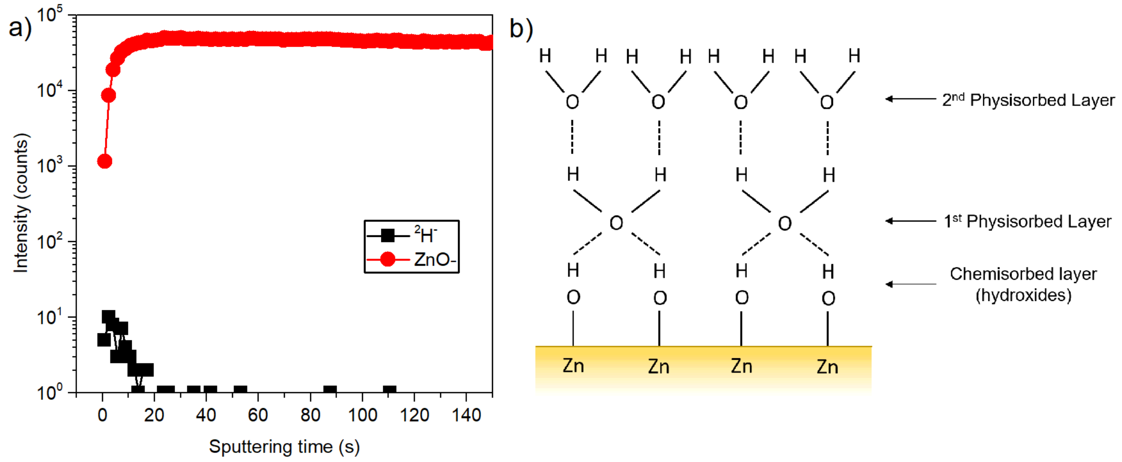

Figure 8.1: Analysis of the adsorption of water vapour molecules on ZnO. a) SIMS depth profile of a single crystal ZnO after exposure to deuterium atmosphere and b) multilayer structure of chemisorbed and physisorbed water on the crystalline ZnO surface.

In order to understand the specific effect of moisture on the electronic transport properties of ZnO NWs, *I*-*V* characteristics of symmetric Pt/ZnO NW/Pt devices were acquired in a controlled atmosphere by progressively increasing the RH content in a N_2 environment (details of the measurements setup can be found in section 2.4). Results of these measurements are reported in Figure 8.2 a, where the resistance of the NW was measured as a function of the moisture content after perfoming an annealing at 200°C (black points) and without annealing (blue points). In both cases, it was observed that the NW resistance increased by increasing the moisture content. Higher resistances were observed in the NW that was not previously annealed, reflecting a higher amount of adsorbed species acting as charge traps

as the initial condition, according to previous results reported in section 6.3. In single crystalline ZnO NW devices, water adsorption occurs on non-polar lateral surfaces that are the ones exposed to the environment. The effect of adsorbed OH species on non-polar surfaces of *n*-type ZnO was investigated in the work of Porro et al. [45] by theoretical *ab initio* DFT calculations. In particular, it was reported that these adsorbed species result in the creation of deep surface states at the top of the ZnO valence band. As a result, OH species acting as change traps shift the Fermi level from the bottom of the conduction band to the top of the valence band in *n*-type ZnO. This means that upward band bending occurs at the ZnO surface, with the formation of a depletion region (as similarly previously discussed in section 6.3). Under these conditions, the NW can be modelled as a semiconductor core surrounded by an insulating shell layer ascribable to the depletion region, as schematized in Figure 8.2 b. A higher amout of OH adsorbed species results in a thicker shell insulating layer and a small effective radius r_{eff} of the semiconductor core, thus resulting in an increase of the NW overall resistance.

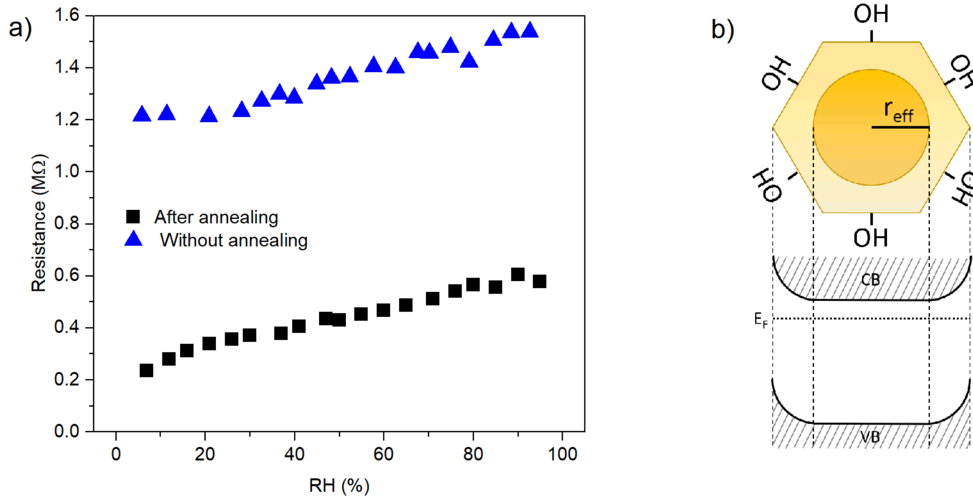

Figure 8.2: Effect of moisture on single NW resistance. a) NW resistance as a function of RH acquired in Pt/ZnO NW/Pt devices. Resistance were extrapolated from *I*-*V* measurements at a reading voltage of 0.4 V. Measurements were performed at various RH content in an N_2 (dry) environment. Black and blue points were obtained by measuring the NW resistance after an annealing at 200°C and without annealing (after ambient exposure), respectively. b) Schematization of upward band bending at the ZnO NW surface as a consequence of OH adsorbed species. The NW can be modelled as a semiconductor core characterized by an effective radius r_{eff} surrounded by a depleted shell layer.

8.3 Effect of moisture on electroforming

In this section, the influence of moisture on the electroforming process is analysed. Note that a detailed discussion on the electroforming process can be found in section 7.3. As initial analysis, our investigation revealed that the electroforming process is strongly suppressed in absence of moisture. As an example, Figure 8.3 a reported the tentative electroforming of a NW device with electrode spacing of 376 nm by progressively increasing the amount of moisture in a N_2 environment. As can be observed, no current jumps can be observed in dry air and for RH = 47 %

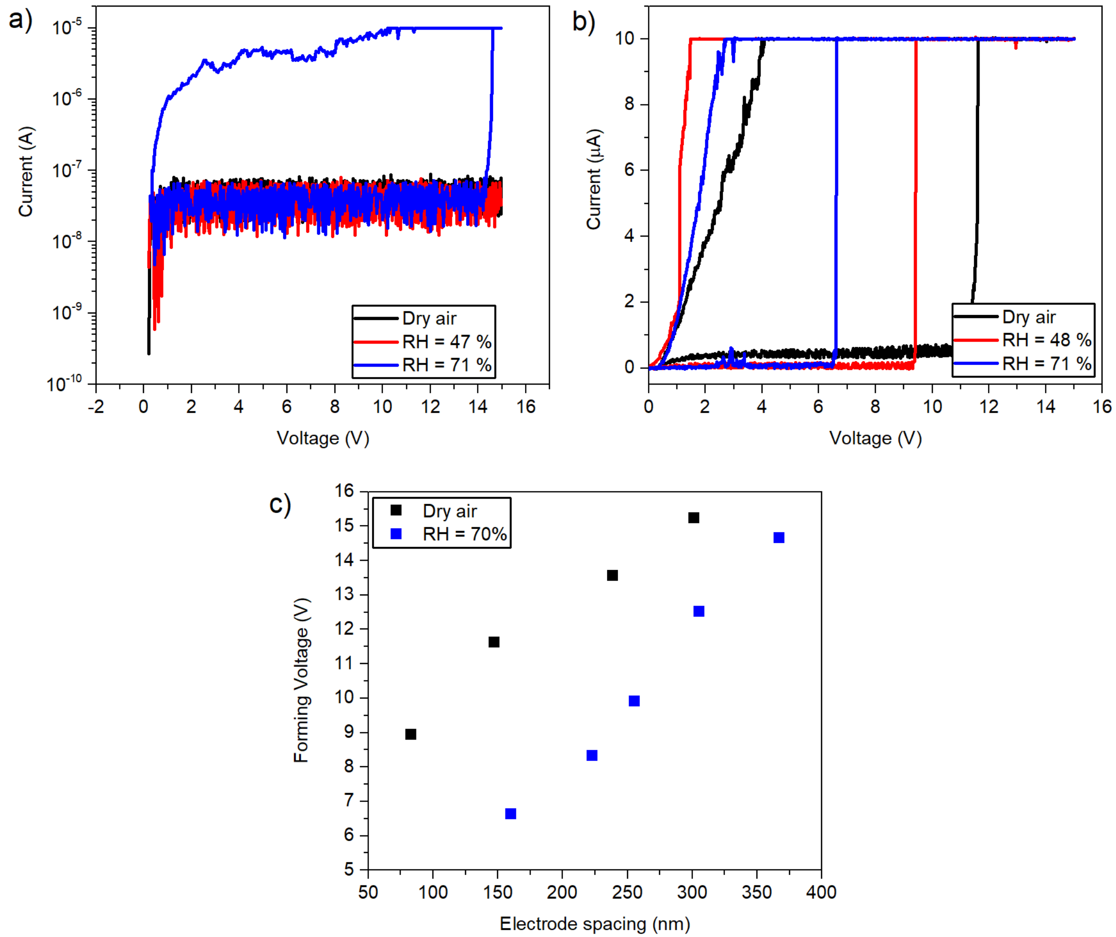

Figure 8.3: Effect of RH on electroforming of Ag/ZnO NW/Pt memristive devices. a) Electroforming process of a NW device with electrode spacing of 376 nm. Electroforming occurred only when RH was increased to 71 %. b) Electroforming of three different devices with electrode spacing of about 150 nm in different RH conditions. c) Forming voltage of single NW devices as a function of electrode spacing for 2 different RH conditions (constant sweep rate of 0.7 V/s).

by applying a voltage ramp until 15 V, meaning that no conductive bridge in between electrodes can be formed in these conditions. Instead, a successful electroforming process can be observed in case of RH = 71 %. In order to further investigate the influence of moisture, three different NW memristors with electrode spacing of ∼ 150 nm were formed at different amount of moisture. As can be observed from Figure 8.3 b, the forming voltage can be decreased from about 11.6 V to 9.4 V and 6.6 V passing from dry conditions to RH =48 % and RH =71 %, respectively. A further prove of the moisture influence on electroforming can be visualized in Figure 8.3 c, where the forming voltage as a function of the electrode spacing (fixed sweep rate of 0.7 V/s) is reported in case of dry air and RH = 70 %. A substantial reduction of the forming voltage was observed in devices electroformed at RH = 70 %. In section 7.3, it was reported that the forming voltage increases by increasing the electrode spacing as well as the voltage sweep rate in air. Results reported in Figure 8.3 b revealed that also the moisture content plays a crucial role during electroforming. In particular, results of these experiments revealed a substantial reduction of forming voltage by increasing the amount of moisture.

8.4 Effect of moisture on resistive switching

Electroforming represents the ideal process for investigating the influence of moisture on redox processes, since the device is initially in the pristine state and no metallic clusters are already present on the NW surface (i.e. ionic migration has to proceed along all the electrode spacing before having the formation of a metallic bridge). However, our observations revealed that moisture can strongly affect also subsequent resistive switching characteristics, where the SET process is driven by ionic migration in the smaller gap in between nanoclusters that are already present on the NW surface after electroforming. In order to elucidate the role of moisture, resistive switching characteristics of the same NW device were evaluated in air (RH ∼30 %) and in dry air (N_2 environment). In air, the single NW memristor exhibited resistive switching behaviour with good stability over cycling, as reported in the *I-V* plot and endurance measurements of Figure 8.4 a and b, respectively. After 25 resistive switching cycles, the sample was measured in a dry environment by stimulating the device with the same voltage ramps. In this case, the device did not exhibit resistive switching, as can be seen in Figure 8.4 c. Note that no SET events were recorded by continously stimulating the device, since the device exhibited always an high resistance state over cycling (Figure 8.4 d). The effect of moisture can be immediately understood by changing the environmental conditions during cycling, as reported in Figure 8.5. Initially, resistive switching characteristics of a NW device were observed in air (see *I-V* characteristic of cycle 1). After 25 cycles, a vacuum pump was started in order to progressively evacuate the chamber. In the meanwhile, electrical responses of the device were continously recorded. A humidity

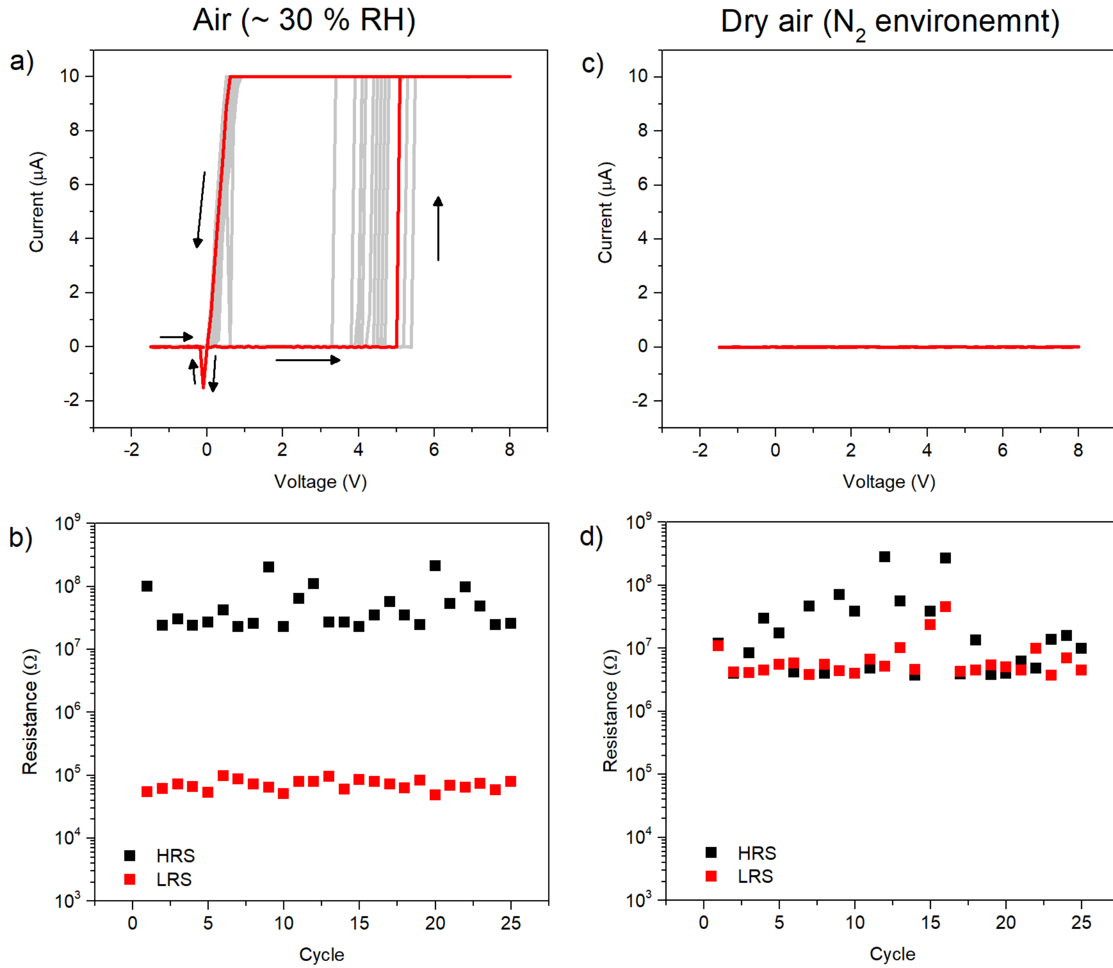

Figure 8.4: Effect of moisture on resistive switching. a) I-V cycles and b)endurance properties of a single NW in air (RH $\sim$30%). c) I-V cycles and d) endurance properties of the same device in dry air (N_2 environment). Resistance values during endurance tests were extrapolated at a reading voltage of 0.4 V.

.

sensor was exploited to record the changes in the RH content when the chamber was evacuated. As can be observed from Figure 8.5, a progressive diminishing of the RH content resulted in a degradation of resistive switching performances (see for example cycle 30 where the SET process resulted to be unstable). This resulted in a total suppression of SET events in vacuum conditions (see cycle 40 where no SET were observed). These experiments revealed that, at least in case of considering the same operating voltage window, SET events are suppressed in absence of moisture. This means that not only the electroforming process but also following SET operations need a certain amount of moisture to proceed.

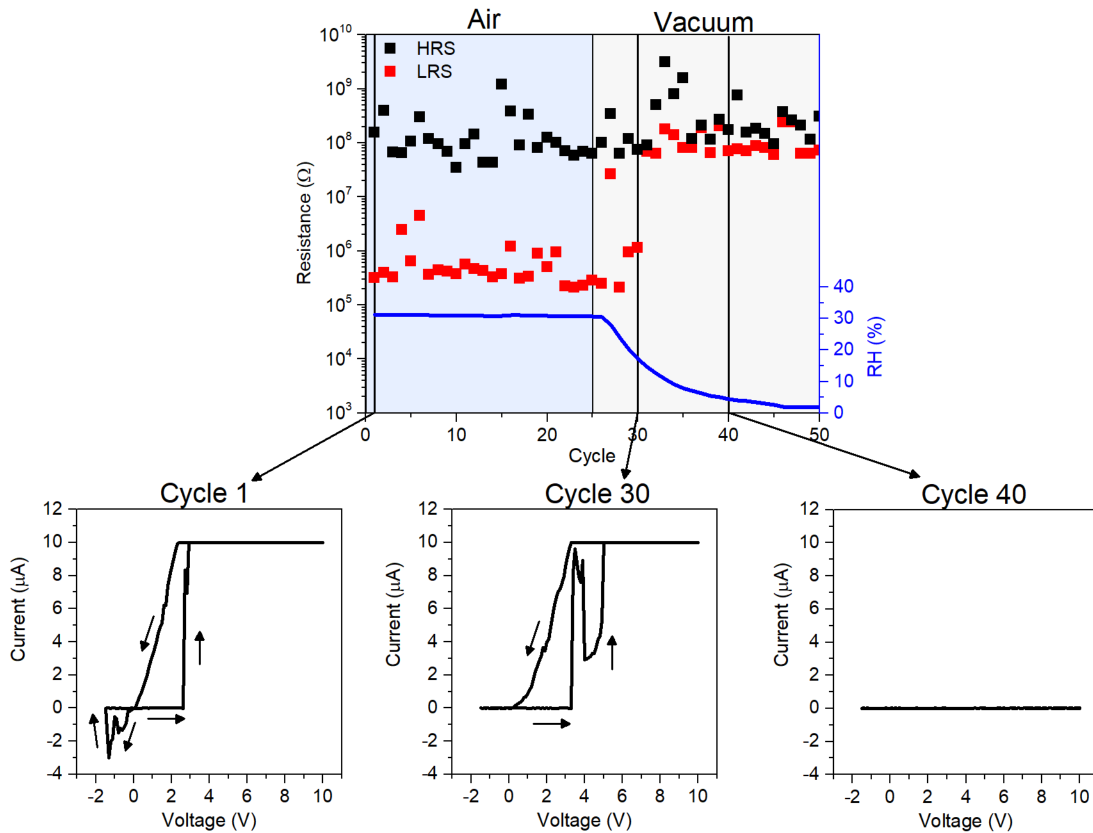

Figure 8.5: Direct observation of the effect of moisture on resistive switching. Initially, the device was cycled in air and exhibited resistive switching characteristics (resistance values were extrapolated at a reading voltage of 1 V). In correspondance of cycle 25, the vacuum pump was started and the chamber was evacuated. The device performances were observed to degrade as the RH content was progressively diminished. The whole I-V characteristic of significant cycles are shown (cycle 1,30 and 40).

8.5 The role of moisture

As recently reviewed [236], moisture was shown to play a key role in determining the device electrochemistry and the switching kinetics. In order to investigate how moisture influences memristive behaviour, it is necessary to remark that a two terminal memristive device can be considered as an electrochemical cell. From the fundamentals of electrochemistry, an electrochemical cell is divided in two compartments also named half-cells, where the oxidation half-reaction and reduction half-reaction occurs separately. Note that both half-cell reactions are necessary for the total cell reaction to proceed. By considering the single NW memristor,

one half-cell reaction is represented by the oxidation of the electrochemical active metal electrode, according to previously discussed electrochemical reactions. Besides these reactions, a counter-electrode half-reaction provided by electrons of OH^- species is needed to keep the electroneutrality of the cell during operations. As discussed by Luebben et al. [238] in thin-film devices, the main contribution in supplying the counter-electrode reaction was shown to involve water redox reactions. In particular, it was shown that this reaction involves reduction of water molecules [236]:

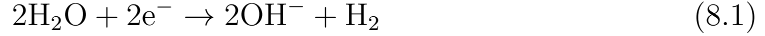

$$2H_2O + 2e^- \rightarrow 2OH^- + H_2 \quad (8.1)$$

Note that water electrolysis at the inert electrode can involve also additional intermediate steps and products. In this framework, it is important to notice that the total reaction rate of the cell is determined by the slower half-cell reaction and, thus, by the catalytic properties towards water reduction of the counter-electrode metal [236]. In the light of these considerations, it is possible to explain results obtained in case of single NW memristive cells. A higher amount of moisture resulted in more water molecules available for the counter-electrode reaction, resulting in a facilitation of conductive filament formation. This turns in lower voltages required for electroforming. In case of single NW devices with small electrode spacing, electroforming process was observed also in dry conditions even if with higher forming voltages. In this case the counter half-cell reaction can be induced by residual water molecules that were not completely desorbed from the NW surface during the evacuation of the chamber. Besides regulating the electrochemistry of the memristive cell, it is not possible to exclude that moisture can affect also the ionic transport properties on the crystalline surface that is covered with an hydrogen-bond network after exposure to a humid environment. Indeed, as discussed by Tsuruoka et al. [240] in case of amorphous thin films, the removal of water molecules can be responsible for the creation of partial defects in the hydrogen-bond network on the surface that reduce the migration speed of metal ions.

Despite the role of the environement on the resistive switching mechansim still needs to be clarified by analyzing, for example, the influence of other gases as well as by investigating the role of the residual atmosphere on the switching mechanism, these results evidenced that the role of the ambient cannot be neglected in order to explain the physical mechansim of switching.

Chapter 9

Conclusions and Perspectives

In this dissertation, memristive devices based on ZnO NWs were realized and the resistive switching mechanism was investigated. The optimized CVD growth process allowed the realization of arrays of high-density and vertically aligned ZnO NWs on a large scale, characterized by mean diameter of about 80 nm and tunable length up to $\sim 1.7\,\mu$m. The analysis of chemical properties of as grown nanostructures revealed high chemical purity, while structural characterizations revelaed that each NW is a single crystal with wurtzite structure. In order to realize reliable memristive devices, the corrosion and dissolution process of ZnO nanostructures was investigated. In particular, it was shown that the wettability properties of the ZnO NW surfaces can be modified by means of electron beam irradiation, preventing ZnO dissolution in water. The mechanism of the e-beam modification of surface properties was analyzed in details, revealing that the formation of an hydrophobic surface layer is responsible for the change in the ZnO surface free energy. Then, resistive switching devices based on as grown ZnO NW arrays were realized by exploiting the Pt growth substrate as bottom electrode and by evaporating a top electrode in a two-terminal capacitor-like configuration. The analysis of the resistive switching mechanism revealed that, in case of NW arrays where a polycrystalline ZnO layer (base layer) is present in between NWs and the Pt substrate as a consequence of the growth process, the resistive switching mechanism is related to the formation/rupture of oxygen vacancies assisted conductive paths along highly oriented grain boundaries of the base layer. In this case, the NWs were reported not to be directly involved in the switching mechanism because of the peculiar device morphology and, thus, the attention was moved to single NW-based devices. For this purpose, it was developed a fabrication process based on a combined optical and electron beam lithography for the realization of devices based on single nanostructures. The realization of single NW devices contacted by means of Pt electrodes allowed the investigation of the electronic conduction mechanism in isolated NWs. Besides evaluating the role of surface effects on the electronic conduction mechanism, *I*-*V*-*T* measurements revealed a two thermally activated

conduction mechansim and a MIT transition at about 365 K. Field-effect measurements were realized by exploiting a back-gate contact in a NW-FET configuration, allowing an extimation of carrier density and mobility as a function of temperature. By coupling ionics to electronics, single NW memristor were realized by contacting ZnO NWs by means of an electrochemically active (Ag) and an electrochemical inert electrode (Pt). The resistive switching mechanism in these devices was deeply investigated by means of a combined approach based on chemical, structural and electrical characterizations, revealing that the memristive behavior has to be ascribed to the migration of Ag^+ ions on the crystalline surface of the NWs while no ionic bulk transport was observed in the NW core. These evidences revealed the importance of surfaces and interfaces as preferential paths for migration of ionic species in memristive devices. By properly controlling the operating conditions, it was possible to regulate the Ag^+ dynamics and to achieve most of the memristive functionalities such as multilevel non-volatile memory, threshold switching with selector capability and neuromorphic functionalities in a single NW device. In particular, it was shown that the Ag^+ dynamics can be exploited for emulating Ca^{2+} dynamics of biological synapses, allowing single NW memristor to emulate short-term plasticity features of biological synapses. The importance of electrochemical properties of metal electrodes in determining device functionalities was discussed by considering Cu instead of Ag as the electrochemical active electrode. Moreover, the investigation of electronic and ionic transport mechanism in controlled atmosphere revealed that moisture plays a crucial role not only for the device electroforming process but also during the following resistive switching operations, affecting the electrochemistry of the memristive cell. The all-in-one functionalities enclosed in a single crystalline NW device togheter with the possibility of direct probing of the conductive path due to the high localization of the switching events make single ZnO NW-based memristive devices suitable model systems for the investigation of the physical mechanism of switching.

Concerning the future perspectives, the single NW memristive model system can be exploited as a platform to clarify the relationship between ionic/electronic processes and memristive functionalities as well as to investigate the role of extrinsic factors, such as the environment, on the physical mechanism of switching. However, one of the main challenges is represented by the implementation of self-assembled NWs in high-density nanodevices, where positioning and manipulation of these nanostructures is required. In this context, integration of NWs can be realized by considering conventional crossbar architectures built by stacking ordered NWs. However, a more fascinating alternative is representd by the realization of memristive devices based on NW random networks. Indeed, taking inspiration from biological neural networks, complex networks can be exploited for the realization of Touring's unorganized machines where the global behaviour arises from the randomly distributed interconnections of simple processing units. The same concept can be applied to NW random networks, where the global behaviour is

determined by the memristive dynamics of the randomly distributed NW units. In this framework, the development of NW random networks can pave the way for the hardware implementation of biological inspired computing paradigms beyond Von Neumann's computational architecture.

Bibliography

1. Chua, L. Memristor-The missing circuit element. *IEEE Trans. Circuit Theory* **18,** 507–519. ISSN: 0018-9324 (1971).
2. Chua, L. & Sung Mo Kang. Memristive devices and systems. *Proc. IEEE* **64,** 209–223. ISSN: 0018-9219 (1976).
3. Vongehr, S. & Meng, X. The Missing Memristor has Not been Found. *Sci. Rep.* **5,** 11657. ISSN: 2045-2322 (Dec. 2015).
4. Abraham, I. The case for rejecting the memristor as a fundamental circuit element. *Sci. Rep.* **8,** 10972. ISSN: 2045-2322 (Dec. 2018).
5. Strukov, D. B., Snider, G. S., Stewart, D. R. & Williams, R. S. The missing memristor found. *Nature* **453,** 80–83. ISSN: 0028-0836 (May 2008).
6. Waser, R. & Aono, M. Nanoionics-based resistive switching memories. *Nat. Mater.* **6,** 833–840. ISSN: 1476-1122 (Nov. 2007).
7. Chua, L. Resistance switching memories are memristors. *Appl. Phys. A* **102,** 765–783. ISSN: 0947-8396 (Mar. 2011).
8. Yang, J. J. *et al.* Memristive switching mechanism for metal/oxide/metal nanodevices. *Nat. Nanotechnol.* **3,** 429–433. ISSN: 1748-3387 (July 2008).
9. Sawa, A. Resistive switching in transition metal oxides. *Mater. Today* **11,** 28–36. ISSN: 13697021 (June 2008).
10. Waser, R., Dittmann, R., Staikov, G. & Szot, K. Redox-Based Resistive Switching Memories - Nanoionic Mechanisms, Prospects, and Challenges. *Adv. Mater.* **21,** 2632–2663. ISSN: 09359648 (July 2009).
11. Ielmini, D. Resistive switching memories based on metal oxides: mechanisms, reliability and scaling. *Semicond. Sci. Technol.* **31,** 063002. ISSN: 0268-1242 (June 2016).
12. Waser, R. in *Memristive Phenom. - From Fundam. Phys. to Neuromorphic Comput. 47th IFF Spring Sch. 2016 - Lect. Notes* 15–37 (2016). ISBN: 978-3-95806-091-3.

13. Valov, I. Redox-Based Resistive Switching Memories (ReRAMs): Electrochemical Systems at the Atomic Scale. *ChemElectroChem* **1,** 26–36. ISSN: 21960216 (Jan. 2014).

14. Valov, I., Waser, R., Jameson, J. R. & Kozicki, M. N. Electrochemical metallization memories—fundamentals, applications, prospects. *Nanotechnology* **22,** 289502. ISSN: 0957-4484 (July 2011).

15. Valov, I. & Lu, W. D. Nanoscale electrochemistry using dielectric thin films as solid electrolytes. *Nanoscale* **8,** 13828–13837. ISSN: 2040-3364 (2016).

16. Wedig, A. *et al.* Nanoscale cation motion in TaO x , HfO x and TiO x memristive systems. *Nat. Nanotechnol.* **11,** 67–74. ISSN: 1748-3387 (Jan. 2016).

17. Jo, S. H. *et al.* Nanoscale Memristor Device as Synapse in Neuromorphic Systems. *Nano Lett.* **10,** 1297–1301. ISSN: 1530-6984 (Apr. 2010).

18. Ohno, T. *et al.* Short-term plasticity and long-term potentiation mimicked in single inorganic synapses. *Nat. Mater.* **10,** 591–595. ISSN: 1476-1122 (Aug. 2011).

19. Wong, H.-S. P. *et al.* Metal–Oxide RRAM. *Proc. IEEE* **100,** 1951–1970. ISSN: 0018-9219 (June 2012).

20. Prezioso, M. *et al.* Training and Operation of an Integrated Neuromorphic Network Based on Metal-Oxide Memristors. *Nature* **521,** 61–64. ISSN: 0028-0836 (Dec. 2014).

21. Du, C., Ma, W., Chang, T., Sheridan, P. & Lu, W. D. Biorealistic Implementation of Synaptic Functions with Oxide Memristors through Internal Ionic Dynamics. *Adv. Funct. Mater.* **25,** 4290–4299. ISSN: 1616301X (July 2015).

22. La Barbera, S., Vuillaume, D. & Alibart, F. Filamentary Switching: Synaptic Plasticity through Device Volatility. *ACS Nano* **9,** 941–949. ISSN: 1936-0851 (Jan. 2015).

23. Kim, S. *et al.* Experimental Demonstration of a Second-Order Memristor and Its Ability to Biorealistically Implement Synaptic Plasticity. *Nano Lett.* **15,** 2203–2211. ISSN: 1530-6984 (Mar. 2015).

24. Wang, Z. *et al.* Memristors with diffusive dynamics as synaptic emulators for neuromorphic computing. *Nat. Mater.* **16,** 101–108. ISSN: 1476-1122 (Jan. 2017).

25. Kim, M.-K. & Lee, J.-S. Short-Term Plasticity and Long-Term Potentiation in Artificial Biosynapses with Diffusive Dynamics. *ACS Nano* **12,** 1680–1687. ISSN: 1936-0851 (Feb. 2018).

26. Wouters, D. in *Memristive Phenom. - From Fundam. Phys. to Neuromorphic Comput. 47th IFF Spring Sch. 2016 - Lect. Notes* 945–976 (2016). ISBN: 978-3-95806-091-3.

27. Van den Hurk, J., Linn, E., Zhang, H., Waser, R. & Valov, I. Volatile resistance states in electrochemical metallization cells enabling non-destructive readout of complementary resistive switches. *Nanotechnology* **25,** 425202. ISSN: 0957-4484 (Oct. 2014).
28. Citri, A. & Malenka, R. C. Synaptic Plasticity: Multiple Forms, Functions and Mechanisms. *Neuropsychopharmacology* **33,** 18–41. ISSN: 0893-133X (Jan. 2008).
29. Milano, G., Porro, S., Valov, I. & Ricciardi, C. Recent developments and perspectives for memristive devices based on metal oxide nanowires. *Adv. Electron. Mater.* Accepted Manuscript.
30. Zaffora, A. *et al.* Electrochemical Tantalum Oxide for Resistive Switching Memories. *Adv. Mater.* **29,** 1–6. ISSN: 15214095 (2017).
31. Lin, K.-L. *et al.* Electrode dependence of filament formation in HfO 2 resistive-switching memory. *J. Appl. Phys.* **109,** 084104. ISSN: 0021-8979 (Apr. 2011).
32. Bricalli, A. *et al.* Resistive Switching Device Technology Based on Silicon Oxide for Improved ON–OFF Ratio—Part II: Select Devices. *IEEE Trans. Electron Devices* **65,** 122–128. ISSN: 0018-9383 (Jan. 2018).
33. Zhang, H. *et al.* Ionic doping effect in ZrO2 resistive switching memory. *Appl. Phys. Lett.* **96,** 123502. ISSN: 0003-6951 (Mar. 2010).
34. Park, K. & Lee, J.-S. Flexible resistive switching memory with a Ni/CuO x /Ni structure using an electrochemical deposition process. *Nanotechnology* **27,** 125203. ISSN: 0957-4484 (Mar. 2016).
35. Laurenti, M., Porro, S., Pirri, C. F., Ricciardi, C. & Chiolerio, A. Zinc Oxide Thin Films for Memristive Devices: A Review. *Crit. Rev. Solid State Mater. Sci.* **42,** 153–172. ISSN: 1040-8436 (Mar. 2017).
36. Porro, S. *et al.* A multi-level memristor based on atomic layer deposition of iron oxide. *Nanotechnology* **29,** 495201. ISSN: 0957-4484 (Dec. 2018).
37. Panda, D. & Tseng, T.-Y. Perovskite Oxides as Resistive Switching Memories: A Review. *Ferroelectrics* **471,** 23–64. ISSN: 0015-0193 (Oct. 2014).
38. Celano, U. *et al.* Imaging the Three-Dimensional Conductive Channel in Filamentary-Based Oxide Resistive Switching Memory. *Nano Lett.* **15,** 7970–7975. ISSN: 1530-6984 (Dec. 2015).
39. Yang, Y. & Huang, R. Probing memristive switching in nanoionic devices. *Nat. Electron.* **1,** 274–287. ISSN: 2520-1131 (May 2018).
40. Park, J., Lee, S. & Yong, K. Photo-stimulated resistive switching of ZnO nanorods. *Nanotechnology* **23,** 385707. ISSN: 0957-4484 (Sept. 2012).

41. Younis, A. *et al.* High-Performance Nanocomposite Based Memristor with Controlled Quantum Dots as Charge Traps. *ACS Appl. Mater. Interfaces* **5,** 2249–2254. ISSN: 1944-8244 (Mar. 2013).

42. Lai, Y., Xin, P., Cheng, S., Yu, J. & Zheng, Q. Plasma enhanced multistate storage capability of single ZnO nanowire based memory. *Appl. Phys. Lett.* **106,** 031603. ISSN: 0003-6951 (Jan. 2015).

43. Park, J., Song, H., Lee, E. K., Oh, J. H. & Yong, K. ZnO Nanowire Based Photoelectrical Resistive Switches for Flexible Memory. *J. Electrochem. Soc.* **162,** H713–H718. ISSN: 0013-4651 (July 2015).

44. Lee, S., Park, J.-b., Lee, M.-j. & Boland, J. J. Multilevel resistance in ZnO nanowire memristors enabled by hydrogen annealing treatment. *AIP Adv.* **6,** 125010. ISSN: 2158-3226 (Dec. 2016).

45. Porro, S. *et al.* Multiple resistive switching in core–shell ZnO nanowires exhibiting tunable surface states. *J. Mater. Chem. C* **5,** 10517–10523. ISSN: 2050-7526 (2017).

46. Russo, P., Xiao, M., Liang, R. & Zhou, N. Y. UV-Induced Multilevel Current Amplification Memory Effect in Zinc Oxide Rods Resistive Switching Devices. *Adv. Funct. Mater.* **28,** 1706230. ISSN: 1616301X (Mar. 2018).

47. Lu, W. & Lieber, C. M. Nanoelectronics from the bottom up. *Nat. Mater.* **6,** 841–850. ISSN: 1476-1122 (Nov. 2007).

48. Ielmini, D., Cagli, C., Nardi, F. & Zhang, Y. Nanowire-based resistive switching memories: devices, operation and scaling. *J. Phys. D. Appl. Phys.* **46,** 074006. ISSN: 0022-3727 (Feb. 2013).

49. Kim, S. I., Lee, J. H., Chang, Y. W., Hwang, S. S. & Yoo, K.-H. Reversible resistive switching behaviors in NiO nanowires. *Appl. Phys. Lett.* **93,** 033503. ISSN: 0003-6951 (July 2008).

50. Nagashima, K. *et al.* Intrinsic Mechanisms of Memristive Switching. *Nano Lett.* **11,** 2114–2118. ISSN: 1530-6984 (May 2011).

51. Yen-De Chiang *et al.* Single-ZnO-Nanowire Memory. *IEEE Trans. Electron Devices* **58,** 1735–1740. ISSN: 0018-9383 (June 2011).

52. Huang, Y.-T. *et al.* In Situ TEM and Energy Dispersion Spectrometer Analysis of Chemical Composition Change in ZnO Nanowire Resistive Memories. *Anal. Chem.* **85,** 3955–3960. ISSN: 0003-2700 (Apr. 2013).

53. Wu, W. & Wang, Z. L. Piezotronic Nanowire-Based Resistive Switches As Programmable Electromechanical Memories. *Nano Lett.* **11,** 2779–2785. ISSN: 1530-6984 (July 2011).

54. Karthik, K. R. G. *et al.* A ZnO nanowire resistive switch. *Appl. Phys. Lett.* **103,** 123114. ISSN: 0003-6951 (Sept. 2013).

55. Huang, Y., Luo, Y., Shen, Z., Yuan, G. & Zeng, H. Unipolar resistive switching of ZnO-single-wire memristors. *Nanoscale Res. Lett.* **9,** 381. ISSN: 1556-276X (2014).

56. Lai, Y. *et al.* Resistive Switching of Plasma–Treated Zinc Oxide Nanowires for Resistive Random Access Memory. *Nanomaterials* **6,** 16. ISSN: 2079-4991 (Jan. 2016).

57. Zhang, R. *et al.* Enhanced non-volatile resistive switching in suspended single-crystalline ZnO nanowire with controllable multiple states. *Nanotechnology* **27,** 315203. ISSN: 0957-4484 (Aug. 2016).

58. Zhang, R. *et al.* Enabling selectivity and fast recovery of ZnO nanowire gas sensors through resistive switching. *Sensors Actuators B Chem.* **238,** 357–363. ISSN: 09254005 (Jan. 2017).

59. Yang, Y. *et al.* Nonvolatile resistive switching in single crystalline ZnO nanowires. *Nanoscale* **3,** 1917. ISSN: 2040-3364 (2011).

60. Qi, J. *et al.* Current self-complianced and self-rectifying resistive switching in Ag-electroded single Na-doped ZnO nanowires. *Nanoscale* **5,** 2651. ISSN: 2040-3364 (2013).

61. Wang, B. *et al.* Resistive switching in Ga- and Sb-doped ZnO single nanowire devices. *J. Mater. Chem. C* **3,** 11881–11885. ISSN: 2050-7526 (2015).

62. O'Kelly, C., Fairfield, J. A. & Boland, J. J. A Single Nanoscale Junction with Programmable Multilevel Memory. *ACS Nano* **8,** 11724–11729. ISSN: 1936-0851 (Nov. 2014).

63. O'Kelly, C. J. *et al.* Associative Enhancement of Time Correlated Response to Heterogeneous Stimuli in a Neuromorphic Nanowire Device. *Adv. Electron. Mater.* **2,** 1500458. ISSN: 2199160X (June 2016).

64. Lin, L. *et al.* Plasmonic-Radiation-Enhanced Metal Oxide Nanowire Heterojunctions for Controllable Multilevel Memory. *Adv. Funct. Mater.* **26,** 5979–5986. ISSN: 1616301X (Sept. 2016).

65. Fan, Z., Fan, X., Li, A. & Dong, L. In situ forming, characterization, and transduction of nanowire memristors. *Nanoscale* **5,** 12310. ISSN: 2040-3364 (2013).

66. Liang, K.-D. *et al.* Single CuO x Nanowire Memristor: Forming-Free Resistive Switching Behavior. *ACS Appl. Mater. Interfaces* **6,** 16537–16544. ISSN: 1944-8244 (Oct. 2014).

67. Bae, S.-H. *et al.* The Memristive Properties of a Single VO 2 Nanowire with Switching Controlled by Self-Heating. *Adv. Mater.* **25,** 5098–5103. ISSN: 09359648 (Sept. 2013).

68. He, X. *et al.* Memristive properties of hexagonal WO3 nanowires induced by oxygen vacancy migration. *Nanoscale Res. Lett.* **8,** 50. ISSN: 1556-276X (2013).

69. Oka, K., Yanagida, T., Nagashima, K., Tanaka, H. & Kawai, T. Nonvolatile Bipolar Resistive Memory Switching in Single Crystalline NiO Heterostructured Nanowires. *J. Am. Chem. Soc.* **131,** 3434–3435. ISSN: 0002-7863 (Mar. 2009).

70. Oka, K. *et al.* Resistive-Switching Memory Effects of NiO Nanowire/Metal Junctions. *J. Am. Chem. Soc.* **132,** 6634–6635. ISSN: 0002-7863 (May 2010).

71. Nagashima, K. *et al.* Resistive Switching Multistate Nonvolatile Memory Effects in a Single Cobalt Oxide Nanowire. *Nano Lett.* **10,** 1359–1363. ISSN: 1530-6984 (Apr. 2010).

72. Nagashima, K. *et al.* Switching Properties of Titanium Dioxide Nanowire Memristor. *Jpn. J. Appl. Phys.* **51,** 11PE09. ISSN: 0021-4922 (Nov. 2012).

73. He, L. *et al.* Memory and Threshold Resistance Switching in Ni/NiO Core–Shell Nanowires. *Nano Lett.* **11,** 4601–4606. ISSN: 1530-6984 (Nov. 2011).

74. Hsu, C.-W. & Chou, L.-J. Bipolar Resistive Switching of Single Gold-in-Ga 2 O 3 Nanowire. *Nano Lett.* **12,** 4247–4253. ISSN: 1530-6984 (Aug. 2012).

75. Huang, C.-H., Chang, W.-C., Huang, J.-S., Lin, S.-M. & Chueh, Y.-L. Resistive switching of Sn-doped In 2 O 3 /HfO 2 core–shell nanowire: geometry architecture engineering for nonvolatile memory. *Nanoscale* **9,** 6920–6928. ISSN: 2040-3364 (2017).

76. Cheng, B., Ouyang, Z., Chen, C., Xiao, Y. & Lei, S. Individual Zn2SnO4-sheathed ZnO heterostructure nanowires for efficient resistive switching memory controlled by interface states. *Sci. Rep.* **3,** 3249. ISSN: 2045-2322 (Dec. 2013).

77. Flowers, P. F., Catenacci, M. J. & Wiley, B. J. High-speed, solution-coatable memory based on Cu–SiO 2 core–shell nanowires. *Nanoscale Horizons* **1,** 313–316. ISSN: 2055-6756 (2016).

78. Manning, H. G., Biswas, S., Holmes, J. D. & Boland, J. J. Nonpolar Resistive Switching in Ag@TiO 2 Core–Shell Nanowires. *ACS Appl. Mater. Interfaces* **9,** 38959–38966. ISSN: 1944-8244 (Nov. 2017).

79. Huang, C.-W., Chen, J.-Y., Chiu, C.-H. & Wu, W.-W. Revealing Controllable Nanowire Transformation through Cationic Exchange for RRAM Application. *Nano Lett.* **14,** 2759–2763. ISSN: 1530-6984 (May 2014).

80. Herderick, E. D., Reddy, K. M., Sample, R. N., Draskovic, T. I. & Padture, N. P. Bipolar resistive switching in individual Au–NiO–Au segmented nanowires. *Appl. Phys. Lett.* **95,** 203505. ISSN: 0003-6951 (Nov. 2009).

81. Park, K. & Lee, J.-S. Controlled synthesis of Ni/CuOx/Ni nanowires by electrochemical deposition with self-compliance bipolar resistive switching. *Sci. Rep.* **6,** 23069. ISSN: 2045-2322 (Sept. 2016).

82. Brivio, S. *et al.* Low-power resistive switching in Au/NiO/Au nanowire arrays. *Appl. Phys. Lett.* **101,** 223510. ISSN: 0003-6951 (Nov. 2012).

83. Huang, Y.-C. *et al.* Improvement of resistive switching in NiO-based nanowires by inserting Pt layers. *Appl. Phys. Lett.* **101,** 153106. ISSN: 0003-6951 (Oct. 2012).

84. Brivio, S. *et al.* Bipolar resistive switching of Au/NiO x /Ni/Au heterostructure nanowires. *Appl. Phys. Lett.* **103,** 153506. ISSN: 0003-6951 (Oct. 2013).

85. Zhang, F. *et al.* Realization of Rectifying and Resistive Switching Behaviors of TiO2 Nanorod Arrays for Nonvolatile Memory. *Electrochem. Solid-State Lett.* **14,** H422. ISSN: 10990062 (2011).

86. Huang, C.-H. *et al.* ZnO 1– x Nanorod Arrays/ZnO Thin Film Bilayer Structure: From Homojunction Diode and High-Performance Memristor to Complementary 1D1R Application. *ACS Nano* **6,** 8407–8414. ISSN: 1936-0851 (Sept. 2012).

87. Senthilkumar, V., Kathalingam, A., Kannan, V., Senthil, K. & Rhee, J.-K. Reproducible resistive switching in hydrothermal processed TiO2 nanorod film for non-volatile memory applications. *Sensors Actuators A Phys.* **194,** 135–139. ISSN: 09244247 (May 2013).

88. Huang, Y.-C. *et al.* Using binary resistors to achieve multilevel resistive switching in multilayer NiO/Pt nanowire arrays. *NPG Asia Mater.* **6,** e85–e85. ISSN: 1884-4049 (Feb. 2014).

89. Huang, C.-H., Chou, T.-S., Huang, J.-S., Lin, S.-M. & Chueh, Y.-L. Self-Selecting Resistive Switching Scheme Using TiO2 Nanorod Arrays. *Sci. Rep.* **7,** 2066. ISSN: 2045-2322 (Dec. 2017).

90. Xiao, M., Musselman, K. P., Duley, W. W. & Zhou, Y. N. Reliable and Low-Power Multilevel Resistive Switching in TiO 2 Nanorod Arrays Structured with a TiO x Seed Layer. *ACS Appl. Mater. Interfaces* **9,** 4808–4817. ISSN: 1944-8244 (Feb. 2017).

91. Prakash, A. *et al.* Resistive switching memory characteristics of Ge/GeOx nanowires and evidence of oxygen ion migration. *Nanoscale Res. Lett.* **8,** 220. ISSN: 1556-276X (2013).

92. Lee, S., Lee, J., Park, J., Choi, Y. & Yong, K. Resistive Switching WOx-Au Core-Shell Nanowires with Unexpected Nonwetting Stability Even when Submerged Under Water. *Adv. Mater.* **24,** 2418–2423. ISSN: 09359648 (May 2012).

93. Tseng, Z.-L. *et al.* Electrical bistability in hybrid ZnO nanorod/polymethylmethacrylate heterostructures. *Appl. Phys. Lett.* **97,** 212103. ISSN: 0003-6951 (Nov. 2010).

94. Chang, W. Y., Lin, C. A., He, J. H. & Wu, T. B. Resistive switching behaviors of ZnO nanorod layers. *Appl. Phys. Lett.* **96,** 242109. ISSN: 0003-6951 (June 2010).

95. Li, L., Zhang, Y. & Chew, Z. A Cu/ZnO Nanowire/Cu Resistive Switching Device. *Nano-Micro Lett.* **5,** 159–162. ISSN: 2150-5551 (July 2013).

96. Chew, Z. J. & Li, L. A discrete memristor made of ZnO nanowires synthesized on printed circuit board. *Mater. Lett.* **91,** 298–300. ISSN: 0167577X (Jan. 2013).

97. Park, S. *et al.* Resistive switching characteristics of sol-gel based ZnO nanorods fabricated on flexible substrates. *Phys. status solidi - Rapid Res. Lett.* **7,** 493–496. ISSN: 18626254 (July 2013).

98. Dugaiczyk, L. *et al.* Resistive switching in single vertically-aligned ZnO nanowire grown directly on Cu substrate. *Chem. Phys. Lett.* **575,** 112–114. ISSN: 00092614 (June 2013).

99. Yoo, E. J., Shin, I. K., Yoon, T. S., Choi, Y. J. & Kang, C. J. Resistive Switching Characteristics of ZnO Nanowires. *J. Nanosci. Nanotechnol.* **14,** 9459–9464. ISSN: 15334880 (Dec. 2014).

100. Sun, Y. *et al.* High On–Off Ratio Improvement of ZnO-Based Forming-Free Memristor by Surface Hydrogen Annealing. *ACS Appl. Mater. Interfaces* **7,** 7382–7388. ISSN: 1944-8244 (Apr. 2015).

101. Shen, G.-H. *et al.* Low switching-threshold-voltage zinc oxide nanowire array resistive random access memory. *Thin Solid Films* **618,** 90–94. ISSN: 00406090 (Nov. 2016).

102. Jasmin, A., Porro, S., Pirri, C. F., Ricciardi, C. & Chiolerio, A. *Polymer coated ZnO nanowires for memristive devices* in *2015 IEEE 15th Int. Conf. Nanotechnol.* (IEEE, July 2015), 496–498. ISBN: 978-1-4673-8156-7. doi:10.1109/NANO.2015.7388647. http://ieeexplore.ieee.org/document/7388647/.

103. Anoop, G., Panwar, V., Kim, T. Y. & Jo, J. Y. Resistive Switching in ZnO Nanorods/Graphene Oxide Hybrid Multilayer Structures. *Adv. Electron. Mater.* **3,** 1600418. ISSN: 2199160X (May 2017).

104. Simanjuntak, F. M. *et al.* Role of nanorods insertion layer in ZnO-based electrochemical metallization memory cell. *Semicond. Sci. Technol.* **32,** 124003. ISSN: 0268-1242 (Dec. 2017).

105. Cagli, C. *et al.* Resistive-Switching Crossbar Memory Based on Ni-NiO Core-Shell Nanowires. *Small* **7,** 2899–2905. ISSN: 16136810 (Oct. 2011).

106. Nirmalraj, P. N. *et al.* Manipulating Connectivity and Electrical Conductivity in Metallic Nanowire Networks. *Nano Lett.* **12,** 5966–5971. ISSN: 1530-6984 (Nov. 2012).
107. Bellew, A. T., Bell, A. P., McCarthy, E. K., Fairfield, J. A. & Boland, J. J. Programmability of nanowire networks. *Nanoscale* **6,** 9632–9639. ISSN: 2040-3364 (2014).
108. Fairfield, J. A., Rocha, C. G., O'Callaghan, C., Ferreira, M. S. & Boland, J. J. Co-percolation to tune conductive behaviour in dynamical metallic nanowire networks. *Nanoscale* **8,** 18516–18523. ISSN: 2040-3364 (2016).
109. Du, H. *et al.* Engineering Silver Nanowire Networks: From Transparent Electrodes to Resistive Switching Devices. *ACS Appl. Mater. Interfaces* **9,** 20762–20770. ISSN: 1944-8244 (June 2017).
110. Manning, H. G. *et al.* Emergence of winner-takes-all connectivity paths in random nanowire networks. *Nat. Commun.* **9,** 3219. ISSN: 2041-1723 (Dec. 2018).
111. Stieg, A. Z. *et al.* Emergent Criticality in Complex Turing B-Type Atomic Switch Networks. *Adv. Mater.* **24,** 286–293. ISSN: 09359648 (Jan. 2012).
112. Fan, D. L., Zhu, F. Q., Cammarata, R. C. & Chien, C. L. Manipulation of nanowires in suspension by ac electric fields. *Appl. Phys. Lett.* **85,** 4175–4177. ISSN: 0003-6951 (Nov. 2004).
113. Papadakis, S. J., Gu, Z. & Gracias, D. H. Dielectrophoretic assembly of reversible and irreversible metal nanowire networks and vertically aligned arrays. *Appl. Phys. Lett.* **88,** 233118. ISSN: 0003-6951 (June 2006).
114. Whang, D., Jin, S., Wu, Y. & Lieber, C. M. Large-Scale Hierarchical Organization of Nanowire Arrays for Integrated Nanosystems. *Nano Lett.* **3,** 1255–1259. ISSN: 1530-6984 (Sept. 2003).
115. Fan, Z. & Lu, J. G. Zinc Oxide Nanostructures: Synthesis and Properties. *J. Nanosci. Nanotechnol.* **5,** 1561–1573. ISSN: 15334880 (Oct. 2005).
116. Janotti, A. & Van de Walle, C. G. Fundamentals of zinc oxide as a semiconductor. *Reports Prog. Phys.* **72,** 126501. ISSN: 0034-4885 (Dec. 2009).
117. Wang, Z. L. Nanostructures of zinc oxide. *Mater. Today* **7,** 26–33. ISSN: 13697021 (June 2004).
118. Zhang, Y., Ram, M. K., Stefanakos, E. K. & Goswami, D. Y. Synthesis, Characterization, and Applications of ZnO Nanowires. *J. Nanomater.* **2012,** 1–22. ISSN: 1687-4110 (2012).
119. Baruah, S. & Dutta, J. Hydrothermal growth of ZnO nanostructures. *Sci. Technol. Adv. Mater.* **10,** 013001. ISSN: 1468-6996 (Jan. 2009).

120. Wang, Z. L. Zinc oxide nanostructures: growth, properties and applications. *J. Phys. Condens. Matter* **16,** R829–R858. ISSN: 0953-8984 (June 2004).

121. Djurišić, A. B., Chen, X., Leung, Y. H. & Man Ching Ng, A. ZnO nanostructures: growth, properties and applications. *J. Mater. Chem.* **22,** 6526. ISSN: 0959-9428 (2012).

122. Yao, B. D., Chan, Y. F. & Wang, N. Formation of ZnO nanostructures by a simple way of thermal evaporation. *Appl. Phys. Lett.* **81,** 757–759. ISSN: 0003-6951 (July 2002).

123. Lyu, S. C., Zhang, Y., Lee, C. J., Ruh, H. & Lee, H. J. Low-Temperature Growth of ZnO Nanowire Array by a Simple Physical Vapor-Deposition Method. *Chem. Mater.* **15,** 3294–3299. ISSN: 0897-4756 (Aug. 2003).

124. Zhang, Z., Wang, S. J., Yu, T. & Wu, T. Controlling the Growth Mechanism of ZnO Nanowires by Selecting Catalysts. *J. Phys. Chem. C* **111,** 17500–17505. ISSN: 1932-7447 (Nov. 2007).

125. Zha, M. *et al.* Large-area self-catalysed and selective growth of ZnO nanowires. *Nanotechnology* **19,** 325603. ISSN: 0957-4484 (Aug. 2008).

126. Ji, L.-W. *et al.* Effect of seed layer on the growth of well-aligned ZnO nanowires. *J. Phys. Chem. Solids* **70,** 1359–1362. ISSN: 00223697 (Oct. 2009).

127. Wan, H. & Ruda, H. E. A study of the growth mechanism of CVD-grown ZnO nanowires. *J. Mater. Sci. Mater. Electron.* **21,** 1014–1019. ISSN: 0957-4522 (Oct. 2010).

128. Meng, G. *et al.* One step synthesis of vertically aligned ZnO nanowire arrays with tunable length. *Appl. Surf. Sci.* **256,** 6543–6549. ISSN: 01694332 (Sept. 2010).

129. Menzel, A. *et al.* Role of Carrier Gas Flow and Species Diffusion in Nanowire Growth from Thermal CVD. *J. Phys. Chem. C* **116,** 5524–5530. ISSN: 1932-7447 (Mar. 2012).

130. Alsultany, F. H., Hassan, Z. & Ahmed, N. M. Catalyst-free growth of ZnO nanowires on ITO seed layer/glass by thermal evaporation method: Effects of ITO seed layer laser annealing temperature. *Superlattices Microstruct.* **92,** 68–79. ISSN: 07496036 (Apr. 2016).

131. Wen, B., Sader, J. E. & Boland, J. J. Mechanical Properties of ZnO Nanowires. *Phys. Rev. Lett.* **101,** 175502. ISSN: 0031-9007 (Oct. 2008).

132. Yan, R., Gargas, D. & Yang, P. Nanowire photonics. *Nat. Photonics* **3,** 569–576. ISSN: 1749-4885 (Oct. 2009).

133. Chiu, S.-P., Lin, Y.-H. & Lin, J.-J. Electrical conduction mechanisms in natively doped ZnO nanowires. *Nanotechnology* **20,** 015203. ISSN: 0957-4484 (Jan. 2009).

134. Sidiropoulos, T. P. H. *et al.* Ultrafast plasmonic nanowire lasers near the surface plasmon frequency. *Nat. Phys.* **10,** 870–876. ISSN: 1745-2473 (Sept. 2014).

135. Wan, Q. *et al.* Fabrication and ethanol sensing characteristics of ZnO nanowire gas sensors. *Appl. Phys. Lett.* **84,** 3654–3656. ISSN: 0003-6951 (May 2004).

136. Stassi, S. *et al.* Functionalized ZnO nanowires for microcantilever biosensors with enhanced binding capability. *Anal. Bioanal. Chem.* **409,** 2615–2625. ISSN: 1618-2642 (Apr. 2017).

137. Soci, C. *et al.* ZnO Nanowire UV Photodetectors with High Internal Gain. *Nano Lett.* **7,** 1003–1009. ISSN: 1530-6984 (Apr. 2007).

138. Chang, P.-c. & Lu, J. G. ZnO Nanowire Field-Effect Transistors. *IEEE Trans. Electron Devices* **55,** 2977–2987. ISSN: 0018-9383 (Nov. 2008).

139. Zhang, Y., Nayak, T., Hong, H. & Cai, W. Biomedical Applications of Zinc Oxide Nanomaterials. *Curr. Mol. Med.* **13,** 1633–1645. ISSN: 15665240 (Nov. 2013).

140. Pierson, H. O. *Handbook of Chemical Vapor Deposition: principles, technology and applications* (ed Andrew, W.) ISBN: 0815514328. doi:10.1016/B978-081551432-9.50006-1 (May 1999).

141. Wongchoosuk, C. *et al.* Controlled Synthesis of ZnO Nanostructures: The Role of Source and Substrate Temperatures. *J. Phys. Chem. C* **115,** 757–761. ISSN: 1932-7447 (Jan. 2011).

142. Menzel, A. *et al.* Tuning the Growth Mechanism of ZnO Nanowires by Controlled Carrier and Reaction Gas Modulation in Thermal CVD. *J. Phys. Chem. Lett.* **3,** 2815–2821. ISSN: 1948-7185 (Oct. 2012).

143. Cultrera, A., Amato, G., Boarino, L. & Lamberti, C. A modified cryostat for photo-electrical characterization of porous materials in controlled atmosphere at very low gas dosage. *AIP Adv.* **4,** 087134. ISSN: 2158-3226 (Aug. 2014).

144. Geng, C. *et al.* Well-Aligned ZnO Nanowire Arrays Fabricated on Silicon Substrates. *Adv. Funct. Mater.* **14,** 589–594. ISSN: 1616-301X (June 2004).

145. Xu, C.-L. *et al.* Low-temperature growth and optical properties of radial ZnO nanowires. *Mater. Lett.* **58,** 3976–3979. ISSN: 0167577X (Dec. 2004).

146. Fan, H. J., Werner, P. & Zacharias, M. Semiconductor Nanowires: From Self-Organization to Patterned Growth. *Small* **2,** 700–717. ISSN: 1613-6810 (June 2006).

147. Xiang, B. *et al.* Rational Synthesis of p-Type Zinc Oxide Nanowire Arrays Using Simple Chemical Vapor Deposition. *Nano Lett.* **7,** 323–328. ISSN: 1530-6984 (Feb. 2007).

148. Kang, Y.-H., Choi, C.-G., Kim, Y.-S. & Kim, J.-K. Influence of seed layers on the vertical growth of ZnO nanowires. *Mater. Lett.* **63,** 679–682. ISSN: 0167577X (Mar. 2009).

149. Yousefi, R. & Kamaluddin, B. Dependence of photoluminescence peaks and ZnO nanowires diameter grown on silicon substrates at different temperatures and orientations. *J. Alloys Compd.* **479,** L11–L14. ISSN: 09258388 (June 2009).

150. Oh, S. *et al.* The mechanism of ZnO nanorod growth by vapor phase transportation. *Phys. E Low-dimensional Syst. Nanostructures* **42,** 2285–2288. ISSN: 13869477 (July 2010).

151. Giri, P., Dhara, S. & Chakraborty, R. Effect of ZnO seed layer on the catalytic growth of vertically aligned ZnO nanorod arrays. *Mater. Chem. Phys.* **122,** 18–22. ISSN: 02540584 (July 2010).

152. Ramgir, N. S. *et al.* Reactive VLS and the Reversible Switching between VS and VLS Growth Modes for ZnO Nanowire Growth. *J. Phys. Chem. C* **114,** 10323–10329. ISSN: 1932-7447 (June 2010).

153. Jeong, J. S. & Lee, J. Y. Investigation of initial growth of ZnO nanowires and their growth mechanism. *Nanotechnology* **21,** 475603. ISSN: 0957-4484 (Nov. 2010).

154. Zhu, G. *et al.* Synthesis of vertically aligned ultra-long ZnO nanowires on heterogeneous substrates with catalyst at the root. *Nanotechnology* **23,** 055604. ISSN: 0957-4484 (Feb. 2012).

155. Saunders, R. B., Garry, S., Byrne, D., Henry, M. O. & McGlynn, E. Length versus Radius Relationship for ZnO Nanowires Grown via Vapor Phase Transport. *Cryst. Growth Des.* **12,** 5972–5979. ISSN: 1528-7483 (Dec. 2012).

156. Podrezova, L. V., Porro, S., Cauda, V., Fontana, M. & Cicero, G. Comparison between ZnO nanowires grown by chemical vapor deposition and hydrothermal synthesis. *Appl. Phys. A* **113,** 623–632. ISSN: 0947-8396 (Nov. 2013).

157. Gomez, J. L. & Tigli, O. Zinc oxide nanostructures: from growth to application. *J. Mater. Sci.* **48,** 612–624. ISSN: 0022-2461 (Jan. 2013).

158. Lord, A. M. *et al.* Enhanced Long-Path Electrical Conduction in ZnO Nanowire Array Devices Grown via Defect-Driven Nucleation. *J. Phys. Chem. C* **118,** 21177–21184. ISSN: 1932-7447 (Sept. 2014).

159. Fanni, L. *et al.* Increasing Polycrystalline Zinc Oxide Grain Size by Control of Film Preferential Orientation. *Cryst. Growth Des.* **15,** 5886–5891. ISSN: 1528-7483 (Dec. 2015).

160. Evans, J. E., Lord, A. M., Smith, N. A., Ward, M. B. & Wilks, S. P. General Integration of Vertical Nanowire Arrays with Silicon for Highly Parallel Electronic Device Applications. *J. Phys. Chem. C* **122,** 24716–24724. ISSN: 1932-7447 (Nov. 2018).

161. Tiggelaar, R., Sanders, R., Groenland, A. & Gardeniers, J. Stability of thin platinum films implemented in high-temperature microdevices. *Sensors Actuators A Phys.* **152,** 39–47. ISSN: 09244247 (May 2009).

162. Milano, G. *et al.* Tuning ZnO Nanowire Dissolution by Electron Beam Modification of Surface Wetting Properties. *J. Phys. Chem. C* **122,** 8011–8021. ISSN: 1932-7447 (Apr. 2018).

163. Al-Sabahi, J., Bora, T., Al-Abri, M. & Dutta, J. Controlled Defects of Zinc Oxide Nanorods for Efficient Visible Light Photocatalytic Degradation of Phenol. *Materials (Basel).* **9,** 238. ISSN: 1996-1944 (Mar. 2016).

164. Jung, Y., Yang, W., Koo, C. Y., Song, K. & Moon, J. High performance and high stability low temperature aqueous solution-derived Li–Zr co-doped ZnO thin film transistors. *J. Mater. Chem.* **22,** 5390. ISSN: 0959-9428 (2012).

165. Zhang, B., Zhou, H.-B., Han, E.-H. & Ke, W. Effects of a small addition of Mn on the corrosion behaviour of Zn in a mixed solution. *Electrochim. Acta* **54,** 6598–6608. ISSN: 00134686 (Nov. 2009).

166. Cuscó, R. *et al.* Temperature dependence of Raman scattering in <math display="inline"> <mrow> <mi>ZnO</mi> </mrow> </math>. *Phys. Rev. B* **75,** 165202. ISSN: 1098-0121 (Apr. 2007).

167. Russo, V., Ghidelli, M., Gondoni, P., Casari, C. S. & Li Bassi, A. Multiwavelength Raman scattering of nanostructured Al-doped zinc oxide. *J. Appl. Phys.* **115,** 073508. ISSN: 0021-8979 (Feb. 2014).

168. Zhang, R., Yin, P.-G., Wang, N. & Guo, L. Photoluminescence and Raman scattering of ZnO nanorods. *Solid State Sci.* **11,** 865–869. ISSN: 12932558 (Apr. 2009).

169. Manjón, F. J., Marí, B., Serrano, J. & Romero, A. H. Silent Raman modes in zinc oxide and related nitrides. *J. Appl. Phys.* **97,** 053516. ISSN: 0021-8979 (Mar. 2005).

170. Zhou, J., Xu, N. S. & Wang, Z. L. Dissolving Behavior and Stability of ZnO Wires in Biofluids: A Study on Biodegradability and Biocompatibility of ZnO Nanostructures. *Adv. Mater.* **18,** 2432–2435. ISSN: 0935-9648 (Sept. 2006).

171. Pan, Z., Tao, J., Zhu, Y., Huang, J.-F. & Paranthaman, M. P. Spontaneous Growth of ZnCO 3 Nanowires on ZnO Nanostructures in Normal Ambient Environment: Unstable ZnO Nanostructures. *Chem. Mater.* **22,** 149–154. ISSN: 0897-4756 (Jan. 2010).

172. Cimatu, K. A., Mahurin, S. M., Meyer, K. A. & Shaw, R. Nanoscale Chemical Imaging of Zinc Oxide Nanowire Corrosion. *J. Phys. Chem. C* **116,** 10405–10414. ISSN: 1932-7447 (May 2012).

173. Chen, X., Ng, A. M. C., Djurišić, A. B., Ling, C. C. & Chan, W. K. Hydrothermal treatment of ZnO nanostructures. *Thin Solid Films* **520,** 2656–2662. ISSN: 00406090 (Jan. 2012).

174. Kim, J., Jeong, H. S., Ahn, Y. H., Lee, S. & Park, J.-Y. Effects of humidity on the electrical characteristics of ZnO nanowire devices. *Phys. status solidi* **209,** 972–976. ISSN: 18626300 (May 2012).

175. Qi, J. *et al.* Dissolving behavior and electrical properties of ZnO wire in HCl solution. *RSC Adv.* **5,** 44563–44566. ISSN: 2046-2069 (2015).

176. David, C. A. *et al.* Dissolution Kinetics and Solubility of ZnO Nanoparticles Followed by AGNES. *J. Phys. Chem. C* **116,** 11758–11767. ISSN: 1932-7447 (May 2012).

177. Jiang, C. & Hsu-Kim, H. Direct in situ measurement of dissolved zinc in the presence of zinc oxide nanoparticles using anodic stripping voltammetry. *Environ. Sci. Process. Impacts* **16,** 2536–2544. ISSN: 2050-7887 (2014).

178. Yadav, K., Mehta, B. R., Lakshmi, K. V., Bhattacharya, S. & Singh, J. P. Tuning the Wettability of Indium Oxide Nanowires from Superhydrophobic to Nearly Superhydrophilic: Effect of Oxygen-Related Defects. *J. Phys. Chem. C* **119,** 16026–16032. ISSN: 1932-7447 (July 2015).

179. Yadav, K., Mehta, B. R., Bhattacharya, S. & Singh, J. P. A fast and effective approach for reversible wetting-dewetting transitions on ZnO nanowires. *Sci. Rep.* **6,** 35073. ISSN: 2045-2322 (Dec. 2016).

180. Egerton, R., Li, P. & Malac, M. Radiation damage in the TEM and SEM. *Micron* **35,** 399–409. ISSN: 09684328 (Aug. 2004).

181. Aronov, D. & Rosenman, G. Surface energy modification by electron beam. *Surf. Sci.* **601,** 5042–5049. ISSN: 00396028 (Nov. 2007).

182. Aronov, D., Molotskii, M. & Rosenman, G. Electron-induced wettability modification. *Phys. Rev. B* **76,** 035437. ISSN: 1098-0121 (July 2007).

183. Torchinsky, I. & Rosenman, G. Wettability Modification of Nanomaterials by Low-Energy Electron Flux. *Nanoscale Res. Lett.* **4,** 1209–1217. ISSN: 1931-7573 (Oct. 2009).

184. Yoshiie, T., Iwanaga, H., Shibata, N., Ichihara, M. & Takeuchi, S. Orientation dependence of electron–irradiation damage in zinc oxide. *Philos. Mag. A* **40,** 297–301. ISSN: 0141-8610 (Aug. 1979).

185. Seshadri, K. *et al.* Electron-Beam-Induced Damage in Self-Assembled Monolayers. *J. Phys. Chem.* **100,** 15900–15909. ISSN: 0022-3654 (Jan. 1996).

186. Botman, A., Mulders, J. J. L. & Hagen, C. W. Creating pure nanostructures from electron-beam-induced deposition using purification techniques: a technology perspective. *Nanotechnology* **20,** 372001. ISSN: 0957-4484 (Sept. 2009).

187. Djenizian, T., Santinacci, L. & Schmuki, P. Electron beam-induced carbon masking for electrodeposition on semiconductor surfaces. *Appl. Phys. Lett.* **78,** 2940–2942. ISSN: 0003-6951 (May 2001).

188. Torchinsky, I., Molotskii, M. & Rosenman, G. Induced superhydrophobicity in ZnO nanomaterial. *J. Nanoparticle Res.* **12,** 2427–2433. ISSN: 1388-0764 (Sept. 2010).

189. Sabayev, V., Aronov, D., Oster, L. & Rosenman, G. Electron-induced surface reactivity modification in Zinc oxide-based thin films. *Appl. Phys. Lett.* **93,** 144104. ISSN: 0003-6951 (Oct. 2008).

190. Snyder, R. G. & Scherer, J. R. Band structure in the C–H stretching region of the Raman spectrum of the extended polymethylene chain: Influence of Fermi resonance. *J. Chem. Phys.* **71,** 3221–3228. ISSN: 0021-9606 (Oct. 1979).

191. Gong, Y.-T., Li, B.-H., Pei, T., Lin, C.-H. & Lee, S. Raman investigation on carbonization process of metal-organic frameworks. *J. Raman Spectrosc.* **47,** 1271–1275. ISSN: 03770486 (Oct. 2016).

192. Socrates, G. *Infrared and Raman characteristic group frequencies: tables and charts* ISBN: 978-0-470-09307-8. doi:10.1002/jrs.1238. arXiv: arXiv:1011.1669v3. http://doi.wiley.com/10.1002/jrs.1238 (John Wiley & Sons, Chichester, Oct. 2001).

193. Halford, R. S. Motions of Molecules in Condensed Systems: I. Selection Rules, Relative Intensities, and Orientation Effects for Raman and Infra-Red Spectra. *J. Chem. Phys.* **14,** 8–15. ISSN: 0021-9606 (Jan. 1946).

194. Milano, G. *et al.* Unravelling Resistive Switching Mechanism in ZnO NW Arrays: The Role of the Polycrystalline Base Layer. *J. Phys. Chem. C* **122,** 866–874. ISSN: 1932-7447 (Jan. 2018).

195. Yuan, F., Zhang, Z., Pan, L. & Xu, J. A Combined Modulation of Set Current With Reset Voltage to Achieve 2-bit/cell Performance for Filament-Based RRAM. *IEEE J. Electron Devices Soc.* **2,** 154–157. ISSN: 2168-6734 (Nov. 2014).

196. Muenstermann, R. *et al.* Correlation between growth kinetics and nanoscale resistive switching properties of SrTiO3 thin films. *J. Appl. Phys.* **108,** 124504. ISSN: 0021-8979 (Dec. 2010).

197. Moriyama, T., Yamasaki, T., Ohno, T., Kishida, S. & Kinoshita, K. Resistance given by tiling grain surface with micro surface structures in polycrystalline metal oxide. *J. Appl. Phys.* **120,** 215302. ISSN: 0021-8979 (Dec. 2016).

198. Yao, I.-C., Lee, D.-Y., Tseng, T.-Y. & Lin, P. Fabrication and resistive switching characteristics of high compact Ga-doped ZnO nanorod thin film devices. *Nanotechnology* **23,** 145201. ISSN: 0957-4484 (Apr. 2012).

199. Shen, X., Puzyrev, Y. S. & Pantelides, S. T. Vacancy breathing by grain boundaries—a mechanism of memristive switching in polycrystalline oxides. *MRS Commun.* **3,** 167–170. ISSN: 2159-6859 (Sept. 2013).

200. Chang, W.-y. *et al.* Unipolar resistive switching characteristics of ZnO thin films for nonvolatile memory applications. *Appl. Phys. Lett.* **92,** 022110. ISSN: 0003-6951 (Jan. 2008).

201. Zhuge, F. *et al.* Improvement of resistive switching in Cu/ZnO/Pt sandwiches by weakening the randomicity of the formation/rupture of Cu filaments. *Nanotechnology* **22,** 275204. ISSN: 0957-4484 (July 2011).

202. Chiu, F.-C., Li, P.-W. & Chang, W.-Y. Reliability characteristics and conduction mechanisms in resistive switching memory devices using ZnO thin films. *Nanoscale Res. Lett.* **7,** 178. ISSN: 1556-276X (2012).

203. Conti, D. *et al.* Resistive switching in sub-micrometric ZnO polycrystalline films. *Nanotechnology* **30,** 065707. ISSN: 0957-4484 (Feb. 2019).

204. Tsai, L.-T., Chiu, S.-P., Lu, J. G. & Lin, J.-J. Electrical conduction mechanisms in natively doped ZnO nanowires (II). *Nanotechnology* **21,** 145202. ISSN: 0957-4484 (Apr. 2010).

205. Stiller, M., Barzola-Quiquia, J., Zoraghi, M. & Esquinazi, P. Electrical properties of ZnO single nanowires. *Nanotechnology* **26,** 395703. ISSN: 0957-4484 (Oct. 2015).

206. Ma, Y.-J. *et al.* Hopping conduction in single ZnO nanowires. *Nanotechnology* **16,** 746–749. ISSN: 0957-4484 (June 2005).

207. Hu, Y. *et al.* Observation of a 2D Electron Gas and the Tuning of the Electrical Conductance of ZnO Nanowires by Controllable Surface Band-Bending. *Adv. Funct. Mater.* **19,** 2380–2387. ISSN: 1616301X (Aug. 2009).

208. Chen, C.-Y. *et al.* Probing Surface Band Bending of Surface-Engineered Metal Oxide Nanowires. *ACS Nano* **6,** 9366–9372. ISSN: 1936-0851 (Nov. 2012).

209. Nishimura, H. Impurity Conduction in the Intermediate Concentration Region. *Phys. Rev.* **138,** A815–A821. ISSN: 0031-899X (May 1965).

210. Norton, P. Formation of the Upper Hubbard Band from Negative-Donor-Ion States in Silicon. *Phys. Rev. Lett.* **37,** 164–168. ISSN: 0031-9007 (July 1976).

211. Chang, P.-C. & Lu, J. G. Temperature dependent conduction and UV induced metal-to-insulator transition in ZnO nanowires. *Appl. Phys. Lett.* **92,** 212113. ISSN: 0003-6951 (May 2008).

212. Mott, N. F. *Metal-Insulator Transitions* 2nd. ISBN: 020321059X 9780203210598 (CRC Press, 1990).

213. Fan, Z. & Lu, J. G. Zinc Oxide Nanostructures: Synthesis and Properties. *J. Nanosci. Nanotechnol.* **5,** 1561–1573. ISSN: 15334880 (Oct. 2005).

214. Yang, Y. *et al.* Size Dependence of Dielectric Constant in a Single Pencil-Like ZnO Nanowire. **12,** 10–13 (2012).

215. Liu, L. *et al.* Oxygen vacancies: The origin of n-type conductivity in ZnO. *Phys. Rev. B* **93,** 235305. ISSN: 2469-9950 (June 2016).

216. Goldberger, J., Sirbuly, D. J., Law, M. & Yang, P. ZnO Nanowire Transistors. *J. Phys. Chem. B* **109,** 9–14. ISSN: 1520-6106 (Jan. 2005).

217. Opoku, C. *et al.* Fabrication of field-effect transistors and functional nanogenerators using hydrothermally grown ZnO nanowires. *RSC Adv.* **5,** 69925–69931. ISSN: 2046-2069 (2015).

218. Milano, G. *et al.* Self-limited single nanowire systems combining all-in-one memristive and neuromorphic functionalities. *Nat. Commun.* **9,** 5151. ISSN: 2041-1723 (Dec. 2018).

219. Milano, G., Boarino, L. & Ricciardi, C. Junction properties of single ZnO nanowires with asymmetrical Pt and Cu contacts. *Submitted.*

220. Chiquito, A. J. *et al.* Back-to-back Schottky diodes: the generalization of the diode theory in analysis and extraction of electrical parameters of nanodevices. *J. Phys. Condens. Matter* **24,** 225303. ISSN: 0953-8984 (June 2012).

221. Osvald, J. Back-to-back connected asymmetric Schottky diodes with series resistance as a single diode. *Phys. status solidi* **212,** 2754–2758. ISSN: 18626300 (Dec. 2015).

222. Liu, Y. *et al.* Approaching the Schottky–Mott limit in van der Waals metal–semiconductor junctions. *Nature* **557,** 696–700. ISSN: 0028-0836 (May 2018).

223. Brillson, L. J. & Lu, Y. ZnO Schottky barriers and Ohmic contacts. *J. Appl. Phys.* **109,** 121301. ISSN: 0021-8979 (June 2011).

224. Ji, X. *et al.* The modulation of grain boundary barrier in ZnMgO/ZnO heterostructure by surface polar liquid. *Sci. Rep.* **4,** 4185. ISSN: 2045-2322 (May 2015).

225. Raffone, F., Risplendi, F. & Cicero, G. A New Theoretical Insight Into ZnO NWs Memristive Behavior. *Nano Lett.* **16,** 2543–2547. ISSN: 1530-6984 (Apr. 2016).

226. Yang, Y. *et al.* Observation of conducting filament growth in nanoscale resistive memories. *Nat. Commun.* **3,** 732. ISSN: 2041-1723 (Jan. 2012).

227. Tsuruoka, T. *et al.* Redox Reactions at Cu,Ag/Ta 2 O 5 Interfaces and the Effects of Ta 2 O 5 Film Density on the Forming Process in Atomic Switch Structures. *Adv. Funct. Mater.* **25,** 6374–6381. ISSN: 1616301X (Oct. 2015).

228. Valov, I. *et al.* Nanobatteries in redox-based resistive switches require extension of memristor theory. *Nat. Commun.* **4,** 1771. ISSN: 2041-1723 (Dec. 2013).

229. Hsiung, C.-P. *et al.* Formation and Instability of Silver Nanofilament in Ag-Based Programmable Metallization Cells. *ACS Nano* **4,** 5414–5420. ISSN: 1936-0851 (Sept. 2010).

230. Simms, B. A. & Zamponi, G. W. Neuronal Voltage-Gated Calcium Channels: Structure, Function, and Dysfunction. *Neuron* **82,** 24–45. ISSN: 08966273 (Apr. 2014).

231. Clapham, D. E. Calcium Signaling. *Cell* **131,** 1047–1058. ISSN: 00928674 (Dec. 2007).

232. Menzel, S., Tappertzhofen, S., Waser, R. & Valov, I. Switching kinetics of electrochemical metallization memory cells. *Phys. Chem. Chem. Phys.* **15,** 6945. ISSN: 1463-9076 (2013).

233. Raffone, F. & Cicero, G. Does platinum play a role in the resistance switching of ZnO nanowire-based devices? *Solid State Ionics* **299,** 93–95. ISSN: 01672738 (Jan. 2017).

234. Zhang, R. *et al.* Enhanced non-volatile resistive switching in suspended single-crystalline ZnO nanowire with controllable multiple states. *Nanotechnology* **27,** 315203. ISSN: 0957-4484 (Aug. 2016).

235. Yang, Y. *et al.* Electrochemical dynamics of nanoscale metallic inclusions in dielectrics. *Nat. Commun.* **5,** 4232. ISSN: 2041-1723 (Dec. 2014).

236. Valov, I. & Tsuruoka, T. Effects of moisture and redox reactions in VCM and ECM resistive switching memories. *J. Phys. D. Appl. Phys.* **51,** 413001. ISSN: 0022-3727 (Oct. 2018).

237. Tsuruoka, T. *et al.* Humidity effects on the redox reactions and ionic transport in a Cu/Ta 2 O 5 /Pt atomic switch structure. *Jpn. J. Appl. Phys.* **55,** 06GJ09. ISSN: 0021-4922 (June 2016).

238. Lübben, M., Wiefels, S., Waser, R. & Valov, I. Processes and Effects of Oxygen and Moisture in Resistively Switching TaO x and HfO x. *Adv. Electron. Mater.* **4,** 1700458. ISSN: 2199160X (Jan. 2018).

239. Heisig, T. *et al.* Oxygen Exchange Processes between Oxide Memristive Devices and Water Molecules. *Adv. Mater.* **30,** 1800957. ISSN: 09359648 (July 2018).

240. Tsuruoka, T. *et al.* Effects of Moisture on the Switching Characteristics of Oxide-Based, Gapless-Type Atomic Switches. *Adv. Funct. Mater.* **22,** 70–77. ISSN: 1616301X (Jan. 2012).

241. Celano, U. *et al.* Imaging the three-dimensional conductive channel in filamentary-based oxide resistive switching memory. *Nano Lett.* **15,** 7970–7975. ISSN: 15306992 (2015).

242. Sze, S. & Ng, K. K. *Physics of Semiconductor Devices* **4,** 44. ISBN: 9780470068328. doi:10.1002/0470068329. http://linkinghub.elsevier.com/retrieve/pii/S0026269282800360%20http://doi.wiley.com/10.1002/0470068329 (John Wiley & Sons, Inc., Hoboken, NJ, USA, Oct. 2006).

243. Cheung, S. K. & Cheung, N. W. Extraction of Schottky diode parameters from forward current-voltage characteristics. *Appl. Phys. Lett.* **49,** 85–87. ISSN: 0003-6951 (July 1986).

244. Norde, H. A modified forward I - V plot for Schottky diodes with high series resistance. *J. Appl. Phys.* **50,** 5052–5053. ISSN: 0021-8979 (July 1979).

245. Olikh, O. Y. Review and test of methods for determination of the Schottky diode parameters. *J. Appl. Phys.* **118,** 024502. ISSN: 0021-8979 (July 2015).

246. Karataş, Ş., Altındal, Ş., Türüt, A. & Özmen, A. Temperature dependence of characteristic parameters of the H-terminated Sn/p-Si(1 0 0) Schottky contacts. *Appl. Surf. Sci.* **217,** 250–260. ISSN: 01694332 (July 2003).

247. Karataş, Ş., Altındal, Ş., Türüt, A. & Çakar, M. Electrical transport characteristics of Sn/p-Si schottky contacts revealed from I–V–T and C–V–T measurements. *Phys. B Condens. Matter* **392,** 43–50. ISSN: 09214526 (Apr. 2007).

248. Pakma, O., Tozlu, C., Kavasoglu, N., Kavasoglu, A. S. & Ozden, S. I–V–T analysing an inhomogeneous Au/Poly(4-vinyl phenol)/p-Si structure with a double Gaussian distribution of barrier heights. *J. Sol-Gel Sci. Technol.* **58,** 244–250. ISSN: 0928-0707 (Apr. 2011).

249. Sharma, M. & Tripathi, S. K. Study of barrier inhomogeneities in I–V-T and C-V-T characteristics of Al/Al 2 O 3 /PVA:n-ZnSe metal–oxide–semiconductor diode. *J. Appl. Phys.* **112,** 024521. ISSN: 0021-8979 (July 2012).

250. Modi, B. P. & Dhimmar, J. M. *The temperature dependent ideality factor effect on I-V characteristics of Schottky diode* in *2012 1st Int. Conf. Emerg. Technol. Trends Electron. Commun. Netw.* (IEEE, Dec. 2012), 1–6. ISBN: 978-1-4673-1627-9. doi:10.1109/ET2ECN.2012.6470063. http://ieeexplore.ieee.org/document/6470063/.

251. Werner, J. H. & Güttler, H. H. Barrier inhomogeneities at Schottky contacts. *J. Appl. Phys.* **69,** 1522–1533. ISSN: 0021-8979 (Feb. 1991).

252. Chand, S. & Kumar, J. Evidence for the double distribution of barrier heights in Pd2Si/n-Si Schottky diodes from I –V –T measurements. *Semicond. Sci. Technol.* **11,** 1203. ISSN: 0268-1242 (Mar. 1996).

253. Özdemir, A. F., Turut, A. & Kökçe, A. The double Gaussian distribution of barrier heights in Au/ n -GaAs Schottky diodes from I – V – T characteristics. *Semicond. Sci. Technol.* **21,** 298–302. ISSN: 0268-1242 (Mar. 2006).

254. Von Wenckstern, H. *et al.* Mean barrier height of Pd Schottky contacts on ZnO thin films. *Appl. Phys. Lett.* **88,** 092102. ISSN: 0003-6951 (Feb. 2006).

Appendix A

Additional data on the tuning of ZnO NW surface wetting properties

Reference paper:

[162] *Milano, Gianluca, et al. "Tuning ZnO Nanowire Dissolution by Electron Beam Modification of Surface Wetting Properties." The Journal of Physical Chemistry C 122.14 (2018): 8011-8021*

A.1 Selectivity of the e-beam induced modification of surface wetting properties

E-beam treatment allows a selective tuning of the surface wetting properties of single selected ZnO NWs. This can be obtained by simply exposing to the e-beam only selected areas of the sample in a SEM chamber. For example, a single selected ZnO NW on a SiO_2 substrate was exposed to e-beam irradiation. After that the sample was immersed in water, the morphology of the e-beam treated NW and the untreated NWs in the surroundings was investigated. As can be observed from Figure A.1, only the e-beam irradiated NW in the red rectangle was not corroded after water interaction while the unirradiated NWs in the surrounding exhibited corrosion.

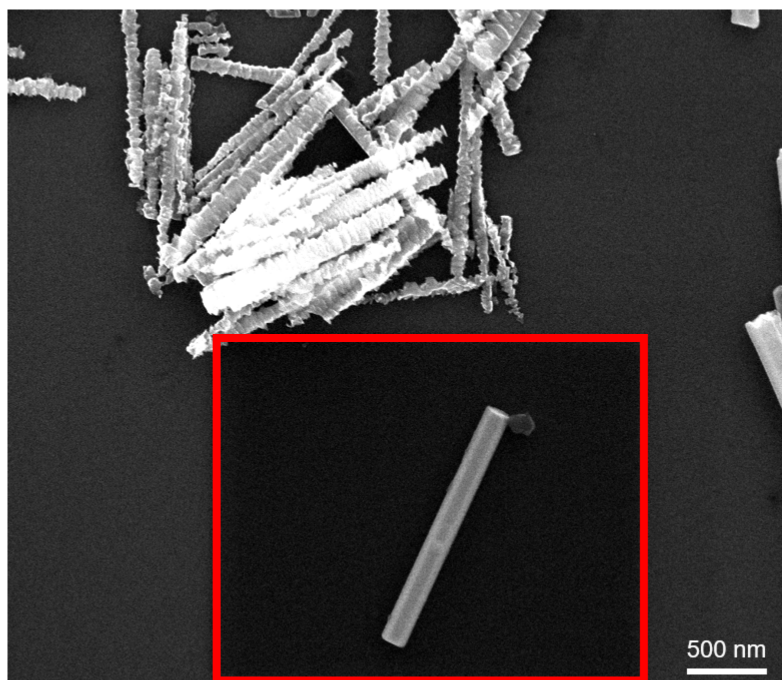

Figure A.1: Selectivity of the modification of surface wetting properties by e-beam irradiation. SEM image of ZnO NWs dispersed on a SiO_2 substrate after 60 min of interaction with water. The area surrounded by the red rectangle was previously e-beam treated. Adapted from [162].

A.2 Effect of plasma treatment

The initial hydrophilicity of the ZnO surfaces can be restored by performing an oxygen plasma treatment (40 W, 60 s). This procedure allows the removal of organic species previously bounded to the surface of ZnO nanostructures by e-beam irradiation. Indeed, NWs that were e-beam irradiated and then exposed to an oxygen plasma experienced again dissolution if immersed in water, as can be seen in Figure A.2. Note that an increased corrosion rate was observed, since almost complete dissolution already occurred after 60 min of water interaction. Probably, this is a consequence of an enhanced surface reactivity immediately after the plasma treatment. These observations demostrated the reversibility of the discussed mechanism of tuning the surface wetting properties of ZnO NWs.

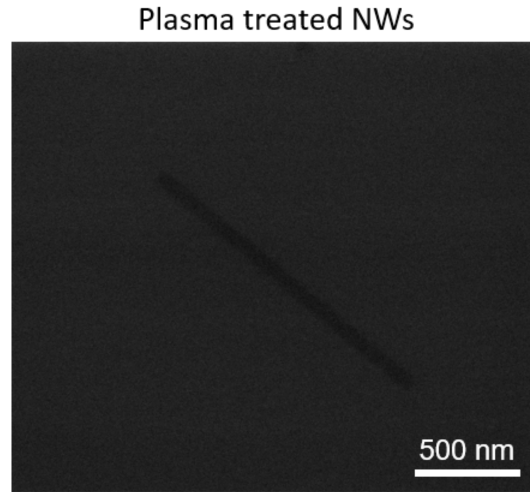

Figure A.2: SEM image of a ZnO NW that was e-beam treated, then treated with an oxygen plasma and subsequently exposed to deionized water for 60 min. Only some residues of ZnO can be observed as a consequence of an almost complete dissolution. Adapted from [162].

A.3 Analysis of e-beam induced chemical changes by means of Raman mapping

In order to further investigate changes in the Raman spectra of e-beam treated ZnO NWs, Raman mapping was performed. For this purpose, a selected portion of vertically aligned ZnO NW arrays was exposed to e-beam and subsequently Raman mapping was performed across this area, as reported in Figure A.3 a. Raman mapping revealed that surface modifications were not punctual but occurred all over the exposed area, further confirming the previously discussed selectivity of this treatment. For a detailed discussion about the change of Raman spectra after e-beam modification refer to section 4.4. As reported in Figure A.3 b and c, an increase of both peak intensity and area was observed in the G peak only in the irradiated area, as a consequence the e-beam induced carbonization of organic species on the ZnO surface. Similarly, the M-C stretching band showed higher intensity only in the irradiated area (Figure A.3 d) due to the formation of Zn-C bonds induced by e-beam energy. Furthermore, two more resolved peaks in the CH region were observed all over the irradiated area, as can be observed from Figure A.3 e where the I_{2925}/I_{2890} ratio is mapped. Instead, color map in Figure A.3 f confirmed that electron beam irradiation was not responsible for generation of defects since no relevant differences in the LO/E_2 ratio can be observed over the analyzed area.

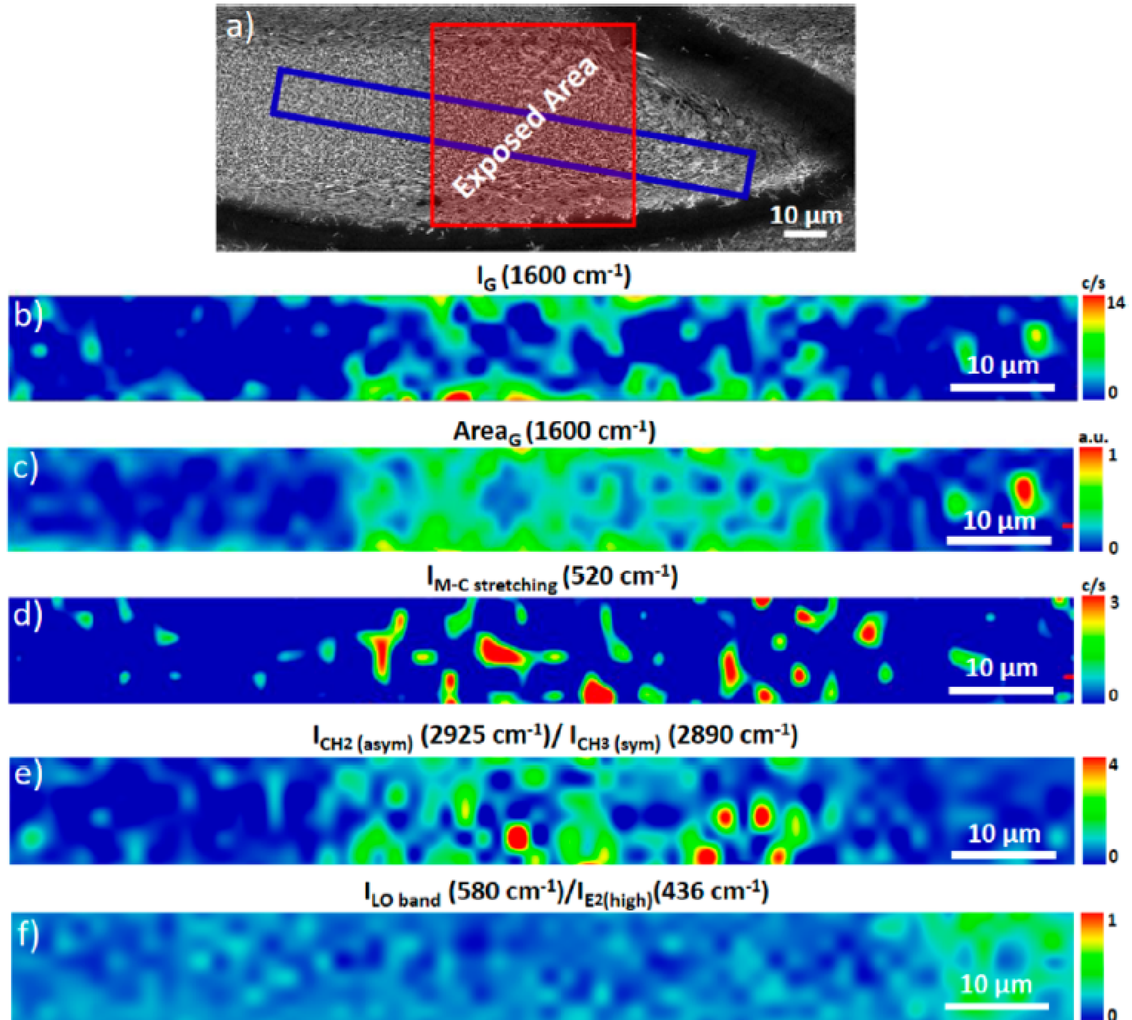

Figure A.3: Selectivity of the modification of surface wetting properties by e-beam irradiation investigated by Raman spectroscopy. SEM image of vertically aligned ZnO NWs where electron beam irradiation was performed (red square) and investigated by means of Raman mapping (blue rectangle). Raman map of b) peak intensity and c) peak area of the G band (1600 cm^{-1}); d) M-C stretching band intensity (520 cm^{-1}); e) intensity ratio map of peaks located at 2925 cm^{-1} and 2890 cm^{-1} (CH region); f) LO band over E_2^{high} peak intensity ratio map. Adapted from [162].

Appendix B

Additional electrical characterization of ZnO NW arrays and polycrystalline base layer

Reference paper:

[194] *Milano, Gianluca, et al. "Unravelling Resistive Switching Mechanism in ZnO NW Arrays: The Role of the Polycrystalline Base Layer." The Journal of Physical Chemistry C 122.1 (2017): 866-874.*

B.1 Electroforming process in ZnO NW arrays

An electroforming step was performed in order to initialize the bipolar resistive switching behaviour of ZnO NW arrays contacted by means of Pt electrodes. A typical example of electroforming process of these devices in presented in Figure B.1. Initially, the application of voltage sweeps resulted in a decrease of the device resistance, as reported in Figure B.1 a where the device is in a lower resistance state after step 4. After this first cycle, a RESET process occurred and the device was turned again to a HRS (Figure B.1 b). After that, the device exhibited an unstable behaviour as reported in Figure B.1 c), and few cycles were necessary to stabilize the electrical characteristic. After few stabilization cycles, the device exhibited stable resistive switching, as reported in Figure B.1 c. Note that a similar procedure was necessary to stabilize all the tested electrical devices based on ZnO NW arrays.

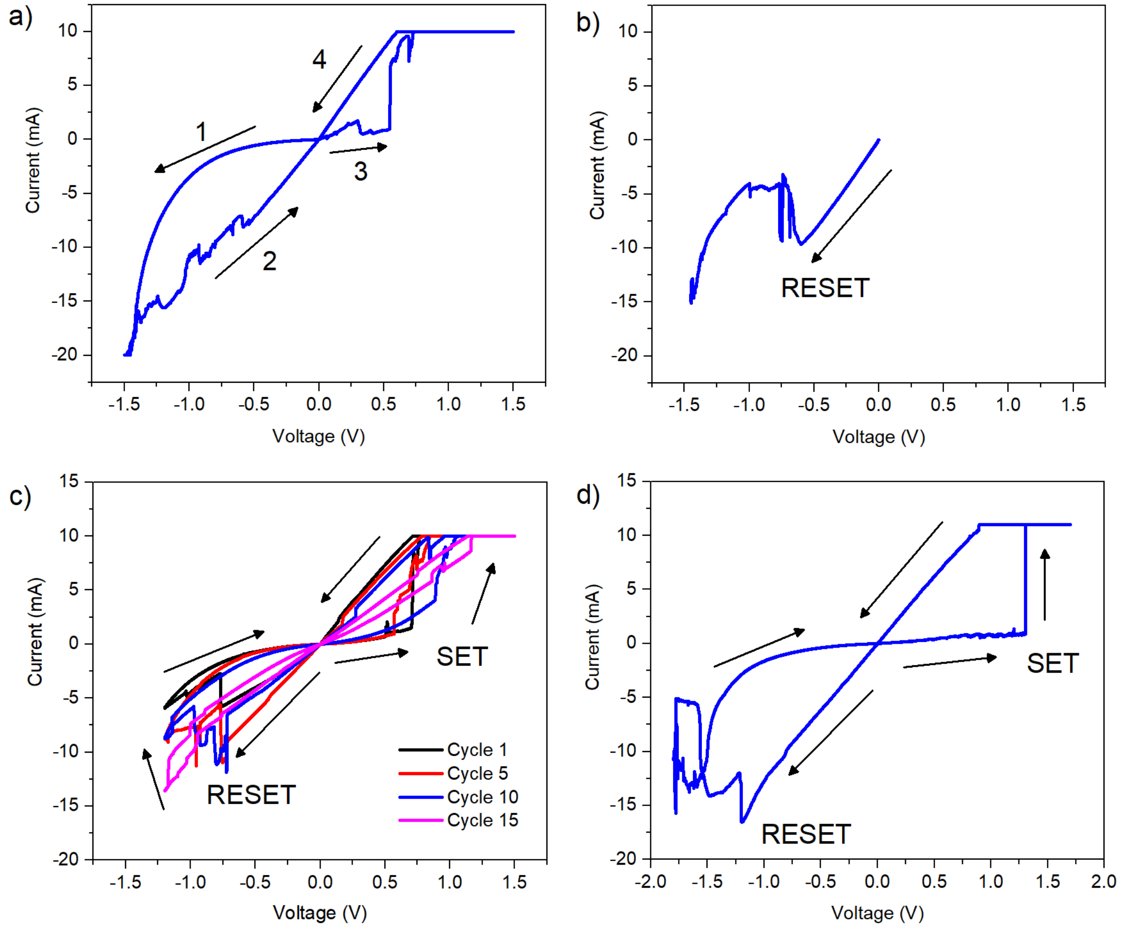

Figure B.1: Electroforming of ZnO NW arrays with Pt electrodes. a) First electroforming cycle and b) the following RESET process. c) Stabilization cycles are necessary before that the device exhibited stable characteristics. d) Bipolar resistive switching characteristic after stabilization. Adapted from [194].

B.2 Resistive switching and compliance current

Resistive switching characteristics are influenced by the externally imposed compliance current (CC). Indeed, the imposed CC influences the filament morphology. In case of ZnO NW arrays, while a linear (ohmic) LRS was observed by imposing a high CC, as reported in Figure 5.5 where CC=11 mA was imposed, low CC resulted in a non-linear LRS, as can be seen by imposing CC=3 mA (Figure B.2 a). Moreover, it is necessary to notice that low values of CC resulted in unstable resistive switching behaviour over cycling, as investigated by means of endurance test that is reported in Figure B.2 b. Here, high variability of LRS and HRS was observed.

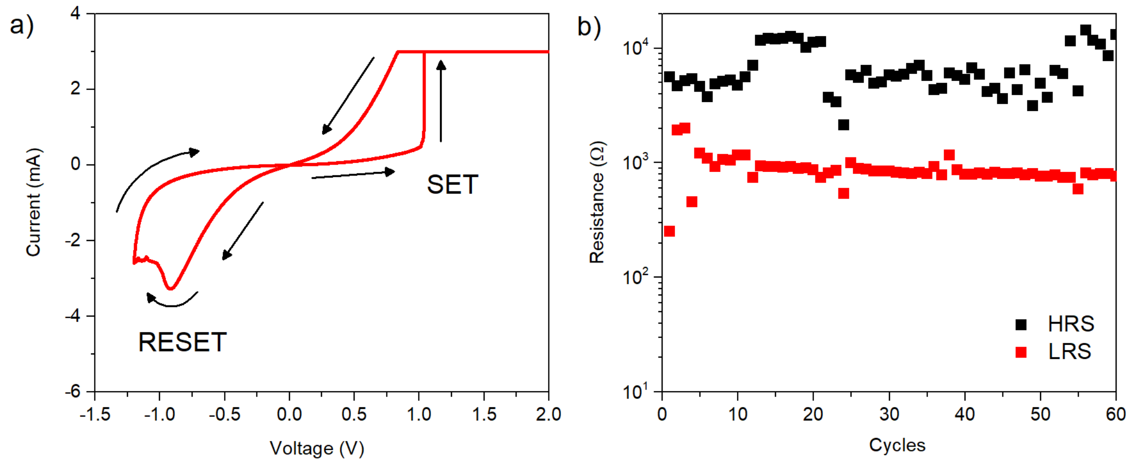

Figure B.2: Resistive switching behaviour of ZnO NW arrays for low applied CC. a) I-V characteristic obtained by imposing a CC of 3 mA and b) endurance properties of the device under these conditions (resistance read at 0.1 V). Adapted from [194].

B.3 Resistive switching and voltage polarity

As a consequence of the symmetric Pt/ZnO/Pt structure, a SET process can be induced also in negative polarity (see Figure B.3) if the conductive channel formation is forced to occur when a negative polarity is applied to the top electrode.

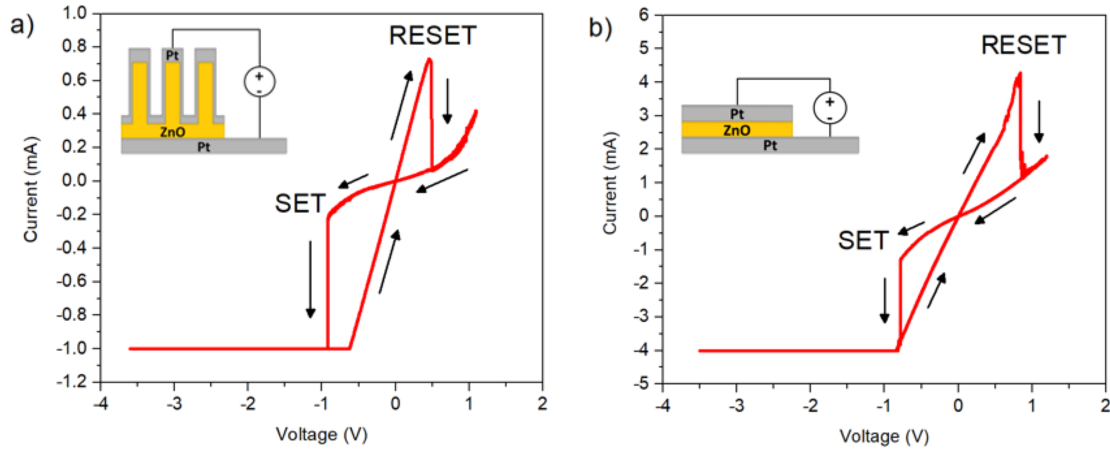

Figure B.3: Resistive switching and voltage polarity. Bipolar resistive switching of a) ZnO NW arrays and b) ZnO base layer with SET process induced with negative polarity applied to the top electrode. Adapted from [194].

B.4 Resistive switching and base layer thickness

ZnO polycrystalline base layers with high thickness exhibited also resistive switching behaviour. In order to investigate this aspect, a ZnO polycrystalline base layer with thickness of ~ 320 nm was considered. A SEM image of the base layer is reported in Figure B.4 a. Despite the high tickness compared to conventional thin film based devices, these layers exhibited bipolar resistive switching characteristics, as reported in Figure B.4 b. Regardless of the high variability of resistance states (Figure B.4 c), it is interesting to notice that values of V_{SET} and V_{RESET} are similar to those obtained in case of base layer with lower thicknesses (refer to section 5.4). These results suggest that the crystallinity and the peculiar structural properties

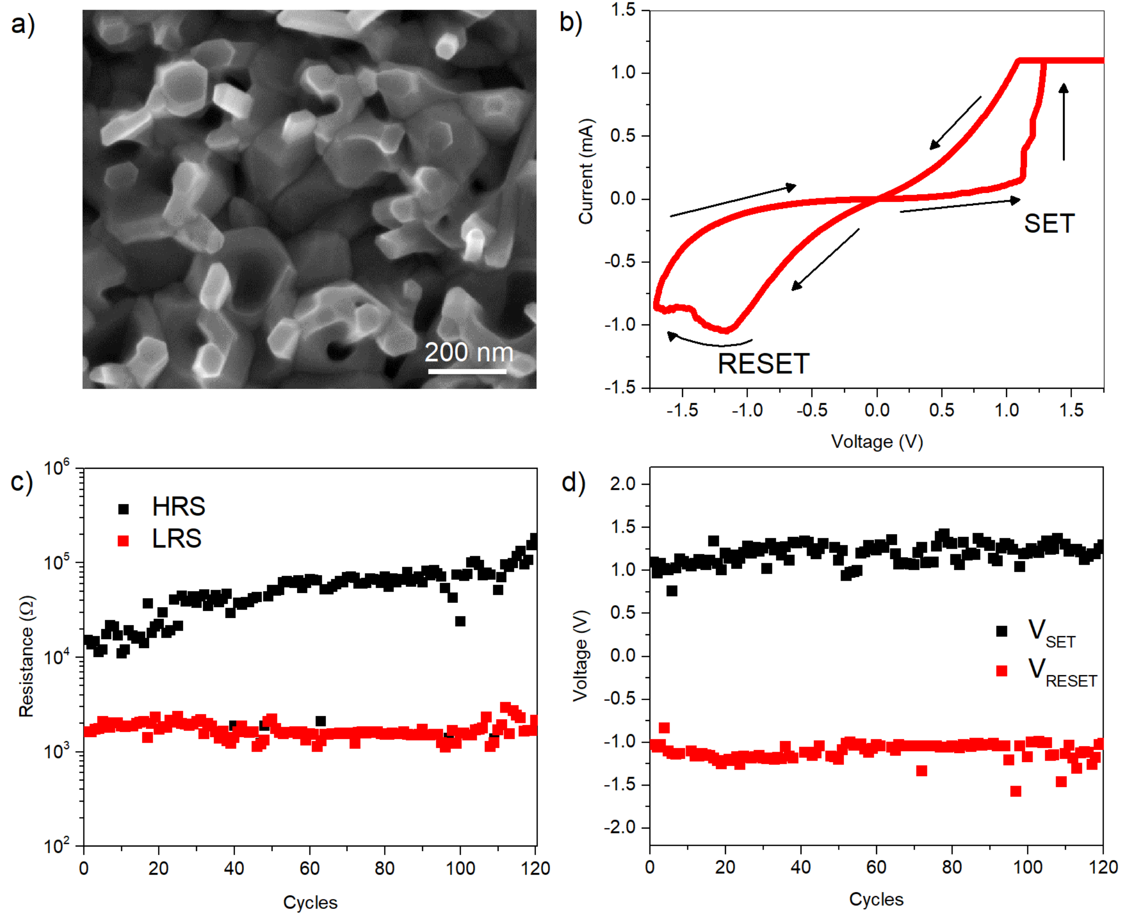

Figure B.4: Resistive switching in a polycrystalline base layer with thickness of ~ 320 nm and contacted by means of Pt electrodes. a) SEM image of the polycrystalline base layer. b) *I-V* characteristic showing bipolar resistive switching. c) Endurance properties (resistance read at 0.1 V) and d) V_{SET} and V_{RESET} as a function of cycles. Adapted from [194].

of ZnO with perpendicularly oriented grain boundaries facilitate resistive switching in films with considerably higher thicknesses than thin-films usually employed as active layers.

B.5 Effect of the metal electrodes

In order to investigate the influence of an electrochemically active electrode, the ZnO base layer was sandwiched in between a Cu electrochemically active electrode and the Pt electrochemically inert bottom electrode. In this configuration, a positive voltage applied to the Cu electrode results in anodic dissolution of Cu atoms with consequent migration of Cu^{z+} host ions in the ZnO matrix to form a metallic bridge in between electrodes that turns the device in a LRS. However, in this case both Cu^{z+} ions and oxygen vacancies are involved, resulting in a conductive path formed of an intermix of both Cu atoms and oxygen vacancies, as previously discussed by Celano et al. [241]. In this scenario, the competition in between the two effects are probably responsible for the high instability of resistive switching over cycing. Cu/ZnO base/Pt devices were characterized by low endurance, as reported in Figure B.5 a. In addition, it was observed that these devices can be easily formed by applying negative polarities to the Cu top electrode (Figure B.5 b), revealing that the switching mechanism is likely to be dominated by oxygen-related defects even in presence of an electrochemically active Cu electrode.

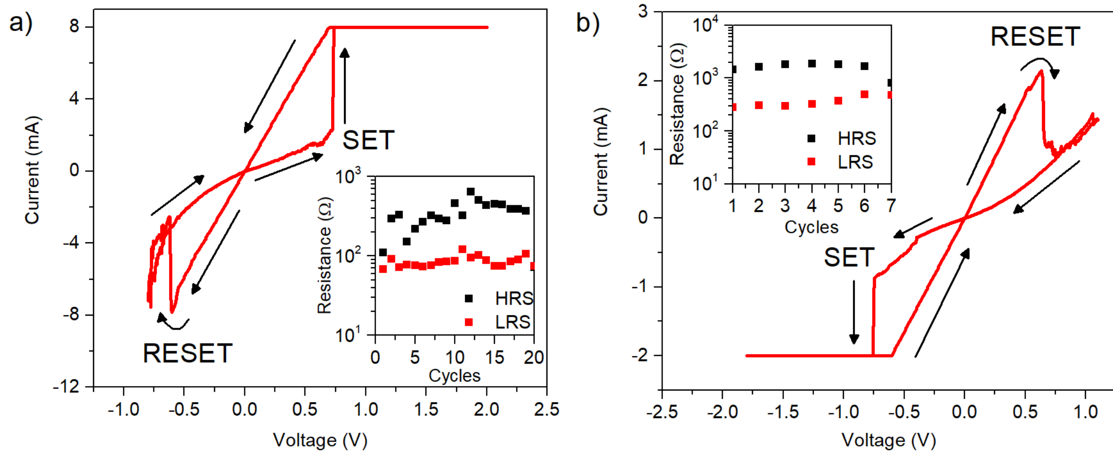

Figure B.5: Bipolar resistive switching of the ZnO base layer with Cu and Pt electrodes. A SET process in these devices can be induced both in a) positive and b) negative polarities applied to the electrochemically active Cu electrodes. In this cofiguration, devices exhibited high resistance variability over cycling with low endurance, as reported in the insets. Adapted from [194]

Appendix C

Junction properties of ZnO NWs with asymmetric electrodes: a case study

Reference paper:

[219] *Milano, Gianluca, et al. "Junction properties of single ZnO nanowires with asymmetrical Pt and Cu contacts", Submitted.*

As discussed in chapter 6 and 7, junction properties of metal-semiconductor interfaces play a key role in determining not only the electronic transport properties but also the physical mechanism of switching. By considering ZnO NWs, it was observed that in the low voltage regime Pt/ZnO junctions can be considered ohmic junctions while Ag/ZnO and Cu/ZnO interfaces give rise to Schottky contacts. In these terms, Ag/ZnO NW/Pt and Cu/ZnO NW/Pt devices can be considered diodes in the low voltage range. In this appendix, a detailed investigation of junction properties of Cu/ZnO NW/Pt devices is presented as a case study, by comparing different methods for junction paramenter extraction.

C.1 Theoretical background

By considering a Schottky barrier at a metal-semiconductor interface, the electronic conduction mechanism in forward voltage bias is regulated by thermionic emission. According to the thermionic emission (TE) model, the current flowing across the junction can be expressed as [242]:

$$I = I_0 \left[exp\left(\frac{q(V - IR_s)}{\eta k_b T} \right) - 1 \right] \tag{C.1}$$

where I_0 represents the saturation current, V the applied voltage to the junction, IR_s the voltage drop on the resistance R_s, q the charge, η the ideality factor that considers the deviation from the ideal TE model, k_b the Boltzmann constant and T the absolute temperature in Kelvin. The saturation current I_0 can be expressed as:

$$I = AA^*T^2exp\left(-\frac{q\phi_b}{k_bT}\right) \tag{C.2}$$

where A is the contact area, A^* the Richardson constant and ϕ_b the Schottky barrier height at zero bias. By considering I-V-T measurements, different methods for junction parameter extraction have been proposed, as discussed in the following.

C.1.1 Forward I-V-T method

By using this method, it is possible to estimate ϕ_b and η as a function of T by considering the semi-logaritmic plot of the I-V-T characteristics. For intermediate voltage bias where R_s can be neglected and under the condition qV - $IR_s \geq 3k_bT$, equation C.1 can be rewritten as:

$$I \cong I_0exp\left(\frac{qV}{\eta k_bT}\right) \tag{C.3}$$

In these terms, ϕ_b and η can be estimated from equation C.2 and C.3:

$$\phi_b = \left(\frac{k_bT}{q}\right) ln\left(\frac{AA^*T^2}{I_0}\right) \tag{C.4}$$

$$\eta = \frac{q}{k_bT}\frac{d(V)}{d(lnI)} \tag{C.5}$$

where I_0 can be obtained from the extrapolation of the current value at $V = 0$ from the lnI-V plot.

C.1.2 Cheung and Cheung method

An alternative way for the estimation of Schottky barrier parameters was proposed by Cheung and Cheung [243] by considering the forward I-V characteristics at high voltages where R_s cannot be neglected. In these conditions, the I-V characteristics can be described by the following equations [243]:

$$\frac{dV}{d(lnI)} = IR_s + \frac{\eta k_bT}{q} \tag{C.6}$$

$$H(I) = V - \frac{\eta k_bT}{q}ln\left(\frac{I}{AA^*T^2}\right) = IR_s + \eta\phi_b \tag{C.7}$$

In this case, R_s and η can be extracted by using eq. C.6. Then, ϕ_b values can be estimated from the previously obtained η values by using eq. C.7. Note that the self-consistency of this method can be evaluated by comparing R_s values obtained from eq. C.6 and C.7.

C.1.3 Norde method

Another approach for extraction of junction parameters was proposed by Norde [244]. In this case, an auxiliary function $F(V)$ have to be defined as [245]:

$$F(V) = \frac{V}{\gamma} + \frac{k_bT}{q} ln\left(\frac{I(V)}{AA^*T^2}\right) \tag{C.8}$$

where γ is an arbitrary parameter greater than η. From eq. C.8, ϕ_b and R_s can be estimated from the relations:

$$\phi_b = F(V_{min}) + \frac{\gamma - \eta}{\eta}\left(\frac{V_{min}}{\gamma} + \frac{k_bT}{q}\right) \tag{C.9}$$

$$R_s = \frac{(\gamma - \eta)k_bT}{qI_{min}} \tag{C.10}$$

where $F(V_{min})$ and V_{min} are the coordinates of the $F(V)$ minimum and I_{min} is the current at V_{min}.

C.1.4 Richardson method

In addition, Schottky barrier heigth can be evaluated by Arrhenius plot of the current saturation I_0, by considering the following relation:

$$ln\left(\frac{I_0}{T^2}\right) = ln(AA^*) - \left[\frac{q\phi_b}{k_bT}\right] \tag{C.11}$$

In these terms, the Schottky barrier height can be retrieved from the slope of I_0/T^2 curves while the Richardson constant A^* can be estimated from the intercept.

C.2 Schottky barrier properties

In order to evaluate Schottky barrier properties, a Cu/ZnO NW/Pt device (SEM image in Figure C.1 a) was measured in the voltage range ± 0.3 V over a wide range of temperatures in vacuum, from 460 K down to 81.5 K. Measured I-V-T characteristics are reported in Figure C.1 b. According to the previously described TE model, a decrease in the forward current was observed by decreasing temperature.

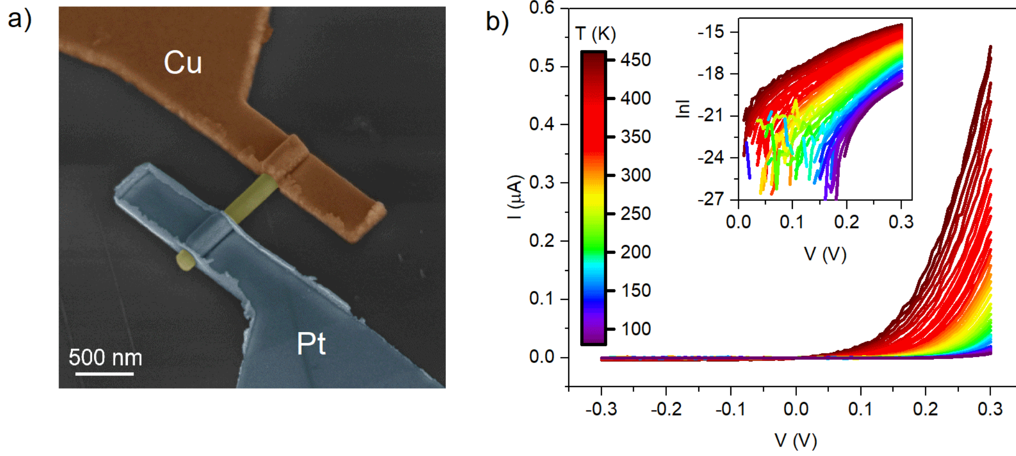

Figure C.1: Device structure and electrical characterization of Cu/ZnO NW/Pt devices. a) SEM image of the device and b) I-V-T measurements performed in vacuum by biasing the Cu electrode and keeping the Pt electrode at ground. The lnI-V plot is presented as inset. Adapted from [219]

C.2.1 Ideality factor and Schottky barrier height

By adopting the previously described methods for the extraction of junction parameters, the temperature dependence of ideality factor and Schottky barrier height can be estimated from I-V-T characteristics. Results are reported in Figure C.2. As can be observed, the ideality factor decreased by increasing temperature while an opposite behaviour was reported for the Schottky barrier height, indicating a deviation from the pure TE model. In particular, by considering the ideality factor, good accordance in between the forward I-V-T method and the Cheung and Cheung method was observed, especially at high temperatures where η tends to 1. Instead, good accordance over the whole range of temperatures was observed in case of the Schottky barrier height calculated by means of different methods. In this case, the Schottky barrier was calculated to increase from $\sim 0.3\,\mathrm{eV}$ to $\sim 0.55\,\mathrm{eV}$ passing from 81.5 K to 460 K. Similar temperature dependent behaviour of η and ϕ were previously observed in a wide range of Schottky diode devices [246–250]. It is important to notice that the ideality factor deviation from 1 is particularly evident at low temperature, where other conduction mechanism such as field emission (FE) and tunnelling are likely to become more relevant, resulting in a deviation from the pure TE model. In addition, the dependence of Schottky barrier heigth and ideality factor on temperature can be strongly influenced by local inhomogeneities at the metal-semiconductor junction, resulting in low and high barrier areas over the whole interface [248, 249]. A potential fluctuation model can be used for describing these barrier inhomogeneities, assuming a normalized Gaussian distrubution of barrier

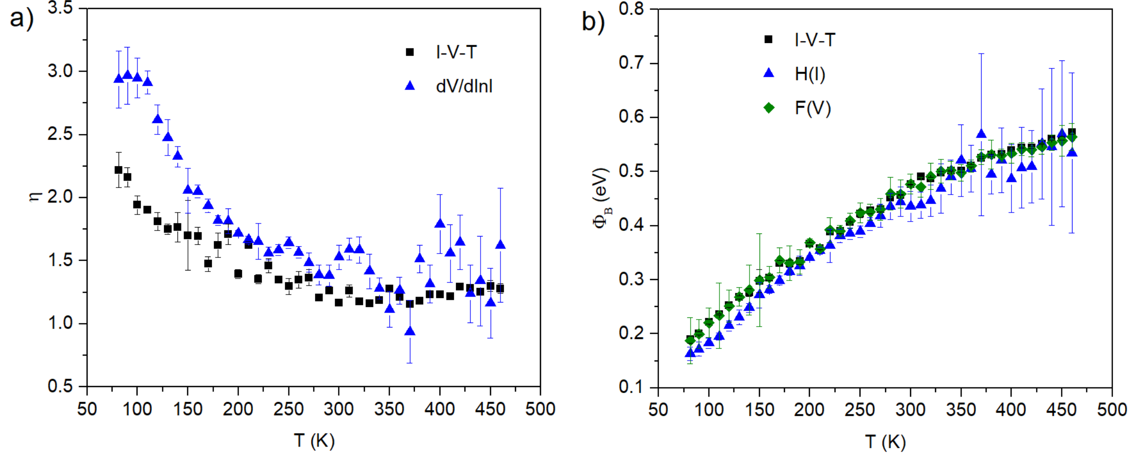

Figure C.2: Junction parameters as a function of temperature. Temperature dependence of a) ideality factor and b) Schottky barrier height calculted with different methods. Black points were obtained from the forward *I*-*V*-*T* method, blue points from the Cheung and Cheng method while green points from the Norde method. All data were estrapolated by considering *I*-*V*-*T* data presented in Figure C.1. Adapted from [219].

heights at the junction [251]:

$$P(\phi_b) = \frac{1}{\sigma_s\sqrt{2\pi}} exp\left(-\frac{(\phi_b - \overline{\phi_b})}{2\sigma_s^2}\right) \tag{C.12}$$

where $\overline{\phi_b}$ is the mean barrier height while σ_s is the standard deviation of the barrier distribution. By considering this model, the current can be obtained through the equation:

$$I(V) = \int_{-\infty}^{+\infty} I(\phi_b, V)P(\phi_b)d\phi \tag{C.13}$$

in which $I(\phi_b, V)$ is described by eq. C.1. In these terms, barrier heights reported in Figure C.2 b can be considered apparent barrier heigths that are expected to have a temperature dependence according to the equation:

$$\phi_{app} = \overline{\phi_b} - \frac{q\sigma_s^2}{2k_bT} \tag{C.14}$$

According to eq. C.14, ϕ_{app} is expected to have a linear dependence on $q/2k_bT$. However, as reported in Figure C.3, data can be interpolated by means of two lines suggesting the presence of two barrier height distributions (G_1 and G_2). Evidences of the presence of two Gaussian barrier height distributions were previously discussed also in other types of Schottky barrier [248, 252, 253]. In this scenario, it is

thus possible to extrapolate values of ϕ_b and σ_s for both distributions. In the G_1 region (190-460 K), $\overline{\phi_{b1}} = (0.733 \pm 0.003)$ eV and $\sigma_{s1} = (0.116 \pm 0.001)$ V while in the G_2 region (81.5-180 K) $\overline{\phi_{b2}} = (0.435 \pm 0.012)$ eV and $\sigma_{s2} = (0.061 \pm 0.002)$ V.

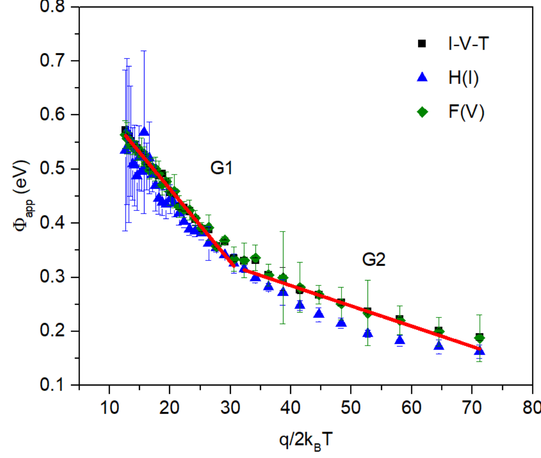

Figure C.3: Apparent barrier height estrapolated with different methods vs $q/2k_bT$. Black points were obtained from the forward I-V-T method, blue points from the Cheung and Cheng method while green points from the Norde method. Two straight lines (in red) are used to interpolate the whole range of data, according to the existance of two Gaussian distribution of barrier heights (G_1 and G_2). Adapted from [219].

By considering the Richardson method, $ln(I_0/T^2)$ vs q/k_bT is presented in Figure C.4 a. Even if linear behaviour is expected from eq. C.11, deviation from linearity was observed. This is attributable to the existance of a double Gaussian distribution, as previously discussed. Indeed, by taking into account G_1 and G_2 distributions, eq. C.11 can be modified as [248, 249]

$$ln\left(\frac{I_0}{T^2}\right) - \frac{q^2\sigma_s^2}{2k_b^2T^2} = ln(AA^*) - \left[\frac{q\phi_b}{k_bT}\right] \tag{C.15}$$

Thus, by considering the double Gaussian distributions G_1 and G_2 with standard deviations σ_{s1} and σ_{s2}, the modified Richardson plot can be obtained as reported in Figure C.4 b. In this case, linear interpolation of data in the G_1 and G_2 regions allows to obtain ϕ_b and A^* from the slope and intercept, respectively. By considering the Schottky barrier heigth, $\overline{\phi_{b1}} = (0.733 \pm 0.005)$ eV and $\overline{\phi_{b2}} = (0.43 \pm 0.02)$ eV in region G_1 and G_2, respectively. These results are in good accordance from the previous extimations from the ϕ_{app} vs $q/2k_bT$ plot. Instead, the Richardson constant was extimated to be 31 $Acm^{-2}K^{-2}$ in region G_1 and 26 $Acm^{-2}K^{-2}$ in region G_2. These values are in qualitative accordance with the theoretical value of

Richardson constant $A^* = 32 Acm^{-2}K^{-2}$ for ZnO [254]. As previously discussed in section ??, the Schottky barrier height at the Cu/ZnO energy barrier strongly differs from the theoretical value obtained from the Schottky-Mott rule as a consequence of the interface chemistry of the M-S junction. Indeed, the theoretical Schottky barrier height at the Cu/ZnO interface is 0.17 eV by considering the work function of Cu (4.46 eV) and the electron affinity of ZnO (4.29 eV).

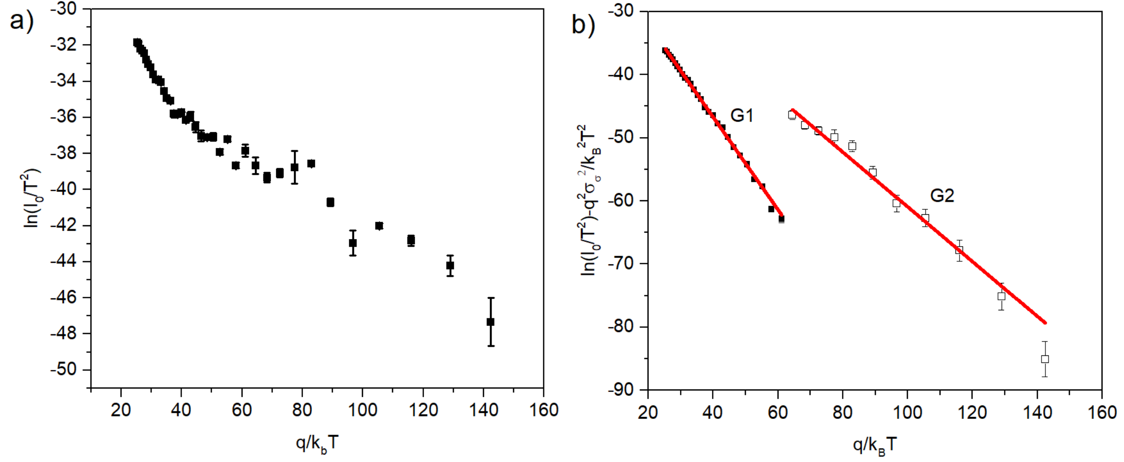

Figure C.4: Richardson plots. a) Ordinary richardson plot of $ln(I_0/T^2)$ vs q/k_bT and b) modified Richardson plot of $ln(I_0/T^2) - q^2\sigma_s^2/2k_b^2T^2$ vs q/k_bT. Deviation from linearity was observed in the ordinary Richardson plot. According to the existance of two Gaussian distribution of barrier heights (G_1 and G_2), two different values of standard deviations were considered in the modified Richardson plot. σ_{s1} was used in region G_1 (full squares) while σ_{s2} was used in region G_2 (open squares) Red lines represent linear interpolation of data. Adapted from [219].

C.3 Series Resistance

The series resistance R_s, that can be approximated as the NW resistance R_{NW} in first approximation, can be obtained by means of eq. C.6, C.7 and C.10. Results of series resistances derived from the previously discussed methods are reported in Figure C.5. As can be observed, resistance values were observed to decrease by increasing temperature, according to the semiconductor behaviour of the ZnO NW. As reported in the inset, where the NW conductivity was calculated by considering dimensions of the measured NW (diameter of 140 nm and electrode spacing of 410 nm), the conduction mechansim is in well agreement with a thermally activated mechansim of conduction as previously discussed in details in chapter 6. However, in this case the whole set of data was interpolated by means of a single conduction

channel. The obtained activation energy obtained was $E_a = (35 \pm 3)$ meV, in good agreement with the value of $E_a = (35.1 \pm 1.2)$ previously calculated in section 6.4 by considering Pt/ZnO/Pt devices.

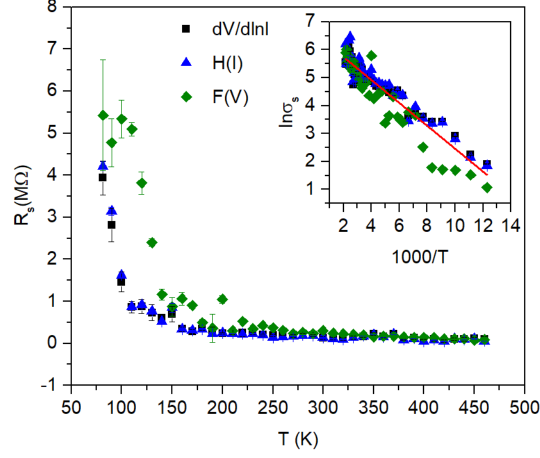

Figure C.5: Temperature dependence of R_s. Black and blue points were obtained from the Cheung and Cheng method while green points from the Norde method. The Arrhenius plot of data is presented as inset, where the whole set of data were interpolated according to a thermally activated mechanism of electronic conduction. Adapted from [219].

This Ph.D. thesis has been typeset by means of the TEX-system facilities. The typesetting engine was pdfLATEX. The document class was `toptesi`, by Claudio Beccari, with option `tipotesi=scudo`. This class is available in every up-to-date and complete TEX-system installation.